THE UNIVERSITY *of* EDINBURGH

Diagnostics and Analytical Modelling for Permanent-Magnet Synchronous Machines

Georgios Skarmoutsos

Doctor of Philosophy

THE UNIVERSITY OF EDINBURGH

2023

To my family and Nina, for everything.

Abstract

This dissertation proposes a novel diagnostic technique that utilises two air-gap search-coils which couple magnetically only under faulty conditions and can detect all the faults occurring in permanent-magnet machines. Furthermore, an existing search-coil-based method was expanded for detecting partial demagnetisation. A formula was developed which detects the frequency spectrum signatures under dynamic eccentricity, again in permanent-magnet machines. In the second stage, a magnetic field calculation algorithm was developed for the two basic rotor geometries of permanent-magnet synchronous machines, i.e. surface-mounted and surface-inset. The dissertation was divided into four parts and seven chapters. The first part is devoted on talking about the motivation that lead to work on this research subject and the objectives that this dissertation aims to satisfy. The fundamentals of permanent-magnet machines are also presented along the machine topologies that are used in this thesis to prove various methodologies and validate algorithms. In the second part, the diagnostic aspect of permanent-magnet machines is examined initially by doing a detailed literature review. The purpose of this comprehensive literature review is to become acquainted with the state-of-the-art fault diagnostic methods, identify what problems the existing methods cannot solve, and use the material for inspiration to develop a new diagnostic method. Afterwards, the review oriented the research towards the direction of air-gap flux monitoring, having single and double search-coil configurations validated using a Finite-Element Analysis software and experimental measurements taken by machines operating in a laboratory environment. The faults studied are partial demagnetisation, inter-turn fault and static-, dynamic- eccentricity. Lastly, based on the gaps found in the literature review, a method is presented to calculate the harmonics excited by the dynamic eccentricity fault. The third part of this thesis dealt with calculating the magnetic field distribution in radial-flux permanent-magnet machines with the surface, -mounted and -inset magnets. What triggered this research are the possibilities that come from having the components of the magnetic field distribution for every angle of the stator and rotor magnetic fields. This technique makes it possible to calculate all operational parameters that project the machines' performance. These are the Back-EMF and the types of torque, cogging, electromagnetic and reluctance. Finite-Element Analysis was used to validate the analytical subdomain model with great success. The fourth and last part of this dissertation summarises the conclusions and contributions of this work along with leads for future work.

Lay Summary

This work proposed a search-coil-based fault detection technique to detect various faults in permanent-magnet machines. The method consists of two single wired search coils wrapped around the rotational and stationary parts of the machine. The two search coils have a pitch such that the voltage on both search coils is zero under healthy conditions. The first search coil is wrapped around the stationary part of the machine and is open-circuited. The second search coil is closed-circuited and acts as an auxiliary coil to generate the signal that is sensed by the search coil placed in the stationary part of the machine and makes it possible to detect all faults. Every fault leaves a different signature on the stationary search coil, meaning that the voltage waveform has a different distribution, and the amplitude is associated with the fault severity. Furthermore, after investigation, it was concluded that without the auxiliary search coil, only the detection of faults which generate moving flux is possible with respect to the stationary part of the machine, i.e. reduction of the magnetic field strength of a magnet and static rotor eccentricity. Other diagnostic methods, such as the one which exploits the amplitude of harmonic components for detecting rotor faults, create additional harmonics which depend on the coil number of the stator winding. Under experimental conditions, the amplitude spectrum of a permanent-magnet machine has a really rich harmonic content, so by knowing the exact harmonics created by a fault, the condition monitoring process becomes more reliable. Another part of the work dealt with calculating the magnetic flux density waveform as a function of machines' exact dimensions and the characteristics of the magnetic materials. The major operational parameters of permanent-magnet machines can be calculated accurately by knowing the magnetic flux density distribution. This analysis divides the machine's geometry into different regions, and solves the governing equations in each subdomain. This work proposes a new way to model the magnetization function, expressed as a difference between two-step functions. The magnetization function is the input in the partial differential equation in the magnet region and the general solution is extracted. Interface conditions between the regions are used to extract the system of equations. Later the system of equations is written in a matrix format and solved using a mathematical software. By calculating the magnetic flux density is possible by knowing the coefficients at every point of every region. Varying the rotor position and calculating the magnetic flux density, lead to the computation various torque types and voltage waveforms. The created computer algorithm presents significant advantages with regard the computational time and the variation of the flexibility in the parameters given as input.

Publications

- G. A. Skarmoutsos, K. N. Gyftakis and M. Mueller, "Detecting Partial Demagnetization in AFPM Generators by Monitoring Speed and EMF Induced in a Supplemental Winding," in IEEE Transactions on Industrial Informatics, Jan 2021, vol. 18, no. 5, pp. 3295-3305, May 2022, doi: 10.1109/TII.2021.3053993.
- K. N. Gyftakis, S. A. Rasid, G. A. Skarmoutsos and M. Mueller, "The Demagnetization Harmonics Generation Mechanism in Permanent Magnet Machines With Concentrated Windings," in IEEE Transactions on Energy Conversion, vol. 36, no. 4, pp. 2934-2944, Dec. 2021, doi: 10.1109/TEC.2021.3071598.
- G. A. Skarmoutsos, K. N. Gyftakis and M. Mueller, "Analytical Prediction of the MCSA Signatures Under Dynamic Eccentricity in PM Machines With Concentrated Non-Overlapping Windings," in IEEE Transactions on Energy Conversion, vol. 37, no. 2, pp. 1011-1019, June 2022, doi: 10.1109/TEC.2021.3123662.
- K. N. Gyftakis, T. A. Garcia-Calva, G. A. Skarmoutsos, D. Morinigo-Sotelo, M. Mueller and R. d. J. Romero-Troncoso, "Detection and Identification of Demagnetization in PM Generators During Transient Conditions," 2021 IEEE 13th International Symposium on Diagnostics for Electrical Machines, Power Electronics and Drives (SDEMPED), 2021, pp. 345-350,
  doi: 10.1109/SDEMPED51010.2021.9605517.
- G. A. Skarmoutsos, K. N. Gyftakis and M. Mueller, "MCSA versus Flux Monitoring for Demagnetization Diagnosis in Axial-Flux PM Generators," 2021 IEEE 13th International Symposium on Diagnostics for Electrical Machines, Power Electronics and Drives (SDEMPED), 2021, pp. 119-125,
  doi: 10.1109/SDEMPED51010.2021.9605530.
- G. A. Skarmoutsos, K. N. Gyftakis and M. A. Mueller, "A New Approach to PM Machine Fault Diagnostics Using Two Magnetically-Coupled Search-Coils," 2022 International Conference on Electrical Machines (ICEM), Valencia, Spain, 2022, pp. 1616-1621, doi: 10.1109/ICEM51905.2022.9910704.
- T. A. Garcia-Calva, K. N. Gyftakis, G. A. Skarmoutsos, M. Mueller, D. Morinigo-Sotelo and R. d. J. Romero-Troncoso, "Advanced Signal Processing Techniques for Demagnetization Detection in PM Generators at Variable Speed," 2022 International Conference on Electrical Machines (ICEM), Valencia, Spain, 2022, pp. 1548-1554, doi: 10.1109/ICEM51905.2022.9910737.

- K. N. Gyftakis, T. A. Garcia-Calva, G. A. Skarmoutsos, D. Morinigo-Sotelo, M. Mueller and R. d. J. Romero-Troncoso, "Demagnetization Monitoring and Identification in PM Generators With Concentrated Windings During Transient Conditions," in IEEE Transactions on Industry Applications, 2022, doi: 10.1109/TIA.2022.3221699.
- K. N. Gyftakis, G. Skarmoutsos, I. Barajas-Solano, J. Burchell and M. Mueller, "Critical Aspects of Demagnetization Faults in Direct Drive Permanent Magnet Generators for Renewables," 2022 IEEE Energy Conversion Congress and Exposition (ECCE), Detroit, MI, USA, 2022, pp. 1-7, doi: 10.1109/ECCE50734.2022.9947661.

Acknowledgements

First and foremost, I would like to thank my supervisors, Associate Professor Konstantinos Gyftakis and Professor Markus Mueller, for all the support and fruitful conversations that contributed to completing this work. I would also like to thank the laboratory technician Jamie Graham for aiding with any experimental work and providing any necessary equipment to conclude the experiments. In particular, I would like to acknowledge my colleague Syidy Ab Rasid for his enormous help during the experiments and for helping solve various challenges, and for all the exciting conversations our interactions offered.

I gratefully acknowledge the financial support provided by the University of Edinburgh for making this work possible.

Finally, I would like to thank my family for supporting me in every decision I made and always being there for me. I would like to thank my partner Marina for supporting me during this process and for everything.

Declaration

I declare that this thesis was composed by myself, that the work contained herein is my own except where explicitly stated otherwise in the text, and that this work has not been submitted for any other degree or professional qualification except as specified.

Georgios Skarmoutsos

Contents

Figures and Tables

Figures

Tables

PART I

Introduction

Chapter 1

Introduction

1.1 The need for monitoring and modelling of PM machines

Permanent-magnet machines machines re-emerged during the last couple of decades with the development of the rare-earth magnets. Apart from high power density, efficiency and constant speed over a wide interval of mechanical charging, they offer precise speed and torque control. As a result, they became an attractive choice for electric traction applications, as well as generators in renewable energy harvesting applications. Machines used various applications, like in industries such as car production or oil extraction cannot shut down as the financial loss becomes too high. On the other hand, some of these faults can cause fatal accidents in transportation and other safety critical applications. Accounting the energy produced and consumed by electric machines, losses caused by faults and aged components constitute a major part of global energy waste. Therefore, the diagnosis of faults at an early stage is paramount to minimize these losses, prevent unscheduled shutdowns and accidents [1].

Generally, electric machines are operating in unfavorable environments and harsh operating conditions so they become susceptible to the appearance of a fault. A fault can be considered as any defect existing in any component of the machine. Specifically, for permanent-magnet machines the major components that are susceptible to a fault are the magnets [2], the axis and the bearings [3] and the stator winding [4]. More specifically, the common reasons that electric machines tend to fail in industrial environments are [5]:

- operation after the standard lifetime
- operation over the nominal power, voltage and current
- asymmetric supply of voltage
- supply of an unbalanced load
- electrical stress from fast switching inverters or unstable ground
- residual stress from manufacturing (eccentricity)
- mistakes during repairs
- harsh application environment (dust, water leaks, environmental vibration, chemical contamination, corrosion, high temperature and altitude).

In renewable energy harvesting applications like offshore wind-farms, it has been reported that that operations and maintenance costs for offshore wind farms could account for up to 30% of the energy costs [6]. Generally in all kind of wind turbines, operational and maintenance costs in the contribution from unforeseen drive train failures and account for up to 25% of the total increased cost of electricity [7]. The generator is a reliable component of a wind turbine, but its failure causes long periods and high economic losses, which serves as motivation for developing condition monitoring methods [7]. Furthermore, in such applications the faults in the systems are caused not only from the electrical generator but also from the gearbox between the turbine and the generator [8].

To speak of the statistics of fault occurrences, bearing faults account for between 21% and 95%, respectively, of all failures [9] in electrical machines, and for induction machines of the size and type used in wind turbines this figure can be higher than 45% [6]. Other statistical findings report 26% of the occurring faults to be reported as stator related in IEEE-IAS [10], 44% are specifically bearing related and 8% are rotor related. The survey was conducted for medium voltage 3-phase induction motors. Studies also show that axial-flux permanent-magnet generators that are used in wind energy suffer mainly from eccentricity and inter-turn fault [11].

The basic three common occurring faults in permanent-magnet machines and that are also studied in this thesis, are the eccentricity, inter-turn fault and demagnetization. Below the faults are briefly described and is explained why their detection in an early stage is meaningful and necessary for any application that the machine is used.

Eccentricity is the only existing fault in a brand new electric machine that is currently being tolerated in a severity up to 10% by the manufacturers [3]. This fault creates additional vibration and noise in the machine and due to the unbalanced magnetic pull, it can be increased gradually till the rotor starts touching with the stator [12]. A number of machines having eccentricity in a production space can increase the noise in the room significantly. Manufacturers suggest that an air-gap a level of 50% is considered to be a serious problem and that the motor should be immediately removed from production [13]. The types of eccentricity are the static, dynamic and their combination, mixed.

Inter-turn fault is a fault occurring on the stator region of electric machines and creates a local hotspot adding additional stress to the machine, leading to a lower life expectancy [4]. Stator failures generally are due to electrical, mechanical, thermal and environmental stress acting on the stator. The dielectric, corona, tracking and transient voltage conditions are some of the electrical stresses leading to inter-turn short circuit failures [14].

Demagnetization faults belong to the category of rotor faults and are considered a severe fault due to its impact in the overall torque of the machine and the additional thermal stress caused to the winding. The additional thermal stress to the machine is created due to the higher current demanded for the supply of the load. This fault is usually caused by the stator armature reaction field, increased temperature and corrosion. However, taking into account the up to date published surveys, the generator mechanism is not clear, as well as the demagnetization distribution on the magnets and the growth rate. Speaking of demagnetization generation mechanisms, studies have shown that oxidation and corrosion change the metallurgical structure of modern permanent-magnets, which leads to irreversible demagnetization. Other factors that can accelerate the demagnetization process can be considered the heat, humidity, and environments containing chlorides [2]. Lastly graduate aging, and damaging of the permanent-magnet, such as cracking can also reduce its magnetic flux. Since permeability of the material is close to air, breakage does not cause unbalanced inductances in the machine, so it behaves similarly to demagnetization caused by the traditional factors mentioned above [15].

The faults mentioned above create the following unwanted operational symptoms in permanent magnet and wound rotor synchronous machines which can also be considered [5]:

- unbalanced line currents and air-gap voltages
- higher overall temperature
- noise and axis mechanical vibration
- lower average torque
- lower efficiency - increased losses
- higher THD (Total Harmonic Distortion)
- lower induced voltage
- unbalanced magnetic pull

The above symptoms caused by faults can on the one hand be seen as further motivation to create additional and more effective condition monitoring methods and on the other hand as critical data to know when designing a fault detection scheme. According to what was discussed above, electric machines have a certain lifespan and this can vary according to the fault that was caused. So the need for monitoring the condition of an electric machine is without question necessary to avoid dangers in safety for transportation applications and high financial losses in production.

The design of diagnostic schemes is achieved by using modelling techniques such as mathematical methods and simulations such as the Finite-Element Analysis that can predict with great accuracy quantities under steady and variable state conditions. With Finite-Element Analysis the impact of a fault in an electric machine can be investigated accurately and reliably which is the first important step in designing a diagnostic method, since the fault symptoms can be considered as signatures that the method should be based on. However,

it is considered a time consuming modelling method, since the machine has to be designed and the periodicity of the machine cannot be exploited. In order to create a diagnostic method one has to investigate the impact of a fault on the electric machine and see what kind of trace is going to leave. So these techniques are considered the cornerstone for creating the major tools in emulating the behaviour of healthy and faulty machines and are proved extremely useful in the design process of condition monitoring schemes. Analytical modelling techniques can be either based on the subdomain model [16] or on magnetic equivalent circuit [17] method, or even their combination [18]. Their purpose is to provide results quicker by considering a certain geometry. Analytical models can also model faulty conditions such as rotor eccentricity [19, 20] and demagnetization [21].

1.2 Problem statement

As discussed above, condition monitoring of permanent-magnet machines is imperative due to the broad spectrum of applications that these machines found theirselves in. These machines are prone to fail after a certain number of working hours, so detecting any type of fault at an early age is imperative for applications which safety or enormous financial loss are in play.

The existing condition monitoring techniques are limited with respect to the amount of faults that they can detect [22], as each fault has a different magnetic impact on the machine. Diagnostic methods which monitor quantities directly measured appear to demand a higher complexity to extract the feature. Furthermore, they appear to find limitations on the monitoring of various faults and are more appropriate for monitoring a specific fault. Furthermore, the latter methods face also the limitation that cannot become generalised easily, due to the different winding topologies.

To overcome the above limitation, air-gap flux monitoring was introduced as an improvement of the conventional sensor-less diagnostic methods. This concept can exploit the magnetic flux in various positions, inside and outside of the machine so it has the ability to take into account the symptoms of a fault in greater detail [22, 1]. Nevertheless, these methods might be simpler but at the same time they fail to manage to detect all faults with the minimum amount of hardware - sensors. The only documented flux-based method that can detect all faults efficiently is documented in [23], although it requires a number of sensors equal to the number of coils of the machine. The latter makes the method impossible to implement in machines used for renewable energy harvesting like wind and wave, due to their high number of coils.

1.3 Objectives

The objectives of this work can be summarized below:

- Development of a cost-effective and industrially applied condition monitoring method to detect all the occurring faults on an early stage and avoid the catastrophic breakdown of the to be monitored permanent-magnet machine.
- Investigation whether any of the widely used condition monitoring methods that are currently used on industry can be improved any further. Improving a method can mean a number of things. For instance, improvement of the fault index sensitivity so that for the same fault severity to have a higher index. The latter will help on making a method capable of detecting faults on low severity levels. Another example can be considered if a method accounts all the manufacturing and operational features of the machine. More specifically, methods that utilise the amplitude spectrum of a quantity for monitoring and detection may not take account the number of machine coils, poles or the connection of the winding. After the investigation, if any method is found that accepts margins for improvement of any kind, like removing one of its limitations an effort will take place to enhance the method.
- Development of an analytical model which will provide more autonomy on modelling faults like the partial demagnetization fault. The main method for analytical modelling in permanent-magnet machines is the subdomain model which every space of interest is divided into regions. In every region an analytical solution is obtained and interface conditions are used to extract an analytical solution for the magneto-static field of each region.

1.4 Summary and thesis outline

The hereunto dissertation is structured as follows:

Chapter 2 offers an introduction to the basics of permanent-magnet machines and the machine topologies used in this thesis for diagnostics and modelling. The motivation for creating this chapter is to provide a smooth transition in regard to the used machines since a variety of machines was used for authoring the thesis.

Chapter 3 conducts a literature review about the faults that occur during the operation of permanent-magnet machines and the methods that have been developed for diagnosing them thus far. The motivation behind this chapter is to understand the impact of each fault in permanent-magnet machines and the mechanism and limitations of the state-of-the-art diagnostic methods. This will pave the way to gathering all the knowledge required to create a new diagnostic method that will be able to overcome the limitation of the current ones.

Chapter 4 proposes a novel diagnostic method which utilizes internal measurements of the magnetic flux to detect all faults which is achieved by using two search-coils in the two main components of a machine - the stationary and the rotational. Initially the chapter extends the single air-gap search-coil method by showing how to detect the partial demagnetization fault in permanent-magnet machines and its limitation on detecting static faults like inter-turn fault and static eccentricity. The limitation of the latter method created the motivation for the development of the diagnostic scheme with the magnetically-coupled search-coils. The proposed method is analysed using Finite-Element Analysis and is validated experimentally using a direct-drive 3-phase permanent-magnet generator designed for wind energy harvesting.

Chapter 5 conducts an effort to take the MCSA (Motor Current Signature Analysis) method one step further by correlating the frequencies that increase in amplitude during faulty conditions. MCSA still remains one of the most popular condition monitoring methods used in the industry due its easy implementation and effectiveness. The motivation behind this chapter came from the realisation that there is no specific formula that correlates the induced frequencies on the winding with the number of poles and coils of the machine. Each machine with different pole and coil combination produces different fault frequencies. This chapter proposes a method to calculate the latter frequencies under dynamic eccentricity which gives insight about which fault frequencies will increase in amplitude.

Chapter 6 proposes a two-dimensional analytical model to calculate the magnetic field distribution on the air-gap of permanent-magnet machines with the aid of Heaviside function. This chapter presents an alternative analytical subdomain model by expressing the magnetization functions in terms of a Heaviside function difference and inserting them in the partial differential equations. Piece-wise interface conditions were used to extract the final analytical solution. The motivation behind this work was to create an analytical model which will provide autonomy in terms of accounting reduction of the residual flux density in parts of a magnet. Models developed for surface -mounted and -inset machines. The analytical model was validated using 2-D Finite-Element Analysis.

Chapter 7 discusses the conclusions and contributions that were extracted by working on this area. Furthermore, future proposals for the continuation of this work are also proposed.

Chapter 2

Permanent-magnet machines

The aim of this chapter is to present and discuss the permanent-magnet machine topologies used on this dissertation. The two topologies used and explained on this work are the radial and axial-flux permanent-magnet machine. The principle of operation, the basic geometry and properties of the materials are discussed. Finally, the geometries of the machines used are presented.

2.1 Geometry of rotor and stator

Electric machines are devices which convert energy from mechanical to electrical and vice versa. The existence of a magnetic field between the stationary and rotational components accomplishes the energy conversion process. The space between these two components is called air-gap and is significant. In the case of permanent-magnet machines, the magnets create the main magnetic field.

Figure 2.1 shows the protogenic three-phase permanent-magnet motor with two magnet poles, three full-pitched coils and six slots. The rotor is the moving component and contains the magnets. The rotor can have surface mounted or buried magnets, and then there is the rotor back-iron and the shaft. The air gap is vital in electro-mechanical conversion process because it is where the magnetic energy is stored. The stator, the stationary part of the device, contains slots which contain the carrying current coils. The rest is parted by a ferromagnetic material, iron of high magnetic permeability. Because copper's permeability is equal to air's, in the positions of the coil-sides or slots, the useful magnetic flux density drops due to the reluctance increment. The reluctance is proportional to the air-gap length, and the air gap on the position of the slot becomes much higher. The latter generates electromagnetic noise which is mainly the cogging torque, which adds up a torque ripple component. To ease this phenomenon, designing iron tooth-tips will reduce the slotting effect's influence. These tooth-tips must be thick enough; otherwise, they will be converted into air for certain rotor positions due to the saturation effect. Furthermore, they create a slot-opening air gap that cannot be too small to be able to pass the wire into the slots. However, alternative designs [24] use slotless stator windings to eliminate the cogging torque signal. Each coil is a phase, in this

case; nevertheless, the number of coils or slots can vary according to pole number. In this case, the coils have a full pitch to exploit the whole magnetic flux generated by the magnets. Fractional pitch coils [25] is a method to shape the Back-EMF (Electro-Motive Force) of a motor by reducing the saturation harmonics at the cost of reducing the fundamental harmonic component. When the number of slots per pole per phase is not an integer, the machine has fractional slots [25], which have advantages in shaping the Back-EMF and reducing cogging torque.

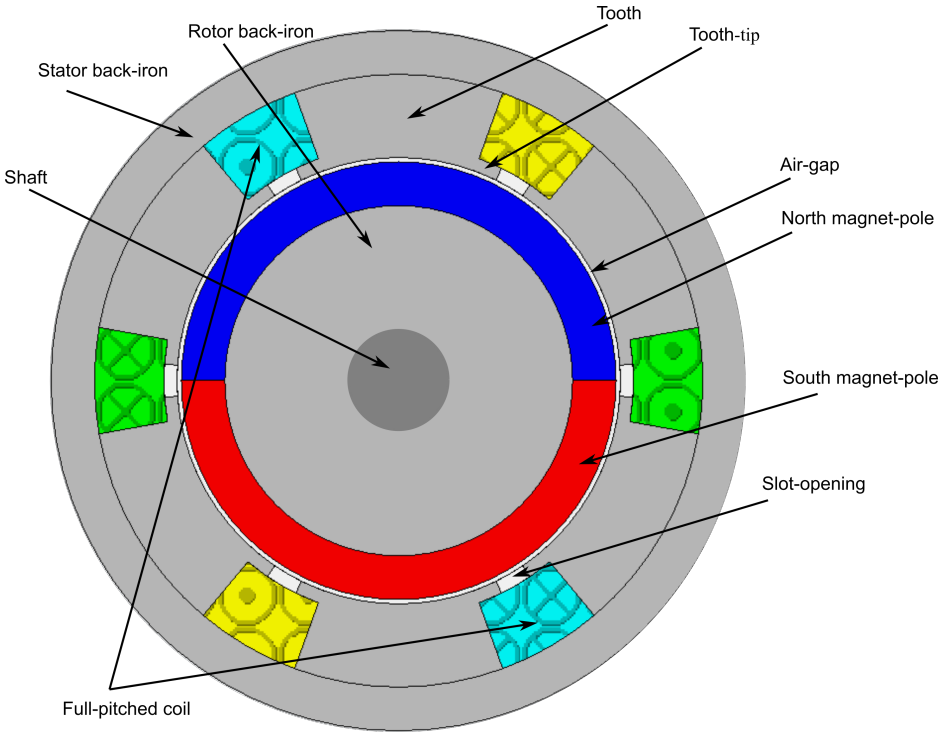

Figure 2.1: Fundamental 2-Dimensional geometry of a permanent-magnet machine.

By looking at the device from a mechanical point of view, Figure 2.2 presents the two sides of a permanent-magnet machine. One can see the bearings where the rotor sits, responsible for providing a low friction motion and keeping the air-gap constant. If the bearings are close to the leakage magnetic field created by the end winding or the magnets, they can get warm due to the eddy currents that they are induced on them. The increased temperature of the bearings will make the lubricant to evaporate faster. The above increases the maintenance demands and can lead to faults like rotor eccentricity, entailing a reduced lifespan of the machine [26]. An unaccounted feature for in the 2-dimensional view of the machine is the end-winding. The end-winding results from the twisted coil heads placing the coil from one slot to the other. Furthermore, the latter creates a magnetic flux which interferes with the magnetic flux produced by the permanent-magnets; however, it has a small influence on the performance of the machine but it distorts the higher harmonic content.

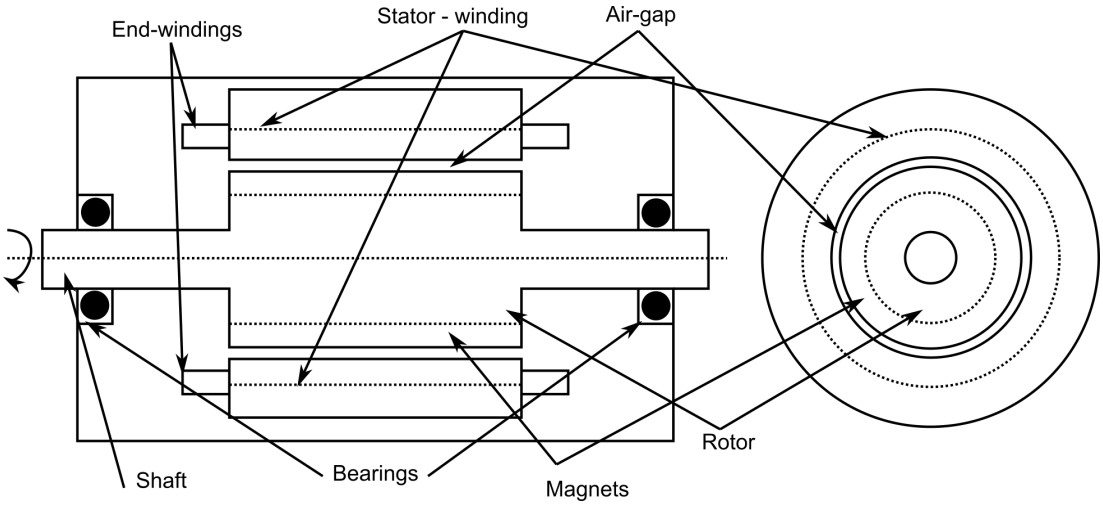

Figure 2.2: Sketch of the two sides of a radial-flux permanent-magnet machine.

2.2 Principle of operation

When we place three coils distributed in space with 120^o spatial phase difference and apply 3 sinusoidal shaped voltages with 120^o time difference, the stator creates a rotating magnetic field. The latter entails that if one leaves a ball made of iron inside the stator bore, the ball will start being attracted by the magnetic field and execute circular motion along the periphery of the stator. Depending on the pitch of the coils, the number of pole pairs in the stator can change. For instance, one can observe from Figure 2.3 that the coils of each phase have a pitch of 180^o, equal to the pole pitch. Expressing the quantity with a rotating vector represents the magnetic flux density of the stator $\overrightarrow{B}_S$. The magnets also create a magnetic flux density vector $\overrightarrow{B}_R$. Both magnetic fields rotate at the same speed, entailing the machine to gain the name 'synchronous'.

For generator operation, we rotate the rotor with a speed and the magnetic flux along the coils starts to vary, inducing an EMF voltage in the phase winding. The latter means that the magnetic flux density vector of the rotor leads one of the stator's. If the generator does not have a load, this means that there is not a current in stator coils, so there is not a magnetic field, and there is no mutual torque in the air gap. The stator winding is fed with a 3-phase voltage with a constant frequency for motor operation. The above creates a rotating magnetic field on the air gap in which its rotational speed depends on the frequency of the voltage. If the rotor is stationary, the stator poles attract or repel the rotor poles not long enough to produce force, meaning that the motor does not produce torque. In this case, there are two solutions. The first solution existed for many years and was used before discovering the three-phase voltage source with a variable frequency, i.e. the voltage inverter. It uses an auxiliary

motor that connects with the motor shaft and rotates at the same speed as the stator's rotating magnetic field. The second solution is to use a 3-phase voltage inverter which will gradually increase the voltage's frequency, so the rotor's speed will always be near the speed of the stator rotating magnetic field. The torque is given by the following equation [27]

$$\overrightarrow{\tau}_{ind} = ct \cdot \overrightarrow{B_R} \times \overrightarrow{B_S}, \tag{2.1}$$

where $\overrightarrow{\tau}_{ind}$, ct, $\overrightarrow{B}_S$ and $\overrightarrow{B}_R$ are the induced torque in the air-gap, a constant which depends on the machines' dimensions, and are the magnetic flux densities created by the magnets and stator, respectively. The air-gap torque depends on the cross product of the two magnetic flux density vectors.

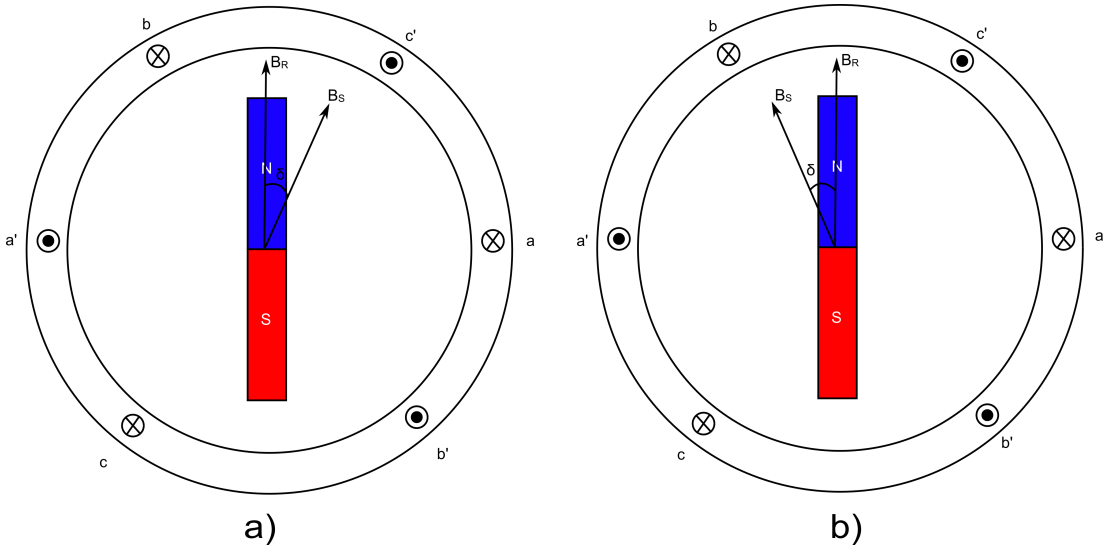

Figure 2.3: Sketch of a two-pole permanent-magnet synchronous a) generator and b) motor.

2.3 Types of permanent-machines

Permanent-magnet machines can be categorised concerning their shape, meaning whether the boundaries of the machine follow cartesian or cylindrical coordinates. Machines with cylindrical boundaries can be either radial-or axial- flux machines, and those with cartesian boundaries are linear.

2.3.1 Machines with cylindrical boundaries

As explained above, these machines belong to two categories that determine the direction of the useful magnetic flux density component. The component is responsible for the energy conversion process. In radial-flux machines is the radial component and in axial-flux machines the axial component. With respect to geometry, radial-flux PM machines fall into the categories

of internal and external rotor machines. The machine in Figure 2.1 is characterised as an internal rotor machine since the rotor is on its interior part. The latter is the primary design used in every application, which requires a rotational electric machine, hence considered the most well-studied. The other category is the machines with the exterior rotor, presented in Figure 2.4 and is an alternative topology mostly used in-wheel motors for electric traction [28].

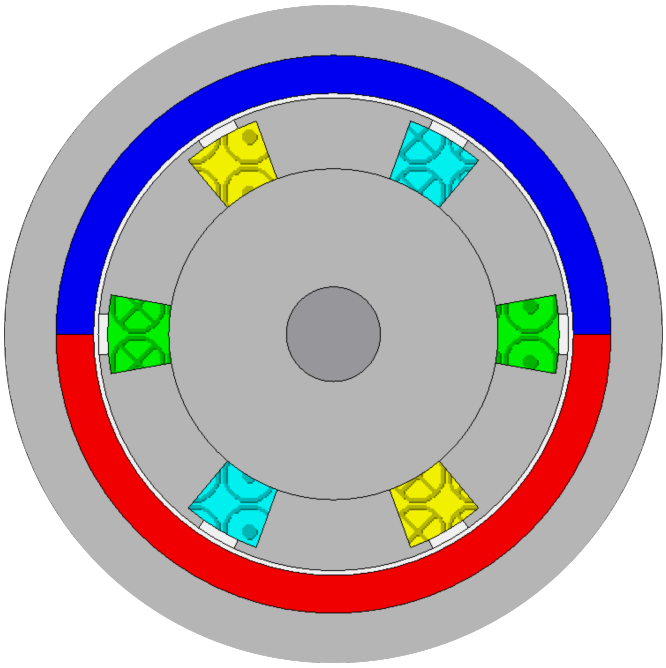

Figure 2.4: Sketch of a two-pole permanent-magnet synchronous external rotor machine.

The other type of machine with cylindrical boundaries is the axial-flux permanent-magnet (AFPM) machine, as illustrated in Figure 2.5. This permanent-magnet machine topology produces more power for the same volume and weight than the radial-flux permanent-magnet (RFPM) machine topology. However, the construction of this machine is much more challenging due to the attractive force between the discs. Furthermore, due to the shorter overall axial length, the ratio of machine diameter to length is high, which increases the probability of eccentricity [12]. More specifically, the AFPM machine has a smaller volume and less active material mass for a given power rating than the RFPM machine [29]. In RFPM machines, the torque is proportional to the square of the diameter times the axial length, and in AFPM machines is roughly the cube of the diameter [29]. The above-mentioned entails the power density advantage of axial-flux permanent-magnet machines is lost when the length-to-diameter ratio increases. Specifically, the power density advantage is lost near the point which the radius equals twice the length of comparing RFPM machine [29]. A remarkable advantage of the AFPM machines is that the power rating can be increased by stacking disc machines on the same shaft. The latter offers the advantage that the radius of the machine can be decreased by increasing the axial length, which can be useful for applications where there

are space constraints towards a dimension. As Figure 2.5b illustrates, each coil is a phase and the three different colours show the three different phases. This winding is overlapping as phase-coil has a span same as the pole span. Phase A is spanned from 0^o till 180^o and its colour is green. Phase B is spanned from 120^o till 300^o and its colour is light blue. Lastly, phase C is spannedf from 240^o till 60^o and of of yellow colour.

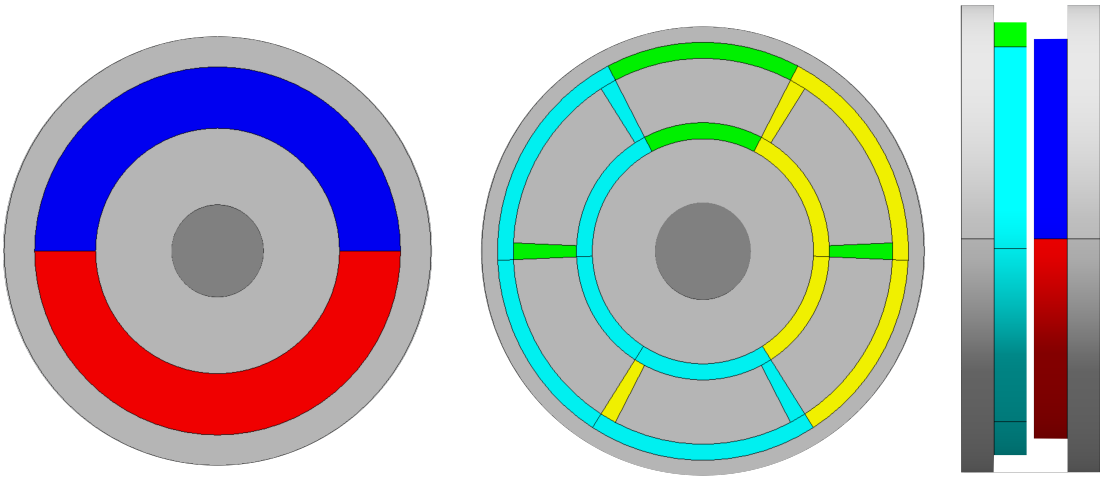

Figure 2.5: 2-Dimensional views of a 2 pole - 3 coil permanent-magnet axial-flux permanent-magnet machine, a) rotor with magnets b) stator with coils and c) axial view of the machine.

2.3.2 Machines with cartesian boundaries

These machines execute linear motion, so they are quite used in wave energy converters [30]. Figure 2.6 presents a sketch of a linear permanent-magnet machine. The rotor is composed of the back-iron, and the magnets which move linearly, so the magnetic flux varies along the coils. However, if the rotor starts moving on the side that departs, the coils will stay outside the magnetic flux, which will significantly impact the machine. To solve the above problem, a rotor with a higher length than the stator is used [30]. Furthermore, the latter increases the cost of the machine due to the increased need for permanent-magnet and ferromagnetic material.

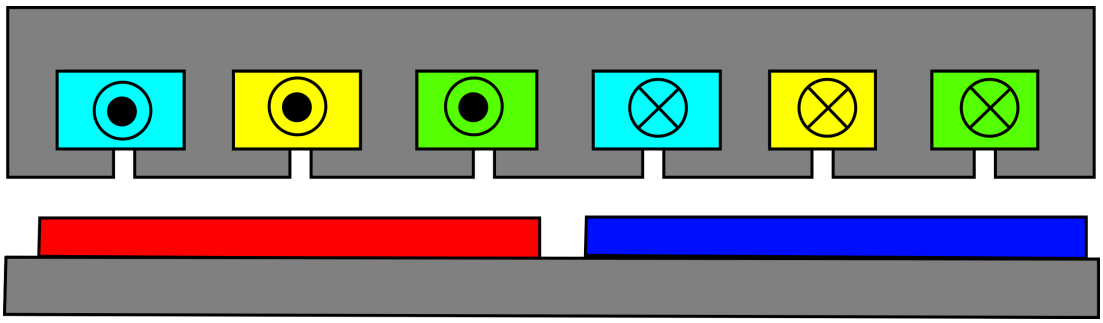

Figure 2.6: 2-Dimensional view of a linear permanent-magnet machine with 2 surface-mounted magnet poles and 6 slots.

2.4 Permanent-magnet materials used

This section presents the permanent-magnet materials used in this type of machines. Furthermore, the equations which correlate the magnetic flux density $\overrightarrow{B}$ and magnetic field intensity $\overrightarrow{H}$ are displayed. The magnetisation $\overrightarrow{M}$, expresses the magnetic field strength a magnet possesses if it was a coil carrying a current I.

The permanent-magnet materials used for machine manufacturing are alnico, ferrite (ceramic), samarium-cobalt, and neodymium-iron-boron (NdFeB). Ferrite types are popular because they are not expensive; however, they have low residual flux density which limits them to low-performance applications. On the other hand, the rare earth types, samarium-cobalt and Nd-Fe-B offer the highest performance, with the NdFeB taking the first position since they are cheaper than Samarium-Cobalt. Every magnetic material has a hysteresis loop or a B-H characteristic. The maximum energy produced by the magnet is defined by the number $(BH)_{max}$, which is the rectangle on the characteristic with maximum surface. The permanent-magnet is created by passing a magnetic field into a ferromagnetic material with a large hysteresis loop and then removing it. The material will have a residual or remanent magnetic flux density.

To obtain the two points of interest in the magnetic characteristic, i.e. the remanent magnetic flux density B_{rem} and the coercive magnetic field intensity H_c, two tests are taking place on the magnet [25]. For the first test, the two dipole edges of the magnet are 'shorted' using a ferromagnetic material of infinite permeability. The test converts magnetic field intensity equal to zero in the boundaries of the magnets. Hence, by measuring the magnetic flux density with a Gauss meter, the residual magnetic flux density of the magnet is measurable. This residual magnetic flux density is the maximum the magnet can produce by itself. The second test is to place the magnet in a medium with approximately zero magnetic permeability. More specifically, the latter entails that there will be no strong magnetic path since the magnetic flux lines always aim to follow the minimum reluctance path. This entails that the magnetic flux density on the boundaries of the magnet vanishes. At this point, the magnitude of the field intensity across the magnet is equal to the negative of the coercivity or coercive force, denoted H_c. The B-H characteristic of a magnetic material is presented in Figure 2.7 for 20^{o}C. The relation between the magnetic flux density and magnetic field intensity for NdFeB magnets is linear. The equation of the line for the 2nd quadrant is

$$B = \mu_0 \mu_r H + B_{rem}, \tag{2.2}$$

where μ_r is the slope of the characteristic in the second quadrant. The definition of the magnetisation of a permanent-magnet is

$$M = \frac{B_{rem}}{\mu_0}. \tag{2.3}$$

Accounting equations (2.2) and (2.3) the equation that yields is

$$B = \mu_0 \mu_r H + \mu_0 M. \tag{2.4}$$

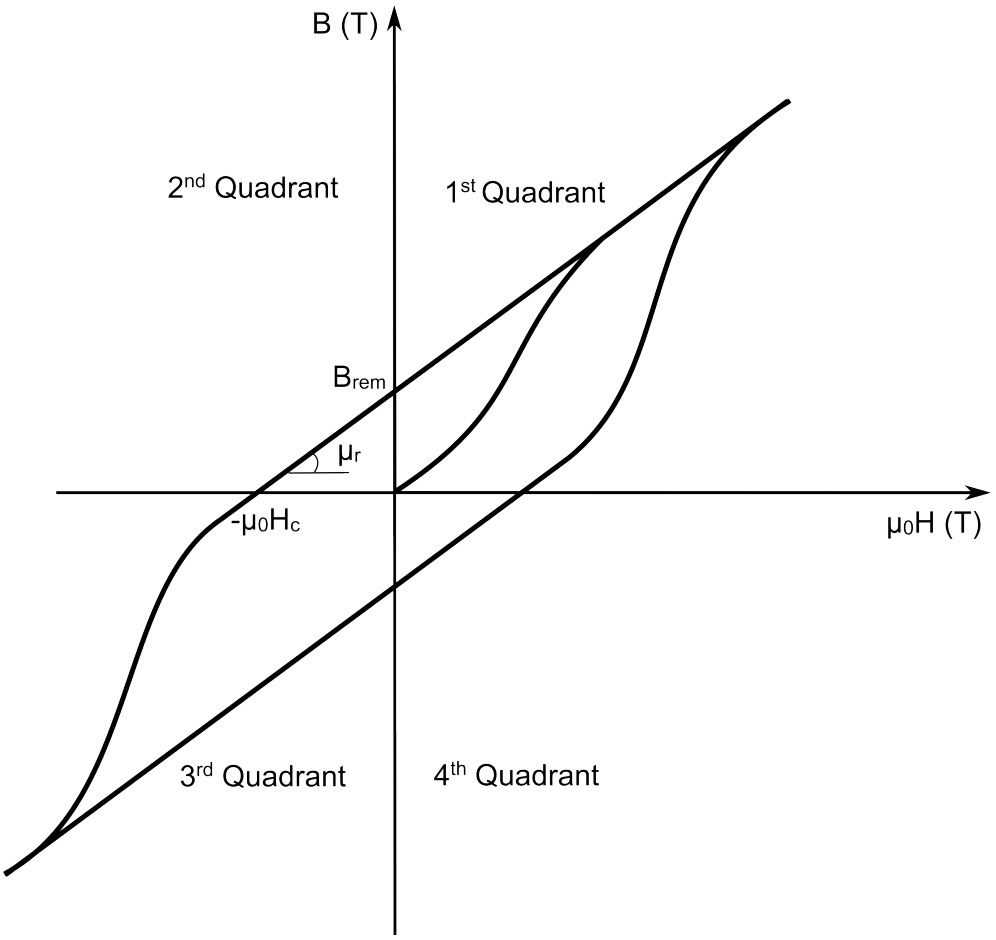

Figure 2.7: Magnetic characteristic of a permanent-magnet material with the key points emphasised.

The permeance coefficient P_c expresses the slope of a line drawn from the origin to the characteristic and is used to define the point of operation. More specifically, it expresses the equivalent permeance of the magnetic circuit so it depends on the magnet length and the airgap. For instance, when the magnet operates at the coercivity point, P_c is zero and infinite when the point of operation is at the remanence.

Rare earth magnets, like NdFeB (Neodymium-Ferrite-Boron) and SC (Samarium-Cobalt) have a straight demagnetisation line on the second quadrant, and the relative recoil permeability is slightly higher than unity. Ferrite magnets have a nonlinear demagnetisation characteristic on the second quadrant at room temperature for low permeance coefficient values [25]. Alnico magnets were the ones used before the rare earth magnets from the mid-1940s till the end of the 1960s due to the very high remanent magnet flux density B_{rem} [29]. However, Alnico magnets have nonlinear magnetic characteristics due to the low coercivity, as Figure 2.8 suggests. Therefore, this magnet can easily be magnetised and demagnetised.

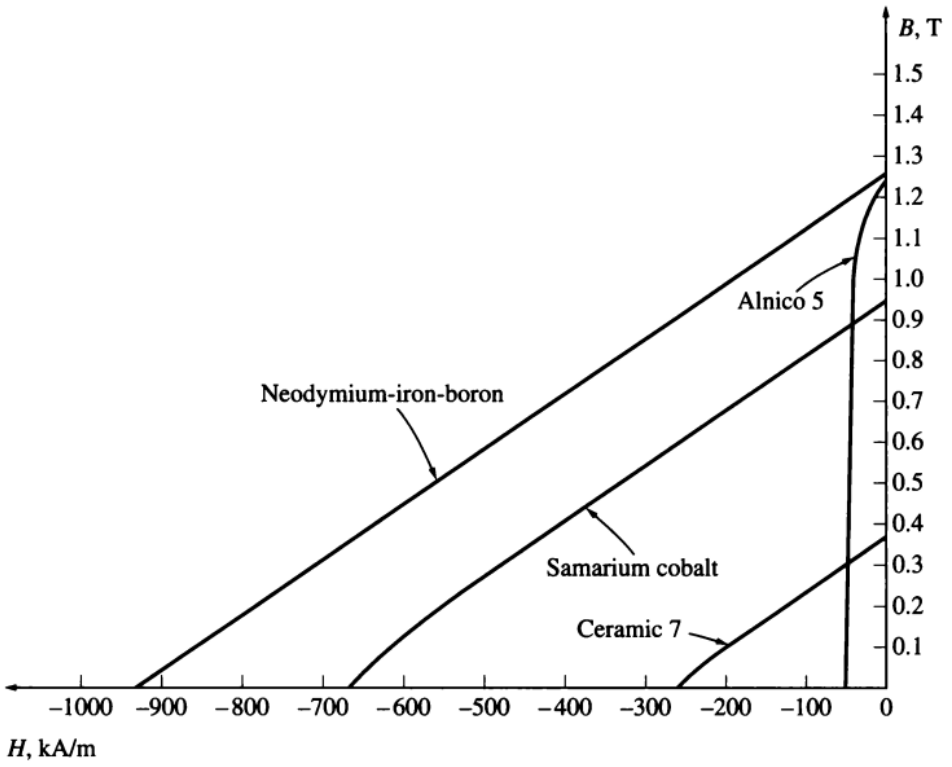

Figure 2.8: Magnetic characteristics for the common PM materials used in machine manufacturing [27].

At higher temperatures, the characteristic of the materials starts to shift toward the origin of the graph. The latter entails that both coercivity and remanence reduce. The reduction of the coercivity is higher than the remanent magnetic flux density, as the characteristic has the tendency to create a "knee" point. The effect of temperature on the remanence B_{rem} is approximately linear, and the following equation describes it for a specific temperature T [25]

$$B_{rem}(T) = B_{rem}(T_0)\left(1 + \Delta_B\left(T - T_0\right)\right), \tag{2.5}$$

where the reference temperature T_0 is usually the room temperature of the permanent-magnet. Δ_B is the reversible temperature coefficient. For NdFeB magnet materials, as the temperature drops, the normal demagnetisation characteristic reduces, as Figure 2.9 presents. When the temperature increases, the knee point appears in the second quadrant for the temperature T_3, as illustrated in Figure 2.9, making the characteristic nonlinear for a field intensity interval. The work presented in [26] proposes a method to calculate the operational point of the characteristic for a permanent-magnet material under operation.

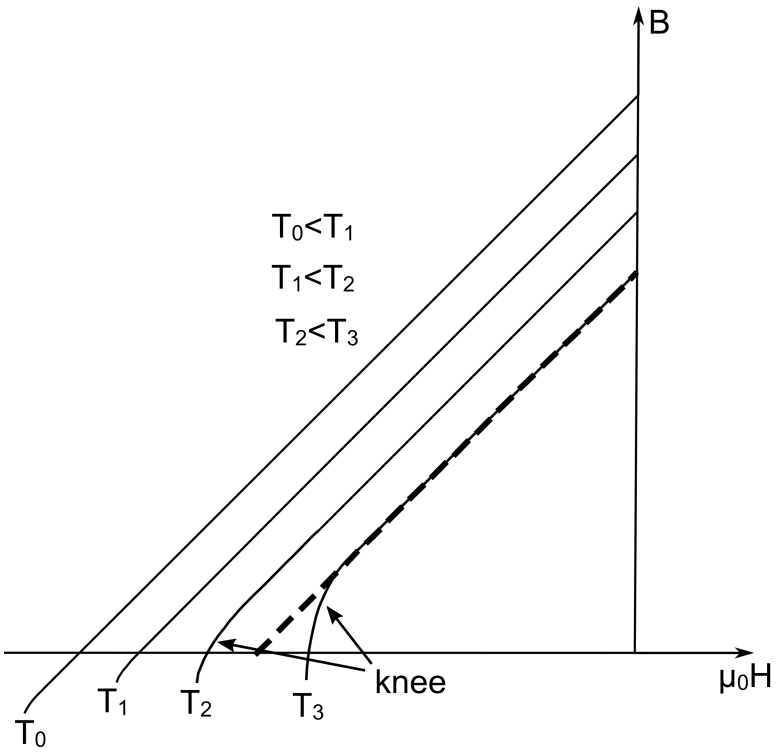

Figure 2.9: Variation of the magnetic characteristic with temperature increment [25].

2.5 Description of the machines used in this dissertation

This section presents the permanent-magnet machines that are going to be used in the next chapters of this dissertation.

2.5.1 Axial-flux generators

The permanent-magnet machines used in this thesis are both of radial- and axial-flux topologies. The winding types used for most applications are the overlapping and non-overlapping winding. In Figure 2.10, one can see the side view of an axial-flux PM generator with 24 coils and 32 magnet poles. The axial-flux PM machines used are of the double-rotor single-stator topology. Designing renewable energy harvesting generators means that the speed

of the prime mover, i.e. wind turbine, tidal turbine and wave energy converter, is low, so to accomplish a higher power output the torque has to be increased. The increased torque entails a physically large and heavy machine since it depends on the radius of the rotor as it is perpendicular to the force vector distance. In Figure 2.11, one can see the three discs of the generator. Each phase has eight coils, which are in series or parallel and the coil-phase sequence alternates per coil. The coil for $\theta = 0^o$ belongs to phase A, the coil at $\theta = 15^o$ belongs to phase B, and the coil at phase C is at $\theta = 30^o$. By using different colours, we can discriminate the phases from each other. The high number of magnet poles means that a low speed will produce a high-frequency EMF signal on the stator winding. So by having a machine which produces a large torque at low speeds and an EMF signal near the grid frequency means that the machine can be used as a direct drive generator in renewable energy applications. In a direct drive operation, there is no need for a gearbox, which entails a system with reduced losses and maintenance costs and noise. Usually, direct drive machines do not have iron in the stator. Machines without iron core in the stator, have a lower magnetic flux density due to the higher reluctance in the air-gap. The higher reluctance, causes lower magnetic flux and in turn, air-gap magnetic flux density. The lower magnetic flux density causes lower electromagnetic torque. However, the absence of ferromagnetic material in the stator eliminates the attractive forces. The latter makes the fabrication of very big machines easier. Another significant advantage of the generators with core-less stators is the absence of cogging-torque, which adds a torque ripple to the main torque under on-load operation, causing vibration and noise. Lastly, the core losses, the hysteresis and eddy-current losses cease to exist, increasing marginally the machine's efficiency. Figure 2.12 displays the photograph of the actual axial-flux permanent-magnet generator. The equation that correlates the speed of the generator with the electrical frequency according to [27] is

$$n_s = \frac{120 f_s}{P}. \tag{2.6}$$

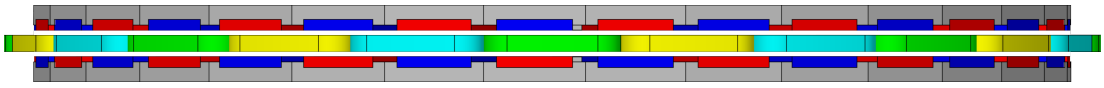

Figure 2.10: Geometry of the axial-flux PM machine for renewable energy harvesting lateral side view.

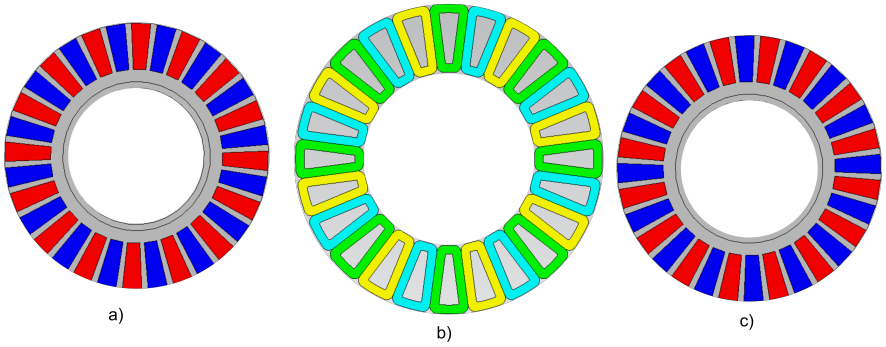

Figure 2.11: Geometry of the axial-flux PM machine a) left rotor b) stator c) right rotor.

Figure 2.12: Axial-flux PM generator in the laboratory.

Another axial-flux permanent-magnet generator used in this dissertation is the one displayed in Figure 2.13. This machine has a much lower diameter than the one displayed in Figure 2.10, and it has a lower number of poles meaning that a gearbox has to be present when connected with the turbine. However, the machine's configuration is the same; the stator is coreless and has the same type of winding. Figure 2.13 demonstrates the number of poles is 12, and the number of coils is 9, meaning that each phase has three coils. Figure 2.14 displays the photo of the actual generator.

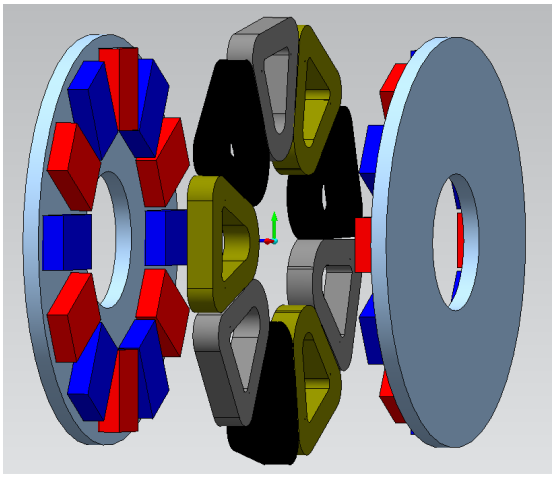

Figure 2.13: Low power core-less axial-flux permanent-magnet generator.

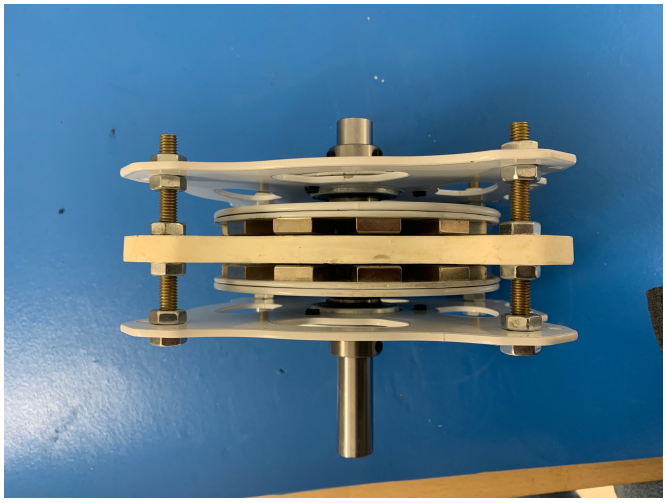

Figure 2.14: Low power axial-flux PM generator in the laboratory.

2.5.2 Radial-flux machines

Various radial-flux PM (Permanent-Magnet) machines in this dissertation used for proving concepts and validating algorithms. Figures 2.15 and 2.16 present two surface-mounted permanent-magnet generators. Figure 2.15 presents an air-cored radial-flux PM machine with 12 magnet poles and nine coils, three coils connected in series per phase. This machine is analogous to the axial-flux PM machine, presented in Figure 2.13. The machine illustrated in Figure 2.16 is of the same topology, with the only difference being that it has a stator core. It has eight poles and 12 slots, meaning that each phase has four coils connected in series. These two machines were mostly used to validate diagnostic concepts using FEA (Finite-Element Analysis).

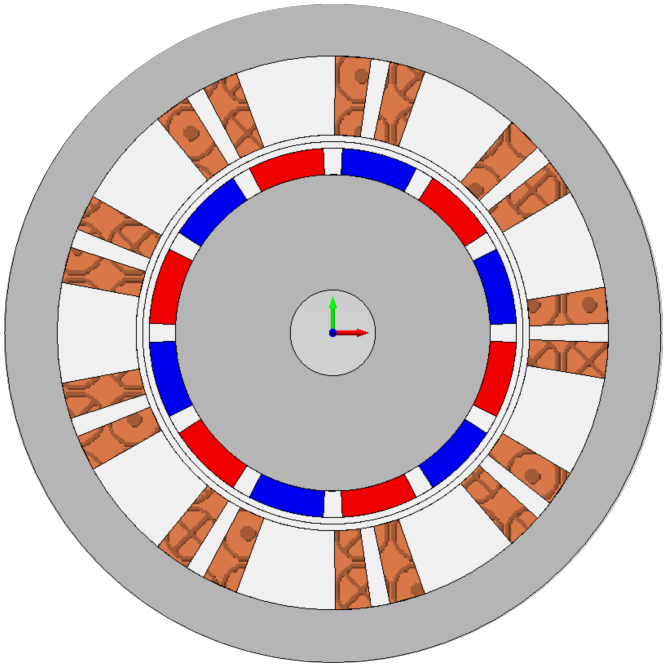

Figure 2.15: Air-cored radial-flux surface-mounted permanent-magnet generator.

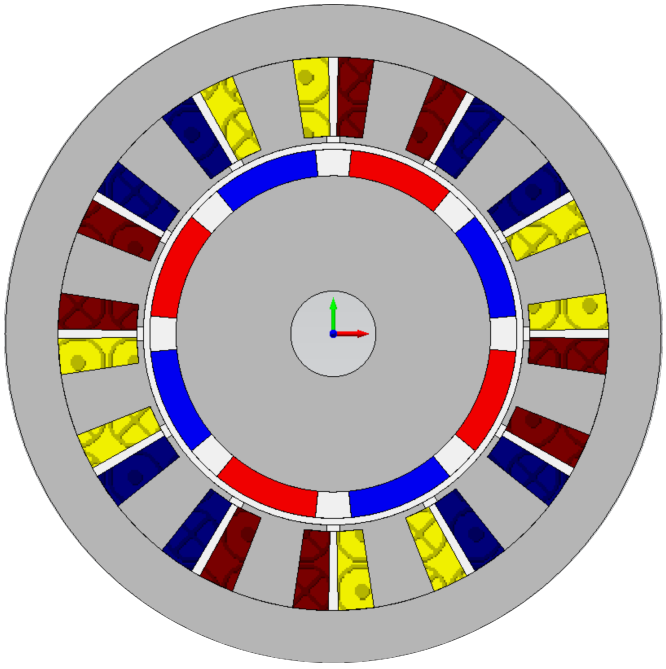

Figure 2.16: Radial-flux permanent-magnet generator with stator core.

Figures 2.17 and 2.18 illustrate permanent-magnet synchronous machines with 12 slots and 4 poles, which also have a cored stator. In this stator design, the winding is overlapping, meaning that the phases couple magnetically. The total magnetic flux passing from a coil also depends significantly on the magnetic flux of the adjacent coils. Figure 2.17 presents the

topology with surface-mounted magnet rotor and Figure 2.18, the surface-inset topology. The main difference between the two topologies comes in the different shapes of the magnetic flux density waveform. In the machine with surface-mounted magnets, the normal component of the magnetic flux density reduces with a slower rate, beginning from the edge of the magnet air-space till the end of the pole pitch. On the contrary, in the machine with surface-inset magnets, it drops rapidly to zero because there is a highly permeable ferromagnetic material, i.e. iron. The magnetic field intensity vanishes inside the iron volume, meaning that the magnetic flux density is also going to be zero. Another significant difference concerning the major operational parameters of the machine comes with the electromagnetic torque. The second machine topology has a salient pole rotor, implying that the iron poles of the rotor have the tendency to align with the rotating magnetic field of the stator.

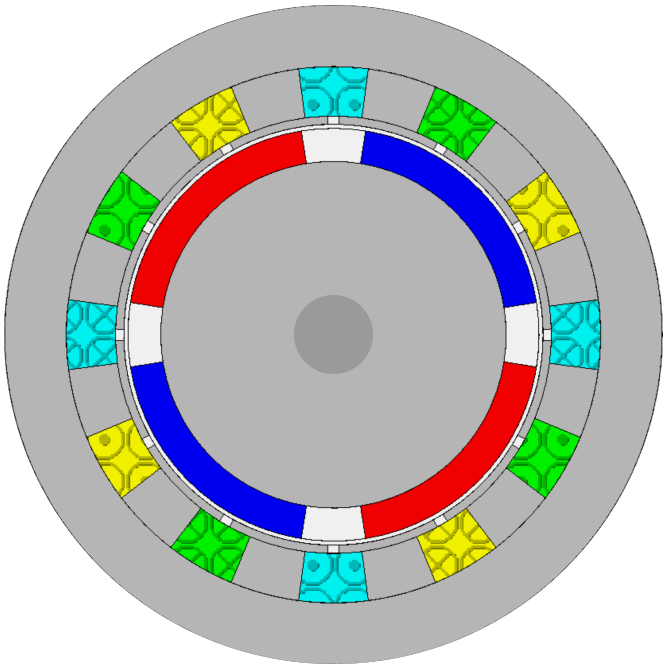

Figure 2.17: Surface-mounted PM synchronous machine with 12 slots and 4 poles.

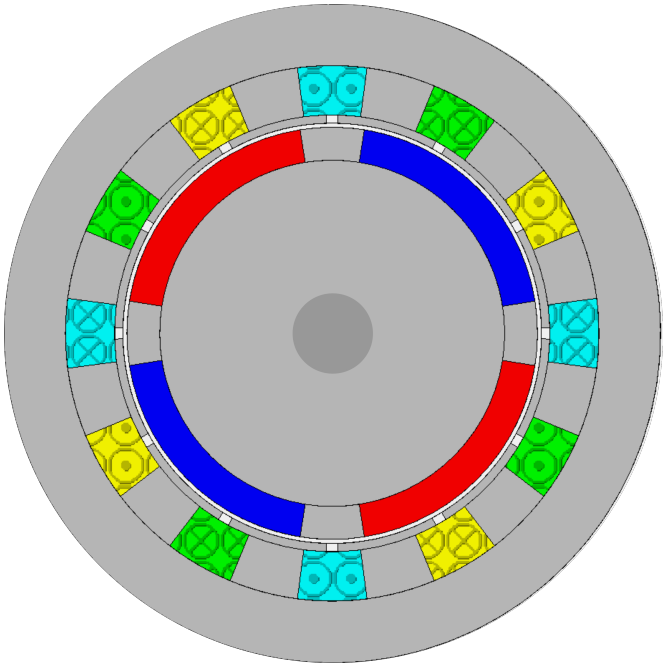

Figure 2.18: Surface-inset PM synchronous machine with 12 slots and 4 poles.

PART II

Diagnostics for permanent-magnet synchronous machines

Chapter 3

Literature review on the occurring faults and state-of-the-art diagnostic methods for permanent-magnet synchronous machines

This chapter discusses the current literature in regard to the common faults occurring in permanent-magnet machines and the state-of-the-art diagnostic methods to detect these. The reason for investigating initially the faults is to understand their impact on an operating electric machine and the kind of signature they leave (magnetic, thermal or acoustic). By studying the existing diagnostic methods will initially offer a clear understanding with regard to the mechanism of the diagnostic methods and their implementation. Secondly, will be able to identify the limitations that the existing methods suffer from. Lastly, by knowing the limitations of the methods in the literature will help in the development on a new method which will be able to cover the existing limitations. The discrimination of the methods happened with regard to whether the diagnostic methods provide a monitoring quantity using the aid of additional sensor devices. The two considered method categories (sensored and sensorless) are compared with each other and their advantages and drawbacks are discussed with the goal to choose in which category the proposed method will fall. For clatification purposes the word diagnosis is referred to finding out what is the exact fault that happened to the machine, where exactly and what is the severity of the fault. For clarification, the hereunto process studies a machine that already has a fault in an early stage and not a machine that is healthy, but there are indications that a fault may happen soon.

3.1 Faults during the operation of PM synchronous machines

The occurring faults in permanent-magnet synchronous machines can be divided into magnetic, mechanical and electrical. The main faults are the inter-turn fault, partial demagnetisation and static-, dynamic- eccentricity. This section presents the common faults occurring in permanent-magnet machines, their mechanism and evolvement. Their impact, however, is translated into a variant magnetic flux on the air gap, which can either be static or dynamic. This unbalanced flux is considered the key quantity for diagnosis since it is the "signature" a fault leaves to the operating machine. Another way to distinguish the faults would be to categorise them depending on where the machine is located. In this case, the inter-turn fault would be categorised as a "stator" fault, whereas demagnetisation and eccentricity as 'rotor' faults. Nevertheless, the categorisation was chosen according to whether the faults create unbalanced magnetic flux, which moves as the rotor rotates or remains stationary. As it is going to be explained in the next subsections, the inter-turn and static eccentricity fault fall into the category of "static faults" and partial demagnetisation and dynamic eccentricity at "dynamic faults".

3.1.1 Static faults

This subsection discusses the static faults, explains their impact on the operation of the PM machine and talks about how it affects the machine's lifespan.

Inter-turn fault

The coils used in electric machines are created by making an insulated loop wire of many turns. The inter-turn fault is caused by thermal stress of the winding insulation, which can be caused by operating the machine higher than the rated current. Furthermore, due to the non-ideal design of the machine, there will be a small unbalance in the three stator currents amplitudes, which can lead to faster thermal degradation in the coils of the phase with the slightly higher current. The environmental condition is one of the major reasons this fault may occur [5]. High humidity also has an impact on the chemical composition of the insulating material. In high altitudes, the cooling capability of the air reduces, entailing a fast insulation degradation rate and resulting in a quicker shorting of the first turn. Figure 3.1 plots how many hours the insulation can survive under a certain temperature. Depending on the type of insulation, the lifespan varies accordingly. It is clear by inspection of the figure how important the winding is to be in as low a temperature as possible, as the insulation lifespan decreases exponentially with the temperature increment.

When one turn shorts in a coil, depending on the way that the turns are distributed, the neighboring turn is possible to short as well, due to the hotspot created by the fault. However, it is not clear how much is required for such thing to happen or if it is possible to happen in all the operating enviroments. Hypothetically, if many turns short and the whole coil ends

up being shorted, this can lead to a ground fault, which happens when at least one turn connects electrically with the stator iron, which in turn connects with the earth and leads to the catastrophic breakdown of the machine. Figure 3.2 illustrates a coil in the stator core of a slotted machine, which has a coil with one turn short. The healthy part of the coil is shown and functions normally, contributing to the energy conversion process. The shorted turn is an individual circuit inside the rotating magnetic fields; the rotor and the stator. The loop is stationary with respect to the two rotating magnetic fields; hence there will be an induced voltage which will depend on the superposition of the two magnetic fields. Because the loop is closed-circuited, there will be a current called short-circuit current or loop current. This current is proportional to the

- speed,
- number of shorted turns,
- plane area of the loop,
- impedance of the loop,
- contact resistance between the shorted wire,
- total magnetic flux density penetrating the loop.

The current is not dependent on the loading condition of the machine directly. By loading condition, is meant the amount of current flowing the phases.

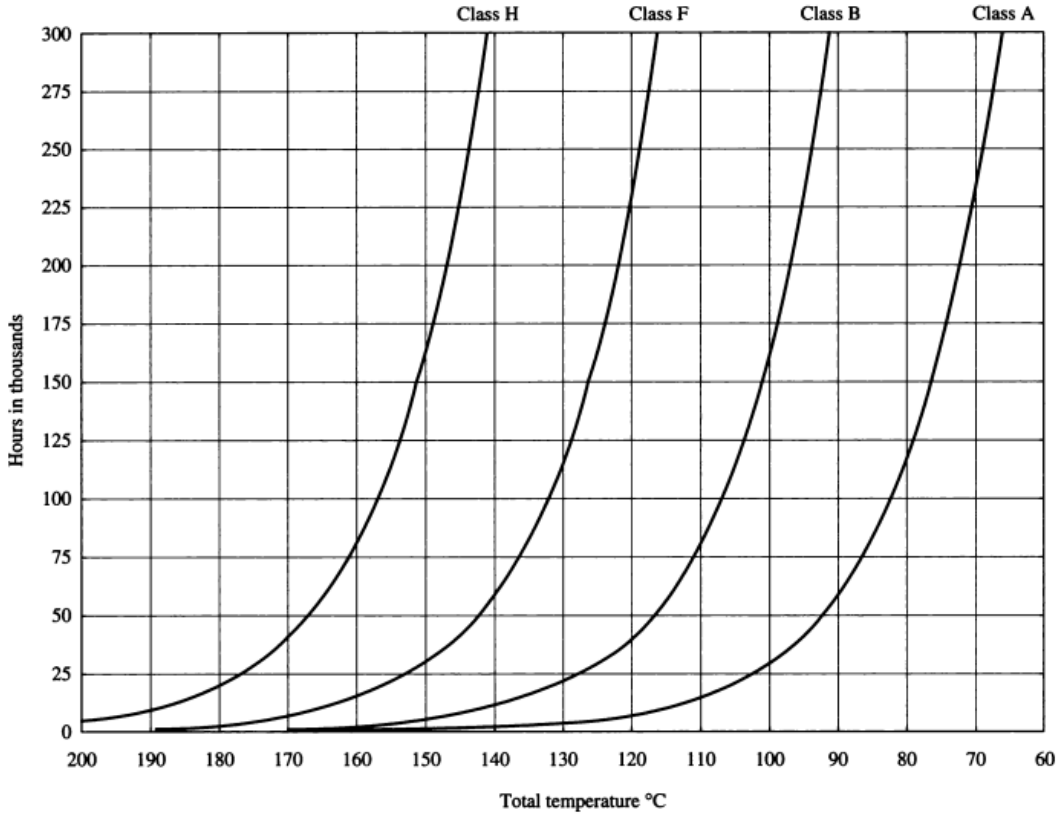

Figure 3.1: Plot of mean insulation life versus winding temperature for the typical insulation classes [27].

The current on the loop varies with the position of the two magnetic fields. However, for small loading conditions, i.e. low δ torque angle, the current in the loop varies with the position of the rotor magnetic field. More specifically, according to [27], the peak value occurs when approximately the magnet's centre passes from each conductor. Hence the magnetic field is of sinusoidal form, neglecting the higher order harmonics. Considering what was said above, the magnetic flux created by the loop will be time or rotor position varying. Because the loop is stationary in space, the magnetic flux created by the loop will be static. The inter-turn fault must be detected in the earliest stage possible [31] to avoid the insulation failure of the machine's stator winding. There is a lot of ongoing research for developing condition monitoring methods, and schemes for detecting the inter-turn fault [4]. Concerning the detection of this fault, except realising that this fault happened to the permanent-magnet machine, to detect the fault, ideally, the number of shorted turns and the position of the asymmetry has to be calculated [4]. However, it is necessary to detect the fault at its minimum severity of 1 turn. To be more specific, what matters most is the current flowing on the loop, as this is what creates the hotspot. This current causes degradation and depending on how the turns on the coil are distributed, its severity over time can increase. The objective is always

to detect the fault at its earliest stage. The magnetic signature of the fault is the time varying but fixed in space magnetic flux produced by the current carrying conductors of the loop. The thermal signature of the fault is the increased temperature on the position where the shorted loop is located.

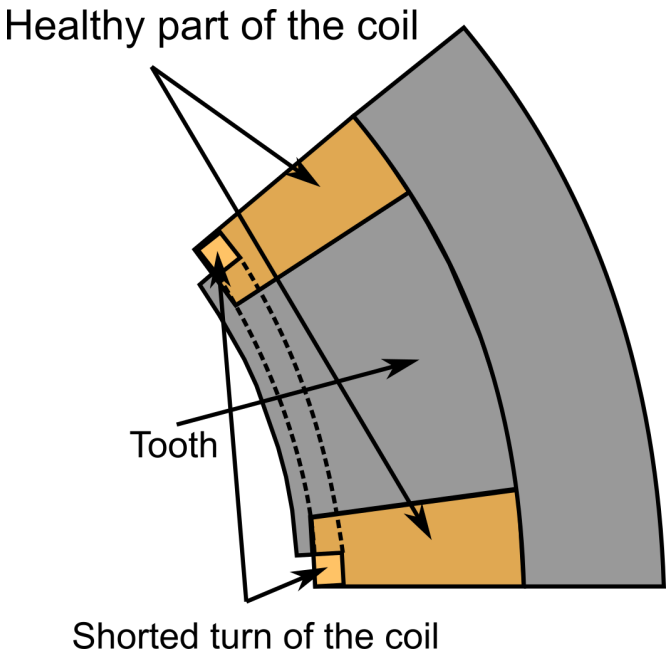

Figure 3.2: Sketch of a coil wrapped around a tooth with one turn shorted.

Static eccentricity

Rotor eccentricity is considered the only fault manufacturers tolerate in a brand new electric machine for a percentage lower than 10% [3]. Manufacturers suggest that an air gap of a level of 50% is considered to be a serious problem such that the motor should be immediately removed from production [13]. The fault can also be created by supplying an unbalanced load. Due to the unbalanced currents in the phases, an attraction force is generated, which gradually increases with time. When the distribution around the axis of the machine is not uniform, it is considered another cause of eccentricity. Static eccentricity happens when the rotor's rotational axis is displaced from the fictitious axis of the stator. The rotor rotates into a new axis which has a distance from the stator axis. This entails ending up with an air gap which is not constant but has one position where it is the minimum length and another where it has the maximum length. These two positions have 180^o spatial difference. The air gap is divided into two regions; one where the air gap is higher than the air gap in the healthy condition and one lower. Respectively the reluctance for the corresponding angle intervals will

be higher and lower compared to the healthy condition. Furthermore, there are also two points where the air gap stays the same as the one that the healthy state of the machine has. These two points have 180^o spatial difference as well; as a pair, they have 90^o difference from the pair of the other two positions.

What was mentioned above can be realised schematically, using Figure 3.3, in which the two centres are also presented. In the case of the healthy condition, the rotor centre is identified with the stator centre. However, in the case of the static eccentricity fault, by inspection, the rotor centre is shifted towards a constant location, and so the rotor rotates with respect to this centre. This fault also has a location like the inter-turn fault. The inter-turn fault probably has a location that coincides with the shorted loop's position. The location of static eccentricity is defined as the position where the minimum air gap is located. Hence, this fault is also a static asymmetry as it does not move with the rotation of the rotor.

One of the major reasons static eccentricity happens in a permanent-magnet machine is bearings. Usually, the rotational part of an electric machine "sits" in two bearings. According to Figure 3.4, the bearing is a mechanical device with two rings or races which enclose the bearing ball [5]. One race is mounted on the rotational component of the machine, and the other is on the stationary. As one component rotates, the bearing balls rotate around the stationary race, and the end result is a smooth and perpetual motion. The bearing balls are of spherical geometry to reduce the friction surface, and there is the lubrication for further friction reduction. The attractive forces between stator and rotor are applied in the bearings, so under eccentricity and other faulty conditions, the bearing lifespan reduces when this force becomes even higher. The bearing fault can cause eccentricity depending on how it can break. Figure 3.5 shows a schematic of a method to manipulate the races of the bearing to implement static eccentricity in radial-flux PM motors [32].

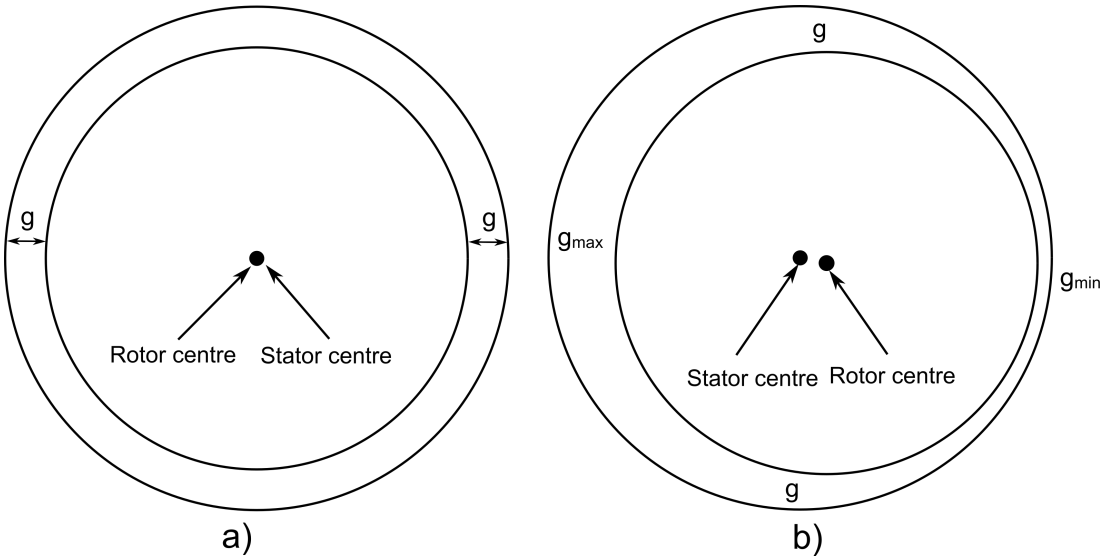

Figure 3.3: Rotor eccentricity schematic a) healthy case, b) static eccentricity.

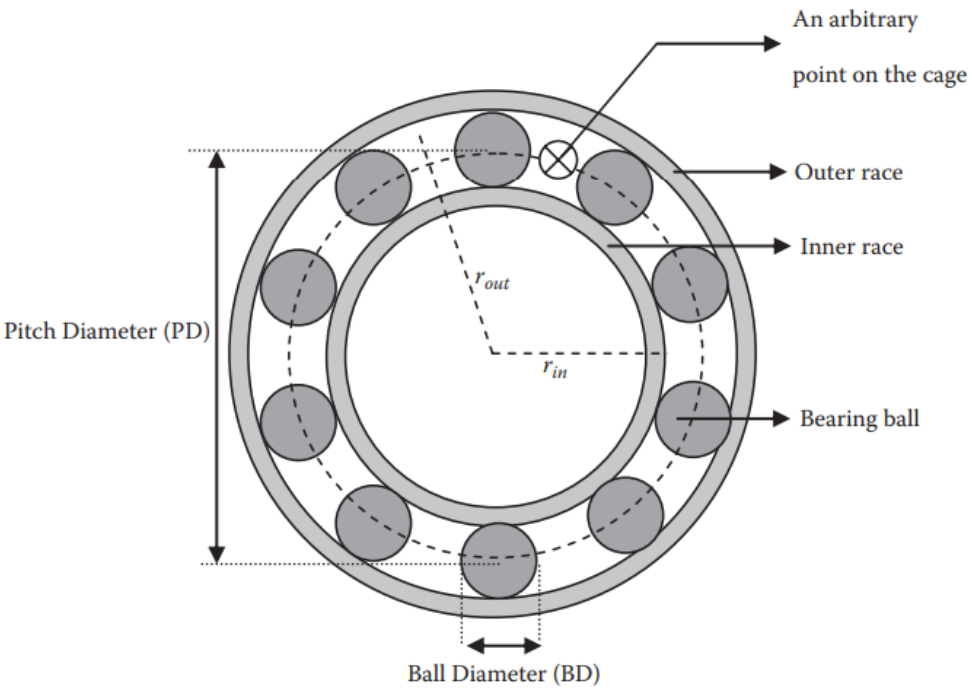

Figure 3.4: Typical bearing geometry [5].

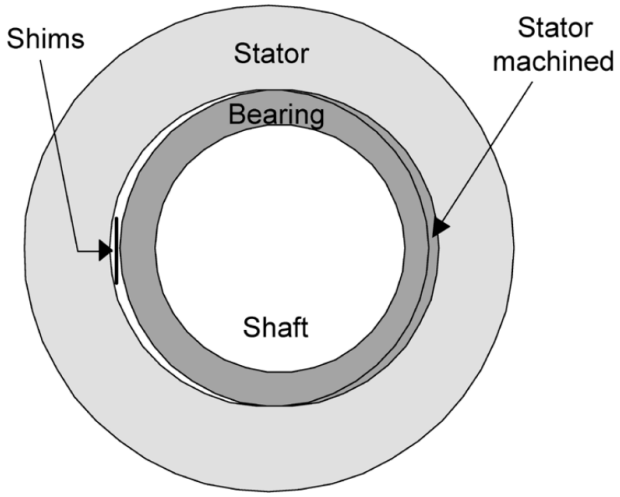

Figure 3.5: Sketch showing implementation of static eccentricity [32].

The static eccentricity factor (SEF) is a measure which expresses how severe the fault is. It is defined as the ratio of the minimum air-gap over the normal air-gap length. It is a percentage which expresses how much the air gap varied compared to the initial one. It is calculated along with the position of the minimum air-gap [33, 12].

3.1.2 Dynamic faults

This subsection discusses the dynamic faults, explains their impact on the operation of the permanent-magnet machine and discusses how they affect the machine's lifespan. For clarification, the term "dynamic" is meant a fault which is a magnetic asymmetry which rotates around the air gap, and not a faulty condition where the condition of the machine is transient.

Partial demagnetization

Partial demagnetisation is defined as the fault which happens when one of the magnets is getting demagnetised. Demagnetisation reduces a magnet's remanent magnetic flux density B_{rem}. High temperatures, armature reaction magnetic fields, corrosion due to humidity, small edge breakages, or cracks [34, 2, 35], are the common causes of demagnetisation. NdFeB materials have a high coercivity, making demagnetisation by armature reaction fields less likely. However, these materials are temperature sensitive [2]. Demagnetised motors demand a higher stator current to produce the same electromagnetic torque since the magnetic flux density produced by the rotor reduces on average. The same applies to the generator operation when having a constant output. Increased current in the stator winding entails more thermal stress in the insulation, which eventually leads to the machine's reduced life span. This fault creates a moving asymmetry which offers the advantage of easier diagnosis through the stator winding of the machine. The reason is that the asymmetry created by the fault is in relative motion with respect to the stationary coils of the stator or any additional winding placed. The asymmetry induces voltage frequencies which can be used as fault identifiers [2].

Partial demagnetisation occurs when at least one of the magnets of a machine is getting irreversibly demagnetised. The word "irreversibly" refers to the fact that the residual flux density of the magnet reduces on a permanent basis. When the temperature of the magnet increases, the magnetic characteristic starts to move parallel towards the origin, as illustrated in Figure 2.9. In order for the magnet to be irreversibly demagnetized, the load line has to intersect with the knee point of the characteristic. The increase in temperature brings the knee point closer to the load line and makes the magnet easier to become demagnetized. Figure 3.7 considers that the magnet works under a no-load condition so only the load line depends only on the permeance of the air-gap. A load can be seen in Figure 3.6 which moves parallel with respect to the permeance line, keeping its gradient constant.

The following are two main cases that can demagnetise a magnet irreversibly. A strong stator armature reaction magnetic field will make the load line to depart from the origin and start shifting towards the left, continuing being parallel to the permeance line, as explained on [36]. The latter will make the load line to approach the knee point as presented in Figure 3.6. After the armature reaction field ceases to be applied, there will be a new magnetic characteristic whose orientation will depend on which operating point the field brought the

characteristic at. In Figure 3.6, one can see an intuitive new characteristic which is demagnetised and passes from the operating point created by the armature reaction field. This new demagnetised characteristic will be permanent for the magnet. The temperature increase can shift the demagnetised characteristic to a new one that will intersect with the load line. Furthermore, the characteristic becomes more nonlinear with the increment of temperature. If the temperature reaches a certain point, the knee point will shift towards the right. If the knee point intersects to the load line, the magnet becomes irreversibly demagnetised. The new demagnetised characteristic will pass from that operating point, as was illustrated in Figure 3.7.

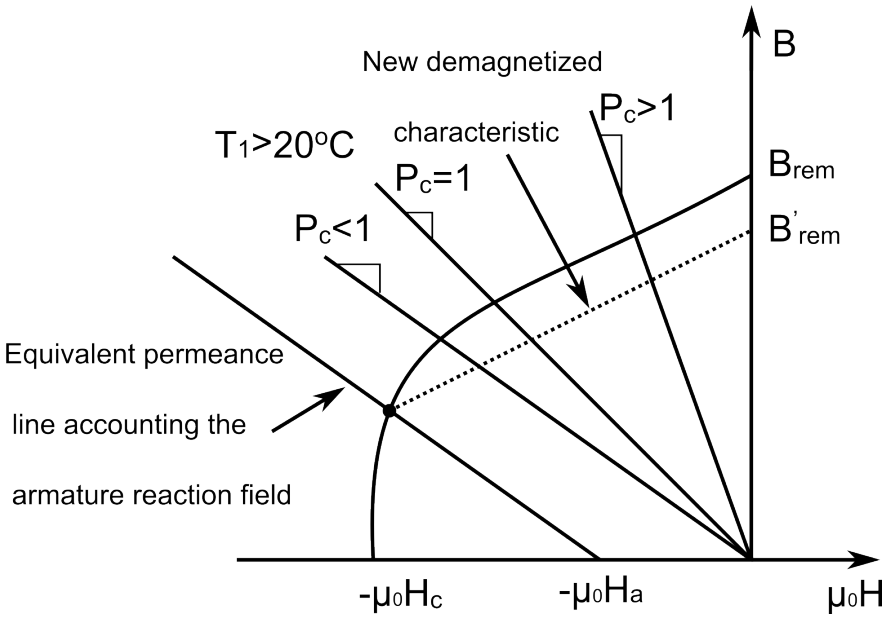

Figure 3.6: Irreversible demagnetization due to a strong armature reaction field in the PM material.

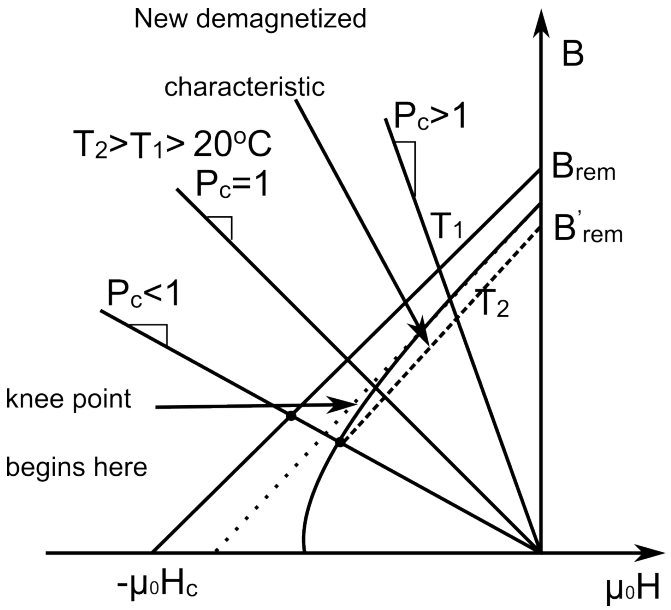

Figure 3.7: Irreversible demagnetization due to the increased temperature in the PM material.

Dynamic eccentricity

In dynamic eccentricity, the positions of the maximum and minimum air gap move with the mechanical speed of the rotor. Figure 3.8 presents the uniform air gap case next to the dynamic eccentricity case. In this condition, the rotor is displaced just like in the case of static eccentricity, with the difference that the rotor axis of rotation does not stay stationary but moves. The axis erases the trajectory of a circular motion, and the centre of this motion is the stator axis. The latter event entails that the minimum and maximum air gaps are moving with the rotational speed of the rotor. Dynamic eccentricity generates fractional harmonics on the stator current of the machine, like the partial demagnetization fault. The latter occurs since there is relative motion between the stationary conductors of the stator and the asymmetry. This fault creates also additional harmonic components on the torque, increasing its ripple, which means more noise radiated from the machine. The fault increases the unbalanced magnetic pull, which in this case, its maximum value varies with the location of the minimum air gap. Due to the attractive force between the rotor and the stator the minimum air-gap length can increase further. Eccentricity does not influence the machine's output power significantly. Still, it is a fault that creates noise as there are additional forces acting on the bearings and on final stage may create friction between the rotor and stator, eventually. Partial demagnetization and the inter-turn fault have a more substantial impact on the power output of a permanent-magnet machine. The severity of eccentricity is possible to increase gradually over time once the first occurrence, and can lead to friction between the rotor and the stator eventually. Nevertheless, it is not clear the increment rate of the fault severity, for this fault as well. Figure 3.9 shows the sketch of a method to implement dynamic eccentricity by manipulating the races of the bearing [32].

Mixed eccentricity

Mixed eccentricity is a more realistic fault case, as a machine always has a small amount of both eccentricities. The eccentricities originate from the bearing imperfections and dimension tolerances. This type of eccentricity is the superposition of two faults. The location of the two eccentricities can be the same or different.

Rotor ovalisation

The machines used for renewable energy generation tend to be very large when there is no intermediate gearbox. The latter means that the attractive forces in the air-gap become very high and the rotor ceases to be of circular shape. The axis of rotation stays in place. More specifically, this fault creates two minimum and two maximum air-gaps and behaves similar to dynamic eccentricity as it creates unbalanced magnetic flux which moves around the air-gap. This kind of phenomenon is considered one of the constrains that does not allow to have a reduced air-gap length when the size of the machine increases.

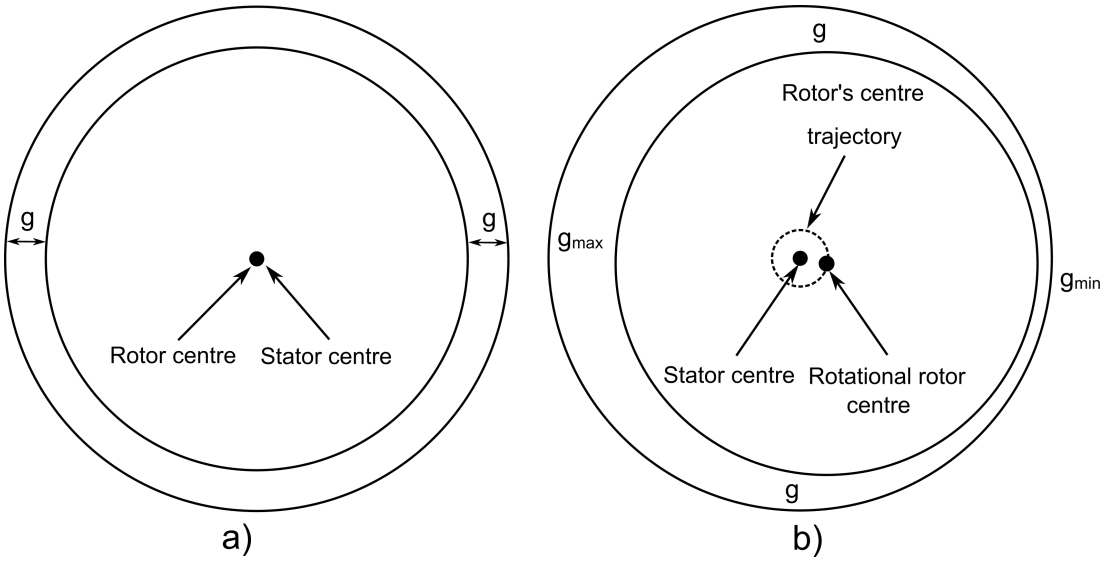

Figure 3.8: Rotor eccentricity schematic a) healthy case, b) dynamic eccentricity.

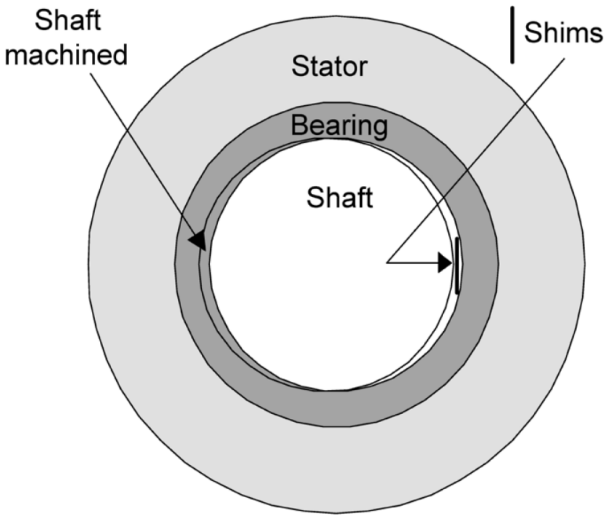

Figure 3.9: Sketch showing implementation of dynamic eccentricity [32].

3.2 Diagnostic techniques in permanent-magnet machines

This section presents and discusses state-of-the-art diagnostic techniques. The methods are presented in great detail, and the number of faults that the technique can detect is explained. Furthermore, the advantages and disadvantages of each method are analysed. Lastly, the methods are also reviewed on whether they have possibilities to be used under stationary or non-stationary conditions.

3.2.1 Sensorless diagnostic methods

Condition monitoring of electrical machines involves monitoring signals and extracting features from them. A signal, if exploited properly, can offer insight of the health status of the operating machine. If the machine is faulty, proper signal processing can provide identification of the fault, the fault severity percentage and the location of the fault in static faults. The monitored signal is preferred to be online since it is easier to do real-time processing, and the machine does not have to switch off and slow down production. Offline methods offer the advantage of more sophisticated tests, like applying voltages in the stator winding for specific purposes. Offline tests make it possible to disassemble the machine, so it is possible to inspect its components. By disassembling the machine, during an eccentricity event, by inspecting the air gap, the occurrence of the fault is easy to validate. If one uses a Gauss-meter, then the health condition of the magnets can be determined [37]. Methods that require disassembling the machine are invasive, so it is much harder to be implemented on an industrial scale.

However, sensors and other devices require installation only once, during manufacturing ideally, so it is considered an attractive choice for condition monitoring. Several review papers have been published in the past decade that present the state-of-the-art diagnostic methods in permanent-magnet synchronous machines [38, 2, 34, 3, 4, 39, 1, 22, 40].

The first and most popular method in condition monitoring is the Motor Current Signature Analysis or MCSA, which took its name because researchers started applying it to induction machines which usually work as motors. This method samples the stator current signal while the motor or generator operates using a current probe and a data acquisition system. Fast Fourier Transform or FFT using a programming code is applicable by extracting the signal to a computer as a data column. The result is that the amplitude spectrum of the signal is displayed on the screen, so the harmonic content of the machine is visible. This method has been applied chiefly for rotor faults, like partial demagnetisation and dynamic eccentricity. When the faults mentioned above occur in the machine, they generate new harmonic frequencies in the stator current of the machine. Various demagnetisation diagnosis methods have been created [41, 32], as well as for dynamic eccentricity [42]. Partial demagnetisation and static eccentricity generate similar harmonic patterns in the phase current [43]. Distinguishing the two faults can be done by monitoring the dynamic behaviour and appearance of the harmonics in the two faulty conditions. [42] validates what is mentioned above, showing that static eccentricity generates harmonics due to the saturation effect in the stator region. In [32] amplitude of the 7^{th} harmonic of the negative sequence current was used to detect static eccentricity and distinguish it from the other faults. When the stator current becomes high, deep saturation occurs, so the harmonic components are eliminated since the magnetic permeability of the stator's material becomes equal to the vacuum permeability. The same applies to the inter-turn fault since it is also a static fault, so more sophisticated processing is required for the signal [44]. In synchronous machines with excitation winding, inter-turn fault induces harmonic components in the field winding, so by monitoring the current of the winding, the fault is detectable [45]. However, in permanent-magnet machines there is no access in any quantity located in the rotor component, so no quantity can be used for monitoring the stator health. The only accessible component is the stator winding, which complicates the development of detection methods for static faults. Uniform demagnetisation fault happens when all the machine magnets demagnetise on the same percentage. However, this type of fault does not create unbalanced magnetic flux in the air gap, meaning that is not detectable with the Motor Current Signature Analysis (MCSA) method.

The harmonics generated by partial demagnetization and dynamic eccentricity depend primarily on the pole number of the machine, and their frequencies are

$$f_{fault} = \left(1 \pm \frac{k}{(P/2)}\right) f_s, \tag{3.1}$$

where f_{fault} is the frequency of the fault harmonic component, P is the total number of rotor poles, f_s is the electrical frequency of stator current or voltage and k is an odd integer. The above equation shows that the harmonics generated will be fractional and depend on the number of poles. However, these frequency components are also winding dependent and, more specifically, will depend on the type of winding and the number of coils and how these coils are connected [46, 47]. Furthermore, when the machine has a parallel path winding and a fault happens, the behaviour changes since currents are flowing between the branches [48]. The first realised gap is that there is no formula correlating the type of winding, the number of coils and the poles with the frequency of the fault signatures.

Back-EMF for motors and EMF for generators is another signal to which MCSA is applied because it is noticeable that this signal reveals more harmonics [49] than the phase voltage. Of course, for this voltage signal to be measured, it is implied that the machine is in an open-circuit condition, so the test happens offline. Another signal to apply this method is the electromagnetic torque of the machine, which can be measured using a torque transducer placed on the machine's shaft. This signal has a DC component and higher-order harmonics. The higher order harmonics can be used for eccentricity [50] and demagnetization fault diagnosis [51].

The work presented in [52] shows that permanent-magnet machines with symmetrical concentrated windings connected in series have harmonic sideband components cancelled under local demagnetisation fault. Furthermore, another method in the literature uses the amplitude of the zero sequence voltage component or ZSVC (Zero-Sequence-Voltage-Component) to detect demagnetisation. The ZSVC is the average value of the phase voltage signals and, under healthy conditions, contains the 3rd harmonics and its odd multiples. When a rotor fault takes place, these harmonics increase in amplitude. The common point in the Y-connected stator winding of PM machines is not accessible, so the authors used three high resistors in the Y connection to create a common artificial point. This technique cannot only measure the ZSVC online, but the ZSVC produced by the modulation technique of the voltage inverter flows to the resistors. Figure 3.10 displays the experimental wire diagram.

The zero sequence component has also been used for inter-turn fault detection in [53] in PM machines with Y-connected stator winding. The method uses the fundamental component of ZSVC as an input to a model, which offers the fault severity and location of the faulty phase as output. The same method was applied for the machines with Δ-connected stator windings, in which, instead, the zero sequence current component or ZSCC is used, and the same model with the previous method was applied on the same paper [53]. Another technique uses the normalised ZSVC 1st harmonic slope and correlation coefficient [54]. The 1st harmonic of the ZSVC is used for fault index extraction. This harmonic is monitored under different speed and load conditions. Vold-Kalman filtering order tracking or VKF-OT algorithm is applied to extract the fundamental harmonic of the ZSVC. The two indices used for fault diagnosis are

the normalised fundamental component slope of the ZSVC and the correlation coefficient. The two indices have been extracted to be independent of the speed and load, which makes this method appropriate for non-stationary conditions. This method is applicable only if there is accessibility at the neutral point of the machine. However, similar results could be obtained using an artificially made neutral point like as [53] suggests. The same method using the VKF-OT algorithm applies to the 3rd harmonic of the stator current [54].

Except for the zero sequence component, other components used for condition monitoring permanent-magnet machines are the negative sequence component of the stator current. The inter-turn fault causes unbalanced phase currents, generating a negative sequence current as well [55]. The unbalance comes from the turn reduction on the shorted coil, as the induced voltage reduces. Furthermore, the amplitude's second order harmonic of the positive sequence voltage in the d-q reference was also proposed for fault diagnosis purposes of the inter-turn fault [56]. These voltages contain even harmonics in faulty conditions. Since the actual voltages were noisy, the control reference voltages were used for monitoring, corresponding to the mean value of the actual voltages over one switching period. For diagnosis, the 2nd harmonic of the positive sequence current is considered, which is proportional to the fault severity of the inter-turn fault. Another method, which exploits the properties that symmetrical components offer, is the one presented in [57]. This method monitors the inter-turn fault, the ratio between negative and positive voltage sequences.

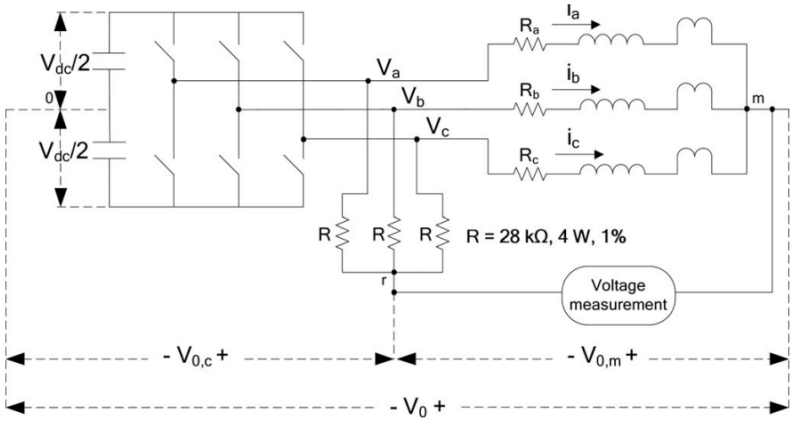

Figure 3.10: Wire connection of the PM motor with the inverter, the stator windings, and the resistor network used to generate an artificial neutral point [52].

[51] presents a method to detect the partial demagnetisation fault in PM motors by analysing the torque. More specifically, the torque ripple increases under demagnetisation fault and the time delay embedding or TDE method is used for extracting and detecting hidden patterns in the time series information. By implementing the TDE on the time series of the torque profile, a 2-dimensional display of the torque series in the phase space is obtained. The rotational

radius is used as an index for fault severity estimation. As the demagnetisation severity increases, the radius of the rotation reduces. The disadvantage of this index is that it depends a lot on the load variations. The latter entails that for reliable monitoring, this fault index has to be monitored for the same load. The variation of the rotational with the demagnetisation severity increment can be seen in Figure 3.11

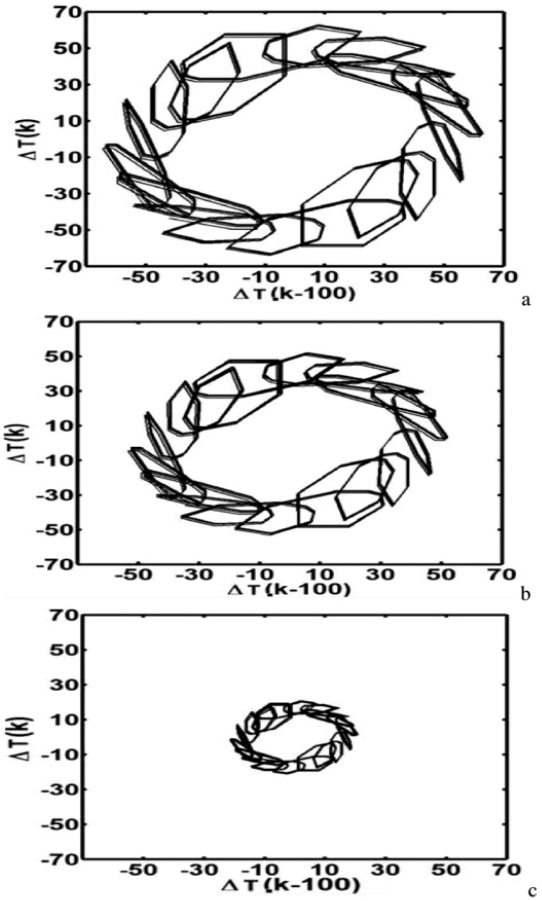

Figure 3.11: Torque first difference phase-space. Healthy (top), 25% demagnetised (middle) and fully demagnetised (bottom) of modelled PM motor by 2-D FEA [51].

Demagnetisation fault reduces the attractive force between rotor and stator, and this force reduction rotates. For the case of static eccentricity, in the region where the air gap is lower than the healthy condition, the attractive force increases and, on the other side, reduces. The same applies to the dynamic eccentricity fault, with the only difference being that these unbalanced magnetic pull rotates with the speed of rotation. Authors of [58] used two force sensors with 90^o spatial phase difference and X and Y components of force distribution calculated experimentally. Later, the force distribution was plotted as function of the other force distribution. The healthy and the faulty condition are different under partial demagnetisation fault, as Figure 3.12 displays.

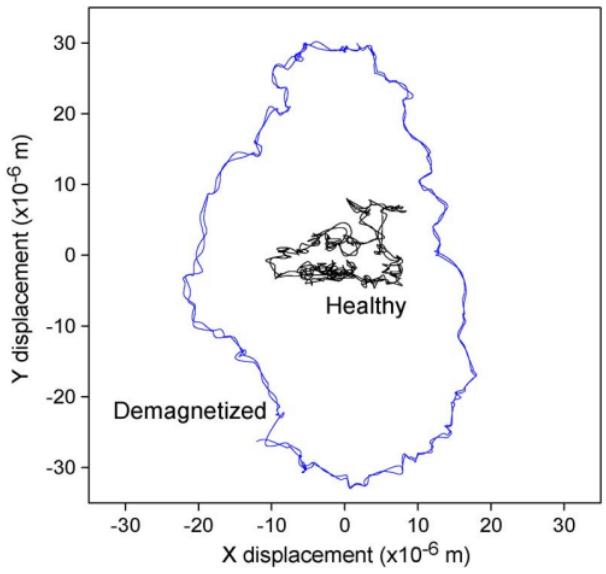

Figure 3.12: Trajectory of the measured target point of the motor shaft in the X–Y plane. A healthy and a partially demagnetised PM motor were measured when running at 1500 r/min under no-load conditions [58].

The authors of [59] proposed a method to detect partial demagnetisation and dynamic eccentricity. The paper proposes to use the differential inductance of the d-axis as a fault indicator quantity for the two faults. The index was extracted experimentally using signal injection by an inverter at standstill conditions. The inverter was injecting both ac and dc fields. Figure 3.13 displays the differential inductance as a function of the d-axis current which varies differently for each fault. [35], presents a similar method in which signal injection is used again. Still, the monitoring quantity is now the steady-state waveform of positive peak plus the negative peak of stator current. More specifically, a square-wave pulsating field is created using the inverter to apply the voltage. The current depends on the two magnetic field vectors. So four stator currents were created for four different angles, as it is shown in Figure 3.14. The summation of the positive plus negative peaks as a function of the pulsating flux vector θ has a sinusoidal form, as shown in Figure 3.15. This method can also detect the uniform demagnetisation fault and the local demagnetisation.

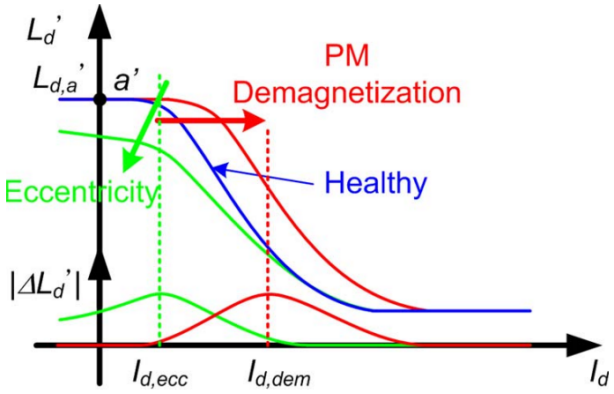

Figure 3.13: Variation in d-axis differential inductance and its variation, versus d-axis current curves with PM demagnetization and eccentricity [59].

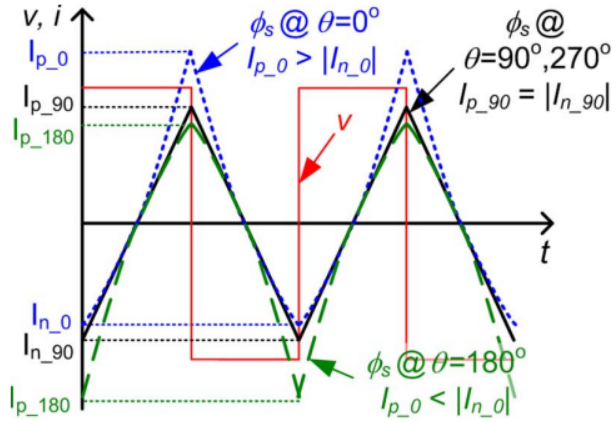

Figure 3.14: Stator current waveform; positive and negative stator current peaks at θ = 0°, 90°, 180°, and 270° [35].

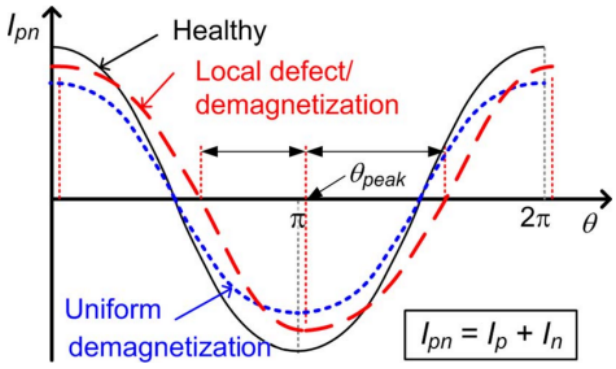

Figure 3.15: Peak summation pattern for PMs with uniform and local demagnetization [35].

The unbalance magnetic pull under eccentricity fault contains different harmonics where 17^{th} and 19^{th} order harmonics have the highest amplitudes [60]. These harmonics are equal to the number of slots minus 1 and the number of slots plus 1, called slot passing vibration harmonics. The amplitudes of these harmonics rise with higher severity, meaning they are appropriate for static and dynamic eccentricity fault diagnosis. These harmonics are the dominant components in the UMP (Unbalanced magnetic pull) vibration signal. Eccentricity fault also generates side-band components at frequencies with the pattern given in (3.1). The incremental rate of the amplitude side-band components can distinguish the static from the dynamic eccentricity.

Other methods use the Park transformation. In many cases, the fault harmonics in the stator current are shadowed by the fundamental harmonic component since the fault harmonics are much smaller in amplitude and near the fundamental. Furthermore, sometimes their amplitude is small enough to make it difficult to distinguish when the noise level is too high. These fault harmonics have even lower amplitude for low eccentricity fault degrees, so it is harder to inspect. Several methods were proposed to eliminate the fundamental harmonic effect on fault harmonics. A method was to use the q-axis current, which is one of the two currents that yield after the Park transformation and appears to be a good identifier for the mechanical unbalances [61, 62]. The reason is that using Park's vector approach or PVA removes the fundamental component from the amplitude spectrum of the current, and the components are analysed using Discreet Wavelet Transform or DWT (Discrete Wavelet Transform). Wavelet transform is a time-frequency signal processing technique to extract fault indicator quantities under non-stationary speed. In [63] the above-mentioned method was used for eccentricity fault diagnosis. This method is online, does not need any sensor implementation, and does not depend on the machine's parameters. Nevertheless, the method requires two signal processing methods, leading to high computational time for index extraction.

The park vector approach is used in sampling the three stator currents in the phase of the machines. Then the three currents are converted from a three-axis reference frame to a two-axis reference frame in which its two components, the d- and q-axis current, are vertical. The equations which correlate the instantaneous phase currents with the d- and q-axis currents are

$$\begin{cases} i_d = \sqrt{\frac{2}{3}} i_a - \sqrt{\frac{1}{6}} i_b - \sqrt{\frac{1}{6}} i_c \\ i_q = \sqrt{\frac{1}{2}} i_b - \sqrt{\frac{1}{2}} i_c \end{cases} . \tag{3.2}$$

The plot of i_d versus i_q under a healthy permanent-magnet machine is approximately a circle. However, under faulty conditions becomes an ellipse. In [30], the concept mentioned above was applied to a machine that has an inter-turn fault and indeed, it became an ellipse. This method is relatively easy to implement. However, three current probes are required to acquire

the three currents, which are expensive. In a Y-connected PM machine, since the three currents in the common point node sum up to zero, knowing two of them makes the third determination possible. The latter and this can reduce the cost of the equipment needed. The extended park vector approach is also proposed for inter-turn fault diagnosis in the same paper. This method monitors the amplitude of specific harmonic on the frequency spectrum on the PVM (Park vector module) signal, which is defined as

$$PVM = \sqrt{i_d^2 + i_q^2}. \tag{3.3}$$

The advantage of this method is that it amplifies the amplitude of the harmonics generated by the inter-turn more sensitive than using only the stator phase current [64]. The harmonics generated in the stator current are caused by the saturation effect that the magnetic flux of the inter-turn fault causes in the stator core, as also explained by [44].

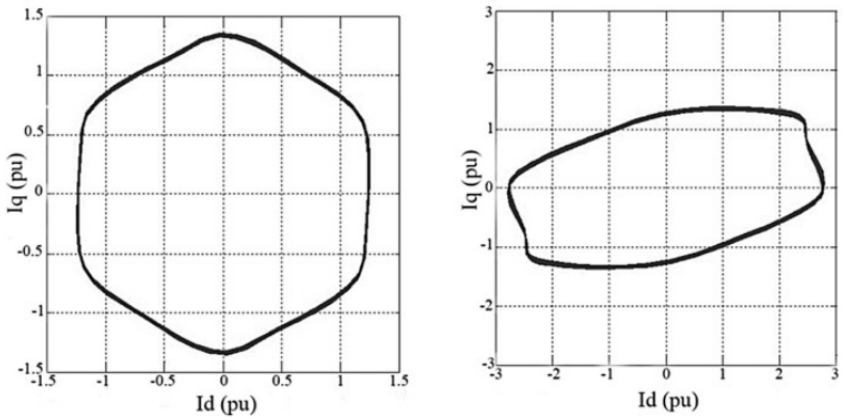

Figure 3.16: Current variations in i_d–i_q plane for a PM motor which is healthy and faulty [30].

When the speed of the machine does not stay constant, the signals of the machine cease to have constant amplitude and frequency. The signal ceases to be periodic, meaning that a fast Fourier transform can not be applied on the signal anymore. Due to this fact, time-frequency signal processing techniques were developed that make it feasible to monitor the amplitude of specific frequencies as the frequency of the signal varies. A long acquisition time is required for a long period to prevent the "spectral leakage" phenomenon and obtain a high resolution. However, this increases the probability of supply voltage and torque oscillations [3]. In these cases, advanced signal processing techniques are required to overcome this challenge [65].

Since the MCSA is not applicable under a transient state, in [66], they converted the MCSA and made it suitable for a transient operation called TMCSA. However, the method is applied in induction motors and not permanent-magnet motors. Short-time Fourier transform is the extended version of the Fast Fourier transform for non-stationary signals [67]. In STFT (Short-Time Fourier-Transform), the transient signal is divided into several time intervals using

windows with fixed length and type, and every window is analyzed by Fourier transform. The latter entails that this technique can't process all signals efficiently. The type and length of the window have to be chosen appropriately depending on the signals, which is impossible. To determine the length of the window, time and frequency resolution drop as a "big" window, which has a better frequency resolution and a "small" window has a better time resolution [67]. This method is adequate for applications where the speed of the machine does not vary suddenly, as the signal will not change fast either.

Nevertheless, STFT cannot solve the problem of analyzing signals with rapid dynamics due to the fixed window length, which results in high spectral leakage. STFT also tends to hide the principal fault harmonics of the signal, as the fundamental harmonic contain the most energy. Several authors started to study multi-resolution signal processing methods. The most common is the Wavelet Transform or WT (Wavelet Transform), which allows for various time and frequency resolutions on the time-frequency plane. Like STFT, WT requires the determination of parameters which are the type of the wavelet function. Fault signatures caused by rotor faults generated have a low order, so the wavelet function has to be chosen accordingly. There are two types of WT; continuous WT or CWT (Continuous Wavelet Transform) and discrete WT or DWT. CWT has a continuous variation in the resolution, which gives sharper results. DWT extracts proper frequency intervals utilizing high- and low-pass filtering, determined by the fault components' order, making the algorithm less time-consuming than CWT [68]. The work presented in [68] applied the two WT algorithms to the stator current of a PM motor with partial demagnetization. In [69], CWT was utilized to detect partial demagnetization fault on a PM motor, using the starting stator current.

Other methods are based on quadratic time-frequency distribution. Linear methods decompose the signal into components; the quadratic forms use energy distributions for distributing the energy of a signal frequency and time domains [70]. In these methods, the whole signal obtains energy over every range, so the resolution is much higher. Wigner-Ville distribution or WVD (Wigner-Ville Distribution) was used to detect dynamic eccentricity in permanent-magnet motors [71]. Another signal processing technique capable of analyzing the time-frequency energy of a signal is the Hilbert transform. However, this transform was developed for application in completely sinusoidal signals, although the non-stationary signals are not. As a solution, the Hilbert-Huang transform or HHT (Hilbert-Huang Transform) uses empirical-model-decomposition or EMD, which decomposes the signal into a limited number of pure oscillating functions called intrinsic mode functions or IMF; hence the transform is applied to each function. In [72, 73] HHT was applied to the stator current to a partially demagnetized PM motor operating under variable speed conditions.

Authors of [74] propose the box-counting method for demagnetization fault diagnosis. Initially, CWT was used to extract the fault signatures under the non-stationary signal. The features prepared by CWD are extracted using the box-counting method. This method considers a threshold, which transforms the components obtained from the CWT matrix into a binary form, i.e. "1" and "0". The threshold is chosen to compromise computational time and statistical simplicity. The box-counting method is applied to the binary matrix, and its output is proposed as a fault index. Figure 3.17 illustrates the square meshing with a length side equal to ε that this algorithm does to the signal. Every iterative process ε is divided into two halves and N number of squares required to cover the signal. The number of required squares has the following ratio

$$N(\varepsilon) \propto \varepsilon^{-FD}, \tag{3.4}$$

where FD is a measure of signal-shape complexity and is used as a fault index. Equation (3.5) can be written as

$$\log N(\varepsilon) = -FD \cdot \log \varepsilon + C. \tag{3.5}$$

Which now, on a logarithmic scale, the relation has become linear. Then linear regression is applied for calculating FD, and the box-counting is obtained. As the demagnetisation severity increases, so does FD.

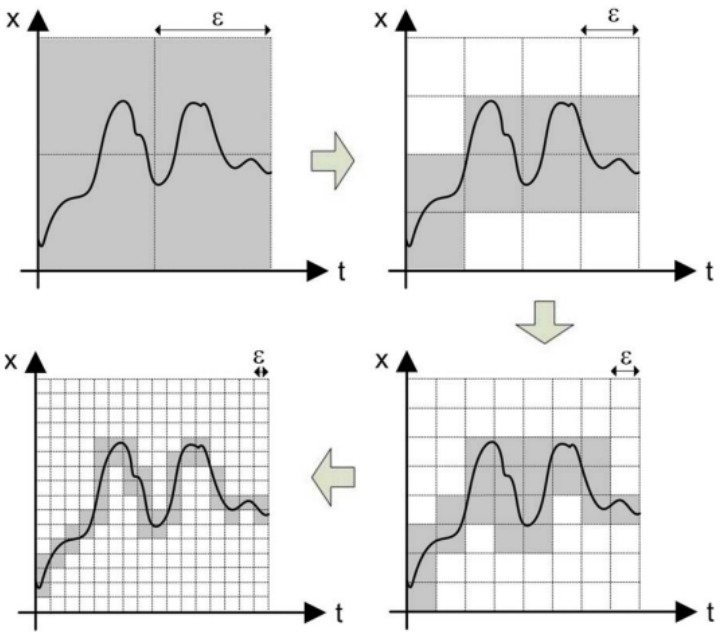

Figure 3.17: Successive reduction by a factor of half of the grid size ε for computing the box-counting FD [74].

The authors of [2] compared various signal processing techniques to examine how complex the algorithms can be in exchange for high resolution. The result was that the quadratic type transforms using the whole signal for each frequency component, which requires a high computational complexity for high resolution. HHT showed an acceptable computational complexity at high resolution. For faults that evolve rapidly, like the inter-turn fault, it is best to use an algorithm which requires less computational time. Since demagnetisation severity does not evolve at a fast rate when it occurs, even the computational complex methods are adequate for monitoring.

The exploitation of physical quantities generated by the machine itself with purpose to detect faults lead to the development of complicated methods. This happens mainly because the winding of the machine is not designed in such manner to exploit the unbalanced magnetic flux created by the faults. Furthermore, the winding configuration acts as a spatial harmonic filter and reduces the induced harmonic frequencies created by faults. By examining all the available literature, the realisation came that none of the state-of-the-art methods can detect all faults. The latter is sensible since having only the quantities of the stator winding is not enough for monitoring since static faults do not induce a signature on the winding. A consequence of the fact that there is no variable magnetic flux that penetrates through the coils of the winding when such a fault takes place. This limitation leads to the development of magnetic flux-based fault diagnosis methods.

3.2.2 Sensor-based diagnostic methods

The two main components of magnetic flux that exist on a permanent-magnet machine are the main magnetic flux and the magnetic leakage flux. The main flux is responsible for energy conversion, as it links the coils with the rotor's magnetic field. The leakage component can be every type of flux which does not contribute to the energy conversion process. Any magnetic flux lines created by the magnets the coils and not used for torque production fall in the category of leakage flux. There is also an amount of flux that radiates outside the machine's stator bore, called stray flux.

Magnetic flux-based fault detection techniques using commercial flux sensors [75, 76, 77, 78], or by using a number of search coils with a proper span [12, 33, 23, 79, 80, 81] is a reliable, low-cost and industrial applied method to extract fault indicator quantities. Their major advantage is the ability to measure the flux at various points and for specific surfaces in an electric machine; as a result, making it possible to exploit the consequences of a fault. Search-coils can be used not only for creating diagnostic techniques but also for real-time position estimation methods in both PMSMs [82] and Induction Motors [83] since they have advantages compared to the sensor-less ones.

Various commercial and hand-made magnetic flux sensors have been developed for creating fault diagnostic schemes in electric machines. Some selection criteria are size, sensitivity, cost and ease of implementation. For instance, if the flux sensor is supposed to be placed externally from the machine, it should have high sensitivity since the magnetic field outside of the machine is very weak. The latter is a consequence of the high magnetic permeability of the stator bore. However, there is no size limitation in this case [22]. The opposite applies to the internal flux sensors.

Hall-effect flux sensors are one of the most popular commercial sensor technologies. These sensors are based on the Hall effect electric field created along a material's dimension. This electric Hall-effect field is generated by applying an electric field on one dimension of a material and a magnetic field on the perpendicular position in that the current flows. Then the electrons flow in the direction of the electric field; since they are inside a magnetic field, a Lorentz force will start to deviate them. The electrons will start moving into the perpendicular position where the primary current flows, so an electric field will start shaping in that dimension. This electric field can be easily measured by placing a voltmeter in that direction. This voltage is on mVolts, meaning that an amplifier is usually needed. These kinds of sensors are used for fault diagnosis of permanent-magnet machines [76, 77, 78], as well as rotor speed and position estimation [84, 85].

Magneto-resistors are variable resistors whose resistance value varies with the intensity of the penetrating magnetic field. More specifically, this sensor is parted by a semiconducting material, in which the magnetic field changes the direction of the moving charges, translated as a variation in its resistance. This sensor was used in [86] to detect an inter-turn fault in induction motors.

Magnetostrictive material is a category of materials that change dimensions with the change of direction of external magnetic fields. [75] presents a Fibre Bragg Grating or FBG with a highly volumetric magnetostrictive material. This sensor was employed to detect the demagnetisation fault. The sensor found applications in bearing health monitoring as well [87]. Materials of similar philosophy are the piezo-electric materials, which in the presence of a force, produce an electric field along the dimension that the force was applied. The opposite also applies, meaning that their dimension changes in the presence of a terminal voltage.

Another type of sensor is flux-gate magnetometers, which are comprised of two sets of coils wrapped around a highly magnetic permeable core [88]. The one winding is called drive, and the other sense. Figure 3.18 illustrates the winding described. The drive winding is toroidal, which means the sense winding is the normal circular coil. The sense winding is placed inside the drive winding, such that if the winding produces magnetic flux, these lines will penetrate parallel to the drive winding. A trapezoidal waveform usually generates the drive coil with a specific frequency. Due to the position of the drive coil, the magnetic flux penetrating the sense coil is zero. Hence, there is no induced voltage in the sense winding. With the application

of an external field to the coil, the magnetic flux inside the drive winding will get disturbed, meaning that the magnetic flux to the sense winding would cease to be zero. At the positions of the slope regions of the trapezoidal waveform, voltage spikes induce in the sense coil. The magnitude and direction of the external magnetic field are estimated by processing the sense coil's spiked-voltage waveform.

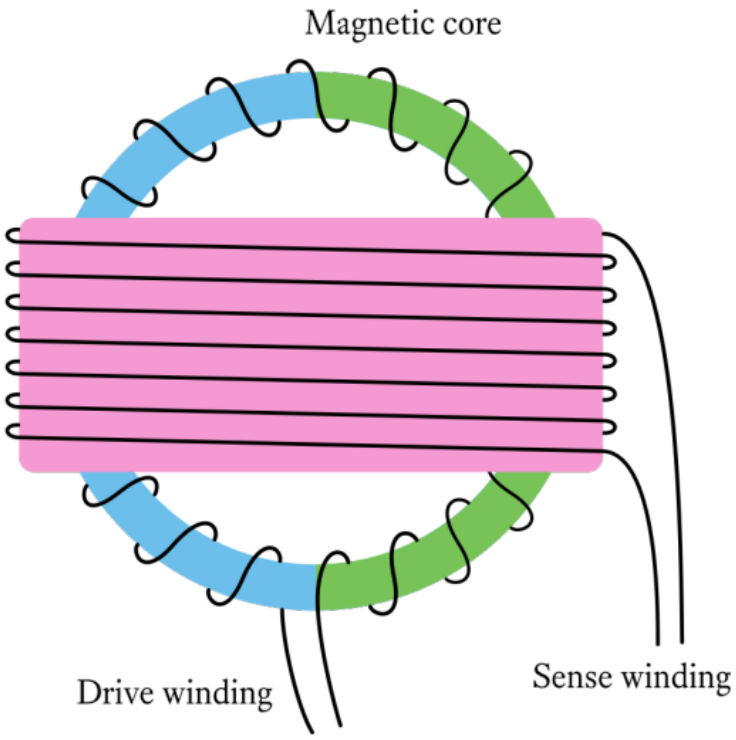

Figure 3.18: A circle-shaped flux-gate sensor [88].

The last category of flux sensors are the classical search coils. The voltage induced on them is proportional to the number of turns, the surface, the magnetic flux density and how fast it varies along the coil's surface. There are commercial and hand-made search coils to develop fault diagnostic schemes for electric machines. Search coils on a printed circuit board or PCB has also been designed for fault diagnosis applications in [89]. Search-coils can come on any geometry chosen by the designer [90, 31, 91, 92]. Depending on their position, these coils can either have an iron core or be coreless if the application does not require demand measuring a weak magnetic field [91]. However, when these kinds of search coils come with an iron core, the core impacts due to the saturation phenomenon, which occurs for high magnetic field intensities. The authors of [93] studied the core impact of applying these coils in the condition monitoring of induction motors. The conclusion was that the cored coils could significantly improve the amplitude of the induced voltage. The core nonlinearity did not play a determinant role in the fault diagnosis process.

By mounting search coils in the stator teeth of a PM motor, a voltage is induced on each search coil under on-load conditions [23]. This induced voltage is the superposition of two voltage components. The one produced by the permanent-magnet field and the one from the armature reaction field. Then, armature and field voltages are filtered using the linear-time-invariant filter to extract the fundamental component. Calculating the amplitude and the phase angle of the armature magnetic field fundamental component was made possible. Later, each tooth's armature component was displayed in a polar graph. Using this polar graph, the estimation of the position and severity of the inter-turn fault is possible. Depending on the fault, the polar plot changes, as shown in Figure 3.20. This method calculates the magnetic field's spatial distribution around the machine's periphery. This method seems capable of detecting all faults; however, in the case of the eccentricity faults, the two polar graphs have a similar pattern as the representation is spatial. This method is invasive since it requires the machine to be disassembled and for the coils to be installed, making it hard to implement in a high number of machines. Lastly, this method has the advantage that only the fundamental harmonic of the voltage is employed for fault diagnosis, simplifying the method. A method of similar philosophy was also applied for induction motors, using not search-coils but hall-effect voltage sensors [94, 95, 96]. More specifically, the method offers a graphical expression for the magnetic field as a function of time and space. The authors of [97] followed a similar approach for detecting the inter-turn fault in brushless dc motors, with the difference that the induced voltages in the search coils are rectified and converted into dc voltages through a half-wave rectifier. Reducing any search coil's fundamental voltage component value translates as an inter-turn fault occurrence. In [98], high order frequency components around switching frequency supported that they have higher sensitivity for inter-turn fault monitoring. A similar approach with [23] was used in [99] for inter-turn fault detection with the difference that the flux sensors were positioned outside the stator frame of the permanent-magnet machine. Hence, the sensed magnetic flux was radial stray. The current magnetic flux density ratio over one of the healthy cases of each sensor, displayed in a polar plot, was used for fault diagnosis.

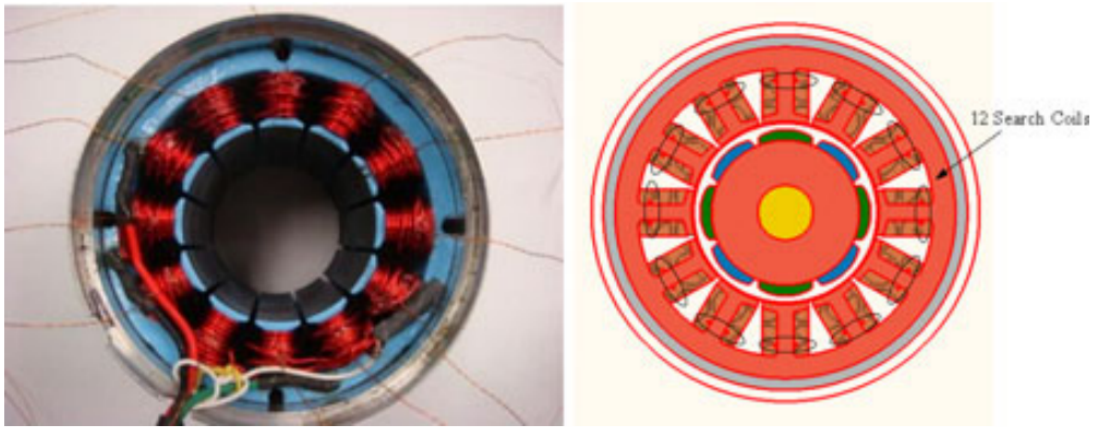

Figure 3.19: Implementation of search coils in a test machine and FEA model [23].

Static eccentricity creates two air-gap regions with a higher or lower length than the healthy state and two points where the air-gap variation is negligible. In [33], two stator mounted search-coils with 180^o difference in space were used to detect static-eccentricity in axial-flux permanent-magnet machines. If the minimum air gap was close to one search coil, its voltage was increasing, and the opposite happens for the maximum air gap; hence the estimation of the fault's position is possible. However, the conclusion was that if the positions where the air gap does not change are upon the search coils, the machine continues to look healthy. This limitation of the method was exceeded using a third coil in [12]. Also, a mathematical model was developed to estimate the static eccentricity factor and the position of the minimum air gap. Figure 3.21 illustrates the 3-D FEA model of the machine with the three search coils.

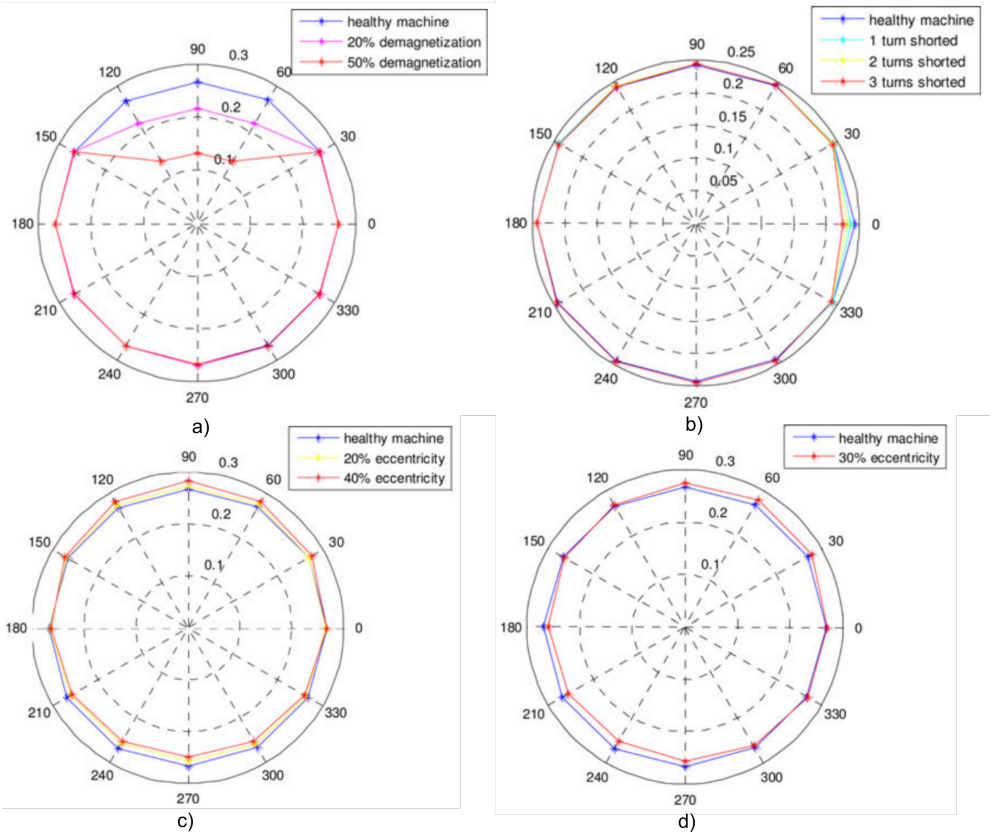

Figure 3.20: Polar graph for each faulty condition, a) demagnetization of a pole pair, b) inter-turn fault, c) static and d) dynamic eccentricity [23].

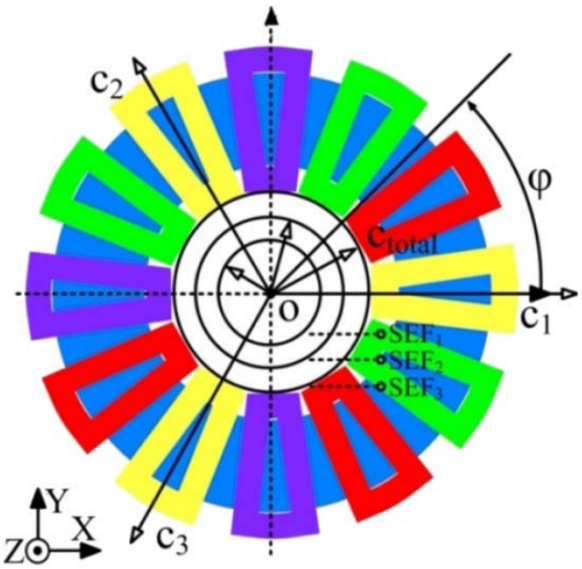

Figure 3.21: Search coil locations; the search coils are mechanically spaced by 120^o and occupy the upper part of six slots [12].

In the work presented in [79], a search coil was used to detect dynamic eccentricity by monitoring the peak-to-peak magnitude of the speed normalized voltage in time as the signal is zero under healthy conditions. The voltage negation comes from the coil span, which corresponds to an odd number of coils and an even number of poles. Figure 3.22 illustrates two PM motor design topologies with the search-coil designed appropriately in each case. In the first case, the PM motor is presented with an internal rotor, and the search coil is spanned along 3 - 4 pole pitches. In the second case, the PM motor has an external rotor, and the search coil is spanned at 3 coil - 2 pole pitches. Since the machine is 3-phase, the current waveform has 120^o phase difference in time. The magnetic flux created by the permanent-magnet field has 180^o phase difference. From the above, the result was that for every rotor position, the magnetic flux induced in the search coil would be zero, and the voltage would also be induced. The latter results in a zero voltage signal under healthy conditions, as shown by Figure 3.23a. Hence, when the dynamic eccentricity fault takes place in the machine, the voltage of the search-coil becomes non-zero as the magnetic flux that penetrates the search-coil ceases to be zero, as Figure 3.23b suggests. Since the search coil is stationary with respect to the rotor's unbalanced magnetic flux, the peak-to-peak value of the voltage was used as a fault indicator. Since the signal is zero under healthy conditions and becomes non-zero under faulty conditions, the specific signal varies only with the speed and the fault severity. So by normalizing the signal over the speed, the signal becomes fault severity dependent only, as Figure 3.23f displays. The latter means that method is ideal for machines operating under non-stationary conditions, speed and load. Lastly, this method uses the signal directly for monitoring, and no further signal processing is required.

For rotor faults, as was discussed above in the sensor-less condition monitoring methods, due to the series connections of the phase's coils, several fault harmonics are cancelled due to the coil connection. One can consider the latter a disadvantage, as many harmonics that could help distinguish between faults using the MCSA method vanish, so the method losses its accuracy. The employment of a flux-sensor offers a solution when monitoring for demagnetization fault harmonics, according to [100, 101].

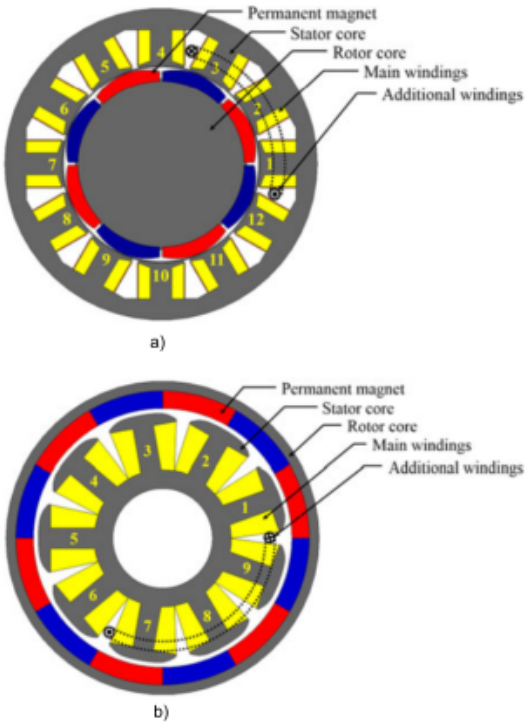

Figure 3.22: Additional winding for three-phase PM a) internal rotor motor with eight poles and 12 slots and b) external rotor motor with 12 poles and nine slots [12].

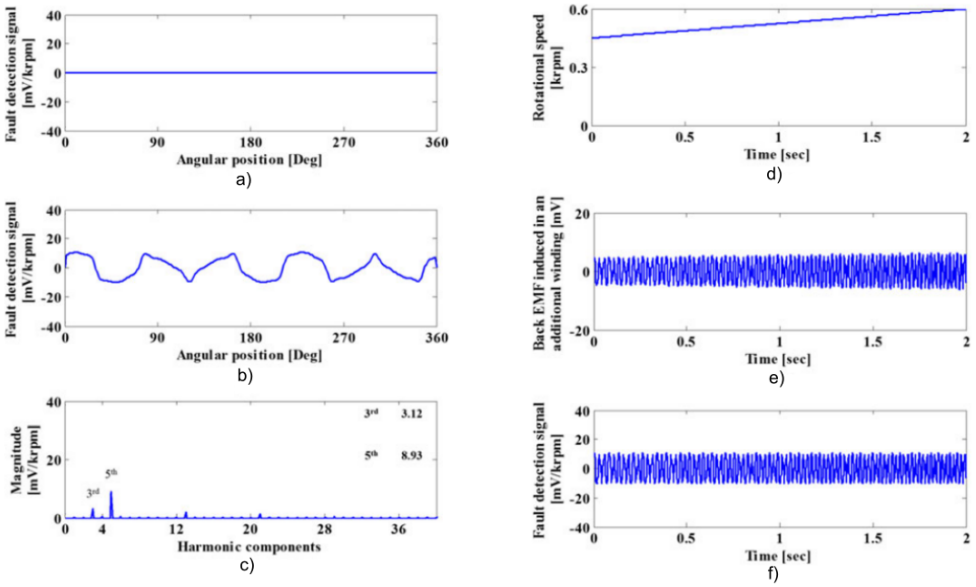

Figure 3.23: Speed normalized voltage for a PM motor with 12 slots and 8 poles under a) healthy, b) 50% dynamic eccentricity condition, c) its spectrum and the d) a transient speed ramp, the corresponding e) voltage waveform and the one in f) speed normalized form [12].

The authors of [81] proposed an approach to identify rotor faults, using a single search coil wrapped around one tooth of an interior permanent-magnet motor. The induced voltage in the search coil for a full mechanical revolution is measured, and then the absolute value of the signal is calculated. The method extracts the peak values of the signal's absolute value, which are related to each magnetic pole. The outcome of the work showed that the peak values had enough information to distinguish the dynamic faults. The distinguished conditions were healthy, load defects, partial and uniform demagnetization and dynamic eccentricity. To extract an indicator quantity independent of the variation of the load, each peak value is normalized with the average value of all peaks. Figure 3.24 presents the results for the search-coil voltage under two fault conditions. The signal shows how partial demagnetization is distinguished from dynamic eccentricity on an experimental scale.

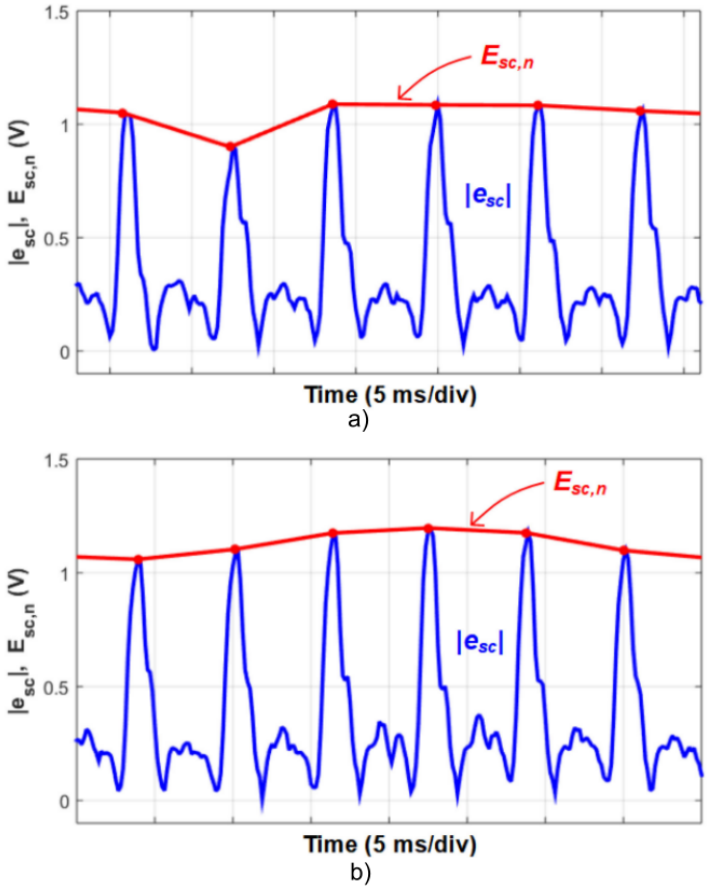

Figure 3.24: Experimental results for the voltage waveform peaks under a) partial demagnetization and b) dynamic eccentricity [81].

3.2.3 Discussion and limitations found in the state-of-the-art diagnostic methods

According the above investigation, diagnostic methods based in sensors which measure the magnetic flux on the air-gap are more efficient than the ones that are placed outside the machine's frame, however the machine must be disassembled for their installation. Moreover, in cases where the sensor is a search-coil, the span can be varied in order to sense only the magnetic flux which is useful for the detection of a fault. So a search-coil can act as a filter that can cut out the magnetic flux created during balanced-healthy conditions. The latter search-coil can generate a search-coil which its induced voltage will not require further signal processing.

In both category types of methods, quantities acquired from the stationary part of the machine are available. So, in fault cases, where the magnetic fault signature stays constant on the air-gap both type of method categories (sensor and sensor-less) unable to offer efficient detection of the faults. On top of that, for the cases which the quantities generated by the machine

itself like stator current are used for detection additional limitations come into play. The en series connections of the coils sums voltage harmonics that have 180^o phase difference, these harmonics are negated and they do not appear in the current. The latter means that the winding is a spatial filter which becomes an obstacle in the condition monitoring process. The signal in sensor-less methods is easier to be captured however to extract the feature is a much more difficult compared to the sensor based methods. In the case of sensor based based methods the above work showed that to be able to detect all faults, the magnetic flux has to be measured in as many positions around the air-gap as possible, like in the case where it is measured as many times as the number of concentrated coils of the machine [23]. By measuring the air-gap magnetic flux in only one point, only dynamic eccentricity and partial demagnetization can be detected efficiently [81]. In the case of static faults, like static eccentricity it was proven in [12] that to account both the fault severity and location, the air-gap flux has to be measured in three different points with 120^o spatial difference. Dynamic eccentricity was detected in [79] using one search-coil which negates the magnetic flux under balanced conditions.

After having this discussion, it is visible now that measuring the magnetic flux from stator is not the solution because for faults that do not cause moving unbalanced magnetic flux, there is no induced harmonic frequencies as there is no relative motion between the flux and conductors placed in the stator. This thesis will make an effort to offer a solution to the problem states above. By finding a way to measure the magnetic flux of the rotor reference frame, it is expected that the faults which cause unbalanced magnetic flux will become detectable. However, at the same time, faults creating moving unbalanced magnetic flux cease to be detectable, since the relative motion of the flux and the conductors ceases to exist. To make it possible to detect both faults categories, a method to accomplish both flux measurements simultaneously has to be invented.

Taking into consideration the review that was done above, the unsolved problems that the existing diagnostic methods cannot solve are the following:

- no formula can correlate the coil-slot and pole number with the harmonic order generated during a rotor fault, i.e., partial demagnetization and dynamic eccentricity.
- no method can detect all faults with a small amount of hardware which will be online. There is no method because only quantities monitored from the stator reference frame are available. The latter entails that there is a need for a method that will be able to transform the faults that are on the stator reference frame into the rotor reference frame. By accomplishing the transformation, it will be possible to extract monitoring quantities proportional to the fault severity. Furthermore, the method is preferred to be as simple as possible, meaning it is preferred to be able to detect the fault without any further signal processing. The reason is that signal processing algorithms are not cost efficient the method loses its simplicity as many other considerations start to add to the process.

- There is not a solid theory which correlates the harmonics generated under fault conditions with the quantities extracted using a single search coil.

Chapter 4

Diagnostics in permanent-magnet machines by monitoring the air-gap flux

This chapter shows how to exploit the air-gap magnetic flux of permanent-magnet machines to detect all faults. The first part of the chapter extends the method which utilises a pitch-dependent search coil to detect partial demagnetisation in axial-flux permanent-magnet generators. The induced voltage on the search-coil for all faults is extracted using simulation and studied. The conclusion is that this search coil configuration can detect partial demagnetisation and dynamic eccentricity. However it cannot detect static faults, i.e. inter-turn fault and static eccentricity. To overcome this limitation, a new novel search-coil configuration is proposed which uses two search coils, one in the rotor and one in the stator, which couple magnetically when a fault occurs. The proposed air-gap flux monitoring scheme designed on a common permanent-magnet machine is presented in Figure 4.1. The span of both search-coils is equal to the span of odd number of coil pitches and even number of pole pitches. The latter meas that the induced voltage under balanced conditions in both search-coils is zero. The search-coil placed in the rotor is shorted and the one in the stator is open circuited. More specifically, for inter-turn fault and static eccentricity the magnetic flux generated in the rotor search-coil induces a voltage on the stator search-coil. Without the closed circuited rotor search-coil the latter type of faults would induce voltage frequencies on the stator search-coil dependent by the location of the fault. The proposed condition monitoring method accomplishes to transform the faults that create stationary unbalanced magnetic flux to faults that create rotating one, making them detectable using For dynamic eccentricity and partial demagnetization, the stator search-coil only is adequate for detection. Every fault leaves a unique signature waveform on the proposed monitoring signal and the amplitude is proportional to the fault severity. This method can detect all types of faults

in permanent-magnet machines at any speed and load. Furthermore, the proposed fault detection signal depends only on the fault severity and the rotational speed. Simulation and experimental results show that the method can evaluate the condition of permanent-magnet synchronous machines.

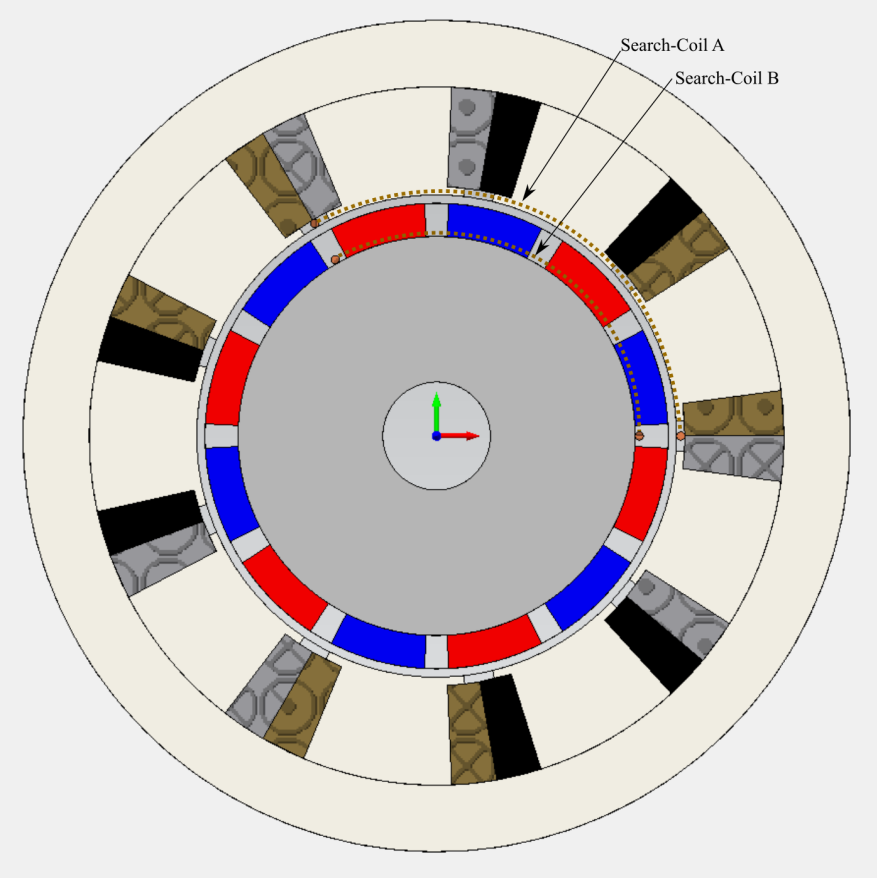

Figure 4.1: A permanent-magnet machine with the proposed search-coil scheme installed.

4.1 Detection of partial demagnetisation in AFPM generators using a search-coil

In this work, the search-coil, which negates the induced voltage under balanced conditions, is used to detect the partial demagnetisation in air-cored permanent-magnet Axial-Flux generators. Its principle is to monitor a speed-normalised fault detection signal. This signal depends only on the demagnetisation severity, as it was extracted using a flux-sensor with a span that negates the induced voltage under balanced conditions. The generator has been designed for marine renewable applications working under variable speed conditions rendering PM health monitoring under nonstantionary conditions imperative. Initially, a mathematical equation for

the electromotive force (EMF) is derived under partial demagnetisation conditions. The equation offers the frequency components related to the fault. Furthermore, an analytical model was also developed that correlates the monitored signal amplitude with the demagnetisation severity. A 3-D finite-element model of the installed winding in the generator is employed to verify the proposed method under steady and variable speed conditions. Figure 4.2 illustrates the wireframe model in an exploded view of the AFPM generator carrying the supplemental winding.

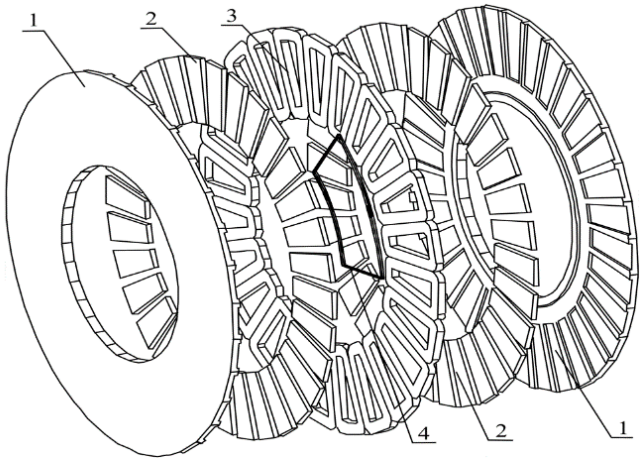

Figure 4.2: Exploded wireframe model of the analysed AFPM generator with the supplemental winding corresponding to a span of 3 coils and 4 pole pitches. 1. Rotor disc, 2. PM, 3. armature coil, and 4. supplemental winding.

4.1.1 Mathematical derivation of induced EMF due to partial demagnetisation fault

This section shows how to derive the induced voltage in the search coil under partial demagnetisation fault with a focus on the harmonics generated on it and how the fault affects the amplitude of the search coil.

EMF induced in a single coil of the stator winding under balanced conditions

When the rotor of a coreless AFPM generator exhibits concentric motion without any fault on it, the air-gap length of the machine is constant, no matter the position of the rotor. The air-gap length of an air-cored double-rotor-single-stator AFPM generator can be considered constant since there is no stator slotting effect; there is only the saliency effect, but in this analysis, it is neglected. The air-gap length under healthy conditions is

$$g_{ideal} = 2h_{PM} + 2g + t_w, \tag{4.1}$$

where h_{PM}, g and t_w are the permanent-magnet axial thickness, air-gap length and axial thickness of the stator winding, respectively.The air-gap permeance for a coreless AFPM generator without partial demagnetisation or any other kind of fault is constant and is equal to

$$\Lambda_{ideal} = \frac{\mu_0}{2\frac{h_{PM}}{\mu_r} + 2g + t_w}, \tag{4.2}$$

where μ_0, and μ_r are the free space's permeability and the magnet's relative recoil permeability. Nd-Fe-B magnets under low operational temperatures, their B-H characteristic can be considered approximately linear and also the recoil permeability equal to unity i.e $\mu_r \approx 1$. The magneto-motive force (MMF) F developed from the permanent-magnets can be expressed using Fourier series composition as follows

$$\mathscr{F}(\theta,t) = \sum_{\nu=odd}^{\infty} \mathscr{F}_{PM,\nu} \cos(\nu p\theta - \nu\omega_s t - \phi_\nu), \tag{4.3}$$

where $F_{PM,\nu}$, ϕ_ν, p, ω_s and t are the magnitude of the ν^{th} MMF PM harmonic, phase angle of the ν^{th} MMF PM harmonic, the number of pole pairs, the electrical angular frequency and time, respectively. The magnetic flux density can be written as a product of the relative air-gap permeance function of the PM magneto-motive force

$$B = \Lambda \cdot \mathscr{F}. \tag{4.4}$$

Expanding (4.2) with binomial series and neglecting higher-order terms and then substituting the final expansion and (4.3) to (4.4) and executing the algebraic calculations it yields

$$B(\theta,t) = \alpha \sum_{\nu=1,3,5}^{\infty} \mathscr{F}_{PM,\nu} \cos(\nu p\theta - \nu\omega_s - \phi_\nu), \tag{4.5}$$

where α is a constant equal to

$$\alpha = \frac{\mu_0}{2h_{PM}} \left(1 - \frac{g}{h_{PM}} - \frac{t_w}{2h_{PM}} + \frac{g^2}{h_{PM}^2} + \frac{gt_w}{h_{PM}^2} + \frac{t_w^2}{4h_{PM}^2}\right), \tag{4.6}$$

depending on the generator's geometrical dimensions. To calculate the magnetic flux Φ, the magnetic flux density wave along the middle air gap facing an armature coil is integrated. Considering an angle element $d\theta$ which corresponds to a surface dS on the coil, a magnetic flux element $d\Phi$ penetrates through it. The magnetic flux of the ξ^{th} coil can be formulated as follows

$$\Phi_\xi(t) = \frac{\left(r_o^2 - r_i^2\right)}{2} \int_{\frac{2\pi}{c}(\xi-1)}^{\frac{2\pi}{c}\xi} B(\theta,t)d\theta, \tag{4.7}$$

where c, r_o, r_i, and ξ are the total number of coils of the stator winding, the outer radious of the magnet, the inner radius of the magnet, and the coil index, respectively. The EMF induced in the ξ^{th} coil winding $\mathscr{E}_\xi(t)$ can be calculated as the time derivative of the magnetic flux penetrating through the ξ^{th} coil with respect to time as follows

$$\mathscr{E}_\xi(t) = -N_c \cdot \frac{d\Phi_\xi(t)}{dt}, \tag{4.8}$$

where N_c is the number of turns in a coil. After substituting (4.5) into (4.7), integrating along the middle of one of two air gaps, and then differentiating with respect to time, the EMF induced in the ξ^{th} armature coil winding of the AFPM generator, under healthy conditions, can be mathematically illustrated as follows

$$\mathscr{E}_\xi(t) = \alpha\left(r_o^2 - r_i^2\right) N_c \omega_r \sum_{\nu=odd}^{\infty} \mathscr{F}_{PM,\nu} \sin\left(\nu p \frac{\pi}{c}\right) \sin\left(\nu p \frac{\pi}{c}(2\xi - 1) - \nu\omega_s t - \phi_\nu\right), \tag{4.9}$$

where ω_r is the mechanical speed of the rotor. For a PM generator under balanced conditions, the induced EMF in the ξ^{th} coil distributed symmetrically in space along the periphery of the stator contains higher harmonic components that distort the fundamental one. Equation (4.9) expresses that in the ξ^{th} stator coil will be induced harmonic components with frequencies νf_s. The voltage in the above analysis describes the EMF or no-load voltage because the magnetic field created by the armature winding has not been considered. The induced voltage on the supplemental winding can be found by integrating the flux over the surface of the winding, which is 4 pole pitches, by substituting (4.5) into (4.7) and integrating over four pole pitches.

EMF Induced in the supplemental winding due to partial demagnetisation

The proper relative air-gap permeance function needs to be extracted to calculate the EMF under partial demagnetisation. The magnetic flux density wave significantly reduces the specific pole pitch in this condition. The air-gap is not constant, but we can consider that its length is increased in that particular magnet pitch as the magnet moves, which means that this increased air-gap length rotates with the mechanical rotational speed.

In Figure 4.3, the air-gap length and the relative permeance are shown along a circle in the mid radius of the magnets under healthy and partial demagnetisation conditions. When the magnet is demagnetised, the air-gap increases with the fault severity. It can be represented as $D = \varepsilon g$, where ε>1 is a factor corresponding to the increment and D can be considered a factor related directly to the fault severity. Moreover, the air-gap permeance in the same angle-pitch will be reduced by $\varepsilon\Lambda$ since fewer magnetic lines will remain in that area. Utilising the logic mentioned above, the air gap under partial demagnetisation is both a function of

space and time

$$g_{demag}(\theta,t) = 2\frac{h_{PM}}{\mu_r} + 2g + t_w + D\left(\frac{1}{2p} + \sum_{k=1}^{\infty}\frac{2}{k\pi}\sin\left(\frac{k\pi}{2p}\right)\cos\left(k\theta - k\omega_r t\right)\right), \tag{4.10}$$

where the last term of the above equation is a constructed pulse wave using Fourier series, which moves with the mechanical rotational speed ω_r, as the demagnetized magnet does.

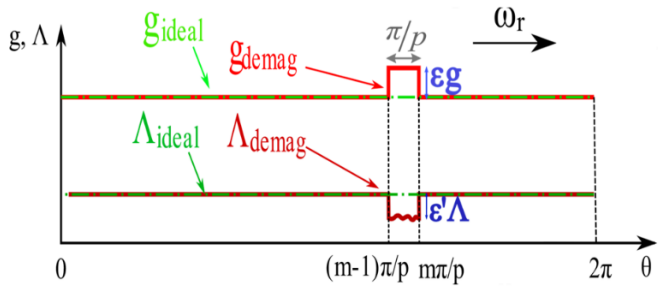

Figure 4.3: The air-gap length along the periphery at a mid radius of the PMs and the air-gap permeance, under healthy and demagnetized conditions.

The relative permeance function under partial demagnetization can be represented as follows

$$\Lambda_{demag}(\theta,t) = \frac{\mu_0}{2\frac{h_{PM}}{\mu_r} + 2g + t_w + D\left(\frac{1}{2p} + \sum_{k=1}^{\infty}\frac{2}{k\pi}\sin\left(\frac{k\pi}{2p}\right)\cos\left(k\theta - k\omega_r t\right)\right)}. \tag{4.11}$$

The above-equation may be further written in the form below

$$\Lambda_{demag}(\theta,t) = \frac{\mu_0}{2h_{PM}}\cdot \left(1 + \frac{g}{t_w} + \frac{t_w}{2h_{PM}} + \left(\frac{D}{4h_{PM}p} + \sum_{k=1}^{\infty}\frac{D}{k\pi h_{PM}}\sin\left(\frac{k\pi}{2p}\right)\cos\left(k\theta - k\omega_r t\right)\right)\right)^{-1}. \tag{4.12}$$

The above equation has been formulated in such a manner to be expanded using the binomial Taylor series. After its expansion, the eventual relative permeance function having one pole pitch demagnetized is

$$\Lambda_{demag}(\theta,t) = \alpha + \beta(D) + \gamma(D)\cdot\sum_{k=1}^{\infty}\cos\left(k\theta - k\omega_r t\right), \tag{4.13}$$

where β, and γ are two constants depending on the generator parameters and partial demagnetization factor and are equal to

$$\begin{aligned}\beta(D) &= \frac{\mu_0 D}{2h_{PM}}\left(\frac{g}{2h_{PM}^2 p}+\frac{t_w}{4h_{PM}p}-\frac{1}{2h_{PM}p}\right)\\ \gamma(D) &= \frac{\mu_0}{2h_{PM}}\left(\frac{D}{h_{PM}}+\frac{2g}{h_{PM}}+\frac{t_w}{h_{PM}}-1\right)\end{aligned}. \tag{4.14}$$

It should be noted that $\beta(0)=\gamma(0)=0$. The MMF can be represented using Fourier series similarly using equation (4.3) with the only difference that the amplitude of every component will be different due to the demagnetization. After employing the equation all over (4.4) again and taking into consideration the equation which connects the rotational speed with the electrical speed

$$\omega_r = \frac{\omega_s}{p}, \tag{4.15}$$

the air-gap magnetic flux density wave with the fault embedded can be calculated as follows

$$\begin{aligned}B_{demag}(\theta,t) &= (\alpha+\beta(D))\cdot\sum_{\nu=odd}^{\infty}\mathscr{F}_{PM,\nu}^{demag}\cos(\nu p\theta-\nu\omega_s t-\phi_\nu)\\ &+\gamma(D)\sum_{\nu=odd}^{\infty}\sum_{k=1}^{\infty}\mathscr{F}_{PM,\nu}^{demag}\frac{D}{k\pi h_{PM}}\sin\left(\frac{k\pi}{2p}\right)\cos(\nu p\theta-\nu\omega_s t)\cos\left(k\theta-\frac{k}{p}\omega_s t\right).\end{aligned} \tag{4.16}$$

After substituting equation (4.16) into (4.7), integrating along the middle air-gap facing three coils or four-pole pitches, the first term of (4.16) will be cancelled and afterwards, differentiating with respect time using (4.8), yields

$$\begin{aligned}\mathscr{E}_{demag,\xi}(t) &= \frac{1}{2}N_c\left(r_o^2-r_i^2\right)\omega_r\gamma(D)\cdot\\ &\sum_{\nu=odd}^{\infty}\sum_{k=1}^{\infty}\mathscr{F}_{PM,\nu}^{demag}\frac{D}{k\pi h_{PM}}\sin\left((\nu p-k)\frac{2\pi}{p}\right)\sin\left((\nu p-k)\frac{2\pi}{p}-\left(\nu-\frac{k}{p}\right)\omega_s t\right)\\ &+\sum_{\nu=odd}^{\infty}\sum_{k=1}^{\infty}\mathscr{F}_{PM,\nu}^{demag}\frac{D}{k\pi h_{PM}}\sin\left((\nu p+k)\frac{2\pi}{p}\right)\sin\left((\nu p+k)\frac{2\pi}{p}-\left(\nu+\frac{k}{p}\right)\omega_s t\right)\end{aligned}. \tag{4.17}$$

The EMF induced in the supplemental winding will have additional time-harmonic components under a stationary rotational speed, which depends on the pole pair number of the AFPM generator. These additional harmonic components have amplitudes which are increasing, and their frequencies are

$$f_{demag} = \left(\nu\pm\frac{k}{p}\right)f_s, \tag{4.18}$$

where ν takes odd values and k integer values, the harmonic frequencies with patterns given by (4.18) of the voltage on the additional winding, normalized by the speed, can be used as a fault indicator as these amplitudes depend only on the fault severity, which gives the major advantage of monitoring for the specific fault under variable speed conditions.

Analytical prediction of the demagnetization severity

In this subsection, the level of demagnetization is calculated theoretically using the geometry of the supplemental winding. According to [29], in an AFPM machine with two rotor discs, the main magnetic field lines that induce the armature voltage are between the opposite magnets in the discs. There are also field lines that flow between the adjacent magnets of each disc, and these also contribute to the voltage generation. Additionally, there is the PM rotor leakage field, which contains all the lines which do not penetrate through the stator coils and the stator leakage field, which does not contribute to the interaction with the main PM rotor field.

When all magnets are healthy, the vector sum of magnetic flux which penetrates through the search coil is zero, which means that there is no voltage induction. For every arbitrary angle of the rotating magnetic field, the total magnetic flux crossing through the additional winding will be zero too. When at least one magnet is demagnetized, the number of the magnetic flux lines in a single-pole pitch reduces, and as this magnet transits through the search coil, the vector sum of the magnetic flux ceases to be zero. As a result, an alternating voltage is generated on the terminals of the search coil. The currents in three coils are in a 120^{o} phase difference, which means that the magnetic flux of each coil also has the same phase difference; hence the resultant magnetic flux, which crosses through the supplemental winding, is zero due to the armature under healthy conditions.

Figure 4.4 illustrates the 2-D view geometry of the additional winding, which occupies 4 pole pitches and 3 coil pitches along the generator periphery for a specific rotor position. The magnetic field waveform, which corresponds to each magnet in that arbitrary position, is also presented. The last permanent magnet on the same figure is demagnetized, and this was modelled by the reduction of the magnetic field on that specific pitch.

The fundamental harmonic of the flux density wave at a time instant can be written as follows

$$B(\theta) = B_g \sin(p\theta), \tag{4.19}$$

where B_g is the peak value of the air-gap magnetic flux density. This value depends on the magnet height, h_{PM}, air-gap thickness, which in this coreless AFPM generator is given by (4.1) and from the relative recoil permeability of the PM, μ_r.

$$\frac{B_{rem}}{\mu_0\mu_r}2h_{PM} = \frac{B_g}{\mu_0\mu_r}2h_{PM} + \frac{B_g}{\mu_0}2g + \frac{B_g}{\mu_0}t_w. \tag{4.20}$$

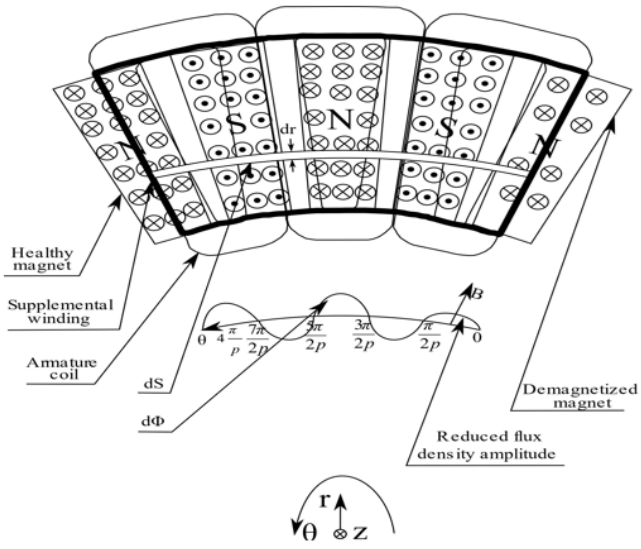

Figure 4.4: The supplemental winding along with the 4 pole and 3 coil pitches and the magnet flux density wave that corresponds to that rotor angular position.

From (4.20), the peak value of the fundamental component of the magnetic flux density is equal with

$$B_g = \frac{B_{rem}}{1 + \mu_r \frac{g+0.5t_w}{h_{PM}}}. \tag{4.21}$$

According to Figure 4.4, an angle element on the additional winding occupies a surface element dS, and through this surface, an element magnetic flux element penetrates from it. The surface element of one pole pitch is given as follows [102]

$$dS = \frac{\pi}{p} r \cdot dr. \tag{4.22}$$

By substituting into (4.7), (4.19) and integrating into the counterclockwise direction along the air-gap facing the additional winding when the magnetic flux density wave is in the position of Figure 4.4, yields the following integral summation

$$\Phi(\theta) = \left(2 - \frac{D}{2}\right) \int_{r_i}^{r_o} B(\theta) \frac{\pi}{2p} r dr - \int_{r_i}^{r_o} B(\theta) \frac{\pi}{p} r dr + \int_{r_i}^{r_o} B(\theta) \frac{\pi}{p} r dr - \int_{r_i}^{r_o} B(\theta) \frac{\pi}{p} r dr. \tag{4.23}$$

The magnetic flux is positive when the vector of magnetic flux density has the same direction as the perpendicular vector of the surface element and negative when their directions are opposite. By calculating the above definite integral summation and considering $\theta = \omega_r t$ due to the rotor rotation, the fundamental harmonic component of the magnetic flux as a function

of time on the additional winding is obtained, as follows

$$\Phi(t) = -D \cdot \frac{\pi}{8p} \left(r_o^2 - r_i^2\right) B_g \sin(\omega_s t). \tag{4.24}$$

When the demagnetized magnet passes region of the sensor, an oscillation is induced with an amplitude, which is proportional to the demagnetization severity. By employing (4.8) all over again, for the specific additional winding with N_{sw} turns, and applying (4.15), the induced voltage is estimated as follows

$$v_{sw}(t) = N_{sw} D \frac{\pi}{8} \left(r_o^2 - r_i^2\right) B_g \omega_r \cos(\omega_s t). \tag{4.25}$$

It is worth mentioning that under fault condition, the currents in the 3 coils that the supplemental winding spans, are no longer symmetrical, so the resultant magnetic flux that penetrates is non-zero. Since the generator does not have a stator core, it is anticipated that this parasitic effect will not have a strong influence as these generators have a negligible armature reaction field [29].

Proposed monitoring signal for partial demagnetization detection

In this subsection, we propose a signal for monitoring the detection of partial demagnetization in AFPM generators. The amplitude of the EMF in a PM generator with a coreless stator is linearly proportional to the rotational speed. Therefore, we propose a fault detection signal in which its shape is used as a fault indicator and its peak-to-peak value is used as a fault severity estimator, as follows

$$FDS(t) = \frac{v_{sw}(t)}{\omega_r(t)}. \tag{4.26}$$

Under stationary speed conditions, the rotational speed is steady, so it is constant in the above equation. When the generator rotor has a varying speed carrying one PM demagnetized in one of its rotors, the signal will remain at the same amplitude due to the speed normalization. Moreover, the fault under nonstationary speed conditions may be diagnosed using the amplitude side-band components of the same signal, which are given by (4.18) normalized by the rotational speed ω_r, using the frequency components with the pattern of (4.17).

Identification of the partial demagnetization from the static and dynamic axis and angular eccentricity conditions

This section demonstrates the analytical derivation of the expected signals, which will be induced on the supplemental winding (sensor) if an eccentricity fault occurs. The term angular eccentricity means the angular rotation of at least one rotor disc around an axis other than the rotational one [103]. A thorough analysis of the angular and axis eccentricity definition has been done in [104, 105]. Great care should be given since misalignment usually refers to the alignment quality between motor and load in radial-flux machines, not the stator and rotor position. Thus we have avoided using the term misalignment to describe the two types of eccentricity faults in axial-flux machines. The angular dynamic eccentricity of a rotor is a condition where the minimum of the air gap rotates with the mechanical speed while the air gap is unequal around the circumference. Axial eccentricity has the same concept, but the direction of eccentricity but the parallel displacement of a rotor in relation to the stator now moves with the mechanical speed. As a result, the voltage on the supplemental winding will consist of continuous oscillations during the whole mechanical period. On the other hand, under a static eccentricity fault, the air gap becomes non-uniform. A voltage will be induced in the sensor coil, which depends on the relative position between the sensor and eccentricity, but the signal will be without oscillations.

The analytical formulae for the fault detection signal can be developed by substituting the respective air-gap function for each case in the permeance function. Eventually, the voltage induced in the supplemental winding under dynamic eccentricity is

$$\begin{aligned}\mathscr{E}_{DE}(t) &= \frac{1}{2}N_c DEF\beta\left(r_o^2 - r_i^2\right)\omega_r \cdot \\ &\sum_{\nu=odd}^{\infty}\mathscr{F}_{PM,\nu}^{DE}\sin\left((\nu p-1)\frac{2\pi}{p}\right)\sin\left((\nu p-1)\frac{2\pi}{p}-\left(\nu-\frac{1}{p}\right)\omega_s t\right) \\ &+\sum_{\nu=odd}^{\infty}\mathscr{F}_{PM,\nu}^{DE}\sin\left((\nu p+1)\frac{2\pi}{p}\right)\sin\left((\nu p+1)\frac{2\pi}{p}-\left(\nu+\frac{1}{p}\right)\omega_s t\right)\end{aligned}, \tag{4.27}$$

and for static eccentricity, the induced voltage in the supplemental winding is

$$\begin{aligned}\mathscr{E}_{SE}(t) &= \frac{1}{4}N_c SEF\beta\left(r_o^2 - r_i^2\right)\omega_r \cdot \\ &\sum_{\nu=odd}^{\infty}\mathscr{F}_{PM,\nu}^{SE}\frac{\nu}{\nu+\frac{1}{p}}\cos\left((\nu p+1)\frac{4\pi}{p}-\nu\omega_s t\right) \\ &+\sum_{\nu=odd}^{\infty}\mathscr{F}_{PM,\nu}^{SE}\frac{\nu}{\nu-\frac{1}{p}}\cos\left((\nu p-1)\frac{4\pi}{p}-\nu\omega_s t\right) \\ &+\sum_{\nu=odd}^{\infty}\mathscr{F}_{PM,\nu}^{SE}\frac{2p\nu^2}{p\nu^2-\frac{1}{p}}\cos\left(\nu\omega_s t\right)\end{aligned}, \tag{4.28}$$

From the two above equations, the following conclusions are made. The various faults induce unique voltage harmonics in the supplemental winding. Meaning that the method can be used to distinguish the faults with each other. Moreover, (4.17) and (4.27) show that specific voltage harmonics are induced in the flux sensor and are multiples of the inverse pole pair number. However, partial demagnetization is an abnormality which is not continuous but happens only in the vicinity while the faulty magnet crosses the sensor. The latter shows that partial demagnetization and dynamic eccentricity faults can be detected by monitoring the sensor's peak-to-peak value of the speed-normalized voltage. At the same time, it is impossible to mistake static eccentricity for either partial demagnetization or dynamic eccentricity.

4.1.2 Finite-Element Analysis of the machine with the supplemental winding

Analysis of the partial demagnetization fault and experimental validation of the healthy model

The AFPM generator and the supplemental winding within its air gap are modelled using a commercial software package which is based 3-D FEA. Figure 4.5 illustrates the experimental rig of the AFPM generator, and Figure 4.6 graphs the phase voltage. The blue line is the data extracted by the FEA model, and the red line is the phase voltage of the actual generator. This procedure was used to validate the model against the real machine. Figure 4.7 shows the solid 3-D FEA model of the three-phase AFPM generator in an exploded view to demonstrate the supplemental winding, which is wound along 3 stator coils. This coil sensor is designed according to the PM geometry to obtain optimized results. The winding of the generator is non-overlapping with coil sequence A-B-C. The major specifications of the generator are archived in Table 4.1.

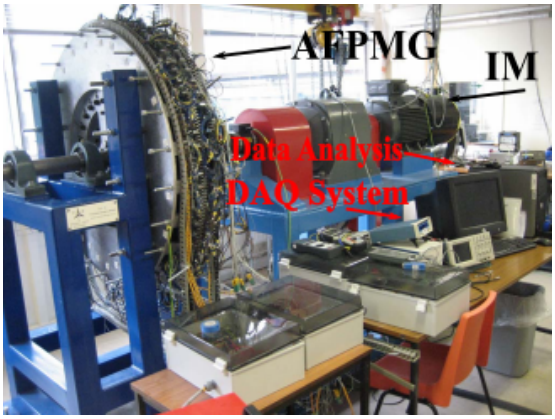

Figure 4.5: Experimental test rig of the AFPM generator to validate the FE model.

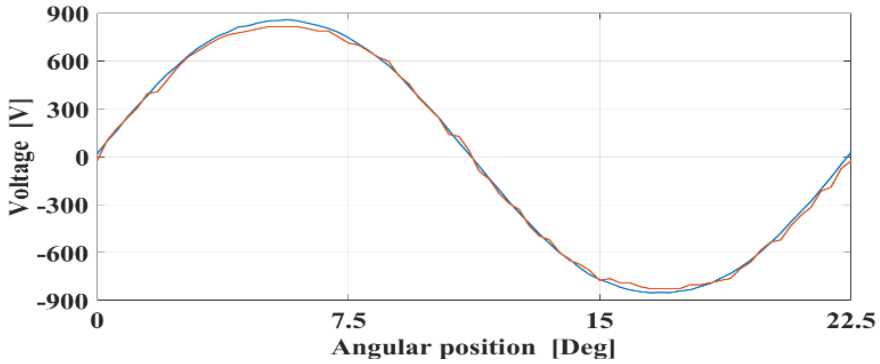

Figure 4.6: Phase voltage waveform at 100 [r/min] of FE (blue) model and the experimental one (red).

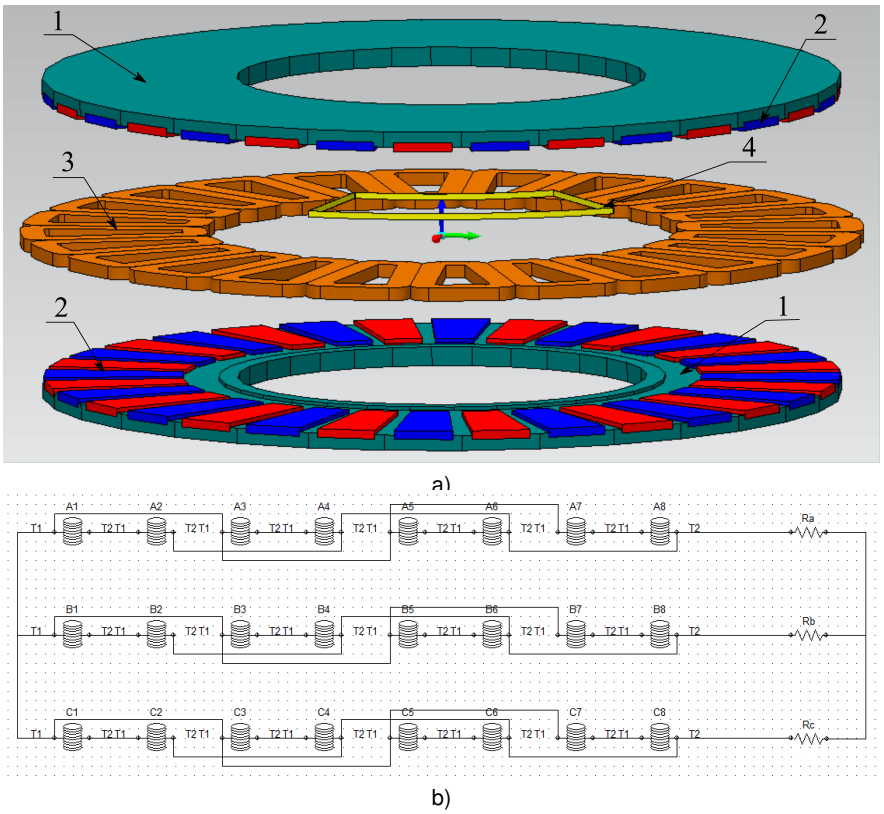

Figure 4.7: a) Exploded view of the axial-flux PM generator's FEA model with the additional winding 1) Rotor disc, 2) PM, 3) armature coil of winding, and 4) the supplemental winding and b) winding layout for the cases where the machine has parallel path winding.

Figure 4.8a displays the no-load axial magnetic field component along a pitch in the middle of the air gap is plotted for 0-100% demagnetization in incremental steps of 10%. The purpose was to validate that the reduction in the magnetic flux density is linear as there are two magnets in each pitch and that the additional harmonic components derived in (4.18) do not affect the degree of reduction. The $B-H$ characteristic remained linear in the second quadrant for

Table 4.1: Specifications of the Axial-Flux PM Machine

Parameter	Value
Apparent power [kVA]	12.52
No-load voltage line-to-line RMS [kV]	3.86
Rotational speed [rpm]	375
Number of coils-c	24
Number of pole-pairs	16
Magnet remanence (20^o C) [T]	1.247
Turn number of an armature coil	640
Turn number of the supplemental coil	1
Number of parallel paths	4
Magnet-coil clearance [mm]	3.5
Winding connection	Y
Inner/Outer magnet radius - r_i, r_o [mm]	300/460
Thickness of the winding - t_w [mm]	15
Magnet thickness - h_{PM} [mm]	10

all demagnetization states. In Figure 4.8b, the on-load axial magnetic flux density component along a circle for 50% partial demagnetization is demonstrated for two rotor positions, which corresponds to positions where the fault detection signal takes its maximum value. The purpose is to investigate the magnetic field magnitude distortion due to the armature reaction that the circulating currents create. The parallel path connections appear to create currents that distort the magnetic flux density wave and cause its value to fluctuate according to the specific winding configuration. As a result, a mean value for the magnetic field magnitudes should be employed for the analytical calculation. The demagnetization fault inserted in the simulation by reducing the slope of the $B-H$ characteristic in the second quadrant.

In Figure 4.9, the fault detection signal during the interval where a magnet crosses the sensor is plotted for 10 different demagnetization severities in increments of 10%. The peak-to-peak value increases with the fault severity level, followed by lower peak-to-peak amplitude increments caused by the magnetic flux generated by the circulating currents flowing in the parallel paths. Figure 4.10 presents the fault detection signal for 50% and 100% demagnetization when the generator has no parallel paths. The conclusion from the latter is that the

parallel paths cause additional oscillations in the sensor signal. Figure 2.10 illustrates the fault detection signal in the time and frequency domain for healthy and two demagnetization cases for a mechanical period. The dB normalization settled with base 1 [mVsec/rad] and not with the fundamental harmonic as it is negated due to the supplemental winding topology.

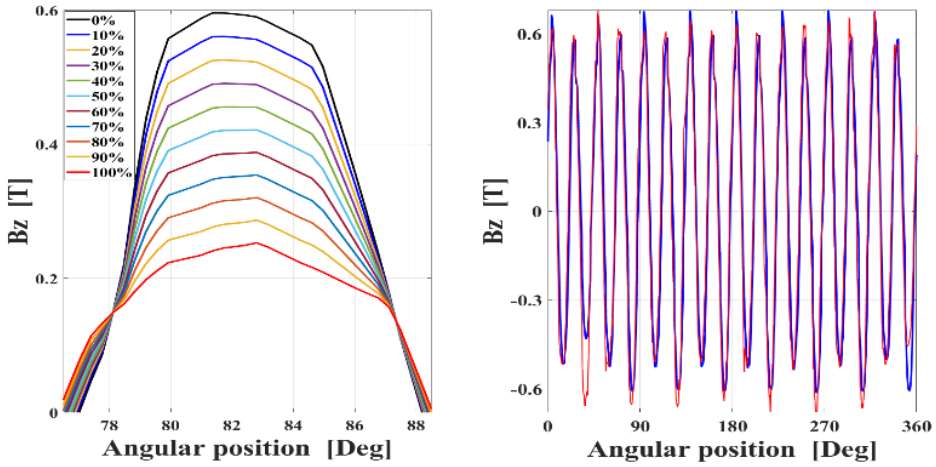

Figure 4.8: Axial component of a) the no-load magnetic flux density wave for 10 demagnetization severities with 10% step reductions and b) on-load magnetic flux density when a magnet is demagnetized.

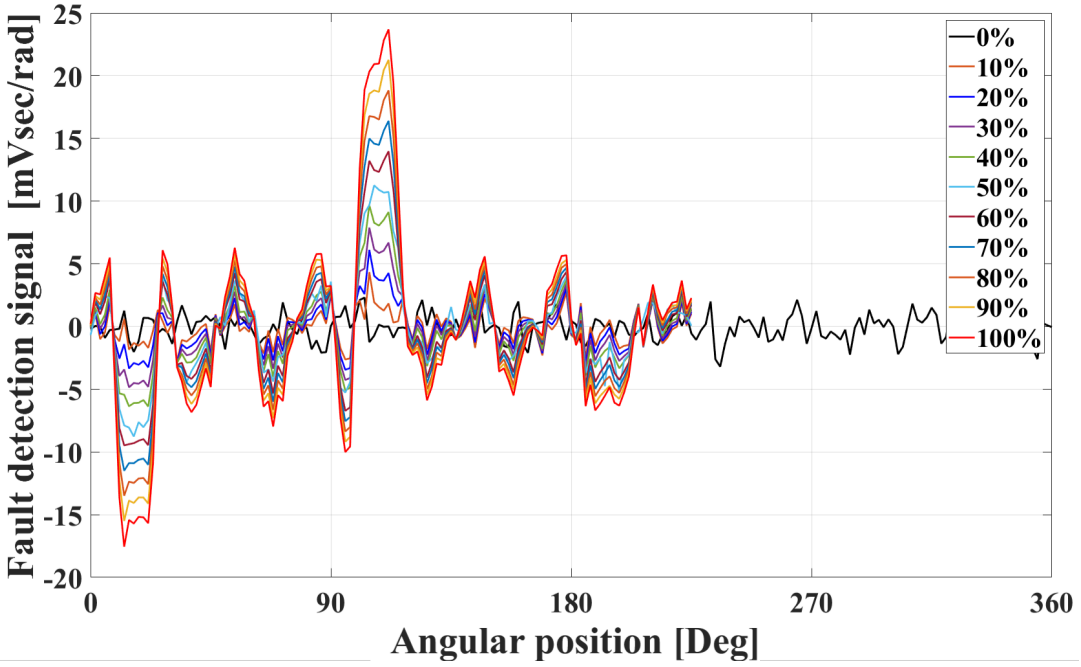

Figure 4.9: Fault detection signal for 0% up to 100% demagnetization severity with increments of 10% of a PM with 4 parallel paths.

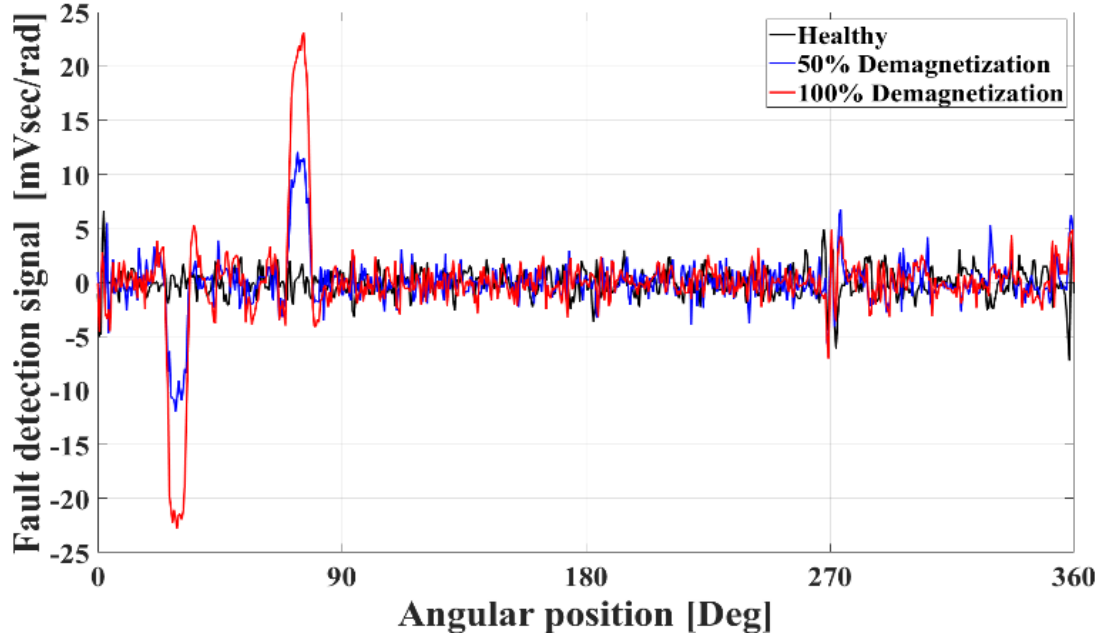

Figure 4.10: Fault detection signal with no parallel paths for healthy, 50% and 100% demagnetization of a PM.

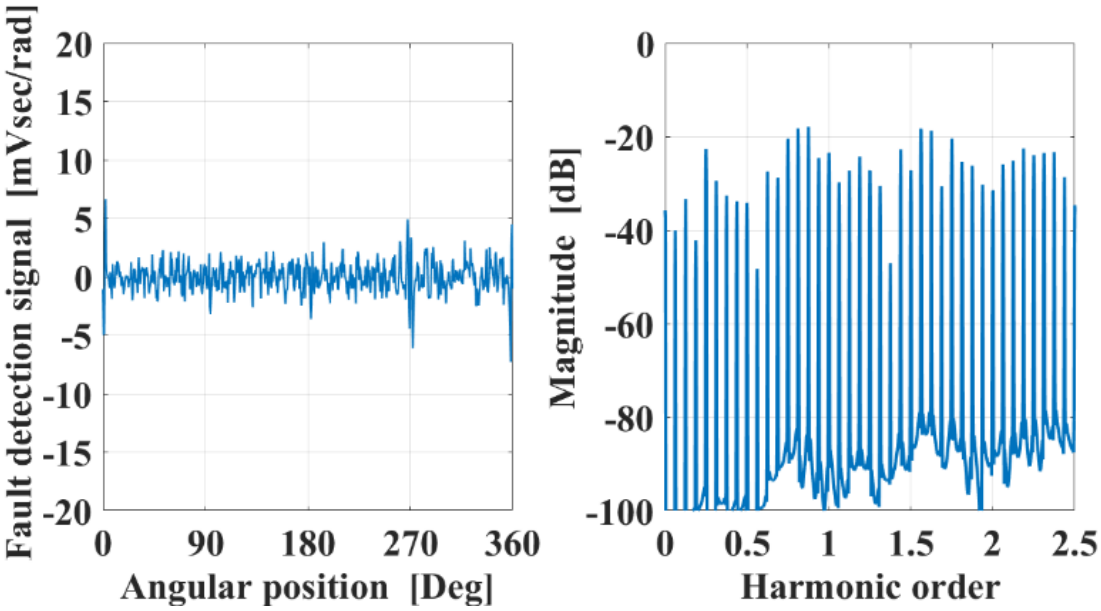

Figure 4.11: Fault detection signal in time (left column) and frequency (right column) domain under healthy conditions for the 4 parallel path winding configuration.

Under healthy conditions, the signal is approximately zero, as shown in Figure 4.11 (left graph). A small fluctuation is caused by the armature reaction end-winding leakage field. Regarding the cases in which a PM was demagnetized for about 40%, as shown in Figure 4.12 and 80%, as Figure 4.13 supports. Oscillations are generated, which depend on only

the demagnetization level. The amplitude of the oscillations remains constant because the voltage signal is normalized with speed, and under healthy conditions, the signal approaches zero. With the rise in demagnetization severity, the magnitude of the peak-to-peak magnitude of the oscillation increases linearly. Lastly, the amplitude side-bands with the pattern given by (4.18) are increased with the demagnetization severity, and their alteration is nonlinear and was theoretically proven by (4.17). In Figure 4.14, the alteration of the normalized peak-to-peak summation magnitudes for each demagnetization factor is presented. The peak-to-peak value of the fault detection signal can be used as a fault index for partial demagnetization detection. The design parameters is obtained by consulting Table 4.1. The air-gap magnetic flux density is obtained through (4.21), equal to 0.582 [T]. To estimate the fault severities for the cases of Figure 4.10, in which the machine is under 50% and 100% partial demagnetization, the peak-to-peak amplitude of the fault detection signal substituted in (4.25) and the demagnetization percentage D is 45% and 86%, respectively. As a result, extracting the peak-to-peak value of the sensor output signal over time and considering the basic machine parameters can lead to the estimation of the fault severity level. As shown earlier, due to the parallel-path winding configuration, a further deviation is caused by the analytical model due to the additional oscillations, which slightly reduce the peak-to-peak value of the fault detection signal. However, the peak-to-peak value can still give a decent approximation for the fault severity level.

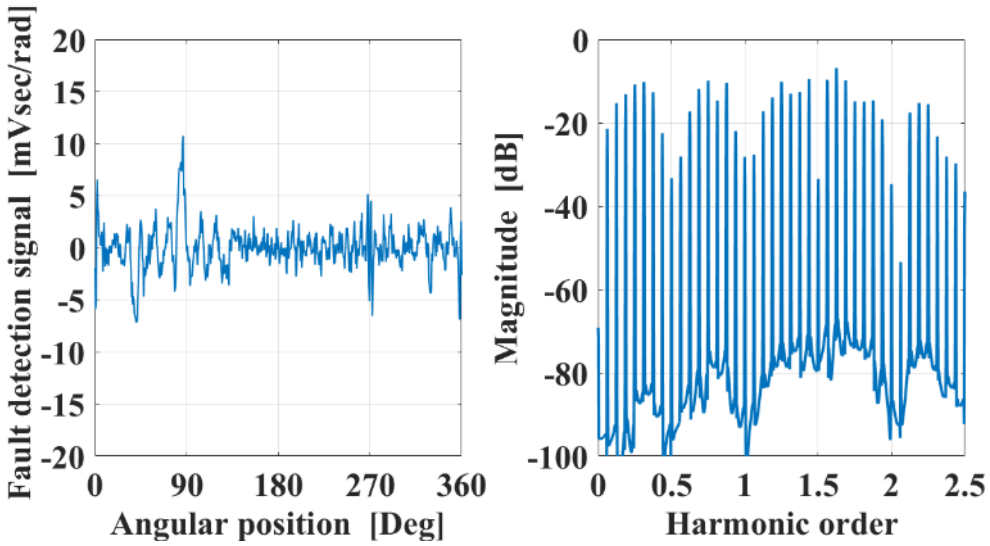

Figure 4.12: Fault detection signal in time (left column) and frequency (right column) domain under 40% partial demagnetization for the 4 parallel path winding configuration.

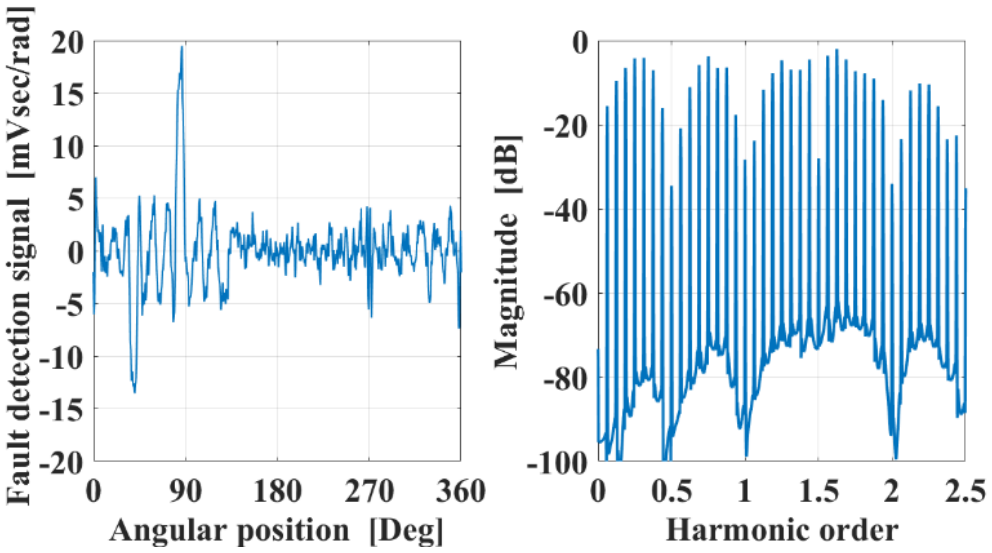

Figure 4.13: Fault detection signal in time (left column) and frequency (right column) domain under 80% partial demagnetization for the 4 parallel path winding configuration.

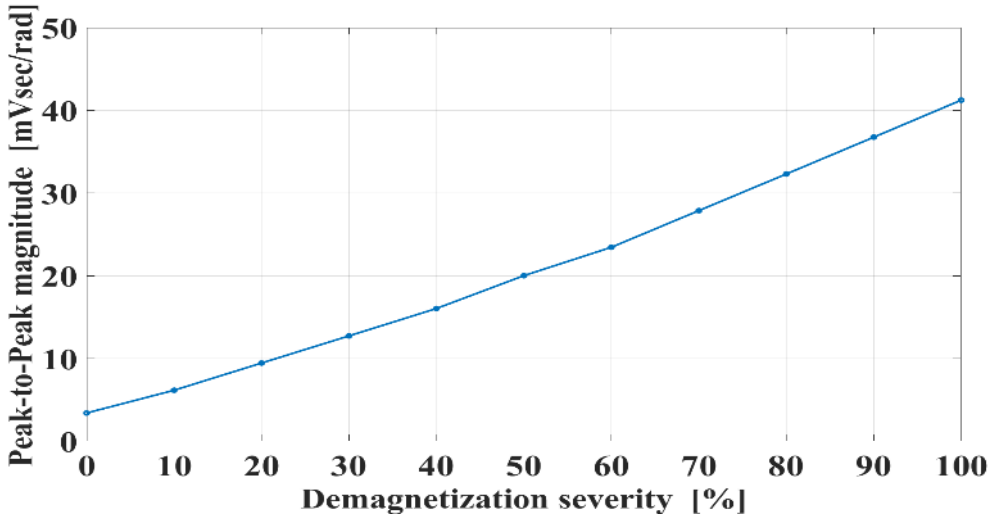

Figure 4.14: FEA results for the peak-to-peak magnitude of the fault detection signal for 10 demagnetization severities with increments of 10% for the machine with 4 parallel path winding.

In Figures 4.15, 4.16 and 4.17 the fault detection signal is displayed for healthy 40% and 80% partial demagnetization in time (left) and time-frequency domain (right) under an acceleration of 100 [rpm] in 0.9 seconds starting at a speed of 250 [rpm]. Figure 4.15a and 4.15b (left column) validate that the peak-to-peak amplitudes of the fault detection signal remain steady under this state. Moreover, the right columns in Figures 4.15, 4.16 and 4.17 (right column) show that the frequency trajectories of the fault harmonics remain steady as the speed increases, and their magnitudes increase only with the fault severity.

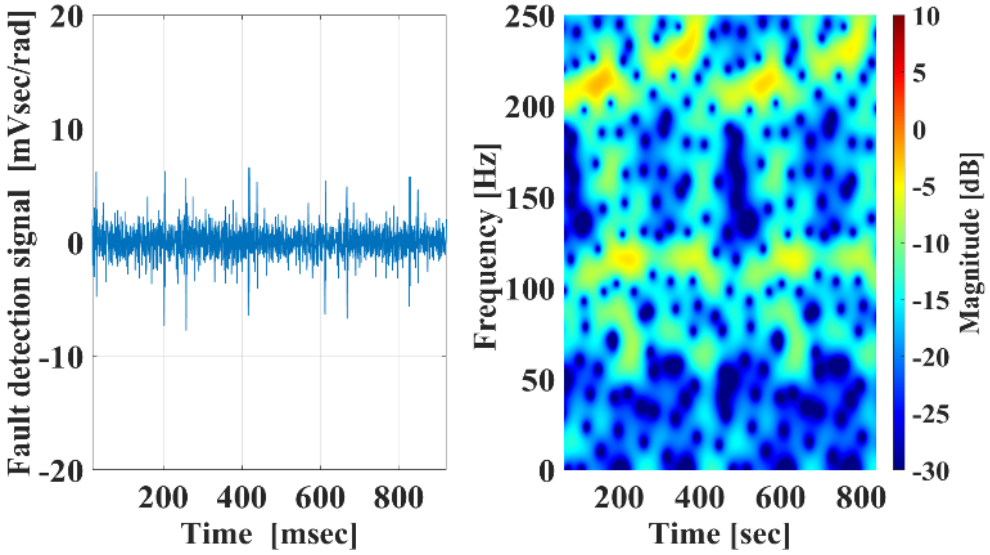

Figure 4.15: Fault detection signal under a transient rotor speed in time (left) and time-frequency domain under healthy conditions for the machine with the parallel path winding.

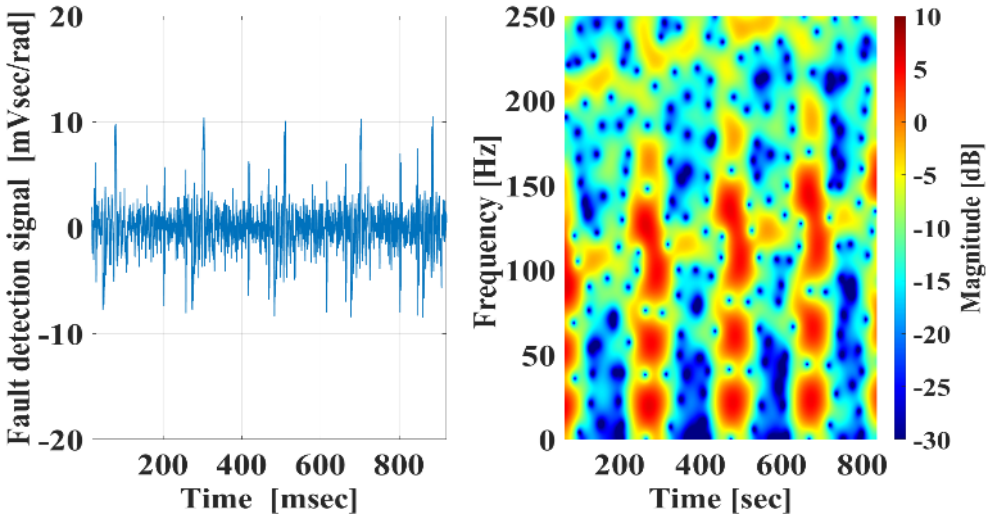

Figure 4.16: Fault detection signal under a transient rotor speed in time (left) and time-frequency domain under 40% partial demagnetization for the machine with the parallel path winding.

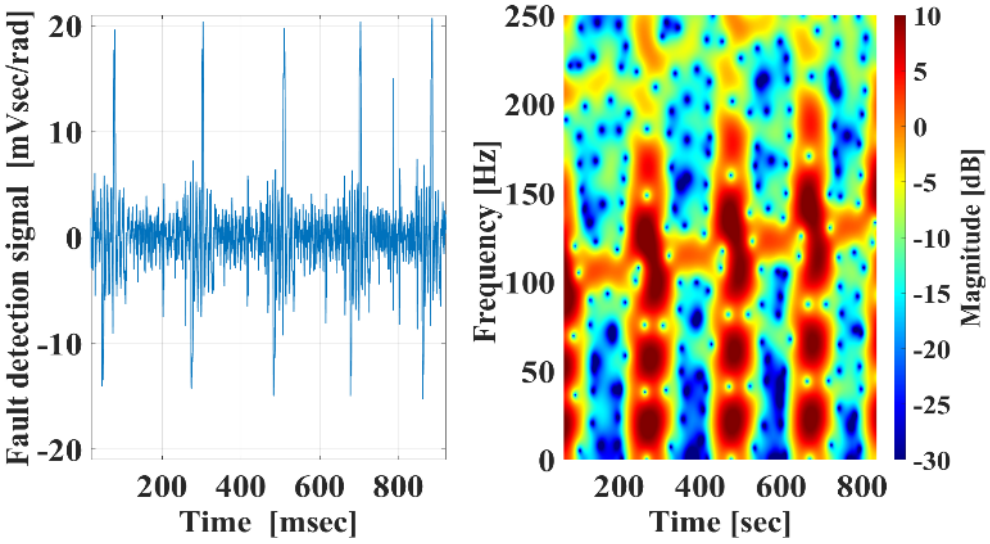

Figure 4.17: Fault detection signal under a transient rotor speed in time (left) and time-frequency domain under 80% partial demagnetization for the machine with the parallel path winding.

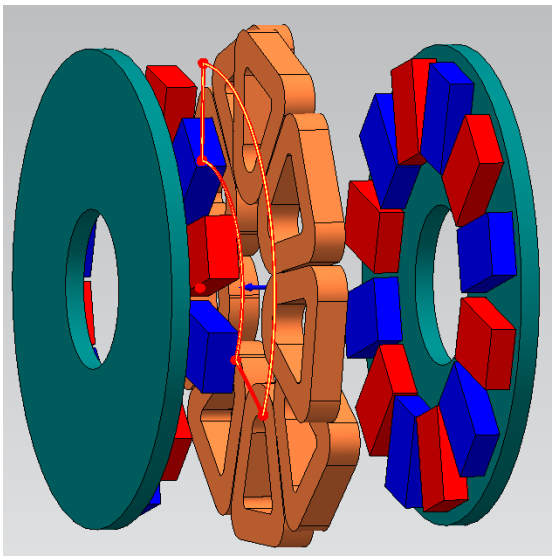

Figure 4.18: FEA model of the axial-flux generator with the search-coil.

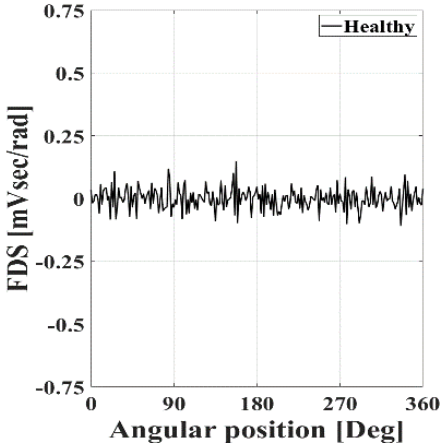

Figure 4.19: Fault detection signal under healthy condition when the generator rotates at 1000 rpm.

Impact of the other faults on the proposed signal

In this part of the work, the 3-D FEA model of an axial-flux PM generator with specifications for the axis and angular eccentricity faults is extracted using 3-D FEA in an axial-flux generator to achieve discrimination with the partial demagnetization fault. In Figure 4.18, the model of the generator is presented with the air-gap search-coil. Figure 4.19 fault detection signal for healthy condition, to validate that it is zero. The generator has 9 coils and 12 poles and has the same type of winding as the initial. In Figure 4.20 the fault detection signal is presented in the time domain for the cases of a 70% demagnetized model (which is an equivalent of 35%), unbalanced electric load in which the current in one phase is four times higher, 20% static angular eccentricity, 40% dynamic angular eccentricity, 1 [mm] static axis eccentricity and 2 mm dynamic axis eccentricity. From the figure, the conclusion is that for each fault, the signal's waveform is unique. As a result, all faults can be distinguished except the unbalanced electric load fault since it does not impact the search coil. Moreover, detecting the dynamic faults is feasible since the magnetic flux stays unbalanced on the search coil throughout the mechanical period. The peak-to-peak magnitude can be used as a fault index. Lastly, the two misalignment faults, axis and angular, induce a similar waveform on the search coil. Nevertheless, the waveforms are still distinguishable by inspection.

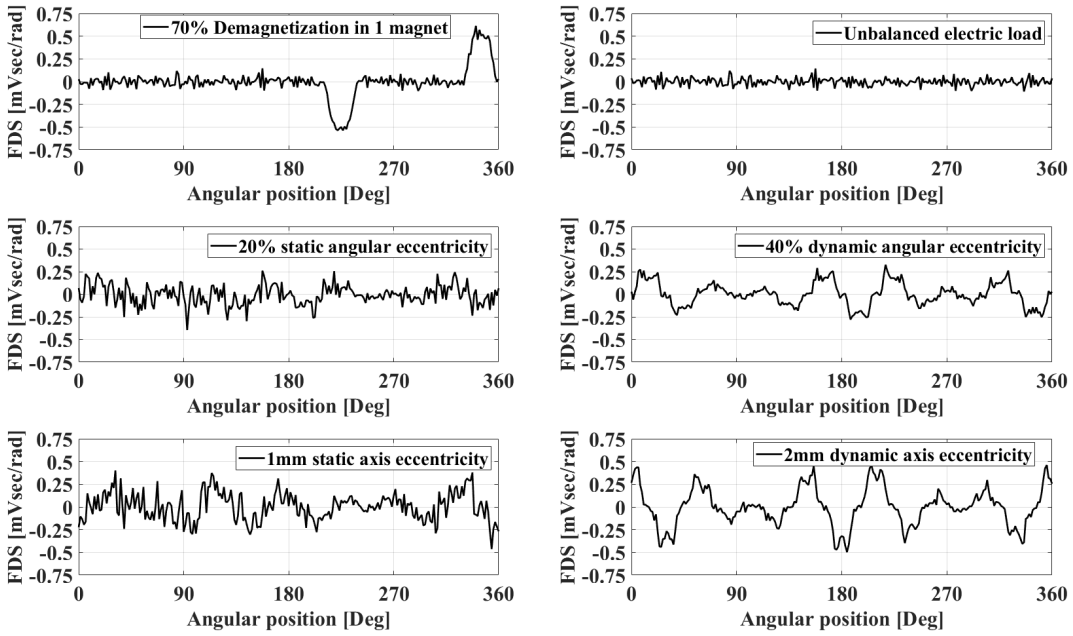

Figure 4.20: The speed-normalized voltage signal for all fault cases.

4.1.3 Summary and conclusions of the method with the single search-coil

The above work extended the method which utilizes the search-coil that negates the induced voltage detection of permanent-magnet health monitoring of air-cored axial-flux generators designed for marine energy applications. The peak-to-peak value of the induced speed-normalized voltage on the supplemental winding can be used as a fault indicator signal as it depends only on the fault severity. A Short-Time-Fourier-Transform offers also adequate results detect the fault using the amplitude-frequency components under steady and variable speed states.

Compared to a single pitch search-coil, the advantage of this method is that the fault can be detected without any further signal processing since the signal is zero under healthy conditions. Moreover, it can detect low severities since the ripple of the signal is negligible. When the partial demagnetization fault occurs, an oscillation is induced on the search coil in which the peak-to-peak value is connected with the demagnetization severity percentage, according to equation (4.25). Under uniform demagnetization, the total magnetic flux penetrating the coil is zero, so this technique can only detect a partial demagnetization fault. The single-pitched search-coil can detect uniform demagnetization since it senses the voltage in each pole pitch.

The dynamic axis and angular eccentricity faults can also be detected, as the fault detection signal will have a different waveform, and the peak-to-peak value can be used as a fault indication in this case. This method finds application in machines where an additional coil can be implemented, where its span will be capable of negating the voltage under load conditions. The method requires an even number of pole pitches and an odd number of coil pitches within

the span of the sensor. If the number of pole pitches is not even, the signal under healthy conditions will not be zero, and the method requires calibration when first implemented. The method demonstrated in the paper can easily be applied to axial and radial flux PM machines after careful determination of the sensor span, such that the induced voltage due to the rotor and stator magnetic fields is negated.

4.2 Diagnostics for PMSMs using two magnetically-coupled search-coils

This paper presents a new search-coil scheme that makes detecting all faults in Permanent-Magnet Machines feasible. The idea employs two search coils, one placed in the rotor and one in the stator, which couple magnetically under faulty conditions. The shape of the waveform is associated with the type of fault. The amplitude of the monitored sensor is associated with the severity of the fault. The studied faults are the demagnetisation, inter-turn, angular and axis misalignment. The proposed scheme applies to both types of machines, radial- and axial-flux. 2-D FEA results for the radial-flux machine and 3-D FEA results for the axial-flux show that the proposed method is promising for facilitating an experimental layout for condition monitoring applications.

4.2.1 Presentation of the idea and the occurring Faults in PM Machines

Proposed search-coil scheme

This section explains the search-coil scheme along with the studied faults. Figures 4.21 and 4.22 present two 9 coil 12 pole PM radial- and axial-flux machines with the search-coil scheme designed on them, in 2-D and 3-D FEA, respectively. The winding is concentrated and non-overlapping.

Search-coil A is placed in the stator, and search-coil B in the rotor. Both search coils have the same pitch and occupy the minimum number of odd coil pitches and even poles. Search-coil A is open-circuited, and Search-Coil B is short-circuited. For the specific machines, the minimum number of poles is two; for coils is three, and the span of the coils is twice as much as one of the poles. The latter means that the minimum span must equal 3 coil pitches. This number of coil pitches corresponds to 4 pole pitches. With this span, the penetrated magnetic flux on both search coils for every rotor position is zero.

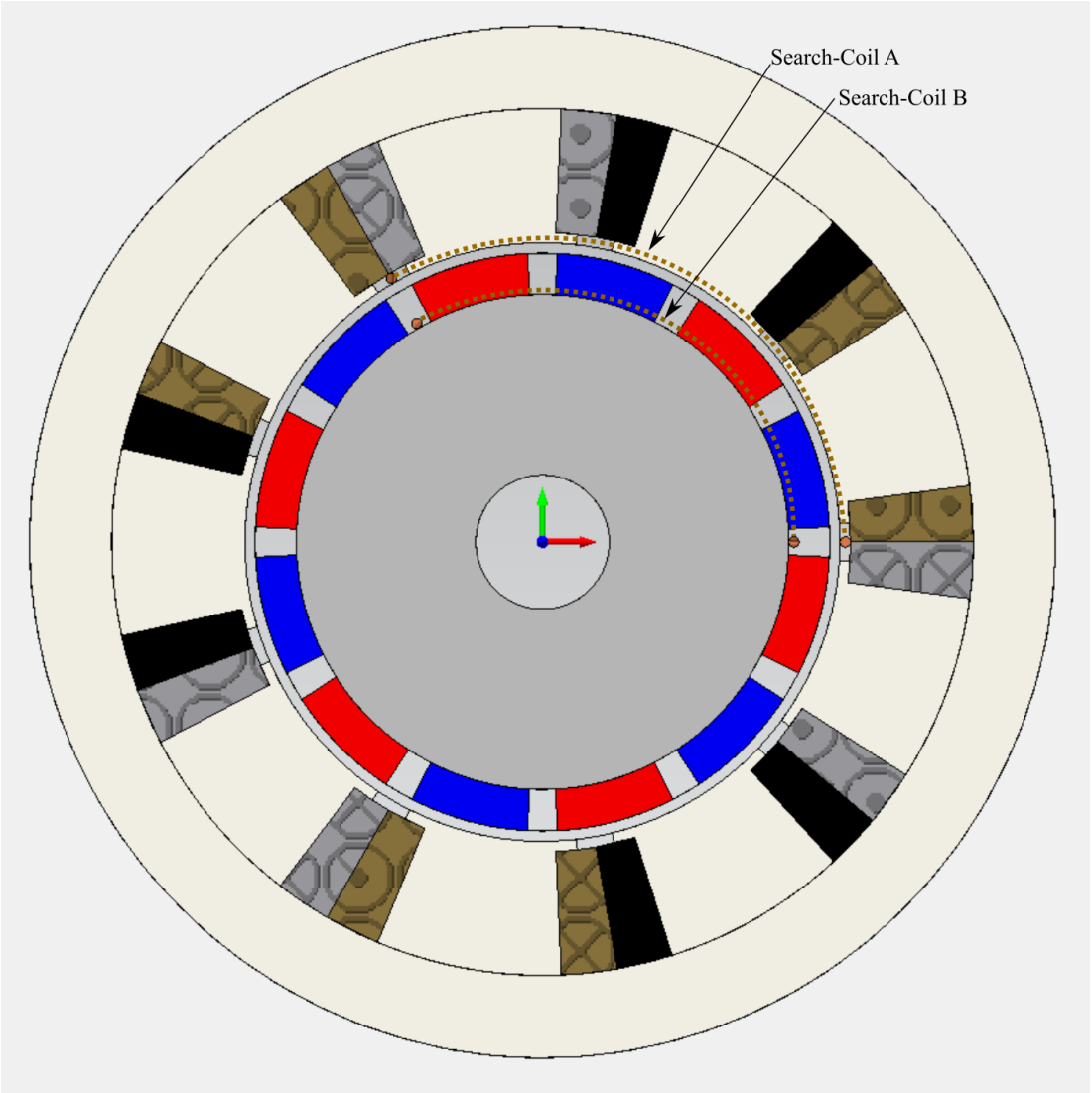

Figure 4.21: FEA model for a 9 coil 12 pole radial-flux PM machine with the two search-coils.

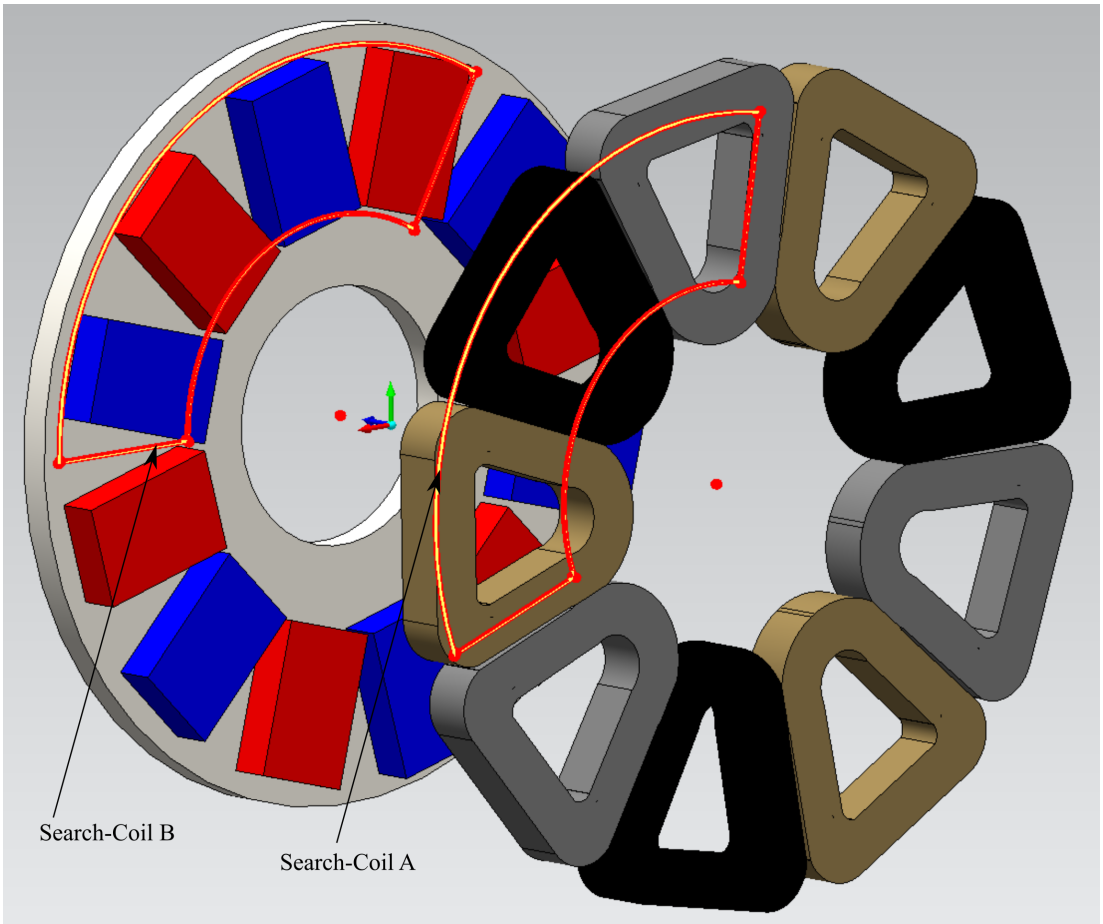

Figure 4.22: FEA model for a 9 coil 12 pole axial-flux PM machine with the two search-coils.

The rotor magnetic field changes its polarity every 180^o electrical angles, so 4 magnets create zero net magnetic flux for every rotor position. The same happens for the magnetic flux created by the stator coils. Each coil current has 120^o electrical degrees phase difference; hence for every rotor position, the induced currents create magnetic flux, which adds up to zero in the search coils. What is said above entails that under healthy conditions, both induced voltage on Search-Coil A and current on Search-Coil B are zero. The magnetic flux on the air gap becomes unbalanced with a fault occurrence. Hence the two search coils start to have induced voltage on their terminals. It should also be noted that when the machine is healthy, there is no electromagnetic interference of Search-Coil B in the air gap of the machines.

Faults occurring in PM machines

The faults in permanent-magnet machines are separated into two categories based on whether they are moving or at a standstill; static and dynamic faults. Static faults are the faults which do not change position as the rotor position varies. These faults are the static angular and axis misalignment and the inter-turn fault. The dynamic faults are the partial demagnetisation

and the dynamic angular and axis-misalignment. In Figures 4.23, and 4.24, the faults of static axis misalignment and inter-turn fault are illustrated, respectively. In Figures 4.25, and 4.26 the partial demagnetization and dynamic axis misalignment, is presented, respectively. The air length appears magnified for clarity.

The static axis misalignment fault or static eccentricity, as shown in Figure 4.23, happens when the rotor axis is displaced, and the centre of rotation is in a new axis which coincides with the rotor axis. In dynamic axis misalignment, shown in Figure 4.26, the rotor axis is also displaced, with the only difference being that the centre of rotation is at the beginning of the axes. If the centre of rotation falls in between, mixed eccentricity happens. In both types of faults, the magnetic flux for 180^o spatial becomes higher compared to healthy conditions, and in the other 180^o becomes lower. For the static fault, this asymmetry is stationary, and for the dynamic fault, it moves with the rotor speed.

The partial demagnetisation fault, displayed in Figure 4.25, occurs when at least one of the magnets has reduced residual flux density. The fault can be considered a moving asymmetry that moves with the rotor speed of rotation. This fault is similar to the dynamic axis misalignment fault, as in both cases, the unbalanced magnetic flux moves with the rotational speed of the rotor. Lastly, in the inter-turn fault, displayed in Figure 4.24, a closed loop is created in one of the coils, which is stationary compared to the rotating magnetic field. The closed-circuited loop leads to a current-carrying loop, in which the current depends on the magnetic field intensity and the speed of rotation, the impedance and its surface. This current creates a magnetic flux which is time-varying but fixed in space. This fault also creates a hot spot, so it is crucial to be detected the earliest possible. For axial-flux machines, the axis and angular static and dynamic misalignment faults are presented in Figure 4.27a and 4.27b.

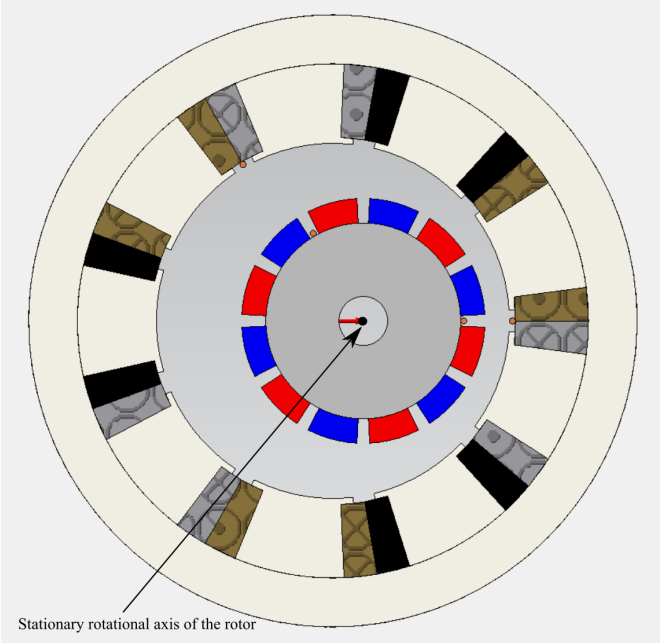

Figure 4.23: 2-D schematic for the radial-flux PM machine with static eccentricity.

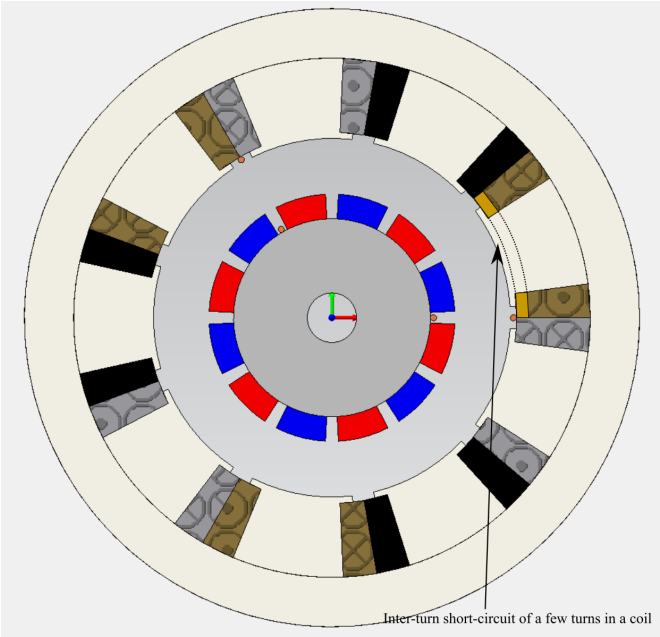

Figure 4.24: 2-D schematic for the radial-flux PM machine with inter-turn fault in one of the stator coils.

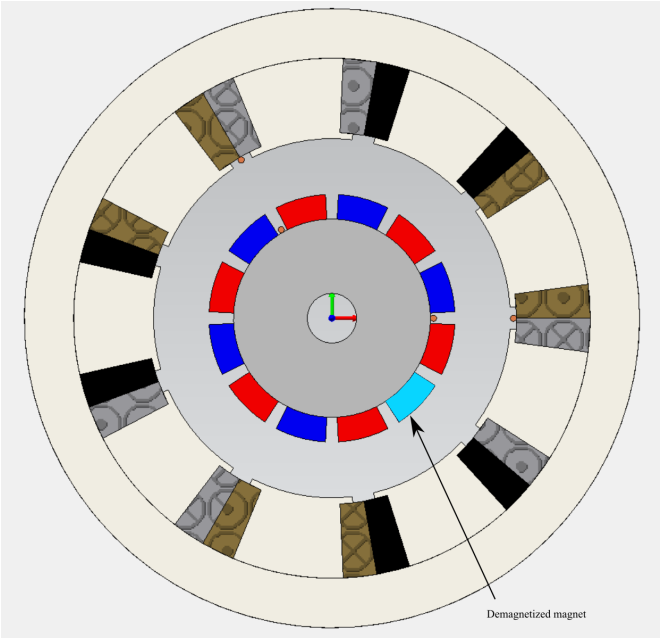

Figure 4.25: 2-D schematic for the radial-flux PM machine with partial demagnetisation.

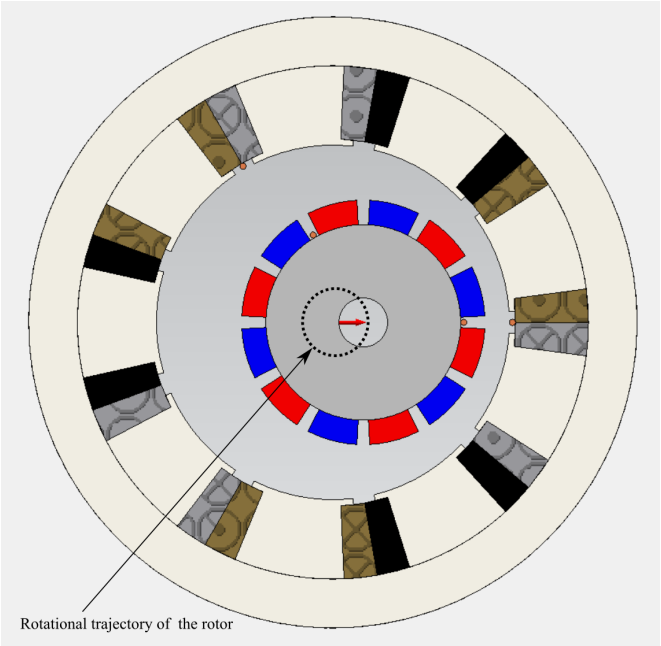

Figure 4.26: 2-D schematic for the radial-flux PM machine with dynamic eccentricity.

4.2.2 Finite-Element-Analysis

This section shows the modelling using simulation and its results. The search coils and the machine was designed using a commercial software FEA package, Simcenter MagNet, by Infolytica/Siemens digital industries. Every faulty condition previously discussed has been modelled and studied. The machine with the designed search coils modelled in a steady and transient condition using a speed-driven simulation. In the speed-driven simulation, the speed is coerced to take any value given by the user. The voltage in Search-Coil A and the current in Search-Coil B are extracted for each fault condition. Two machines were considered; one is self-designed, and it is the radial-flux version of the air-cored axial-flux generator used in Figures 2.13 and 2.14. The purpose of this simulation is to make the first attempt to test if it will provide fault detection signals proportional to the fault severity. In the second stage, the 2-D solid FEA model of a real direct-drive permanent-magnet generator is used to validate the method for two faults. Partial demagnetisation, which is a dynamic fault and inter-turn fault, which is a static fault. The last step was to install the search coils in the direct drive permanent-magnet generator.

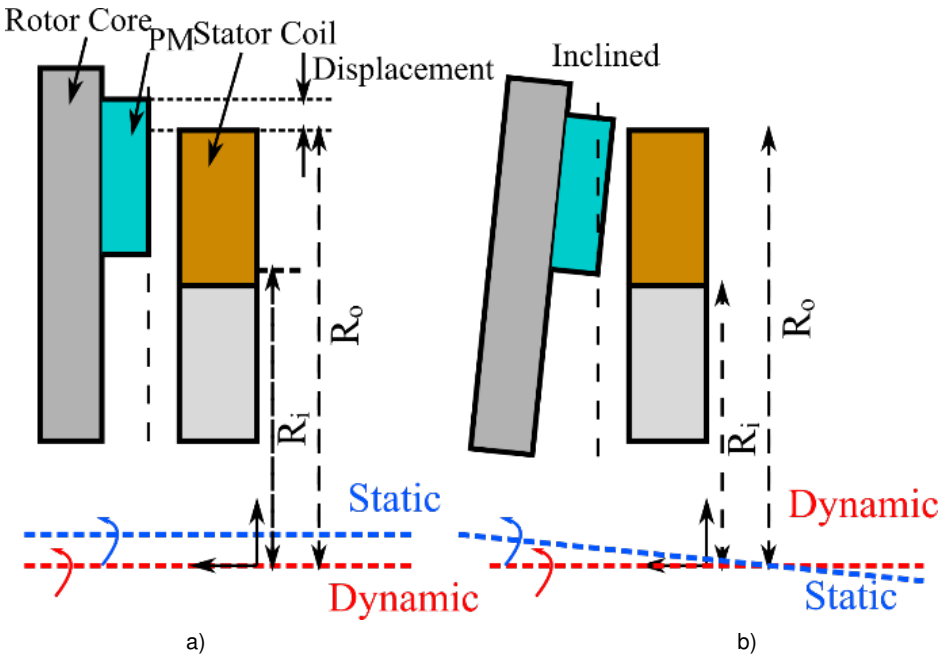

Figure 4.27: Graphical representation of the: a) axis and b) angular misalignment in axial-flux PM machines emphasising the axis of rotation for static and dynamic eccentricity.

Figure 4.28a presents the 2-D FEA results for partial demagnetisation. Since the magnet moves with the rotor speed, there is no relative motion between the asymmetry and Search-Coil B, and as a result, the flux becomes unbalanced only in Search-Coil B. The current in search-coil B is zero, and the voltage in search-coil A is of sine-wave shape. The voltage peaks coincide with the position where the demagnetised magnet passes from the coil sides

of search-coil A. Figure 4.28b presents the results of an inter-turn fault. Since this fault creates a time-varying magnetic flux fixed in space, this flux starts to penetrate the short-circuited Search-coil B. With its turn, the magnetic flux created by B starts to penetrate Search-Coil A. Hence, there is a voltage induced in Search-Coil A that the voltage peaks are equal to the number of poles. Figure 4.28c presents the results for dynamic axis misalignment.

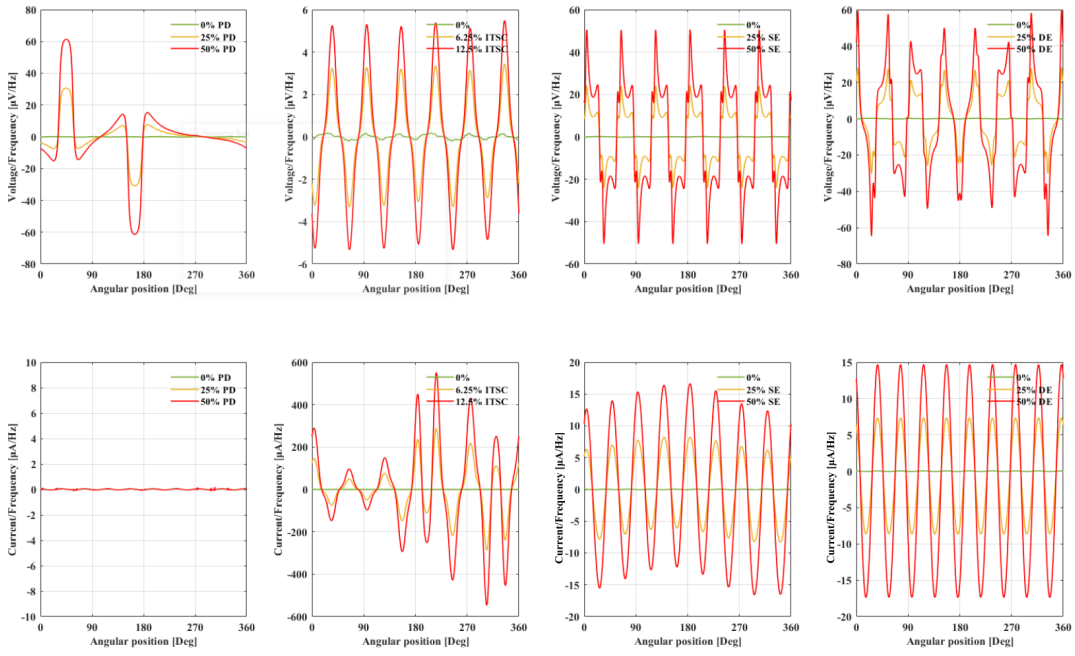

a) b) c) d)

Figure 4.28: Frequency normalized voltage and current of the search-coils A and B for a) 0%, 25%, 50% partial demagnetization, b) 0%, 6.25%, 12.5% inter-turn c) 0%, 25%, 50% static axis misalignment and d) 0%, 25%, 50% dynamic axis misalignment for the radial-flux machine.

Similarly to the demagnetisation condition, this fault creates an asymmetrical air gap that varies over time, resulting in the category of dynamic faults. Due to the eccentric motion of the rotor, Search-Coil B starts to sense magnetic flux passing through it due to the unbalanced stator armature reaction field, and it induces a voltage on Search-Coil A. Due to the rotor magnets' unbalanced flux, there is another additional voltage induction on Search-Coil A. Lastly, Figure 4.28d presents the results for static axis misalignment. The above fault is also a static fault like the inter-turn fault, so the magnetic flux becomes unbalanced in Search-Coil B, and the generated magnetic flux induces a voltage in Search-Coil A. The number of voltage peaks is equal to the number of poles.

In Figures 4.29 and 4.30, the 3-D FEA results are presented for the equivalent axial-flux PM machine. Both types of misalignment faults for the static and dynamic cases are presented. Notably, this method makes distinguishing the two faults for the static and dynamic types feasible. Since the cross-section area of a conductor is inversely proportional to the resistance, it is preferable to choose a conductor with a big surface in the rotor search coil to create a low resistance and increase even more the magnetic flux creates when a fault takes place. The two misalignment faults leave a similar waveform trace on the stator search coil, but the waveforms can still be distinguished.

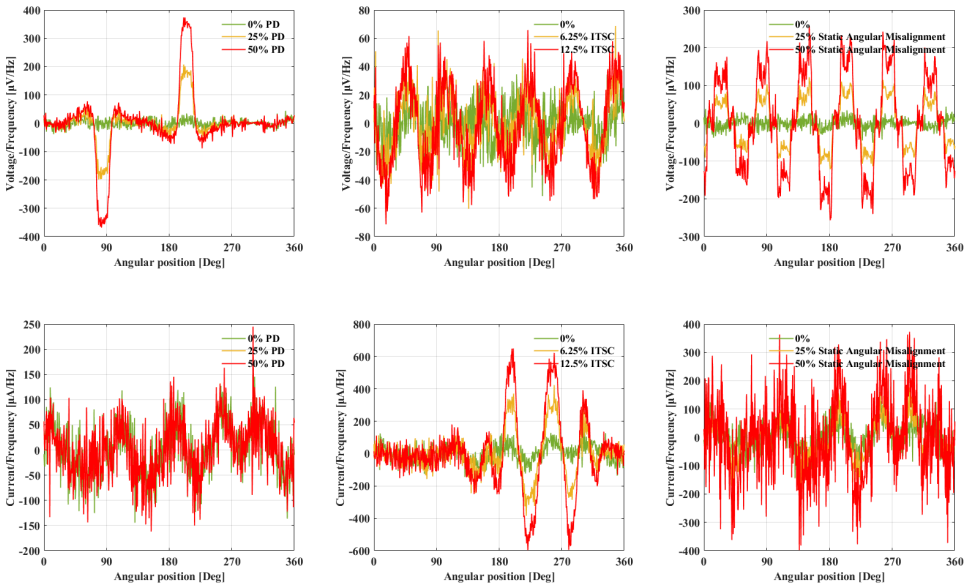

a) b) c)

Figure 4.29: Voltage and current of the search-coils A and B for a) 0%, 25%, 50% partial demagnetization, b) 0% 6.25%, 12.5% inter-turn and c) 0%, 25%, 50% static angular misalignment for the axial-flux machine.

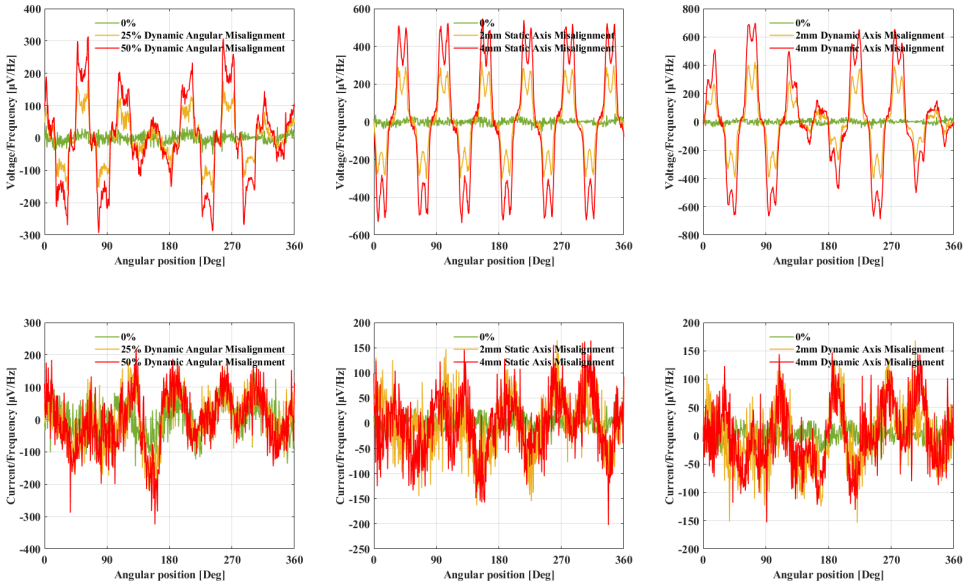

Figure 4.30: Voltage and current of the search-coils A and B for a) 0%, 25%, 50% dynamic angular misalignment, b) 0, 2, 4mm static axis misalignment, and c) 0, 2, 4mm dynamic axis misalignment.

4.2.3 Experimental and simulation results from a PM generator

This section examines the method's validity in a three-phase double rotor core-less radial-flux PM generator. The machine has 24 coils and 32 magnet poles, meaning that in this case, the search coils can have a span of 180^o spatial degrees since the number of coils is an even multiple of three (3x8). Figure 4.31a presents the solid 2-D FEA model of the PM with the two search coils designed on the machine. Figure 4.31b shows the winding layout for the case of the experiment when the machine has partial demagnetization. In all the other cases the coils of each phase are connected in series. The rotating search coil is wound on the outer surface of the rotor shorted. The stationary coil is placed on the stator, is open-circuited, and is the coil whose voltage signal is used for fault detection.

Figure 4.32 presents the actual machine with the search coils installed in on its airgap. The generator has 8 coils per phase and 4 parallel paths; however, there is access to the terminals of each coil, so any connection is possible. The search-coil voltage is measured under three different states. It is worth mentioning that the search-coils were mounted using glue on the surface of the rotor the stator after alcohol was used to clean the surface. As the machine is low speed, the centrifugal forces are not that large so there is no need to use more secure ways to mount the rotor search-coil. Epoxy resin can also be used as a more effective way

to mount the rotor search-coil. To clarify, the machine supplies a 3-phase symmetric load resistive load in all conditions. To validate that the search coils were installed correctly, it is examined if the voltage under balanced-healthy conditions is zero. That is going to be the first measurement. A negligible voltage ripple is expected due to the end winding leakage

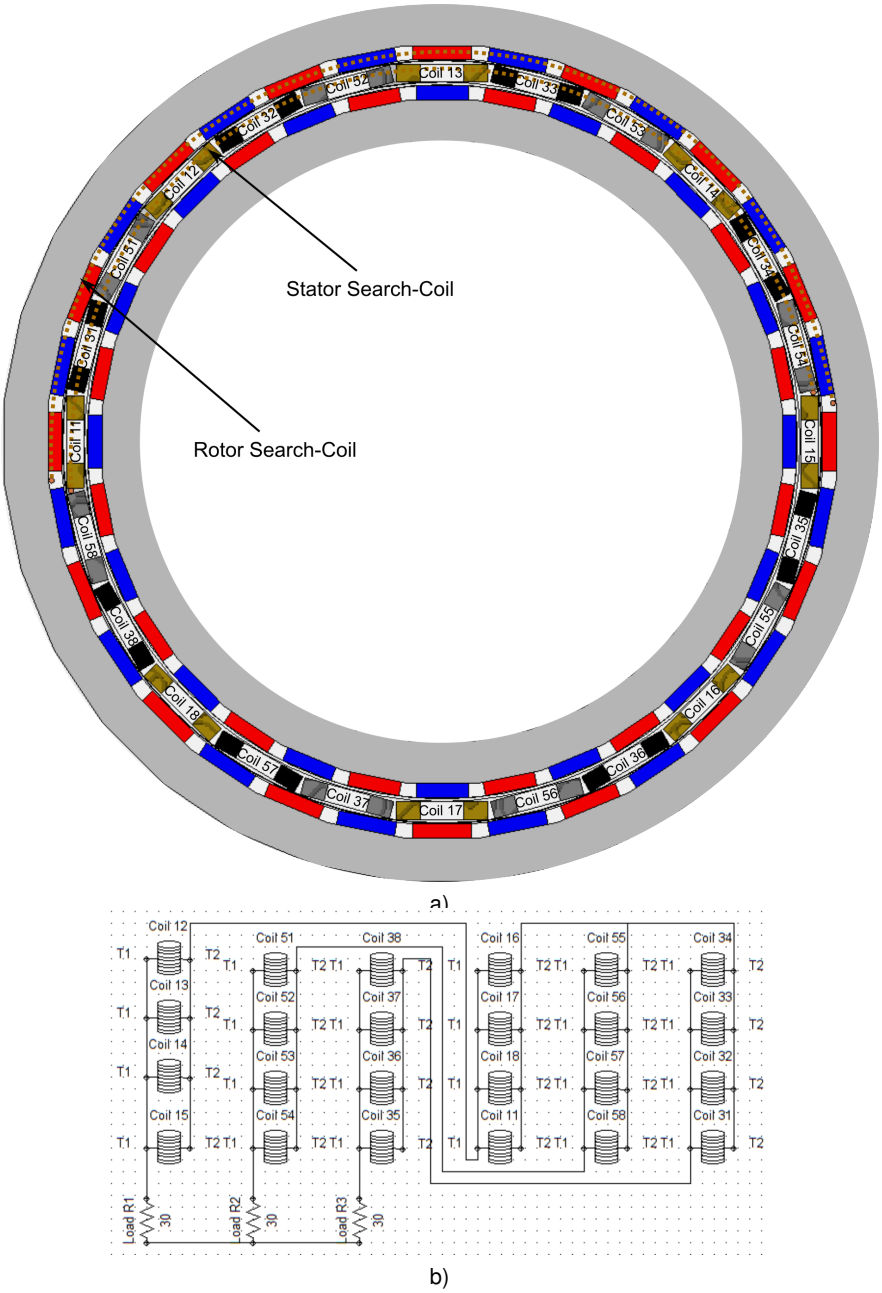

Figure 4.31: a) Solid 2-D FEA model of the double rotor radial-flux permanent-magnet generator with the two search-coils installed and b) winding layout for the partial demagnetization experiment.

field and the low eccentricity percentage pre-exists in an electric machine. The other two measurements will cover the cases in which the machine has a static and a dynamic fault. The second measurement occurs when the machine has one magnet and its iron segment completely off. In this way, an artificial partial demagnetisation fault is implemented in the machine. In the above condition, the machine has four parallel paths. Furthermore, the third measurement is taken when the machine has an inter-turn fault. To create an artificial inter-turn fault, one of the machine's coils is shorted using a combination of variable resistors. The latter creates a difference in the current of that coil, so it has a different value than the other coils. The loop current equals the current in the phase coils minus the shorted coil current. Each phase's coils have to be connected in series for this measurement.

Figure 4.33 presents the experimental test rig, which includes all the measuring equipment. A 3-phase induction motor drives the permanent-magnet generator, and its speed is adjusted using a 3-phase voltage inverter. A mechanical gearbox is interfered between the two connected shafts to reduce the speed supplied to the generator. The generator used in the experiment is for renewable energy applications, and it is of direct drive, meaning that it is supposed to be coupled directly to the turbine, so it is supposed to work at low speeds. Lastly, the generator supplies a 3-phase symmetric resistive load.

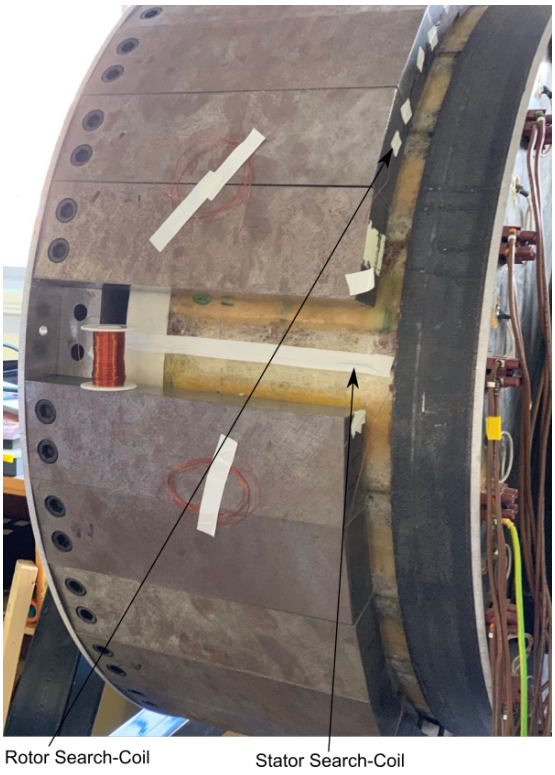

Figure 4.32: Double rotor radial-flux generator with the two search-coils installed.

The signal voltage signal in the stator search coil is measured using a voltage probe. The characteristics of the voltage probes are TESTEC TT-LF 312 with 1:1 scaling, attenuation ratio x1, input impedance 47 pF, bandwidth 15 MHz, rise time 24 nsec, and compensation range 10-60 pF. The voltage probe is connected to a DAQ (Data Acquisition System) which uses a laptop computer as a user interface. The DAQ device is PicoScope 4000 series and model 4824 and the resolution enhancement is set at 16.0 Bits. The resolution enhancement aids in clearing unwanted noise without any filtering. The speed is measured with a hall effect speed sensor fed in the DAQ. The electric period of the voltage signal can be measured by estimating the period of one square-wave pulse. By calculating the inverse of the period, the frequency is calculated. Using (2.6), one can measure the rotational speed by knowing the number of poles. The installed Hall-effect speed sensor on the permanent-magnet generator is presented in the photograph of Figure 4.34.

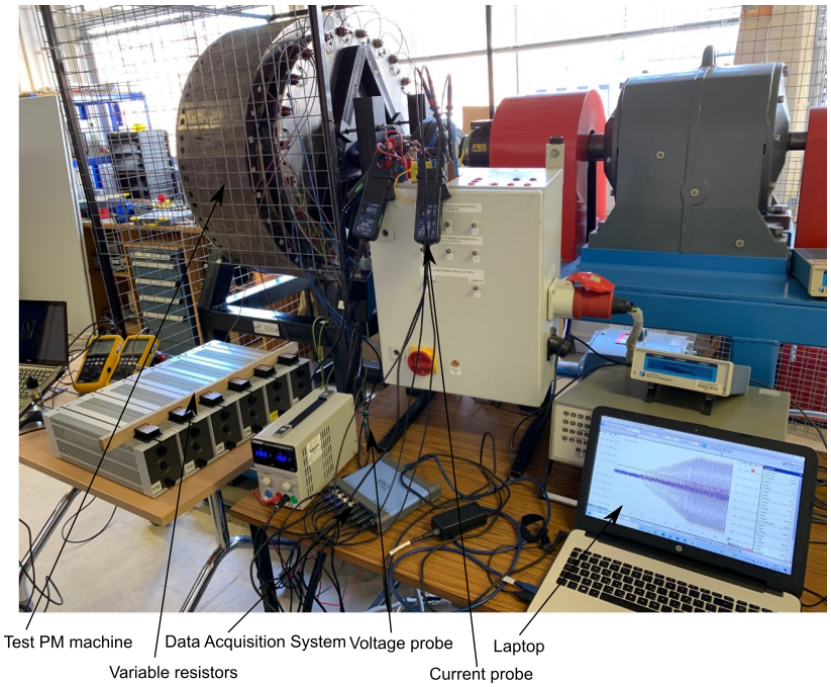

Figure 4.33: Graphical representation of the: a) axis and b) angular misalignment in axial-flux PM machines emphasising the axis of rotation for static and dynamic eccentricity.

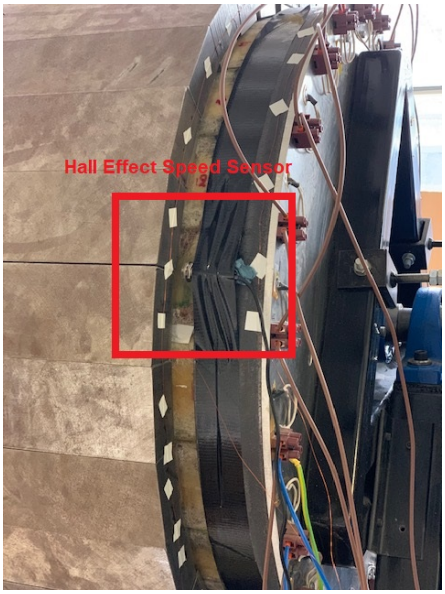

Figure 4.34: The installed Hall-Effect speed sensor in the permanent-magnet generator.

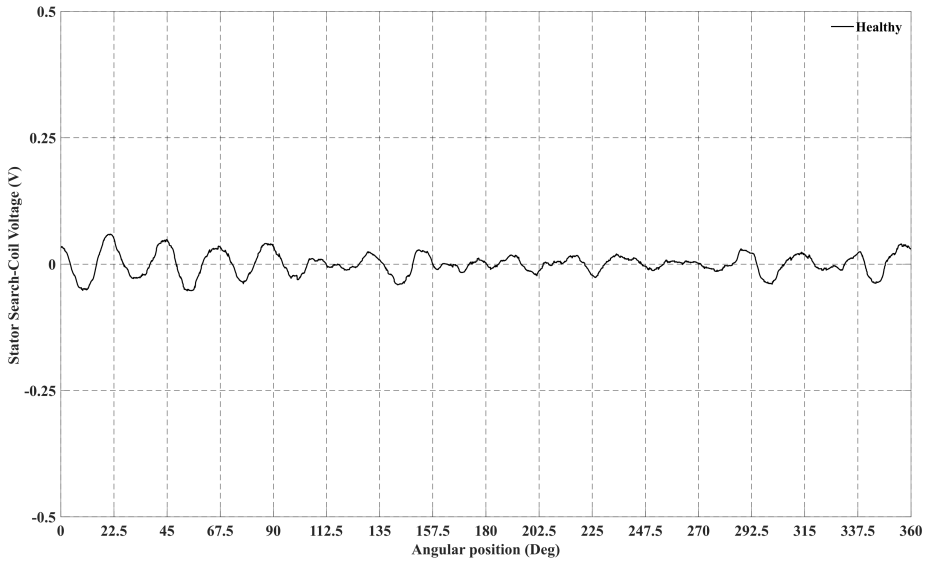

a)

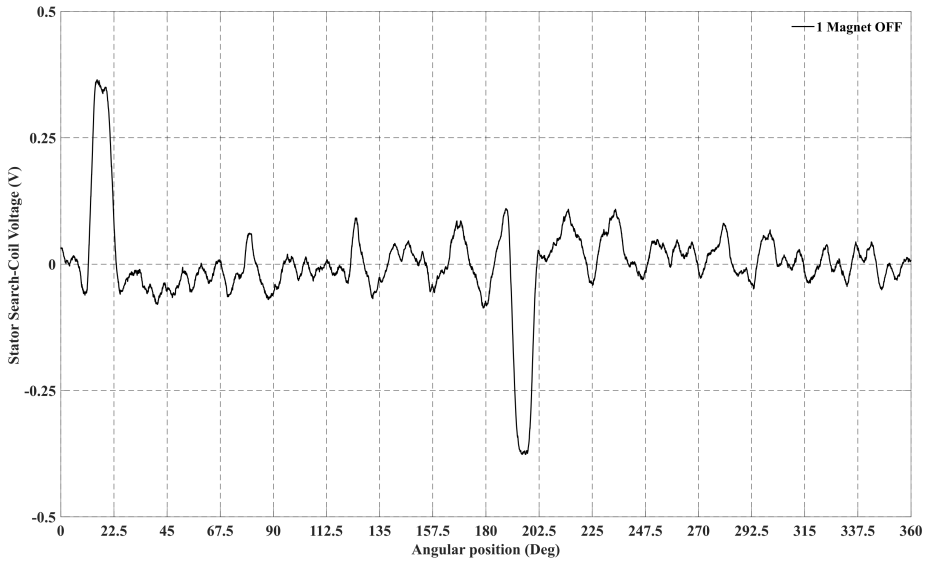

b)

Figure 4.35: Experimental results of the stator search-coil voltage for the generator at 100 rpm with 4 parallel paths at a) healthy condition and with b) one magnet off.

Figure 4.35a 4.35b presents the experimental on-load results of the voltage extracted by the stator search-coil under healthy conditions and having one rotor segment out. Each segment carries one magnet, so removing a segment will create an artificial partial demagnetisation fault. As obtained by simulation, under the healthy condition, the search-coil voltage is zero as there is no penetrating magnetic flux at any of the two search coils. A small ripple caused by

the very small degree of static and dynamic eccentricity a healthy machine carries due to the manufacturing imperfections. Furthermore, the end-windings of the stator winding create a small parasitic magnetic flux which penetrates the search coil and induces a very low voltage ripple. In the case of a partial demagnetisation fault in the generator, the stator search-coil voltage has two peaks. Each peak corresponds to the position where the magnet's centre passes from each coil side of the stator search coil. Due to the parallel path connection, the search coil has some additional flux interference, which distorts the main signal. However, this interference affects the two peaks of the voltage signal significantly, so even in the case of parallel paths, the method can work properly. The experiment validates also the results of the previous section, as the rotor search coil is inactive for this fault since there is no relative motion between the conductors and the magnet field. Due to the circulating currents, a low unbalanced magnetic flux is expected to penetrate through the rotor search-coil. Nevertheless, this interference is small compared to the one that the demagnetised magnet causes.

Figure 4.36a, 4.36b and 4.36c presents the experimental on-load results of the stator search-coil voltage obtained when the generator is under healthy and inter-turn fault conditions, rotating at 10 rpm with no parallel paths. The speed, in this case, could not become very high since every coil is built-up by 205 turns and there 8 coils in every phase, meaning that if the speed becomes high the voltage will become very high. The inter-turn fault was implemented artificially by connecting variable resistors parallel to one of the stator winding coils. The equivalent resistance of two resistors connected in parallel has a lower value than the resistor with the minimum value, meaning that the total impedance of the equivalent coil reduces. Under the same voltage, the stator winding coil will have an increased current flowing on a closed loop. With this technique, the stator current's root-mean-square value can change by varying the resistors' resistance, leading to different fault severity levels. The inter-turn fault can be detected by inspection as it creates an oscillatory signal in the voltage of the stator's search-coil, which increases as the loop current increases. This machine does not have an iron stator core, so the sensitivity of the signal is low; however, it's enough to detect the fault. A conductor of higher diameter can be used on the rotor search-coil to reduce the impedance of the loop. A lower loop impedance will offer a higher current on the loop of the search-coil a higher current induced by the fault and create a stronger magnetic flux. The magnetic flux in relative motion with the stationary stator search-coil will induce a higher voltage. This fault creates magnetic flux, which corresponds to one coil pitch much smaller than the 180^{o} coil span that the search coil has, so no magnetic flux is lost. The purpose of this experiment was to show that the oscillatory voltage signal created on the stator search-coil is proportional to the loop current, which is shown with great success. As a fault identifier and fault index for both fault cases, the shape of the waveform and the amplitude of the stator search-coil voltage can be used. Also, according to Figure 4.36a, the machine has a very low percentage of dynamic eccentricity as the waveform of the stator search-coil voltage suggests. The magnetic flux

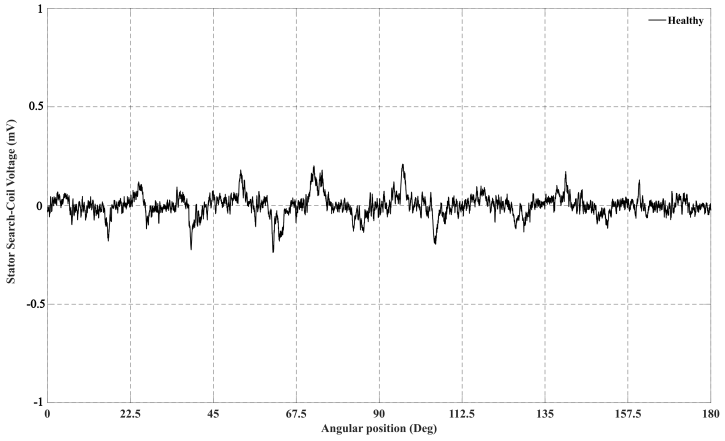

a)

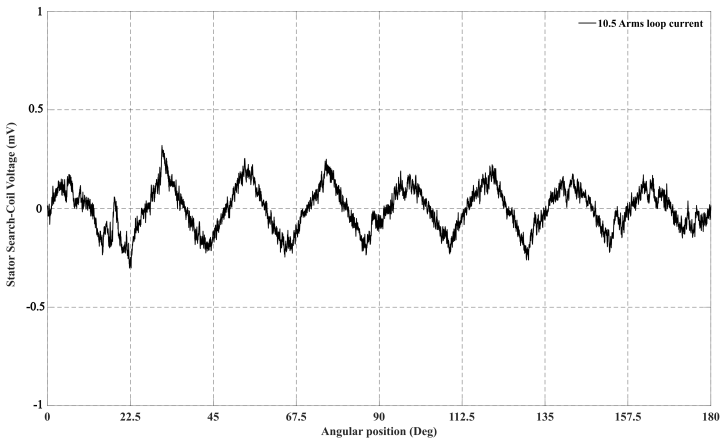

b)

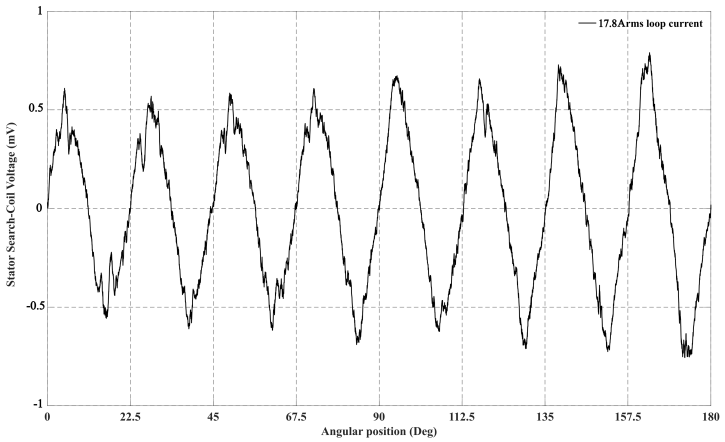

c)

Figure 4.36: Experimental results of the stator search-coil voltage for the generator at 10 rpm with no parallel paths under a) healthy and inter-turn fault conditions with b) 10.5 Arms and c) 17.8 Arms loop current.

created by the dynamic eccentricity fault has a span of 180^{o} which is the same as the pitch of the search coil. The latter means no magnetic flux is lost due to the short-pitching effect. The speed of the machine can be obtained using Figure 4.37, which presents the voltage signal extracted by the Hall-effect speed sensor and is equal to 10.077 rpm.

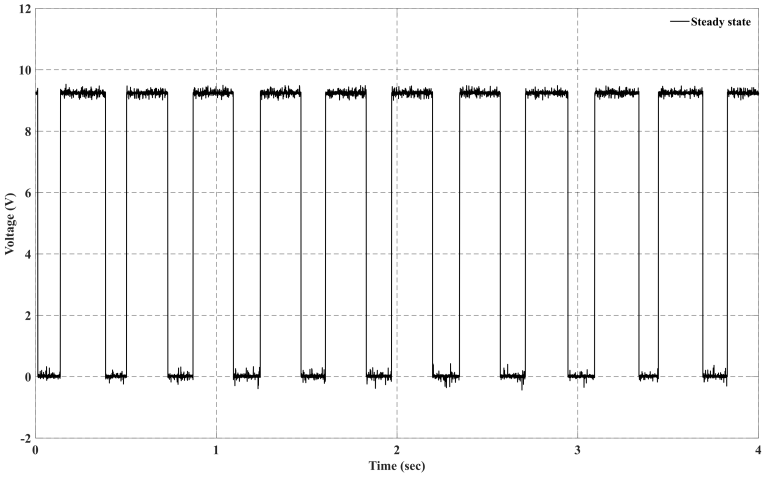

Figure 4.37: Experimental results of the voltage pulse-wave versus time signal extracted by the Hall-Effect speed sensor for the steady-state the machine has inter-turn fault.

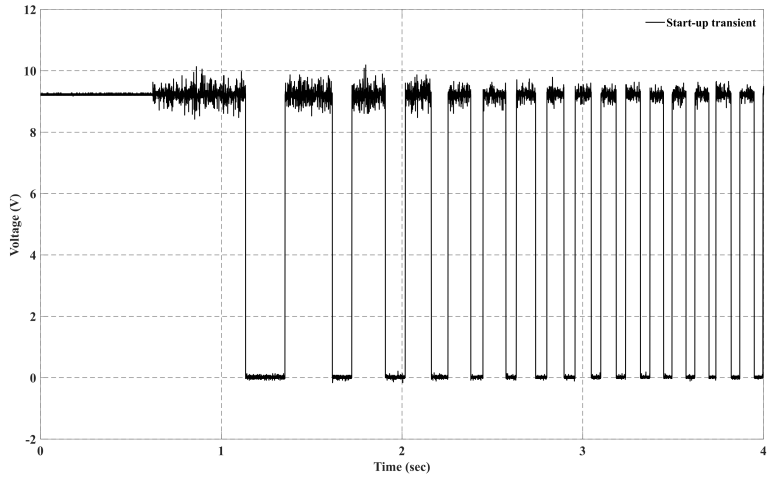

a)

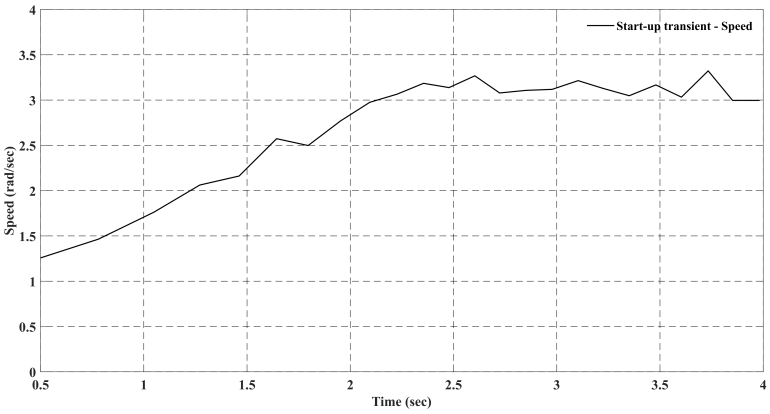

b)

Figure 4.38: Experimental results of the a) voltage pulse-wave versus time signal extracted by the Hall-Effect speed sensor and the corresponding b) speed signal during the start-up transient.

To examine if the method remains effective under variable speed, the stator search coil voltage signal was measured while the machine was accelerating. The speed increases from 0 to 29.043 rpm in 4 seconds, as Figure 4.38a, suggests. Figure 4.38b shows the speed during the captured transient event that Figure 4.38a suggests. The speed was calculated by creating an algorithm. The algorithm calculates the frequency of each pulse which is the electric frequency of the generator. Then a new signal is reconstructed which has the same length as the stator search-coil voltage and the frequency was considered to have have a value which depended by the slope between two different pulses. Figure 4.39a, 4.39b and 4.39c present the signal during the start transient under healthy and inter-turn fault conditions with and without normalisation of the speed-squared. According to Figure 4.39a, the signal increment is negligible as the machine is healthy. There is a low voltage increase which happens due

to the low dynamic eccentricity level that the machine carries, and as the speed increases, so does this unbalanced magnetic flux. Figure 4.39b shows the variation of the amplitude of the signal as the speed increases. Figure 4.39c proves that the square of the speed is proportional to the stator search-coil voltage as the amplitude of the signal becomes constant. In this case the signal depends only the fault severity i.e. the loop current of the inter-turn fault. The latter happens because the fault is static, so the rotor search-coil rotates with the mechanical speed in relation to the static magnetic flux. Then the stator search coil senses the magnetic flux that the rotor search coil broadcasts, and the relative motion between the two search coils equals the mechanical speed. So the signal depends on the square of the speed. Furthermore, additional speed transient simulations using 2-D Finite-Element Analysis were solved under inter-turn fault and partial demagnetisation. The solid model is presented in Figure 4.31. The speed increases linearly from 5 to 40 rpm in a time interval of 10 seconds. All the coils are connected in series. The generator supplies a symmetric resistive load of 150Ω/phase. Figure 4.40 presents the waveform of the mechanical speed in rad/sec for the 2-D FEA simulation. The signals studied are the stator search-coil voltage which is the to-be monitored signal and the rotor search-coil current. The latter cannot be measured, and as explained above, it acts as an auxiliary coil which produces the magnetic flux, which makes the detection of static faults possible.

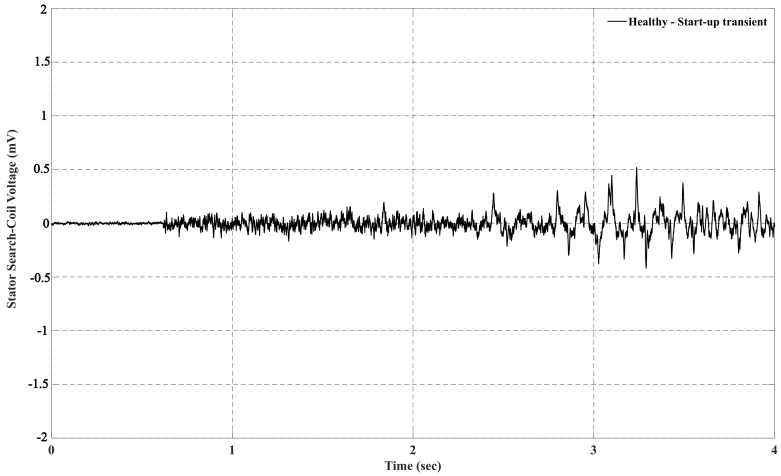

a)

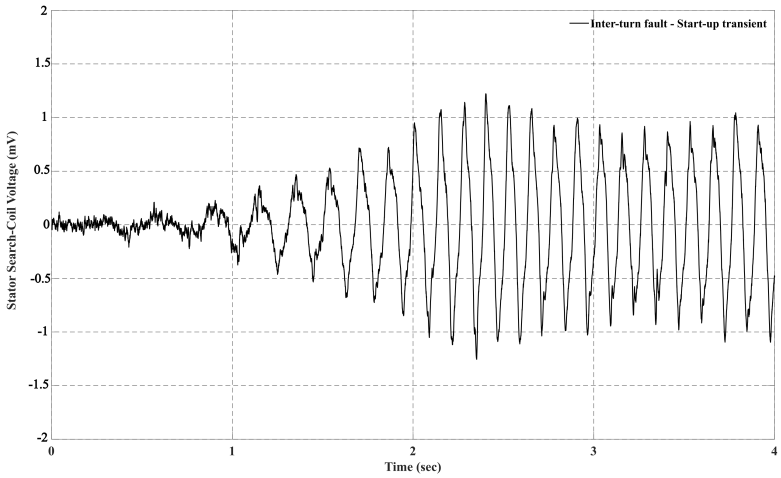

b)

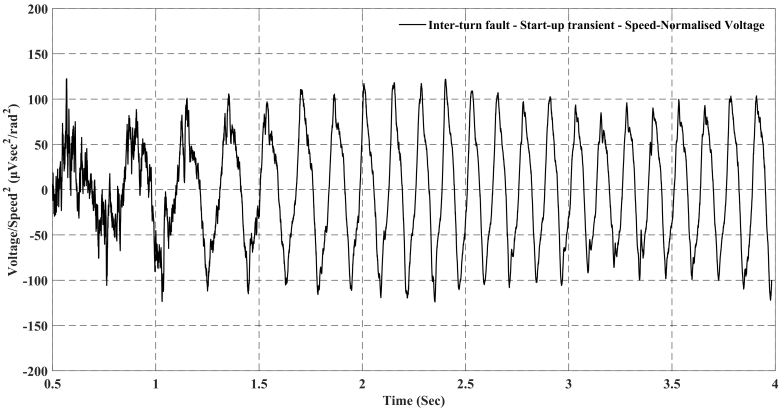

c)

Figure 4.39: Experimental results of the stator search-coil voltage for the generator during the start-up transient at a) healthy and with inter-turn fault conditions b) without and c) with speed-squared normalisation.

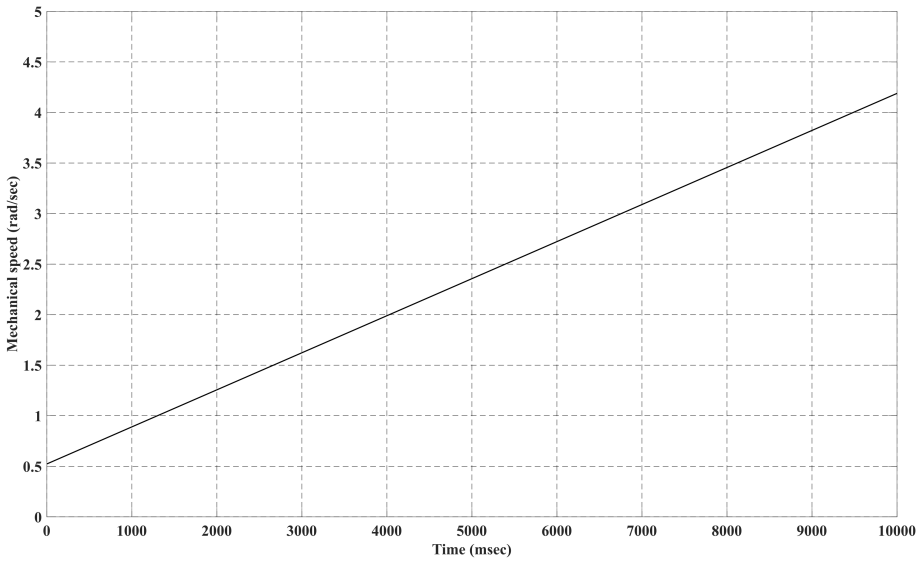

Figure 4.40: Rotor speed waveform versus time for the transient event.

Figure 4.41a presents the stator search-coil voltage signal of the generator under healthy conditions and the transient speed event. By inspection, the signal remains zero as the speed increases as the search coils have interfered in an even number of pole pitches and an odd number of coil pitches. The magnetic flux that penetrates through the stator search-coil is the magnetic leakage flux of the stator winding, although it is negligible. Figure 4.42b presents the stator search-coil voltage signal normalised by the square of the mechanical speed. The signal remains negligible in this case as well. Figure 4.42a illustrates the stator search-coil voltage of the generator when there are two shorted turns in a coil of the phase winding. The signal is not zero anymore, and its amplitude increases as the speed do. As discussed above, the hereunto fault detection signal is proportional to the square of the speed and the current in the shorted loop. The latter means that the signal becomes constant by normalising the signal with the square of the mechanical speed. The speed waveform was presented in Figure 4.40, so by taking the square of this waveform and dividing the voltage signal of Figure 4.42a; a constant signal yields, which the reader can see in Figure 4.42b. The amplitude of the latter signal depends only on the number of shorted turns or in other words, the value of the current in the shorted loop.

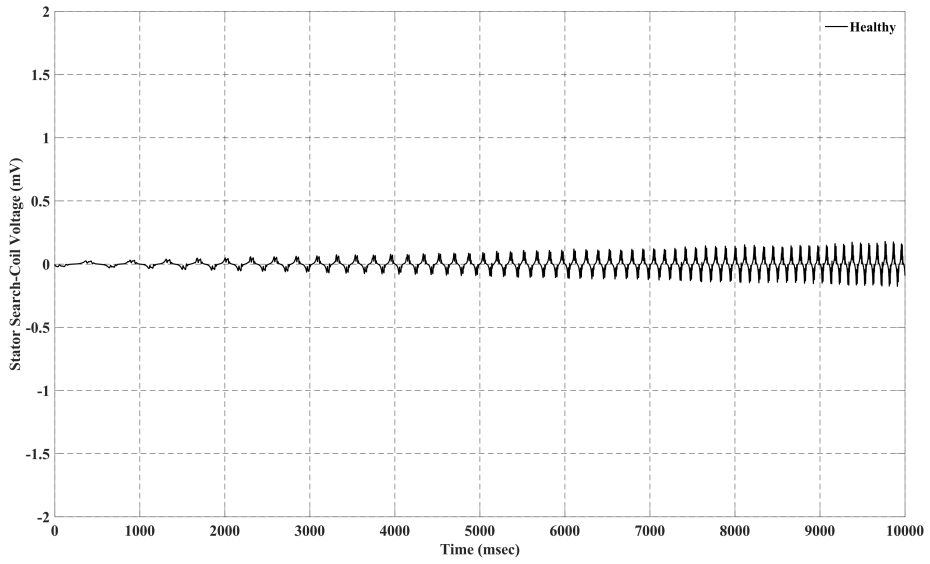

a)

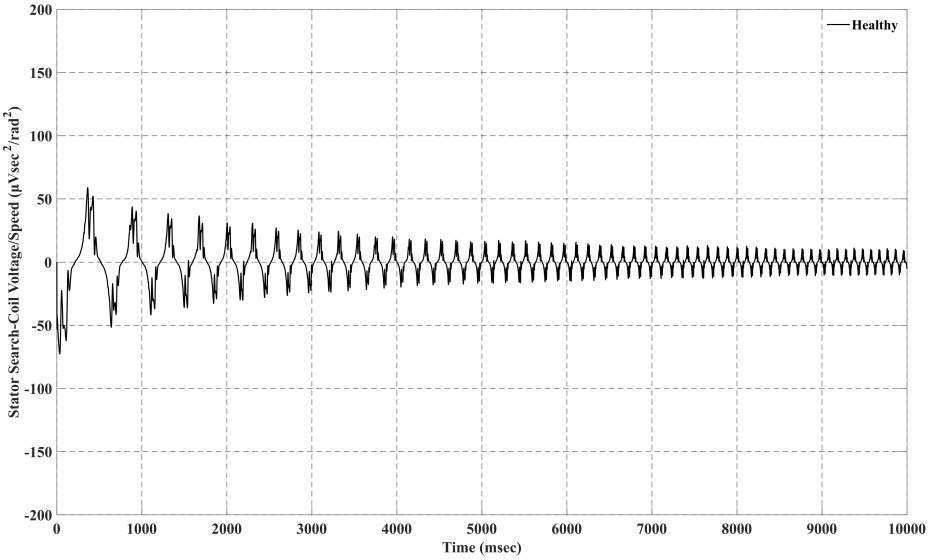

b)

Figure 4.41: a) Stator search-coil voltage of the generator for the studied transient event under healthy conditions and b) stator search-coil voltage normalised with the square of the mechanical speed.

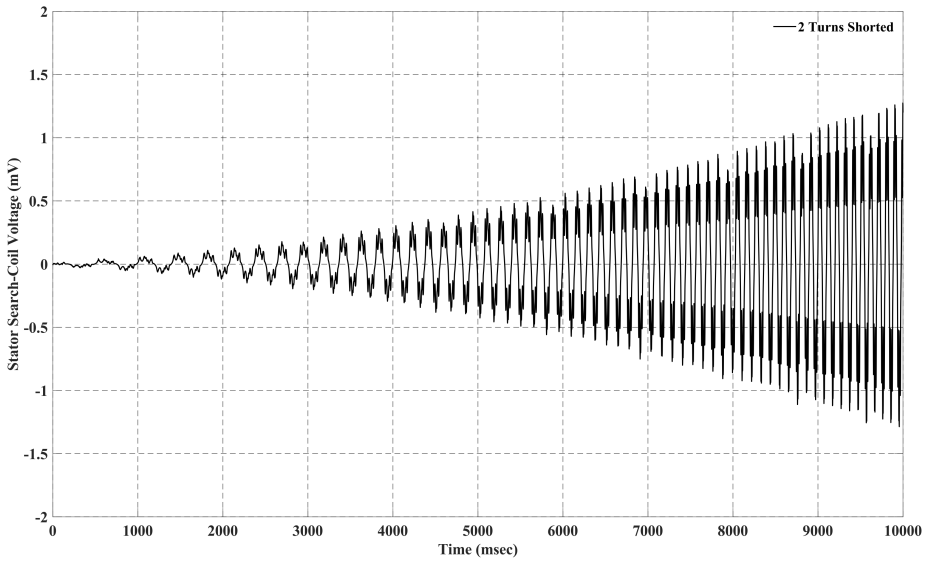

a)

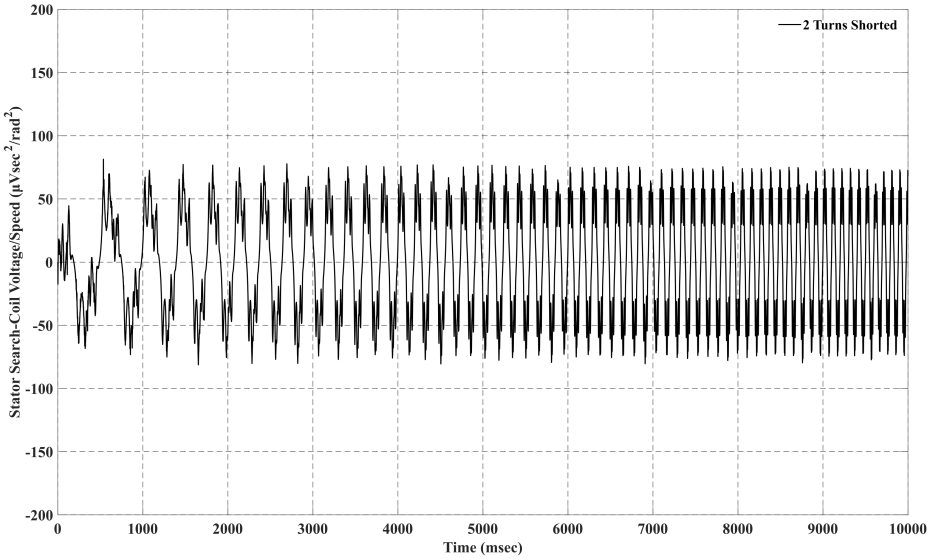

b)

Figure 4.42: a) Stator search-coil voltage of the generator for the studied transient event with 2 turns shorted in the generator's stator winding and b) stator search-coil voltage normalised with the square of the mechanical speed.

Figures 4.43a and 4.43b present the rotor search-coil current for the generator under the same transient event for two cases; when the generator is healthy and when there are two turns shorted on the winding. In Figure 4.43a, one can see that under healthy conditions, the current on the closed-circuited rotor search-coil is zero as the speed increases. In Figure 4.43b, there is an oscillation induced in the positions where the coil sides of the search-

coil pass from the centre of the coil, which contains the shorted turns. Since the magnetic flux source that the current in the shorted turns produces is fixed in space, there will be an induced voltage on the rotor search coil because of the relative motion. The current in search-coil increases proportionally with speed.

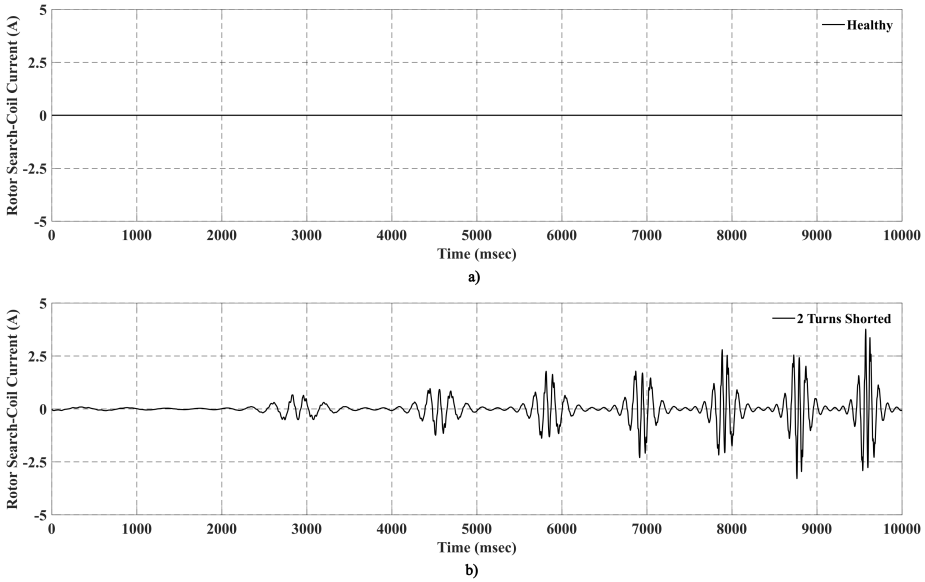

Figure 4.43: Rotor search-coil current of the generator for the studied transient under a) healthy conditions and b) with 2 turns shorted.

Figure 4.44a demonstrates the stator search-coil voltage at the same transient event as above when one of the generator's magnets is 40% demagnetised. The latter means that the 60% of the residual flux density that the magnet remains. Since every pole pitch contains two magnets facing the air gap at the same angle, the magnetic flux density reduction will be slightly less than 20%. It will be less than 20% because the demagnetised magnet of the inner rotor has less volume than the one in the outer rotor. One can see that the signal's amplitude increases with the speed increment. In the type of dynamic faults, the proposed fault detection signal is only proportional to speed and not to the square of the speed. The induced voltage peaks originate from the positions where the demagnetised magnet passes from each coil side of the stator's search coil. Figure 4.44b presents the speed normalised signal for the same transient event. It is visible that the amplitude of the signal remains constant, so in this fault case, the signal depends only on the fault severity, which is the reduction of a magnet's residual flux density. Since the search coil placed in the rotor rotates at the same speed as the rotating magnetic field created by the magnets, there will be no induced current on the coil, as Figure 4.45 supports.

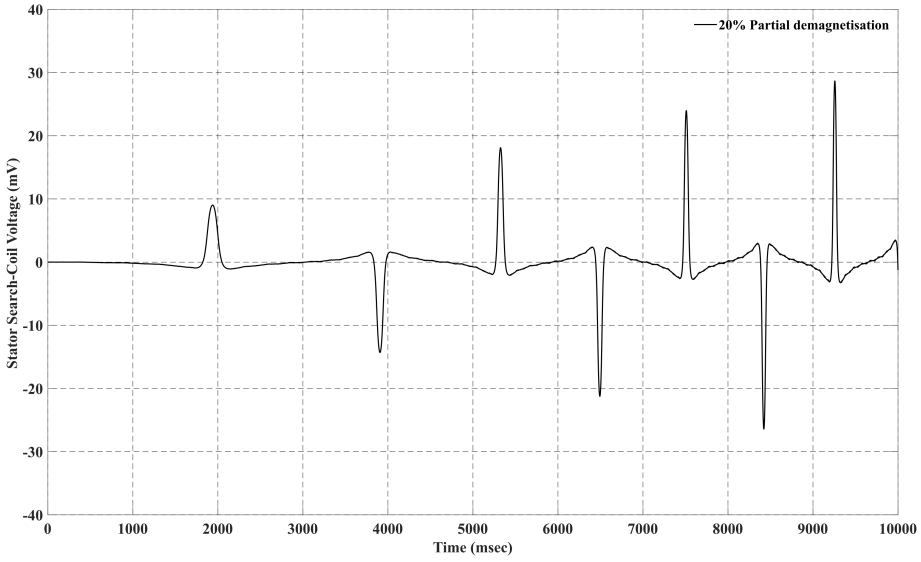

a)

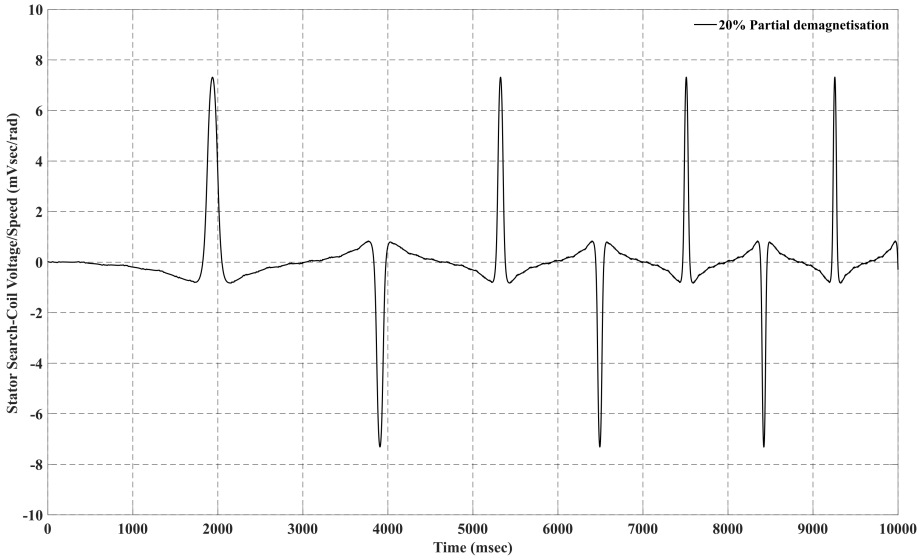

b)

Figure 4.44: a) Stator search-coil voltage of the generator for the studied transient event with 40% partial demagnetisation of a magnet and b) stator search-coil voltage normalised with the mechanical speed.

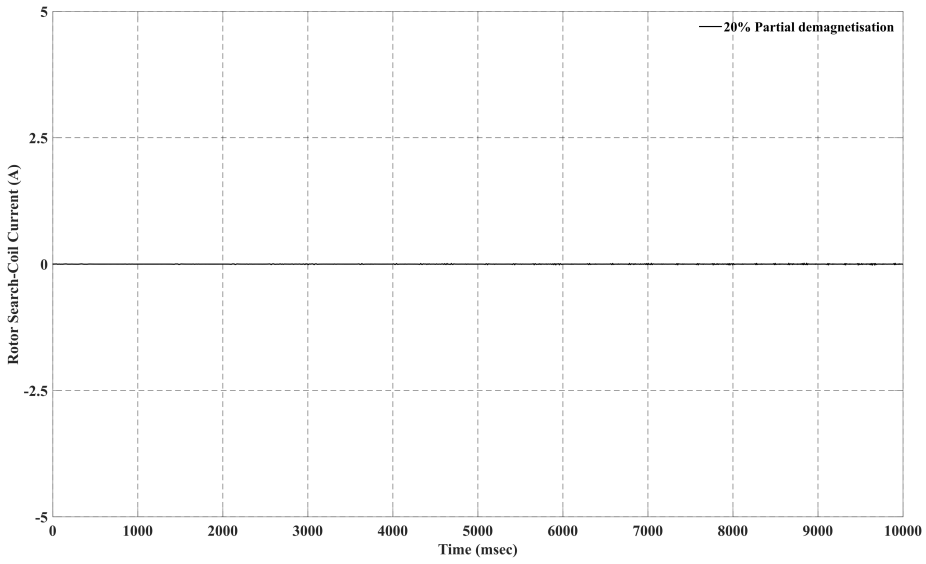

Figure 4.45: Rotor search-coil current of the generator for the studied transient under approximately 20% partial demagnetisation.

Figure 4.46a presents the stator search-coil voltage during the transient event, while the generator has 20% dynamic eccentricity. One can see that the signal amplitude and frequency increases with the speed increment. By normalising the signal with the speed the amplitude of the signal becomes approximately constant for every value of the speed as Figure 4.46b suggests. According to Figure 4.47 due to the unbalance magnetic flux produced by the armature reaction field there is a current on the rotor search-coil. However, the magnetic flux that this current creates is negligible compared to the unbalanced magnetic flux originating from the magnets as there is relative motion between conductors and this flux.

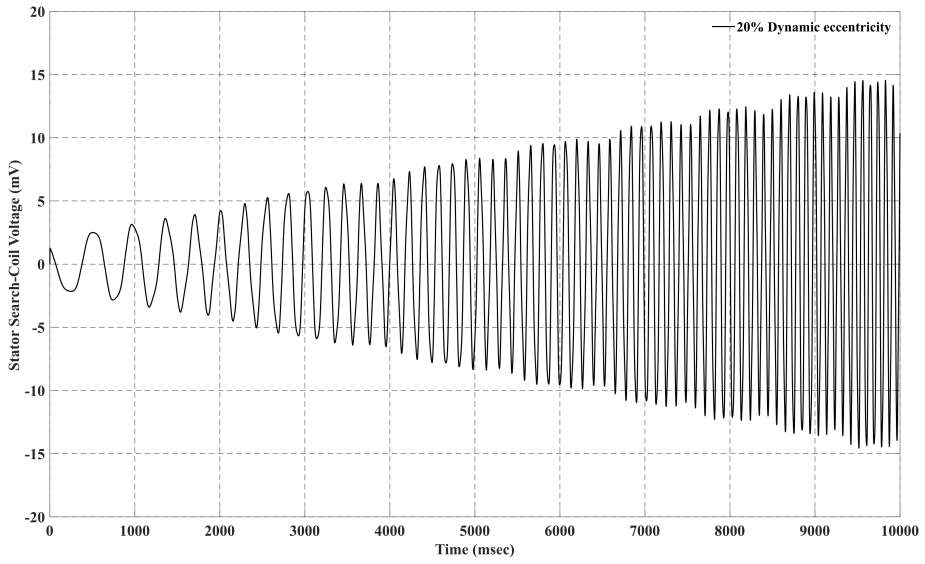

a)

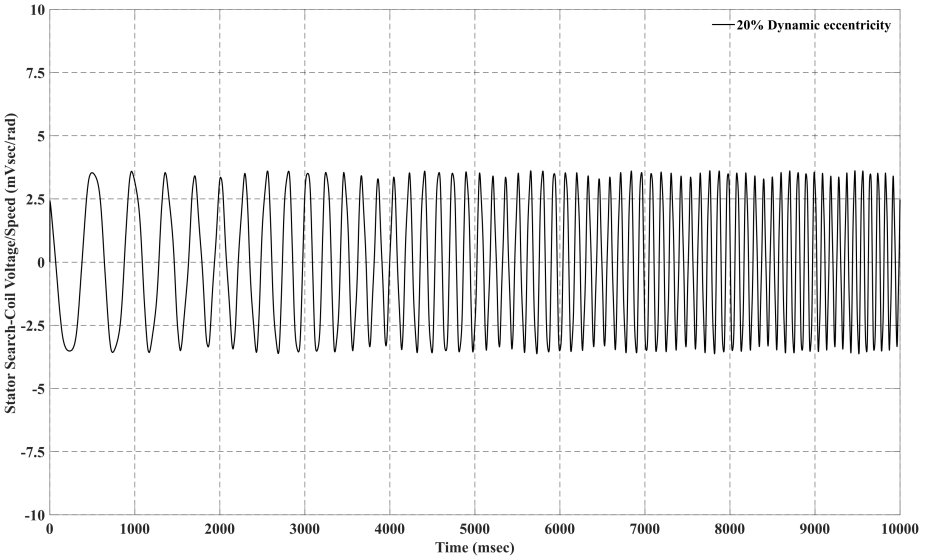

b)

Figure 4.46: a) Stator search-coil voltage of the generator for the studied transient event with 20% dynamic eccentricity and b) stator search-coil voltage normalised with the mechanical speed.

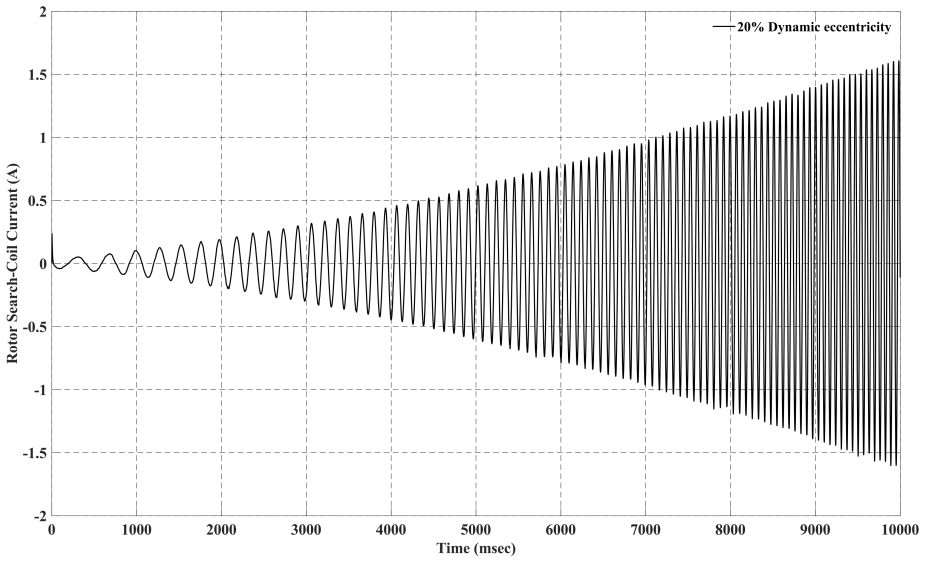

Figure 4.47: Rotor search-coil current of the generator for the studied transient under 20% dynamic eccentricity.

Lastly, static eccentricity under a transient condition is presented. Figure 4.48a presents the stator search-coil voltage during the transient event whilst the machine has 20% static eccentricity on the internal rotor. One can see that the amplitude of the signal increases with the speed increment. Similarly, as done above by normalising the signal with the mechanical speed of the rotor, the signal has a constant amplitude which depends only the fault severity percentage. There is an induced current on the rotor search-coil for this fault as well, meaning that the rotor search-coil creates a magnetic flux that penetrates through the stator search-coil.

The proposed condition monitoring signal depends only on the speed and fault severity. The distribution of the stator search-coil voltage signal offers the identification of which fault occurred. Depending on what fault happened, the signal should be normalised by the mechanical rotational speed or its square. After that, the amplitude of the signal becomes constant as long as the fault severity does not increase. The variation of the signal amplitude will follow the variation of the fault severity. The above method can detect all faults reliably without any further signal processing during variable speed and load conditions.

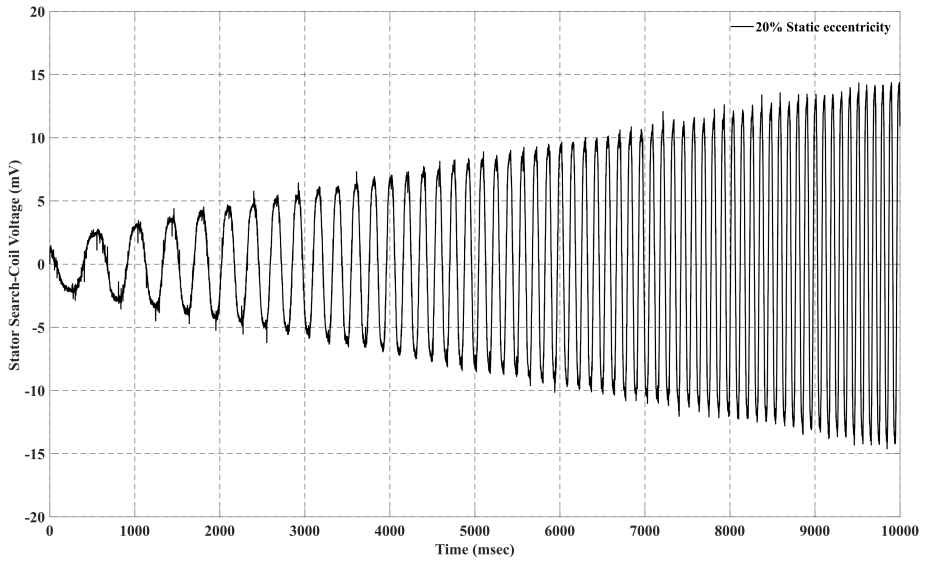

a)

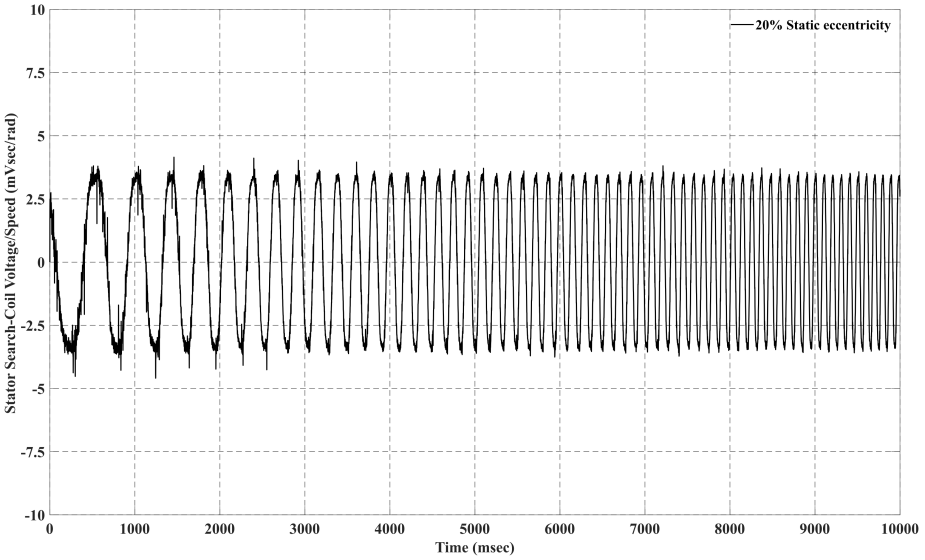

b)

Figure 4.48: a) Stator search-coil voltage of the generator for the studied transient event with 20% static eccentricity in the generator's stator winding and b) stator search-coil voltage normalised with the mechanical speed.

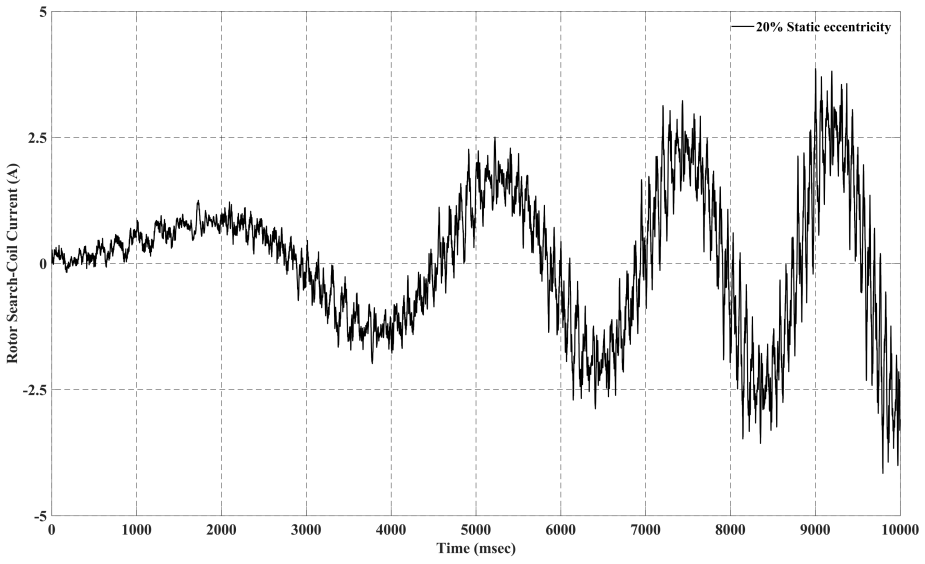

Figure 4.49: Rotor search-coil current of the generator for the studied transient under 20% static eccentricity.

4.2.4 Summary and conclusions of the proposed method

This section proposes a novel diagnostic technique in permanent-magnet machines based on two search coils, one placed in the rotor and one in the stator. The rotor search coil, under faulty conditions, carries a current which creates a magnetic flux that penetrates the stator search coil. Each fault generates a unique waveform in the stator search coil, and the amplitude is proportional to the fault severity. The proposed methodology converts static faults into dynamic ones and makes them detectable. This method overcomes the limitation that the method with the single stator search-coil negates the induced voltage under balanced conditions faces. Finite-Element Analysis results of air-cored radial- and axial-flux machines show that the proposed technique can be used to monitor all the faults under steady and transient operation of permanent-magnet synchronous machines. Experimental results during partial demagnetisation and inter-turn faults on an air-cored radial-flux permanent-magnet generator showed that this method can be used to diagnose static and dynamic faults for stationary and transient conditions. The proposed diagnostic method uses only two single wired search-coils which makes the method cost efficient and less complex compared to the methods based on commercial flux sensors. The permanent-magnet machine used to validate the method experimentally is low speed so the mounting demands for the rotor search-coil were low. For machines operating in higher speeds the mounting demands are going to be higher, so the mounting can become a challenge. Lastly, the method does not require any further signal processing which decreases the cost and increases the applicability even further.

Chapter 5

Prediction of the Motor-Current-Signature-Analysis signatures under rotor faults in permanent-magnet synchronous machines

This work proposes an algorithm based on an analytical model which makes it possible to predict the harmonic fault signatures under dynamic eccentricity in permanent-magnet synchronous machines with a concentrated non-overlapping winding for any slot-pole combination. The motivation behind this work was that there was no proposed formulae which offers the harmonics generated by dynamic eccentricity as a function of both the pole-pair and coil winding number. Currently the literature discusses about the appearance of the fractional harmonic components related to the pole number. A mathematical equation is derived for the machines' EMF under dynamic eccentricity based on the air gap permeance model. Later on, the terms of this equation are inserted in a Fault Signature Block Binary Array in which the position of each cell expresses a specific harmonic frequency component. After substituting the machine's parameters, the array results in zero and nonzero terms. The positions of the nonzero terms express the frequency components excited by this particular fault. 3-D FEA and experimental results of a Permanent-Magnet Axial-Flux Machine are used to validate the proposed algorithm.

5.1 Mathematical formulation of the phase-EMF under dynamic eccentricity

The air gap is constant when a rotor exhibits concentric motion without eccentricity, as illustrated in Figure 5.1a. However, when the eccentric motion the one or both rotor discs obtain an angle relative to the stator disc, the air gap becomes non-uniform. A minimum and maximum air-gap length are then created. When the two air-gaps lengths are constant, the eccentricity fault is static, and no fault-severity-dependent harmonic components are induced on the winding of air-cored machines [106]. A sketch of static eccentricity on a machine is demonstrated in Fig. 5.1b. In machines with iron cores, some fault signatures are induced due to the saturation of the ferromagnetic material in the area where the air-gap length decreases. Alas, they cease to increase in magnitude when the core enters deep saturation [107, 42, 108, 43]. Fig. 5.1c presents a dynamic eccentricity sketch. Under this fault condition, the generated harmonics are proportional to the fault severity level, and fractional harmonic components with orders related to the pole-pair number are generated in the stator variables' spectra [42, 32, 109, 79].

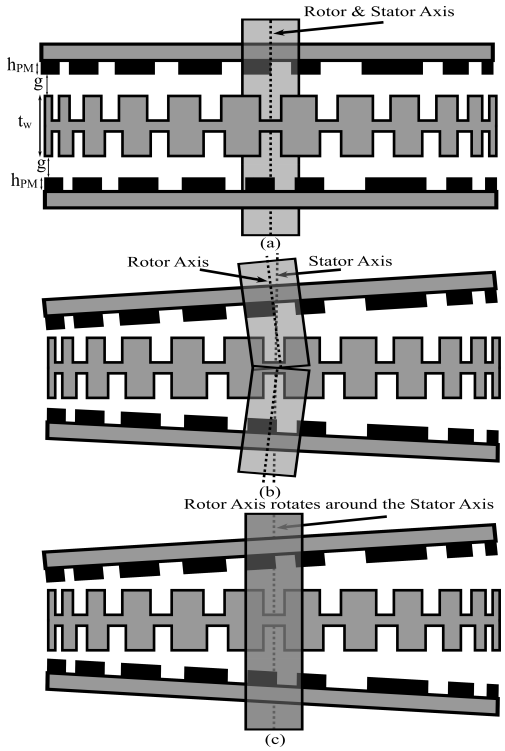

Figure 5.1: Sketch of an air-cored Axial-Flux Permanent-Magnet Machine under a) healthy b) static and c) dynamic eccentricity fault.

5.1.1 Magnetic field expression under dynamic eccentricity

The permeance function for a dynamic eccentricity condition of an air-cored machine can be written using [12, 26, 110, 79]

$$\Lambda_{DE}(\theta,t) = \frac{\mu_0}{\frac{h_{PM}}{\mu_{PM}} + 2g + t_w + DEF\cos\left(\theta - \omega_r t\right)}, \tag{5.1}$$

where μ_0, h_{PM}, μ_{PM}, g, θ, ω_r, t and t_w are the vacuum magnetic permeability, axial height of the PM, recoil permeability of the PM, air-gap length, the axial length of the winding, rotor angular position and rotor mechanical speed, time and winding axial thickness, respectively. The recoil permeability of the magnet can be considered equal to unity $\mu_{PM} \approx 1$. The dynamic eccentricity factor (DEF) is defined similarly as the static eccentricity factor (SEF) in [12]. For a machine with a stator by ferromagnetic core, the axial length of the stator winding will be divided with the iron permeability, which has a high value, so this term may be neglected. To ease the calculations, I wrote the relationship which connects the magnets' axial length with the winding. For the specific test machine, the PM height is equal to the stator winding axial length

$$h_{PM} = t_w \tag{5.2}$$

Considering (5.2), (5.1) can be written as follows

$$\begin{aligned}\Lambda_{DE}(\theta,t) &= \frac{\mu_0}{h_{PM} + 2g + t_w + DEF\cos\left(\theta - \omega_r t\right)} \\ &= \frac{\mu_0}{3h_{PM}} \cdot \left\{1 + \frac{2g}{3h_{PM}} + \frac{DEF\cos\left(\theta - \omega_r t\right)}{3h_{PM}}\right\}^{-1}\end{aligned} \tag{5.3}$$

and since the below equation is applicable

$$\left|\frac{2g}{3h_{PM}} + \frac{DEF\cos\left(\theta - \omega_r t\right)}{3h_{PM}}\right| < 1 \tag{5.4}$$

which stands $\forall\, t > 0 \;\&\; \theta \in [0, 2\pi]$. As a result, (5.3) can be developed using Taylor-Maclaurin expansion. By applying

$$(1+x)^{-n} = \sum_{n=0}^{\infty}(-1)^{n+2}x^n = 1 - x + \ldots + x^n - \ldots,\ |x| < 1, \tag{5.5}$$

(5.3) is written up to the 6$^{\text{th}}$ order term of the series expansion. So, by applying the expansion, the permeance function is written as

$$\Lambda_{DE}(\theta,t) = \alpha + \beta\cos(\theta - \omega_r t) + .. + \eta\cos\big(p(\theta - \omega_r t)\big), \tag{5.6}$$

where α, β, γ, δ, ε, and η are constants which depend on the dimensions of the machine and the dynamic eccentricity factor (DEF). The Magneto-Motive Force (MMF) of the PM has a square-wave form and can be represented using the Fourier series as a function with only odd harmonics. The amplitude of each of these harmonics is inversely proportional to its order as follows

$$\mathscr{F}(\theta,t) = \sum_{k\,odd}^{\infty} \mathscr{F}_{PM,k}\cos(kp\theta - k\omega_s t) \tag{5.7}$$

where ω_s is the electrical speed of the rotating magnetic field created by the PMs, p is the number of machines' pole-pairs, and k is the series index. The space-time varying air-gap magnetic field can be written according to [26]

$$B = \mathscr{F}\cdot\Lambda \tag{5.8}$$

By substituting (5.6) and (5.7) onto (5.8) and by applying the trigonometric identity

$$\cos x\cdot\cos y = \frac{1}{2}\left(\cos(x+y) + cos(x-y)\right) \tag{5.9}$$

a qualitative equation for the expression of the air-gap magnetic field under dynamic eccentricity is obtained. Moreover, the electrical speed connects with the mechanical speed with the following equation

$$\omega_r = \frac{\omega_s}{p}. \tag{5.10}$$

5.1.2 The voltage induced in a tooth-coil under dynamic eccentricity

To calculate the air-gap magnetic flux for the l^{th} concentrated non-overlapping coil, the magnetic flux density is integrated along with a coil pitch as

$$\Phi_l(t) = \frac{r_o^2 - r_i^2}{2}\int_{\frac{2\pi}{s}(l-1)}^{\frac{2\pi}{s}l} B(\theta,t)\,d\theta \tag{5.11}$$

where r_{i} and r_{o} are the internal and external radii of the PMs. By substituting the developed form of (5.8) onto (5.11) and applying the trigonometric identity

$$\sin x - \sin y = \frac{1}{2}\cos\frac{x+y}{2}\cdot\sin\frac{x-y}{2}, \tag{5.12}$$

the magnetic flux is obtained. The induced voltage on the l^{th} coil, which is proportional to the number coil turns N_c can then be obtained as the partial derivative with respect to time with the equation

$$\mathscr{E}_l = -N_c \frac{\partial \Phi_l(t)}{\partial t}. \tag{5.13}$$

5.1.3 Voltage induced in the phase of the machine under dynamic eccentricity

The phase voltage time function for the specific generator is equal to

$$\mathscr{E}_{ph}(t) = \mathscr{E}_1(t) + \mathscr{E}_4(t) + \mathscr{E}_7(t) \tag{5.14}$$

The resulting phase voltage equation is given by

$$\begin{aligned}
\mathscr{E}_{ph}(t) = {} & \frac{N_c \left(r_o^2 - r_i^2\right) \omega_s}{2} \cdot \\
& \Bigg\{ 2\alpha \sum_{k\,odd}^{\infty} \mathscr{F}_{PM,k} \Bigg(\sin\left(kp\frac{\pi}{s}\right) \cdot \Bigg(\sin\left(kp\frac{\pi}{s} - k\omega_s t\right) \\
& + \sin\left(kp\frac{7\pi}{s} - k\omega_s t\right) + \sin\left(kp\frac{13\pi}{s} - k\omega_s t\right) \Bigg) \Bigg) \\
& + \beta \sum_{k\,odd}^{\infty} \mathscr{F}_{PM,k} \Bigg(\sin\left((kp-1)\frac{\pi}{s}\right) \cdot \Bigg(\sin\left((kp-1)\frac{\pi}{s} - \left(k-\frac{1}{p}\right)\omega_s t\right) \\
& + \sin\left((kp-1)\frac{7\pi}{s} - \left(k-\frac{1}{p}\right)\omega_s t\right) + \sin\left((kp-1)\frac{13\pi}{s} - \left(k-\frac{1}{p}\right)\omega_s t\right) \Bigg) \\
& + \sin\left((kp+1)\frac{\pi}{s}\right) \cdot \Bigg(\sin\left((kp+1)\frac{\pi}{s} - \left(k+\frac{1}{p}\right)\omega_s t\right) \\
& + \sin\left((kp+1)\frac{7\pi}{s} - \left(k+\frac{1}{p}\right)\omega_s t\right) + \sin\left((kp+1)\frac{13\pi}{s} - \left(k+\frac{1}{p}\right)\omega_s t\right) \Bigg) \Bigg) \\
& + \ldots + \eta \sum_{k\,odd}^{\infty} \mathscr{F}_{PM,k} \Bigg(\sin\left((kp-6)\frac{\pi}{s}\right) \cdot \Bigg(\sin\left((kp-6)\frac{\pi}{s} - \left(k-\frac{6}{p}\right)\omega_s t\right) \\
& + \sin\left((kp-6)\frac{7\pi}{s} - \left(k-\frac{6}{p}\right)\omega_s t\right) + \sin\left((kp-6)\frac{13\pi}{s} - \left(k-\frac{6}{p}\right)\omega_s t\right) \Bigg) \\
& + \sin\left((kp+6)\frac{\pi}{s}\right) \cdot \Bigg(\sin\left((kp+6)\frac{\pi}{s} - \left(k+\frac{6}{p}\right)\omega_s t\right) \\
& + \sin\left((kp+6)\frac{7\pi}{s} - \left(k+\frac{6}{p}\right)\omega_s t\right) + \sin\left((kp+6)\frac{13\pi}{s} - \left(k+\frac{6}{p}\right)\omega_s t\right) \Bigg) \Bigg) \Bigg\}.
\end{aligned} \tag{5.15}$$

To explain the derivation of the above equations, the voltage time functions of the coils obtained by (5.13), are added. The tested machine has 9 concentrated, non-overlapping coils. As it is a 3-phase machine, 3 coils belong to each phase which are in series, thus, to obtain the phase voltage their instantaneous values should be added. Hence, for $l = 1$, $l = 4$ and $l = 7$. In addition, the first term of (5.15) expresses the voltage under healthy conditions, while the others generated harmonic components due to the dynamic eccentricity fault.

5.1.4 Definition of the Fault Signature Block Binary Array (FSBBA)

In this sub-section, the Fault Signature Block Binary Array ($FSBBA$) is defined, along with the iterative process of the algorithm. Every cell of this array is another array in which the cells are either zeros or ones. The $FSBBA$ matrix is then defined as

$$FSBBA = \begin{bmatrix} A^1_{p,2} \\ A^2_{p,2} \\ \vdots \\ A^N_{p,2} \end{bmatrix} \tag{5.16}$$

where N is the number of rows and expresses the terminal value of the odd k in the model, e.g., $k = 1,\ 3,\ 5,\ \ldots,\ N$. $A^1_{p,2}, A^2_{p,2}, \ldots, A^N_{p,2}$ is the element-arrays of the block matrix. The matrix $A^k_{p,2}$ is constructed using the trigonometric terms of (5.15) as a $p_{\times}2$-sized matrix. Each cell of this matrix contains the summed terms of the phase voltage referred to a specific frequency signature side-band extracted by (5.15) along with a trigonometric term which depends on the coil and pole number. It is defined in the following array format

$$A^k_{p,2} = \begin{bmatrix} A^k_{1,1} & A^k_{1,2} \\ A^k_{2,1} & A^k_{2,2} \\ A^k_{3,1} & A^k_{3,2} \\ A^k_{4,1} & A^k_{4,2} \\ A^k_{5,1} & A^k_{5,2} \\ A^k_{6,1} & A^k_{6,2} \end{bmatrix} \tag{5.17}$$

where p is the number of pole pairs and each element of the block is given by

$$A_{i,j}^{k}=\begin{cases}\sin\left((kp-i)\frac{\pi}{s}\right)\left\{\sin\left((kp-i)\frac{\pi}{s}-\left(k-\frac{i}{p}\right)\omega_s t\right)\right.\\ +\sin\left((kp-i)\frac{7\pi}{s}-\left(k-\frac{i}{p}\right)\omega_s t\right)+\sin\left((kp-i)\frac{13\pi}{s}-\left(k-\frac{i}{p}\right)\omega_s t\right),\\ if\ i=j=1\ or\ i>j\\ \sin\left((kp+j)\frac{\pi}{s}\right)\left\{\sin\left((kp+j)\frac{\pi}{s}-\left(k+\frac{j}{p}\right)\omega_s t\right)\right.\\ +\sin\left((kp+j)\frac{7\pi}{s}-\left(k+\frac{j}{p}\right)\omega_s t\right)+\sin\left((kp+j)\frac{13\pi}{s}-\left(k+\frac{j}{p}\right)\omega_s t\right),\\ if\ i=j>1\ or\ i<j\end{cases} \tag{5.18}$$

By substituting the number of slots and poles in (5.15) the cells of the arrays of the matrix $A_{p,2}^{k}$ negate for specific orders k. More specifically, some negations occur due to the cancellation caused by the summation of trigonometric terms. Otherwise, it may become zero because of the trigonometric function, which multiplies the sums. Each position in the array $A_{p,2}^{k}$ expresses a specific frequency side-band component.

Specifically, element $A_{3,2}^{3}$ expresses the 3$^{\text{rd}}$ right side-band of the fundamental harmonic component. The test-machine is harmonic with order 1.5. The element $A_{5,1}^{5}$ expresses the left-hand-side band of the 5$^{\text{th}}$ harmonic component. Lastly, the element $A_{6,1}^{3}$ expresses the left-hand-side band of the 3$^{\text{rd}}$ harmonic, and since the number of rows is equal to the pole-pair number, the harmonic is the 2$_{\text{nd}}$, which is even. As a result, the cells carrying nonzero values after the substitution are the harmonics of the phase voltage, which are excited under the dynamic eccentricity fault.

The Taylor–Maclaurin expansion was developed up to 6$^{\text{th}}$ order because the test machine has 6 pole pairs. The latter covers the scenario of the slot-pole combination so that only signatures of even order rise. For instance, in a 12 slot – 4 pole-pair PM machine, the excited fault signatures will be the 2$^{\text{nd}}$, 4$^{\text{th}}$, 6$^{\text{th}}$, 8$^{\text{th}}$, etc. The even harmonics generated are a consequence of some coil and pole combinations, the signature side-bands being identified with the even harmonics, which are nonexistent in healthy machines with balanced stator winding. Considering the above, the expansion must always be developed up to p$^{\text{th}}$ to cover those scenarios and provide reliable MCSA–based monitoring.

The algorithm computes the $FSBBA$ matrix using the following method, the value N is provided by the user, which determines the number of iterations to be carried out by the algorithm will or, differently said, the number of the $A_{p,2}^{k}$ matrices to be determined. The size of $A_{p,2}^{k}$ is $p_{\times}2$ and in each cell there are $s/3$ summed terms which define the mathematically proven pattern in (5.15). The array for the specific test machine is given by (5.19). The binary values of array-equation (5.19) are calculated using the equations (5.16), (5.17) and (5.18). The block $A_{p,2}^{k}$ is, in turn, computed by substituting the coil number and the pole-pair number for the specific k-

iteration. Two nested-repetition loops are then implemented to examine each cell of the block $A^k_{p,2}$. An if–type condition is used to determine whether an element is zero or nonzero for each repetition. By applying the algorithm for the 3 – phase 9 coil – 6 pole-pair Axial-Flux Permanent-Magnet machine, the $FSBBA$ after running the algorithm for $N = 3$, becomes

$$FSBBA = \begin{bmatrix} \begin{bmatrix} 0_{0.83} & 0_{1.16} \\ 0_{0.66} & 0_{1.33} \\ 1_{0.5} & 0_{1.5} \\ 0_{0.33} & 0_{1.66} \\ 0_{0.16} & 0_{1.83} \\ 0_{0} & 1_{2} \end{bmatrix} \\ \begin{bmatrix} 0_{2.83} & 0_{3.16} \\ 0_{2.66} & 0_{3.33} \\ 1_{2.5} & 1_{3.5} \\ 0_{2.33} & 0_{3.66} \\ 0_{2.16} & 0_{3.83} \\ 1_{2} & 1_{4} \end{bmatrix} \\ \begin{bmatrix} 0_{4.83} & 0_{5.16} \\ 0_{4.66} & 0_{5.33} \\ 0_{4.5} & 1_{5.5} \\ 0_{4.33} & 0_{5.66} \\ 0_{4.16} & 0_{5.83} \\ 1_{4} & 0_{6} \end{bmatrix} \end{bmatrix}, \tag{5.19}$$

where each element's position expresses the order of each harmonic. The subscript denotes the order of the harmonic. The nonzero elements are the fault signatures that will be excited for the specific machine when the dynamic eccentricity fault occurs.

If the cell is nonzero, it is set to 1, otherwise is set to 0. When the nested loop repetition terminates, the value of block is assigned on the k^{th} row of the block vector-matrix $FSBBA$. After the N repetitions finish, the $FSBBA$ matrix is computed, and the positions of the cells of each block are printed on the user interface screen. Using this information, someone may predict the fault signature frequency side-band components before the MCSA instrumentation is installed on the machine. In Figure 5.2, the process of the flow-chart is illustrated to show how the array with the fault signatures is extracted.

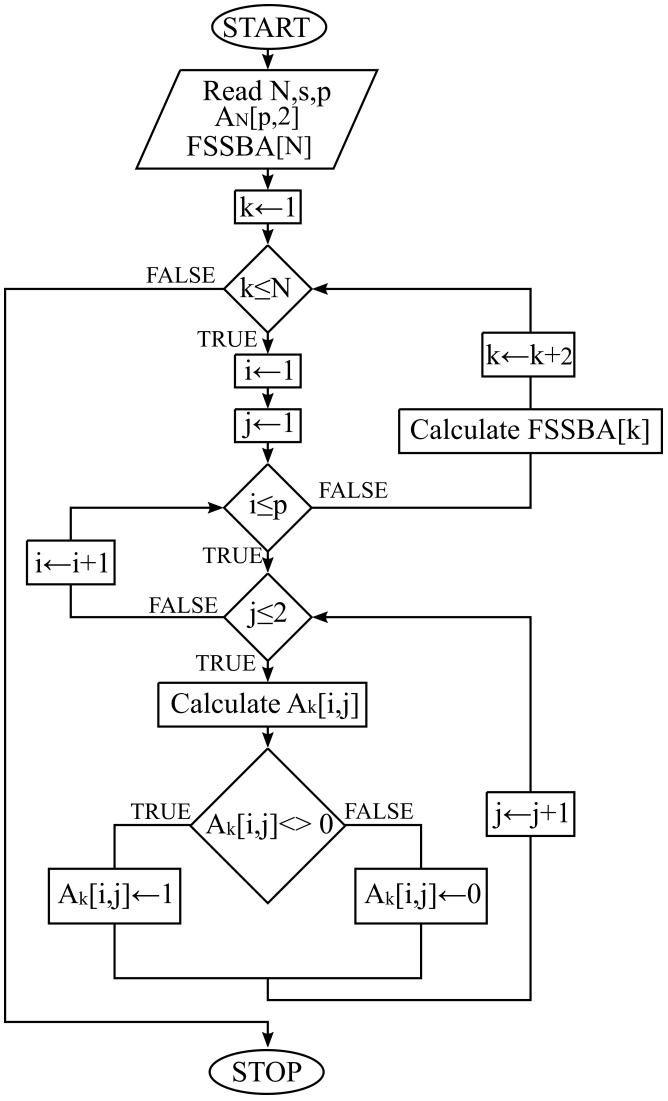

Figure 5.2: Flow-chart of the developed algorithm.

Lastly, since the pattern for a specific machine is revealed, it is feasible to define a fault index (FI) which increases in magnitude as the fault severity increases. Generally, a FI should be approximately proportional and adequately sensitive to the fault severity. Furthermore, even harmonics are ignored for the monitoring of the test machine. Even harmonics should only be considered in the fault for the cases when the algorithm does not suggest fractional-pole-related harmonic components. Both fractional and even harmonic components are presented on the harmonic index, the even ones only rise due to the asymmetry caused by the dynamic eccentricity. The voltage components in the time-domain, which are related to the fault according to (5.19), are the following

$$V_{DE}(t) = \hat{V}_{0.5}\sin(0.5\omega_s t + \phi_{0.5}) + \hat{V}_{2.5}\sin(2.5\omega_s t + \phi_{2.5}) + \hat{V}_{3.5}\sin(3.5\omega_s t + \phi_{3.5}) \quad (5.20)$$

where $\hat{V}_x$ and ϕ_x express the amplitude and phase of the x^{th} harmonic component. A fault index can be defined, which uses the root-mean-square (RMS) value of (5.20) which is more sensitive than monitoring each harmonic since the test machine is air-cored. Equation (5.20) was generated by the ones of the (5.19), so it is about the harmonic components caused by the fault. As a result, the FI is defined as follows

$$FI = \sqrt{\left(\frac{\hat{V}_{0.5}}{\sqrt{2}}\right)^2 + \left(\frac{\hat{V}_{2.5}}{\sqrt{2}}\right)^2 + \left(\frac{\hat{V}_{3.5}}{\sqrt{2}}\right)^2} \quad (5.21)$$

According to (5.19) more harmonic signatures can be used, though the amplitude of each harmonic is inversely proportional to the harmonic order number. Thereby, increasing the harmonic order decreases the excitation of the fault harmonic. Equation (5.21) is suggested to monitor the dynamic eccentricity fault under low sensitivity.

5.2 Validation of the algorithm by means of 3-D Finite-Element Analysis

In this section, the test machine is modelled using 3-D FEA software named Simcenter MagNet by Siemens digital industries. Axial-flux machines, unlike radial-flux machines, can only be modelled reliably using 3-D Computer-Aided-Design or CAD, since the scalar and vector magnetic potentials vary in all directions. Another advantage of the 3-D simulations is that the stator-end winding fields are accounted for in the field solution. Hence, this modelling method is considered the most accurate, with the disadvantage that it is time-consuming and occasionally non-convergent due to the high complexity of the volume mesh grid. In Figure 5.3, the solid model of the machine is illustrated and in Table 5.1 its specifications. Solving the model using the transient with motion analysis means the phase quantities in the time domain are obtained. A Fast-Fourier Transform (FFT) algorithm is then used to calculate the frequency spectra for the stationary signals.

Table 5.1: Specifications of the Axial-Flux PM Machine

Parameter	Value
Apparent power [kVA]	0.5
Number of coils-s	6
Number of pole-pairs	6
Rotational speed [r/min]	500
Magnet remanence (20^o C) [T]	1.35
Magnet-coil clearance [mm]	2
Number of turns per phase	48
Wire diameter [mm]	1.18
Winding connection	Y
Inner/Outer magnet radius [mm]	40/70
Number of total harmonics used in the algorithm - N	3

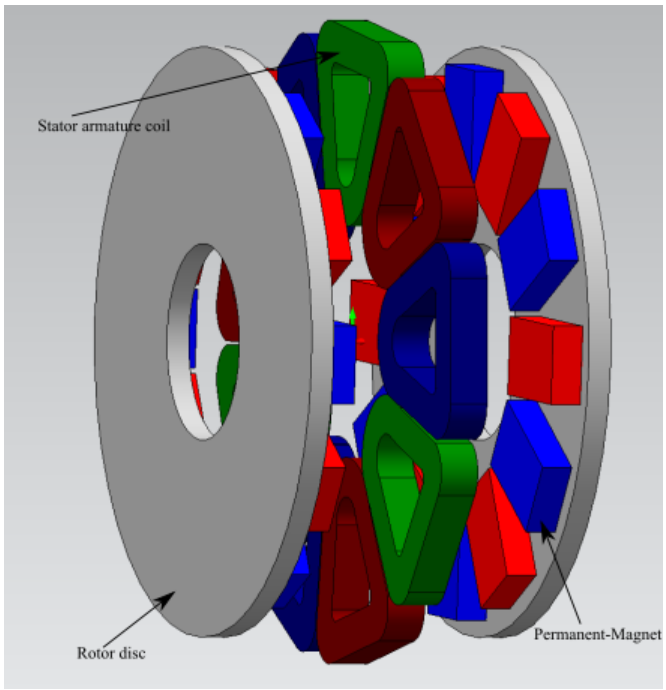

Figure 5.3: 3-D solid model of the test Axial-Flux Permanent-Magnet Synchronous Machine designed in FEA-based software.

In Figures 5.4a, 5.4b and 5.4c the spectra of the test machine are presented for 0%, 20% and 40% dynamic eccentricity, respectively. The dynamic eccentricity factors for the axial-flux machine are implemented using the mathematical model developed in [103]. The 3^{rd} harmonic is absent from the spectrum because the Y-connected stator winding cancels it. As the dynamic eccentricity factor (DEF) increases, the side-bands 0.5^{th}, 2.5^{th} and 3.5^{th} increase. The simulation results are consistent with the results produced by the algorithm. The even harmonic components must be the only harmonics whose magnitude rises when the fault occurs in order for them to be considered for the condition-monitoring of the machine. In other cases, even harmonics are unreliable for monitoring rotor faults since they are associated with various abnormal conditions. Table 5.2 presents the amplitudes of the signatures predicted by the 3-D FEA. All amplitudes are normalized to the fundamental component. The FI has also been calculated and displayed on the last row of Table 5.2. The time-step of the simulation was 0.25 [msec], the total number of nodes was 145.209, edges 448.018, faces 308.778, and the total number of tetrahedra was 5.920. A high signal length was used for the FFT algorithm. The latter aims to obtain accurate magnitude estimation of each harmonic. Lastly the signal was also multiplied by a hamming window.

Table 5.2: Fault Signatures and FI Obtained by 3-D FEA

Harmonic order	0%DE	20%DE	40%DE
0.5	-82.8 dB	-74.6 dB	-72.4 dB
2.5	-87.5 dB	-78.7 dB	-73.7 dB
3.5	-93.2 dB	-77 dB	-70 dB
$FI/FI_{0\%DE}$	1	3.19	5.44

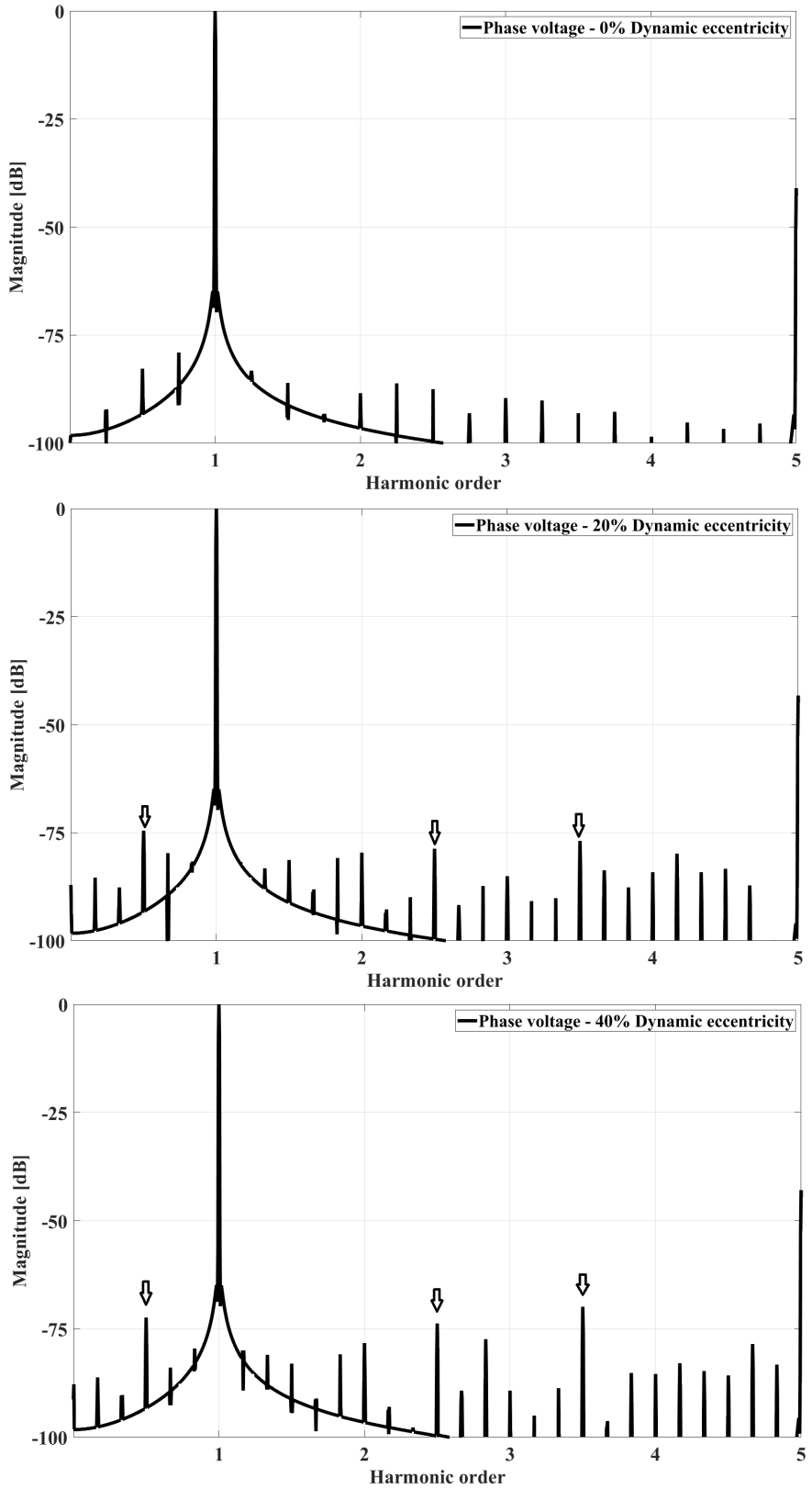

Figure 5.4: 3-D FEA results of the phase voltage amplitude-spectrum for the test machine under 0% (top), 20% (middle), and 40% (bottom) dynamic eccentricity.

5.3 Validation of the algorithm by means of experimental testing

For experimental validation purposes, a test rig was built along with a layout to vary the dynamic eccentricity factor for the test machine. The axial-flux PM machine used in this paper is designed for micro-wind energy harvesting applications for operation under high loads. Thus, the wire diameter of the coils is high; hence the number of turns is low for the given coil volume. In Figure 5.5 and 5.6, the experimental layout is illustrated, which consists of an inverter-fed 3-phase induction motor which is the prime mover of the 3-phase axial-flux PM generator. A 3-phase, Y-connected resistive load, is fed by the generator. The characteristics of the voltage probes are TESTEC TT-LF 312 with 1:1 scaling, attenuation ratio x1, input impedance 47 pF, bandwidth 15 MHz, rise time 24 nsec, and compensation range 10-60 pF. To sample the data a channel of the data-acquisition system is occupied. This commercial equipment can also perform automated real-time spectral signal processing for a fixed signal length. The phase voltage is measured using voltage probes on the terminals of one resistor with the common point. The sampling frequency for the experiment was chosen at 20 kHz. In this case, the time-domain signal is sent to the computer, and a Fast-Fourier Transform (FFT) algorithm on MATLAB is employed to obtain the spectra. Table 5.3 shows the magnitudes of the algorithm signatures obtained by experimental measurements.

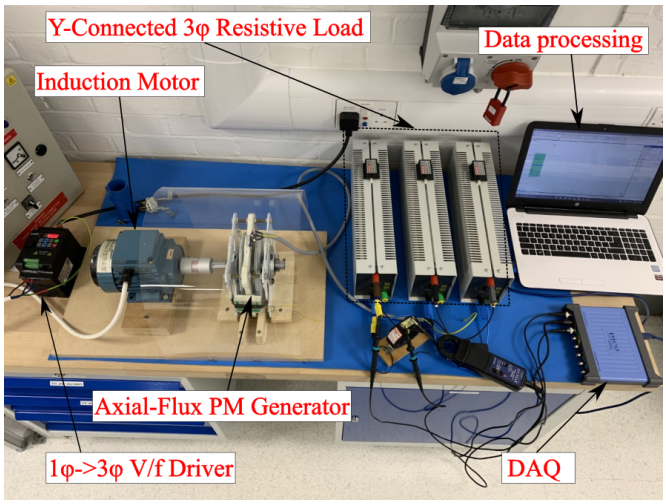

Figure 5.5: 3-D solid model of the test Axial-Flux Permanent-Magnet Synchronous Machine designed in FEA-based software.

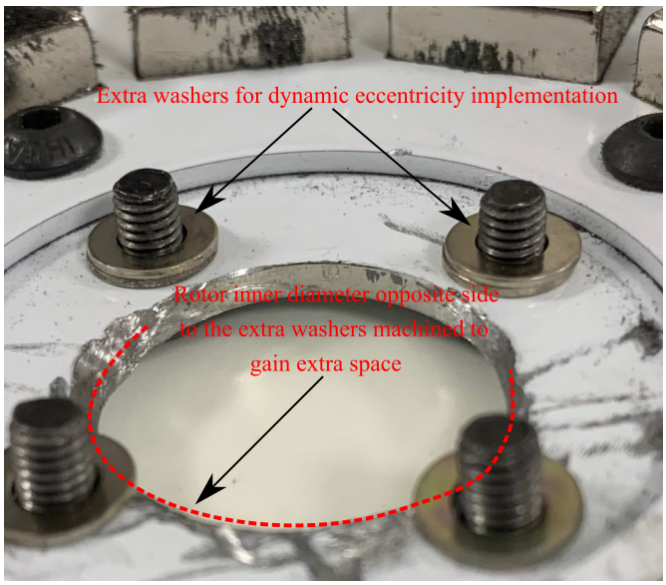

Figure 5.6: 3-D solid model of the test Axial-Flux Permanent-Magnet Synchronous Machine designed in FEA-based software.

In Fig. 5.7a, 5.7b and 5.7c the spectra for 0%, 10% and 20% are presented. By inspection, under the healthy condition, there are pole-pair-related harmonics, which are caused by inherent asymmetries of the generator. The inverter-fed induction motor also transmits harmonics through mechanical coupling, but they are high in frequency,

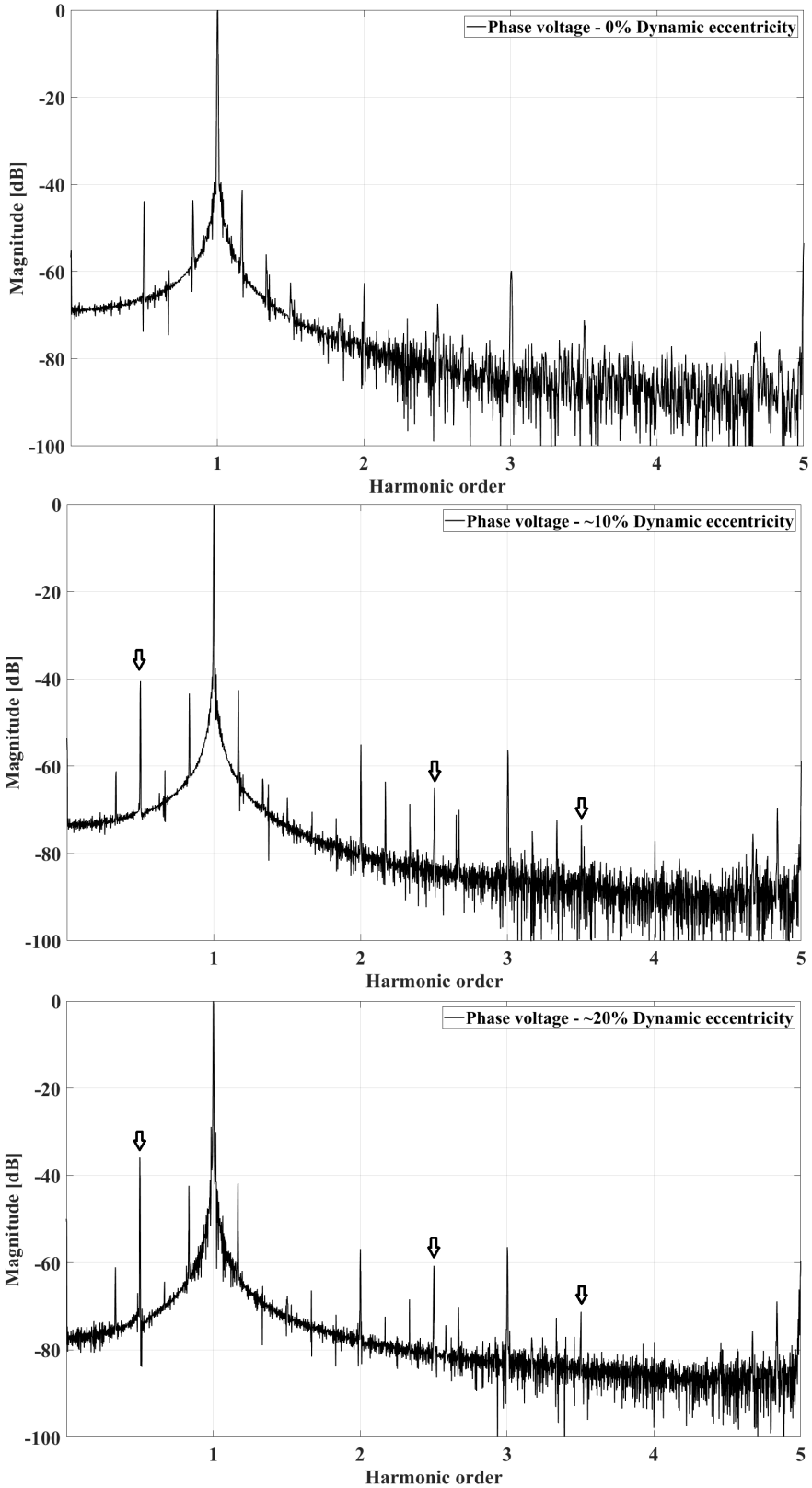

Figure 5.7: Experimental phase voltage amplitude-spectrum for 0% (top), 10% (middle), and 20% (bottom) dynamic eccentricity for 50 Hz drive and load 8 Ω per phase.

so they do not interact with the signatures. The experiment shows that real-time signal processing is necessary as these harmonics are pre-existent in the healthy machine. The aid of the algorithm is also shown by the pre-existent side-bands of $1-1/p$ and $1+1/p$. An inspector would easily assume that these harmonics are dynamic eccentricity related and bring the machine offline to send it to the motor shop for repair, interrupting production. The important aspect, though, is that the harmonics which are excited as the dynamic eccentricity factor increases are per the ones obtained by the proposed algorithm and the $FSBBA$ of (5.19), while the proposed FI is fault-severity sensitive.

Table 5.3: Fault Signatures and FI Obtained by Experimental Measurements

Harmonic order	0%DE	10%DE	20%DE
0.5	-43.9 dB	-40.5 dB	-35.9 dB
2.5	-67.4 dB	-65 dB	-60.7 dB
3.5	-71 dB	-73.6 dB	-71.3 dB
$FI/FI_{0\%DE}$	1	1.48	2.51

5.4 Further Discussion and Comments

This section presents the sequence of actions in the form of steps to show how the algorithm can be utilized for monitoring industrial PM machines. This fault was studied for the case where the two rotor discs are inclined to the same angle for severity purposes. If the two minimum air gaps have 180^o degrees phase difference, no harmonic components are induced on the stator winding since the air gap remains uniform [111]. Most 3-phase inverters are driven using Sinusoidal-Pulse-Width-Modulation (SPWM), leading to high-frequency harmonics on the output voltage of the inverter. The latter means that these harmonics do not interfere with the ones produced by the dynamic eccentricity fault. Also, the slot-harmonics of an induction motor appear in high frequencies [112] compared to the harmonics induced by dynamic eccentricity. Receiving into full consideration everything said above, the following steps that should be done for reliable monitoring.

1. Run the algorithm for a specific permanent-magnet machine and obtain the Fault Signature Block Binary Array $(FSBBA)$.
2. Install the MCSA instrumentation in the machine and mark the amplitudes of the phase voltage or current for the healthy machine.
3. Normalize the amplitude-spectrum of the monitored quantity to the fundamental harmonic component. The latter happens for the case where only the separated harmonic components are about to be monitored.

4. Instead of step 3), if the normalization is avoided, then the amplitudes should be converted to [V] or [A], and the FI of (5.19) should be employed with reference to the $FI_{0\%DE}$.
5. If the harmonic components given by the $(FSBBA)$ start to increase, it means that the dynamic eccentricity factor (DEF) is also increasing.
6. A machine can tolerate eccentricity until a relatively high degree - up to 50-60%, [13] especially if it is air-cored since no Unbalanced Magnetic Pull (UMP) is created. As a result, when the harmonics obtained by the algorithm for the specific machine are the 0.5^{th}, 2.5^{th} and 3.5^{th} or the normalized FI of (5.21) rises above a threshold. The latter implies that the machine has a high dynamic eccentricity and should be put offline and sent to the motor shop for inspection and repair if necessary.

5.5 Summary and conclusions of the method

An algorithm is proposed in this paper, which facilitates the prediction of the fault signature harmonic content in PM machines with concentrated, non-overlapping winding under dynamic eccentricity for any number of coils and poles. The general eccentricity formula shows that the generated harmonics are of the pattern $(1 \pm k/p)fs$. However, this chapter proves that both coil and pole numbers influence the fault generation mechanism. Furthermore, since the experimental harmonic spectrum contains many harmonics generated for various reasons, the proposed algorithm can predict which exact harmonics are generated due to the studied fault. The harmonic signatures proposed by the algorithm agree with the ones obtained by 3-D FEA and the developed experimental rig. The proposed algorithm increases the reliability of the MCSA, a popular industry-utilized condition-monitoring method. Furthermore, the computational time using the proposed algorithm is significantly smaller than the numerical simulation, which demands the machine to be designed and solved. The work described in [113], which proposes a formula to extract the harmonic signatures in permanent-magnet machines under partial demagnetization, showed that the harmonics generated in the two faults are similar. However, the amplitude variation is completely different in each case, as in partial demagnetization, even a low fault severity can create harmonic components with significant amplitude.

PART III

Magnetic field computation in radial-flux permanent-magnet machines

Chapter 6

Analytical calculation of magnetic field distribution in permanent-magnet machines

6.1 Introduction

This chapter proposes an on-load subdomain model-based magnetic field computation algorithm for the two common permanent-magnet synchronous machine rotor topologies, the surface-mounted and -the inset. Analytical models offer faster computation of the machines's quantities and parameterization for the preliminary process of the machine design. Furthermore, they offer a physical insight on how the dimensions and material properties affect the distribution of the machine's signals. Each part of the machine is divided into a region, the governing partial differential equations are solved, and the magnetic vector potential is used. The components of the magnetic field distribution can be obtained. The method proposes a new way of modelling the permanent-magnet excitation using Heaviside functions difference. The magnetization distribution patterns considered are the radial, parallel and Halbach. The analytical solution calculates the back-EMF and each type of torque, i.e. cogging, static and electromagnetic. Finite-Element analysis simulations of 12 slot - 4 pole permanent-magnet synchronous motors were used to validate the results extracted by the analytical model.

6.1.1 Surface-mounted permanent-magnet machine topology

The building blocks of the magnetic field are the magnetic scalar and vector potentials. Both physical quantities have similar properties, with the vector potential having the advantage that it can model a region with current density. The latter happens since the curl of the gradient of the scalar potential is always zero, so it can never be equal to the current density, i.e. $\nabla \times (\nabla \phi) = 0 \neq J$. Another method is to insert the magnetization function in the PDE and

solve it using an analytical technique, as was done in [114] for PM machines with surface-inset magnets. Furthermore, with knowledge of the magnetic field distribution components for every position, the cogging-torque, back-emf, and electromagnetic torque can be calculated [115, 116], stator iron losses [117, 24] and the slot leakage field and inductance [118, 119].

6.1.2 Surface-inset permanent-magnet machine topology

Surface-inset permanent-magnet motor technology has a higher power/torque density than the topology with the surface-mounted magnets because it has more soft magnetic material and an additional torque component, i.e., reluctance torque [120]. Reluctance torque is created due to the tendency of the protruding iron material in the rotor to align with the stator's rotating magnetic field. This type of torque plays a decisive role in designing these kinds of motors since it significantly deforms the torque-angle delta characteristic significantly [114].

Several models have been developed to calculate the magnetic field distribution and other quantities on machines with surface-inset permanent-magnets [121, 122, 123, 114, 115, 120, 124, 125, 126, 127], which most of them use Fourier series to model the excitation. The works mentioned above model surface-mounted permanent-magnet configurations [128, 129, 130, 16, 131, 132, 133, 116, 24, 134, 135] with the only difference that the components of the magnetic field intensity on the region where there isn't magnet material, vanishes. Other more general methods to evaluate the magnetic field distribution on permanent-magnet machines, semi- and analytical, are the magnetic equivalent circuit method [136], the concept of the magnetic charge [137] and conformal mapping [127, 135].

Based on this rotor design, various types of other topologies were developed, like the machine with spoke-type magnets [138], U-shaped interior magnets [139] and others. The goal was to increase and shape the magnetic flux density on the air gap for optimal mutual and reluctance torque production. Another developed technique to shape the air-gap magnetic flux density is magnet shaping like the sinusoidal-based ones [140].

6.2 Geometry of each topology

The analysis below considers a PM motor with overlapping windings and semi-closed slots with Q stator slots and P poles. The center angle of the ith magnet pole and jth stator slot and slot-opening is

$$\begin{cases} \theta_i = (i-1)\,\frac{2\pi}{P} + \theta_{0r},\ 1 \leq i \leq P \\ \theta_j = (j-1)\,\frac{2\pi}{Q} + \theta_{0s},\ 1 \leq j \leq Q. \end{cases} \tag{6.1}$$

where θ_{0r}, θ_{0s}, P, and Q are the initial angle of the rotor magnets and stator slots, number of magnet poles and number of stator slots, respectively.

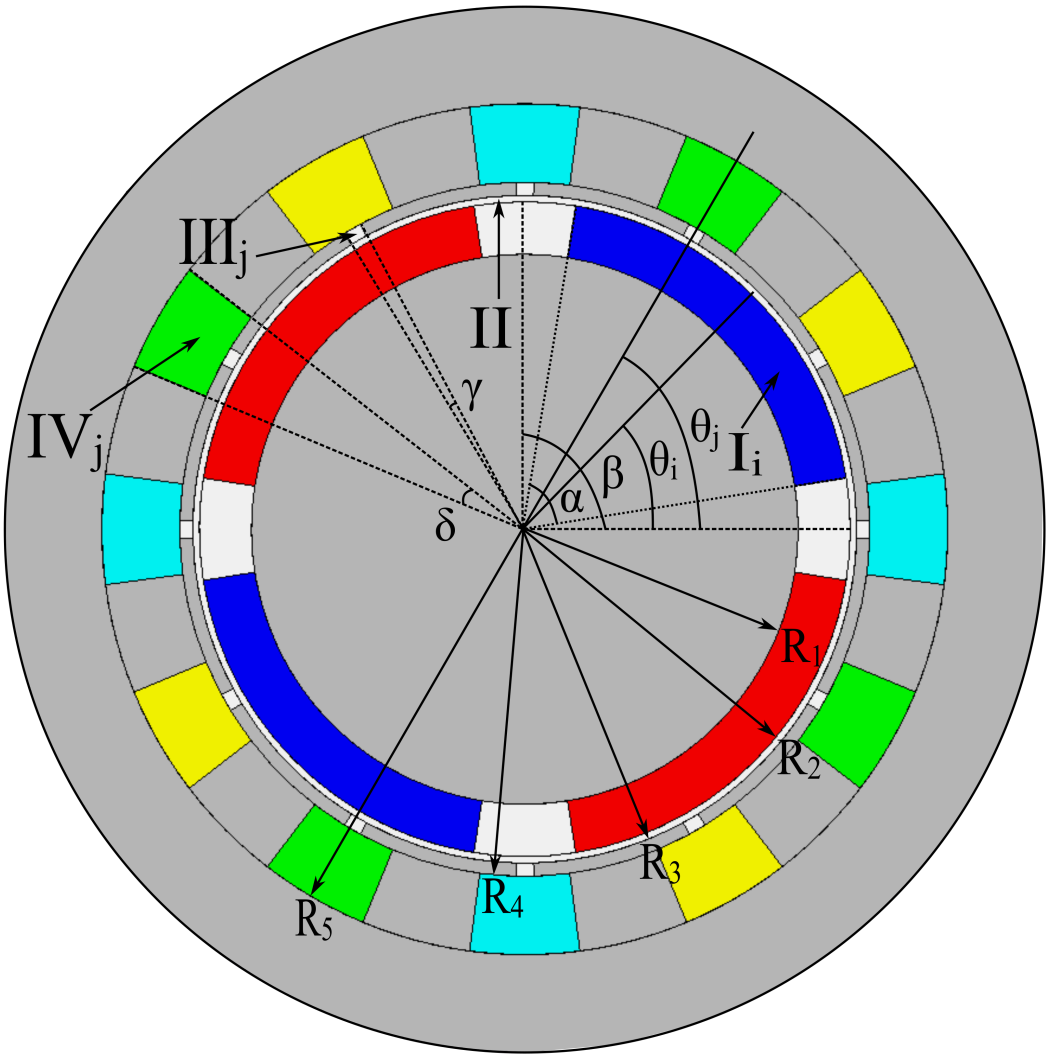

Figure 6.1: Geometric illustration of a 12 slot - 4 pole surface-mounted permanent-magnet machine with overlapping winding where each domain is defined.

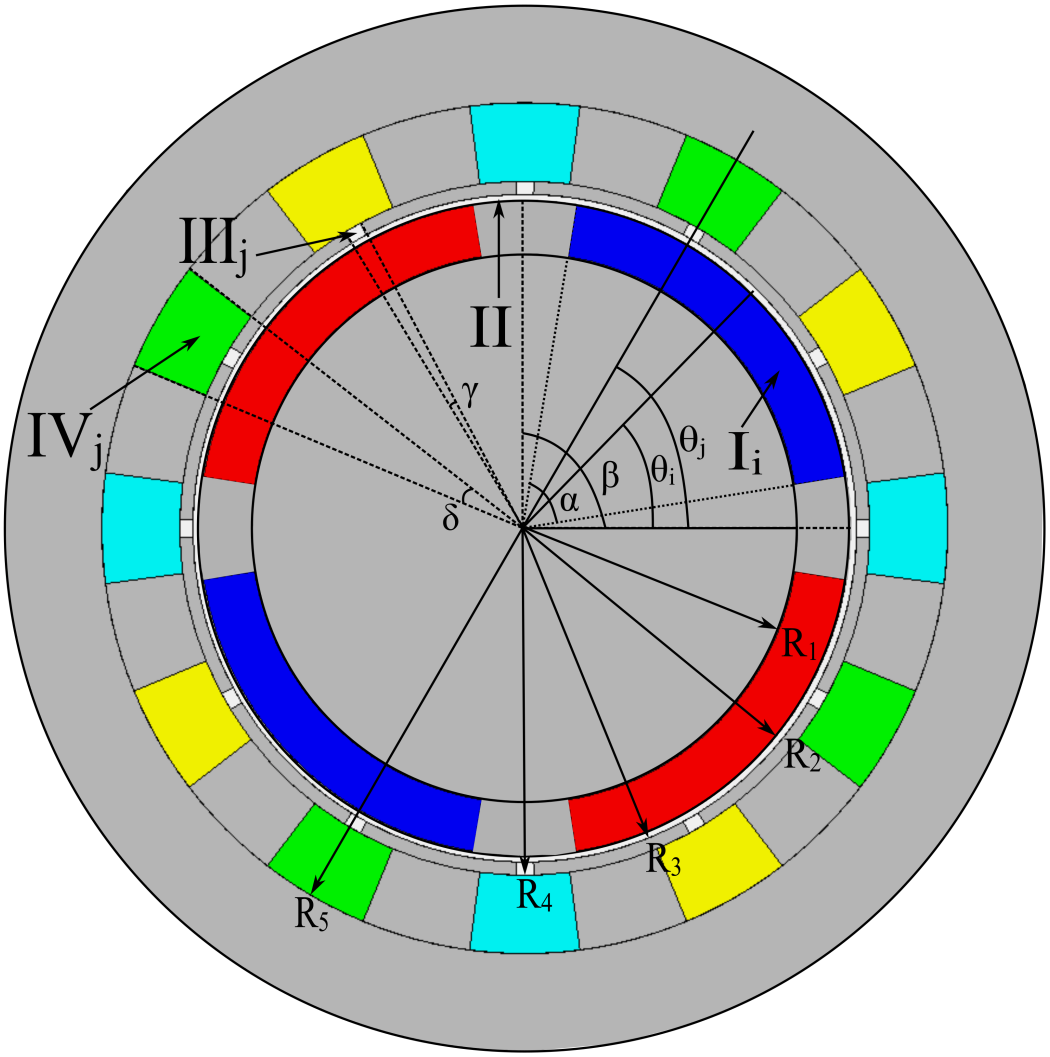

Figure 6.2: Geometric illustration of a 12 slot - 4 pole surface-inset permanent-magnet machine with overlapping winding where each domain is defined.

Table 6.1: Specifications of the *PM* Machine

Parameter	Value
$B_{rem}\ (T)$	1.0
μ_r	1.0
$J_z\ (A/mm^2)$	1.0
P	4
Q	12
α_p	0.8
α (°)	72
β (°)	90
γ (°)	3
δ (°)	15
$R_1/R_2/R_3/R_4/R_5/R_e\ (mm)$	42/50/51/53/65/50.5
$\omega_m\ (rad/sec)$	$2\pi 1500/60$

The simplifications made to extract the analytical solution are the following:

- End winding effects are neglected.
- Stator and rotor iron cores are infinitely permeable.
- All components have regular boundaries.
- The vector potential is invariant along the axial direction.
- There is no saturation effect on the iron.
- The whole Region I_i has recoil permeability μ_r.
- All regions have regular boundaries.
- The magnetic characteristic of the permanent-magnets is forced to be linear for the pre-specified temperature.

According to Figures 6.1 and 6.2, the considered regions are I_i, where $i = 1,2,..,P$ for the i^{th} magnet subdomain, II for the air-gap subdomain, III_j and IV_j, where $j = 1,2,..,Q$ for the slot-opening and slot subdomains. α, β, γ, δ are the angles of the magnet, pole pitch, slot-opening and slot, respectively. The radial dimensions are R_1, R_2, R_3, R_4, R_5, and they express the radius of the back iron, the magnet, the air-gap, the slot-opening and slot regions. The middle of the air-gap value is $R_e = (R_2 + R_3)/2$.

6.3 Magnetic vector potential, field intensity and flux density

This section offers the closed-form solution for each subdomain and the steps taken to extract it. In the PMs (Region I_i), the normal component of the magnetic flux density is the radial; hence the magnetic vector potential has only an axial component. In the slots, the current density is in the axial direction, so the same applies to the magnetic vector potential since it follows the current direction. The magneto-static Maxwell's equation, which correlates the curl of the magnetic field intensity with a current in space, is

$$\nabla \times \overrightarrow{H} = \overrightarrow{J}, \tag{6.2}$$

where $\overrightarrow{H}$ and $\overrightarrow{J}$ are the magnetic field intensity and current density vector functions, respectively. Furthermore, since the magnetic flux density lines are always closed, the magnetic flux density vector is a divergence-free function

$$\nabla \cdot \overrightarrow{B} = 0, \tag{6.3}$$

where the magnetic $\overrightarrow{B}$ is the magnetic flux density vector function. Since (6.3) applies always, there is a vector function in which its curl is equal to the magnetic flux density

$$\overrightarrow{B} = \nabla \times \overrightarrow{A}, \tag{6.4}$$

where $\overrightarrow{A}$ is the magnetic vector potential function. The magnetic flux density vector has the following two components in polar coordinates is

$$\overrightarrow{B} = B_r \hat{e}_r + B_\theta \hat{e}_\theta, \tag{6.5}$$

where B_r and B_θ, are the radial and circumferential component of the magneitic flux density functions, respectively. Accounting (6.4) and (6.5), it is concluded that the magnetic vector potential has only an axial component and that each component is equal with

$$B_r = \frac{1}{r}\frac{\partial A}{\partial \theta} \quad B_\theta = -\frac{\partial A}{\partial r}. \tag{6.6}$$

In permanent-magnet materials, the magnetic flux density is affected by the way the material is magnetized, so the following equation applies

$$\overrightarrow{B} = \mu_0 \mu_r \overrightarrow{H} + \mu_0 \overrightarrow{M}. \tag{6.7}$$

By substituting (6.4) into (6.7) for the magnetic field intensity, and then substituting the emerged equation to (6.2) and by applying the following vector calculus identity

$$\nabla \times \left(\nabla \times \overrightarrow{A} \right) = \nabla \cdot \left(\nabla \cdot \overrightarrow{A} \right) - \nabla^2 \cdot \overrightarrow{A}, \tag{6.8}$$

the first term of the second part of (6.9) can be considered equal to zero since the gradient of a number is always zero. After the deeds, the final PDE is

$$\nabla^2 \cdot \overrightarrow{A} = -\mu_0 \mu_r \overrightarrow{J} - \mu_0 \nabla \times \overrightarrow{M}. \tag{6.9}$$

Equation (6.9) declares that Laplace's PDE (Partial Differential Equation) applies in spaces where there are no excitation terms, i.e. permanent magnets or carrying current conductors. When at least one source exists, then (6.9) expresses Poisson's PDE. The magnet region depends also on the way that material is magnetized. The Laplacian of the magnetic vector potential can either equal zero or not. Furthermore, in the slots of electrical machines, a current flows through a direction on a surface, so a current density exists, which makes the second part of (6.9) nonzero. Considering that the magnetic vector potential has only a z-component, the magnetization vector function is written as

$$\overrightarrow{M}(r, \theta) = M_r \hat{e}_r + M_\theta \hat{e}_\theta, \tag{6.10}$$

where M_r and M_θ are the radial and circumferential component of the magnetization vector function. Since the magnetic vector potential function is expressed in polar coordinates and has only an axial component, the first term of (6.9) is equal to

$$\nabla^2 \cdot A_z = \frac{\partial^2 A_z}{\partial r^2} + \frac{1}{r}\frac{\partial A_z}{\partial r} + \frac{1}{r^2}\frac{\partial^2 A_z}{\partial \theta^2}. \tag{6.11}$$

The second term of the second part of (6.9) accounting (6.10) can be written as

$$\nabla \times \overrightarrow{M} = \frac{\partial M_\theta}{\partial r} + \frac{1}{r} M_\theta - \frac{1}{r}\frac{\partial M_r}{\partial \theta}. \tag{6.12}$$

6.4 Modeling the magnetization distribution patterns

The three basic magnetization patterns used in permanent-magnet machines are radial, parallel and Halbach. In radial magnetization, the magnet has a constant magnetization along its periphery. The latter occurs as all the vectors follow the direction of the radial coordinate. In parallel magnetization, all the vectors are vertical to the magnet, so the normal component of the magnetic flux density starts to drop as the vectors move away from the centre of

the magnet. As the number of magnets in the machine increases, the parallel magnetization converges to the radial. In Halbach magnetization, the vector is oriented appropriately along the magnet's periphery, such that it will be maximum on the centre and zero on the lateral sides of the magnet.

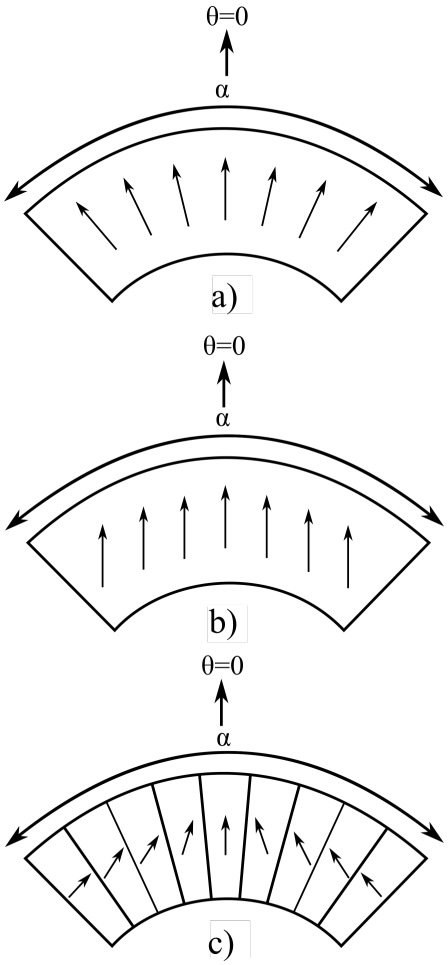

Figure 6.3: Magnetization distribution vectors along the periphery of a magnet for the case of a) radial, b) parallel, and c) Halbach magnetization.

Figure 6.3 illustrates how each magnetization pattern is distributed along the magnet's periphery. Then the vectors of each magnetization pattern are analyzed into two components, radial and tangential. The two components of the magnetization function for each distribution pattern are presented in Figure 6.4. As explained at the beginning of the chapter, the common ways to model the magnetization function is to substitute its components as a number [141], or expand the functions using the Fourier series and then substitute it to the PDE [129].

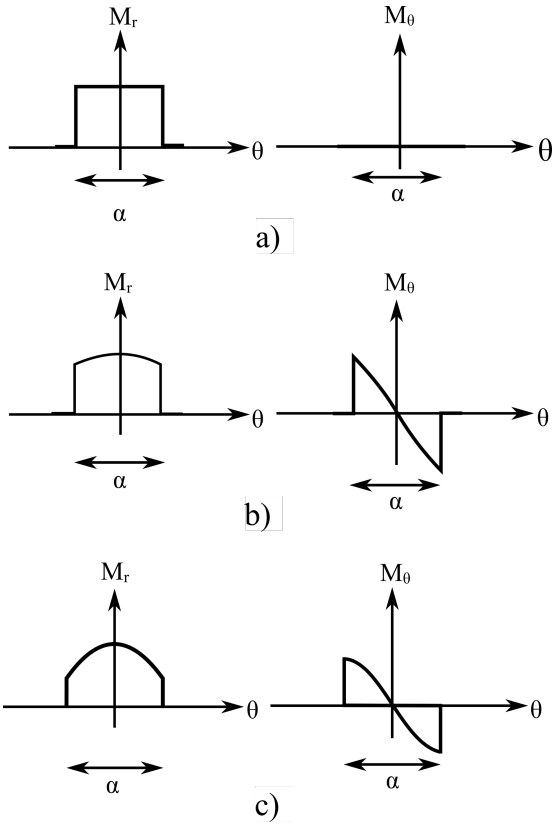

Figure 6.4: Functions of the radial and tangential component of the magnetization distribution for a) radial, b) parallel, and c) Halbach magnetization.

This part of the thesis presents a new way to model the magnetization function using the aid of Heaviside and delta functions. The idea is that the Heaviside function is employed to model a single pulse, and by multiplying the pulse by a function, it can be shaped for each magnetization function.

The magnetization for the interval where there is a magnet is modelled using the difference between two Heaviside functions. The Heaviside function is defined us

$$H(\theta) = \begin{cases} 1 & \text{for} \quad \theta \geq 0 \\ 0 & \text{for} \quad \theta < 0. \end{cases} \tag{6.13}$$

The delta function is defined as

$$\delta(\theta) = \begin{cases} 1 & \text{for} \quad \theta = 0 \\ 0 & \text{for} \quad \theta \neq 0. \end{cases} \tag{6.14}$$

The delta function is a Dirac function, with the only difference the nonzero point is equal with unity and not infinity. For the two functions, the following equality applies

$$\delta(\theta) = \frac{dH(\theta)}{d\theta}. \tag{6.15}$$

The derivative of the Heaviside function is the delta function. The latter happens because, for $\theta = 0$, the value of the Heaviside function changes rapidly to one, so the derivative will be nonzero at that point, and for the rest of the interval, its constant, so the derivative becomes zero. According to what was mentioned above, a rectangular pulse can be modelled using the following function

$$u_i(\theta) = H\left(\theta - \theta_i + \frac{\alpha}{2}\right) - H\left(\theta - \theta_i - \frac{\alpha}{2}\right), \tag{6.16}$$

where $u_i(\theta)$ is a pulse created by Heaviside functions, and if it is differentiated, the result is

$$v_i(\theta) = \delta\left(\theta - \theta_i + \frac{\alpha}{2}\right) - \delta\left(\theta - \theta_i - \frac{\alpha}{2}\right), \tag{6.17}$$

where $v_i(\theta)$ is the difference between two delta functions. The normal and tangential components for radial, parallel and Halbach magnetization are

$$M_r^{I_i}(\theta) = \begin{cases} \frac{(-1)^i B_{rem}}{\mu_0} u_i(\theta), \text{ radial} \\ \frac{(-1)^i B_{rem}}{\mu_0} \cos(\theta - \theta_i) u_i(\theta), \text{ parallel} \\ \frac{(-1)^i B_{rem}}{\mu_0} \cos\left(\alpha_p \frac{\pi}{\alpha}(\theta - \theta_i)\right) u_i(\theta), \text{ Halbach} \end{cases} \tag{6.18}$$

and

$$M_\theta^{I_i}(\theta) = \begin{cases} 0, \text{ radial} \\ -\frac{(-1)^i B_{rem}}{\mu_0} \sin(\theta - \theta_i) u_i(\theta), \text{ parallel} \\ -\frac{(-1)^i B_{rem}}{\mu_0} \sin\left(\alpha_p \frac{\pi}{\alpha}(\theta - \theta_i)\right) u_i(\theta), \text{ Halbach.} \end{cases} \tag{6.19}$$

The relation between the angles of Region I_i is

$$\begin{cases} \alpha = \alpha_p \frac{2\pi}{P} \\ \beta = \frac{2\pi}{P} \\ \alpha = \alpha_p \beta \end{cases}. \tag{6.20}$$

6.5 Solution of Poisson's in the magnet region

This section presents the solution of Poisson's equation for each magnetization excitation using eigenfunction expansions. By substituting (6.18) and (6.19) into (6.12), then into (6.9) and also taking into account that there are no conductivity currents i.e. $\overrightarrow{J} = 0$, the PDE for each magnetization distribution case is

$$\nabla^2 \cdot A_z^{I_i} = \begin{cases} \frac{(-1)^i B_{rem}}{r} v_i(\theta), \text{ radial} \\ \frac{(-1)^i B_{rem}}{r} \cos(\theta - \theta_i) v_i(\theta), \text{ parallel} \\ \frac{(-1)^i B_{rem}\left(1-\alpha_p \frac{\pi}{\alpha}\right)}{r} \sin\left(\alpha_p \frac{\pi}{\alpha}(\theta - \theta_i)\right) u_i(\theta) + \\ + \frac{(-1)^i B_{rem}}{r} \cos\left(\alpha_p \frac{\pi}{\alpha}(\theta - \theta_i)\right) v_i(\theta), \text{ Halbach} \end{cases} . \tag{6.21}$$

$$\text{with} \begin{cases} R_1 \leq r \leq R_2 \\ \begin{cases} \theta_i - \frac{\beta}{2} \leq \theta \leq \theta_i + \frac{\beta}{2}, \text{ Surface-mounted PM machine} \\ \theta_i - \frac{\alpha}{2} \leq \theta \leq \theta_i + \frac{\alpha}{2}, \text{ Surface-inset PM machine} \end{cases} \end{cases}$$

The solution of the above PDE (partial differential equation) offers the magnetic vector potential function in closed form for Region I_i, which is the i^{th} magnet pole. This region interfaces with the air gap, i. e. Region II.

6.5.1 Surface-mounted permanent-magnet machine - Region I_i

The normal component of the magnetic field intensity vanishes on the interface between the pole pitches. The parallel component of the perpendicular unit vector of the magnetic field intensity is continuous on the interface. According to Figure 6.1, the perpendicular unit vector on the lateral sides of each pole pitch has the tangential direction, meaning that the continuous magnetic field intensity component is normal or radial. However, the normal component of the field intensity is zero on that angle so

$$H_r^{I_i}\left(r, \theta_i - \frac{\beta}{2}\right) = 0 \quad H_r^{I_i}\left(r, \theta_i + \frac{\beta}{2}\right) = 0. \tag{6.22}$$

And according to (6.6) and (6.7), (6.22) can be written as

$$\left.\frac{\partial A_z^{I_i}}{\partial \theta}\right|_{\theta=\theta_i-\frac{\beta}{2}} = 0 \quad \left.\frac{\partial A_z^{I_i}}{\partial \theta}\right|_{\theta=\theta_i+\frac{\beta}{2}} = 0, \tag{6.23}$$

for each magnetization pattern. This happens because $u_i(\theta_i-\beta/2)=H(-\beta/2+\alpha/2)-H(-\beta/2-\alpha/2)=0-0=0$ and $u_i(\theta_i+\beta/2)=H(\beta/2+\alpha/2)-H(\beta/2-\alpha/2)=1-1=0$. Hence, the boundary conditions for the PDE are already homogeneous. The latter means no function is required to add up at the solution. Hence, the eigenfunctions of (6.21) are

$$\Theta_l^{I_i}(\theta)=\cos\left(\frac{l\pi}{\beta}\left(\theta-\theta_i+\frac{\beta}{2}\right)\right),\ l=1,2,\ldots,L. \tag{6.24}$$

According to the method of eigenfunction expansions [142, 143], the non-homogeneous terms for each magnetization pattern of (6.21) are written as an expansion based on the eigenfunctions (6.24) of the corresponding PDE, i.e.

$$\sum_{l=0}^{L} f_l^{I_i}(r)\cos\left(\frac{l\pi}{\beta}\left(\theta-\theta_i+\frac{\beta}{2}\right)\right)=\begin{cases}\frac{(-1)^i B_{rem}v_i(\theta)}{r},\ \text{radial}\\ \frac{(-1)^i B_{rem}\cos(\theta-\theta_i)v_i(\theta)}{r},\ \text{parallel}\\ \frac{(-1)^i B_{rem}\left(1-\alpha_p\frac{\pi}{\alpha}\right)\sin\left(\alpha_p\frac{\pi}{\alpha}(\theta-\theta_i)\right)u_i(\theta)}{r}+\\ +\frac{(-1)^i B_{rem}\cos\left(\alpha_p\frac{\pi}{\alpha}(\theta-\theta_i)\right)v_i(\theta)}{r},\ \text{Halbach}\end{cases}. \tag{6.25}$$

By exploiting the orthogonality of the above function, two equations are extracted for the function $f_l^{I_i}(r)$ for each magnetization pattern

$$f_l^{I_i}(r)=\begin{cases}\begin{cases}\frac{(-1)^i B_{rem}}{\beta r}\int_{\theta_i-\frac{\beta}{2}}^{\theta_i+\frac{\beta}{2}} v_i(\theta)d\theta\ (l=0)\\ \frac{2(-1)^i B_{rem}}{\beta r}\int_{\theta_i-\frac{\beta}{2}}^{\theta_i+\frac{\beta}{2}}\cos\left(\frac{l\pi}{\beta}\left(\theta-\theta_i+\frac{\beta}{2}\right)\right)v_i(\theta)d\theta\ (l\geq 1)\end{cases}\\ \begin{cases}\frac{(-1)^i B_{rem}}{\beta r}\int_{\theta_i-\frac{\beta}{2}}^{\theta_i+\frac{\beta}{2}}\cos(\theta-\theta_i)v_i(\theta)d\theta\ (l=0)\\ \frac{2(-1)^i B_{rem}}{\beta r}\int_{\theta_i-\frac{\beta}{2}}^{\theta_i+\frac{\beta}{2}}\cos(\theta-\theta_i)\cos\left(\frac{l\pi}{\beta}\left(\theta-\theta_i+\frac{\beta}{2}\right)\right)v_i(\theta)d\theta\ (l\geq 1)\end{cases}\\ \begin{cases}\frac{(-1)^i B_{rem}\left(1-\alpha_p\frac{\pi}{\alpha}\right)}{\beta r}\int_{\theta_i-\frac{\beta}{2}}^{\theta_i+\frac{\beta}{2}}\sin\left(\alpha_p\frac{\pi}{\alpha}(\theta-\theta_i)\right)u_i(\theta)d\theta+\\ +\frac{(-1)^i B_{rem}}{r}\int_{\theta_i-\frac{\beta}{2}}^{\theta_i+\frac{\beta}{2}}\cos\left(\alpha_p\frac{\pi}{\alpha}(\theta-\theta_i)\right)v_i(\theta)d\theta\ (l=0)\\ \frac{(-1)^i B_{rem}\left(1-\alpha_p\frac{\pi}{\alpha}\right)}{r}\int_{\theta_i-\frac{\beta}{2}}^{\theta_i+\frac{\beta}{2}}\sin\left(\alpha_p\frac{\pi}{\alpha}(\theta-\theta_i)\right)\cos\left(\frac{l\pi}{\beta}\left(\theta-\theta_i+\frac{\beta}{2}\right)\right)u_i(\theta)d\theta+\\ \frac{2(-1)^i B_{rem}}{\beta r}\int_{\theta_i-\frac{\beta}{2}}^{\theta_i+\frac{\beta}{2}}\cos\left(\alpha_p\frac{\pi}{\alpha}(\theta-\theta_i)\right)\cos\left(\frac{l\pi}{\beta}\left(\theta-\theta_i+\frac{\beta}{2}\right)\right)v_i(\theta)d\theta\ (l\geq 1)\end{cases}\end{cases}. \tag{6.26}$$

The solution of the PDE, i.e. the vector potential function, is also written with respect to the eigenfunction expansions

$$A_z^{I_i}(r,\theta)=\sum_{l=0}^{L}R_l^{I_i}(r)\cos\left(\frac{l\pi}{\beta}\left(\theta-\theta_i+\frac{\beta}{2}\right)\right). \tag{6.27}$$

Substituting (6.27) into (6.21) and accounting also (6.11), the following ODE emerges

$$\frac{d^2R_l^{I_i}(r)}{dr^2}+\frac{1}{r}\frac{dR_l^{I_i}(r)}{dr}-\left(\frac{l\pi}{\beta r}\right)^2R_l^{I_i}(r)=f_l^{I_i}(r), \tag{6.28}$$

which is non-homogeneous, can be solved relatively easy by super-positioning the homogeneous with the non-homogeneous solution, which can be found with the method of variation of parameters.

$$R_l^{I_i}(r)=\begin{cases}A_0^{I_i}+B_0^{I_i}\ln r, \text{ if } l=0\\ \sum_{l=1}^{L}A_l^{I_i}r^{\frac{l\pi}{\beta}}+B_l^{I_i}r^{-\frac{l\pi}{\beta}}-F_l^{I_i}r, \text{ if } l\geq 1, \text{ radial, parallel}\\ A_0^{I_i}+B_0^{I_i}\ln r, \text{ if } l=0\\ \sum_{l=1}^{L}A_l^{I_i}r^{\frac{l\pi}{\beta}}+B_l^{I_i}r^{-\frac{l\pi}{\beta}}-G_l^{I_i}r-F_l^{I_i}\left(1-\alpha_p\frac{\pi}{\alpha}\right)r, \text{ if } l\geq 1, \text{ Halbach}\end{cases}, \tag{6.29}$$

which $F_l^{I_i}$, $G_l^{I_i}$ are calculated using (6.26) for each magnetization pattern distribution and are equal with

$$F_l^{I_i}=\begin{cases}\frac{4(-1)^iB_{rem}}{\beta\left(\left(\frac{l\pi}{\beta}\right)^2-1\right)}\sin\left(\frac{l\pi}{2}\frac{\alpha}{\beta}\right)\sin\left(\frac{l\pi}{2}\right), \text{ radial}\\ \frac{4(-1)^iB_{rem}}{\beta\left(\left(\frac{l\pi}{\beta}\right)^2-1\right)}\cdot\sin\left(\frac{l\pi}{2}\frac{\alpha}{\beta}\right)\sin\left(\frac{l\pi}{2}\right)\cos\left(\frac{\alpha}{2}\right), \text{ parallel}\\ \frac{2(-1)^iB_{rem}E_l^{I_i}}{\beta\left(\left(\frac{l\pi}{\beta}\right)^2-1\right)}, \text{ Halbach}\end{cases}.$$
$$G_l^{I_i}=\begin{cases}\frac{4(-1)^iB_{rem}}{\beta\left(\left(\frac{l\pi}{\beta}\right)^2-1\right)}\cdot\sin\left(\frac{l\pi}{2}\frac{\alpha}{\beta}\right)\sin\left(\frac{l\pi}{2}\right)\cos\left(\alpha_p\frac{\pi}{2}\right), \text{ Halbach}\end{cases} \tag{6.30}$$

The above equations show that when $l\pi/\beta=1$, the excitation functions are not defined. The latter happens when $P=2$, so the equations must be resolved for this single case alone. The tangential component of the magnetic field strength on the rotor back iron is zero i.e.

$$H_\theta^{I_i}(R_1,\theta)=0. \tag{6.31}$$

By the aid of (6.6), (6.7) and (6.27) the above equation entails to be equal with

$$\sum_{l=0}^{L} \left.\frac{dR_l^{I_i}}{dr}\right|_{r=R_1} \cdot \cos\left(\frac{l\pi}{\beta}\left(\theta-\theta_i+\frac{\beta}{2}\right)\right) = \begin{cases} 0, \text{ radial} \\ (-1)^i B_{rem}\sin(\theta-\theta_i)u_i(\theta), \text{ parallel} \\ (-1)^i B_{rem}\sin\left(\alpha_p\frac{\pi}{\alpha}(\theta-\theta_i)\right)u_i(\theta), \text{ Halbach} \end{cases} \tag{6.32}$$

By exploiting the orthogonality of the above boundary condition, two initial conditions can be developed for the ODE (6.28), i.e.

$$\left.\frac{dR_l^{I_i}}{dr}\right|_{r=R_1} = \begin{cases} \begin{cases} 0 \text{ if } l=0 \\ 0 \text{ if } l\geq 1, \text{ radial} \end{cases} \\ \begin{cases} 0 \text{ if } l=0 \\ \frac{2(-1)^i B_{rem}}{\beta}E_l^{I_i} \text{ if } l\geq 1, \text{ parallel} \end{cases} \\ \begin{cases} 0 \text{ if } l=0 \\ F_l^{I_i}\left(\left(\frac{l\pi}{\beta}\right)^2-1\right) \text{ if } l\geq 1, \text{Halbach.} \end{cases} \end{cases} \tag{6.33}$$

The final magnetic vector potential for each magnetization distribution pattern can be determined by combining (6.27), (6.29) and (6.33) for each magnetization scenario

$$\begin{aligned} A_z^{I_i}(r,\theta) = A_0^{I_i} + \sum_{l=1}^{L} A_l^{I_i}\frac{P_{l\pi/\beta}(r,R_1)}{P_{l\pi/\beta}(R_2,R_1)}\cos\left(\frac{l\pi}{\beta}\left(\theta-\theta_i+\frac{\beta}{2}\right)\right) + \\ \begin{cases} -\sum_{l=1}^{L} F_l^{I_i}\left(r+\frac{\beta R_1}{l\pi}\left(\frac{R_1}{r}\right)^{\frac{l\pi}{\beta}}\right), \text{ radial} \\ -\sum_{l=1}^{L}\left(F_l^{I_i}r+R_1\left(\frac{\beta}{l\pi}F_l^{I_i}+\frac{2(-1)^i B_{rem}E_l^{I_i}}{l\pi}\left(\frac{R_1}{r}\right)^{\frac{l\pi}{\beta}}\right)\right), \text{ parallel} \\ -\sum_{l=1}^{L} F_l^{I_i}\left(\left(1-\alpha_p\frac{\pi}{\alpha}\right)r+\frac{\beta R_1}{l\pi}\left(\left(\frac{l\pi}{\beta}\right)^2-\alpha_p\frac{\pi}{\alpha}\right)\left(\frac{R_1}{r}\right)^{\frac{l\pi}{\beta}}\right) \\ -\sum_{l=1}^{L} G_l^{I_i}\left(r+\frac{\beta R_1}{l\pi}\left(\frac{R_1}{r}\right)^{\frac{l\pi}{\beta}}\right), \text{ Halbach} \end{cases} \\ \cdot\cos\left(\frac{l\pi}{\beta}\left(\theta-\theta_i+\frac{\beta}{2}\right)\right). \end{aligned} \tag{6.34}$$

The scaling functions $P_z(x,y)$ and $E_z(x,y)$ were proposed by [116, 114] are equal to

$$\begin{aligned} P_z(x,y) &= \left(\frac{x}{y}\right)^z + \left(\frac{y}{x}\right)^z \\ E_z(x,y) &= \left(\frac{x}{y}\right)^z - \left(\frac{y}{x}\right)^z. \end{aligned} \tag{6.35}$$

The scaling functions have many advantages. The first advantage is that they allow for the total number of harmonics to be much higher without ending up with an ill-conditioned matrix and add more accuracy to the analytical solution. Another advantage is that when the interface conditions apply, they isolate each to-be-determined, giving a better intuition about the construction of matrices for the solution of the system. Finally, in the case of slotting and slot-opening, they offer a solution when their dimensions are small.

6.5.2 Surface-inset permanent-magnet machine - Region $\mathbf{I_i}$

Since the radial component of the magnetic field intensity is continuous on the interface, on the lateral boundaries of the magnet is zero

$$H_r^{I_i}\left(r,\theta_i-\frac{\alpha}{2}\right)=0 \quad H_r^{I_i}\left(r,\theta_i+\frac{\alpha}{2}\right)=0. \tag{6.36}$$

By the above equation, if the equations that relate to the magnetic vector potential, the magnetic flux density and field strength are employed, the following two boundaries conditions for the magnetic vector potential are

$$\left.\frac{\partial A_z^{I_i}}{\partial\theta}\right|_{\theta=\theta_i-\frac{\alpha}{2}}=\begin{cases}\frac{(-1)^i B_{rem}}{\mu_0}u_i\left(\theta_i-\frac{\alpha}{2}\right),\\ \frac{(-1)^i B_{rem}}{\mu_0}\cos\left(\frac{\alpha}{2}\right)u_i\left(\theta_i-\frac{\alpha}{2}\right)\\ \frac{(-1)^i B_{rem}}{\mu_0}\cos\left(\alpha_p\frac{\pi}{2}\right)u_i\left(\theta_i-\frac{\alpha}{2}\right)\end{cases},$$
$$\left.\frac{\partial A_z^{I_i}}{\partial\theta}\right|_{\theta=\theta_i+\frac{\alpha}{2}}=\begin{cases}\frac{(-1)^i B_{rem}}{\mu_0}u_i\left(\theta_i+\frac{\alpha}{2}\right)\\ \frac{(-1)^i B_{rem}}{\mu_0}\cos\left(\frac{\alpha}{2}\right)u_i\left(\theta_i+\frac{\alpha}{2}\right)\\ \frac{(-1)^i B_{rem}}{\mu_0}\cos\left(\alpha_p\frac{\pi}{2}\right)u_i\left(\theta_i+\frac{\alpha}{2}\right)\end{cases} \tag{6.37}$$

which (6.37) shows that, unlike for the surface-mounted magnet topology, it is not clear whether the boundary conditions are homogeneous or not. The $u_i(\theta)$ function for each value of the boundary conditions in the lateral boundaries is equal to

$$\begin{aligned}u_i\left(\theta_i-\frac{\alpha}{2}\right)&=H(-\alpha)-H(0^-)=0-0=0\\ u_i\left(\theta_i+\frac{\alpha}{2}\right)&=H(0^+)-H(\alpha)=1-1=0\end{aligned}. \tag{6.38}$$

Generally, the Heaviside function takes the values 0 and 1 at $\theta=0$; meaning it is discontinuous in mathematical terms. By convention is considered that $H(0)=1/2$, meaning that the boundary conditions of (6.37) become non-homogeneous. In this case, it would be compulsory to write the vector potential function as a summation of two functions, as it was

done in [114]; a function that will transform the boundary conditions into homogeneous and a function to be determined. However, this methodology was not followed since the Heaviside function approaches the value 0 for $\theta = \theta_i - \frac{\alpha}{2}$ from the left and from the right for $\theta = \theta_i + \frac{\alpha}{2}$, for each magnetization pattern. The boundary conditions for the PDE are homogeneous in each case, and no function is required to be added to the PDE. Hence, the eigenfunctions of (6.21) are

$$\Theta_l^{I_i}(\theta) = \cos\left(\frac{l\pi}{\alpha}\left(\theta - \theta_i + \frac{\alpha}{2}\right)\right),\ l = 1,2,\ldots,L. \tag{6.39}$$

According to the method of eigenfunction expansions [142, 143], the non-homogeneous terms for each magnetization pattern of (6.21) are written as an expansion based on the eigenfunctions (6.39) of the corresponding PDE, i.e.

$$\sum_{l=0}^{L} f_l^{I_i}(r)\cos\left(\frac{l\pi}{\alpha}\left(\theta - \theta_i + \frac{\alpha}{2}\right)\right) = \begin{cases} \frac{(-1)^i B_{rem} v_i(\theta)}{r}, \text{ radial} \\ \frac{(-1)^i B_{rem}\cos(\theta-\theta_i) v_i(\theta)}{r}, \text{ parallel} \\ \frac{(-1)^i B_{rem}\left(1-\alpha_p\frac{\pi}{\alpha}\right)\sin\left(\alpha_p\frac{\pi}{\alpha}(\theta-\theta_i)\right)u_i(\theta)}{r} + \\ +\frac{(-1)^i B_{rem}\cos\left(\alpha_p\frac{\pi}{\alpha}(\theta-\theta_i)\right)v_i(\theta)}{r}, \text{ Halbach} \end{cases} . \tag{6.40}$$

The function $f_l^{I_i}(r)$ can be determined using the orthogonality of the functions as

$$f_l^{I_i}(r) = \begin{cases} \begin{cases} \frac{(-1)^i B_{rem}}{\alpha r}\int_{\theta_i-\frac{\alpha}{2}}^{\theta_i+\frac{\alpha}{2}} v_i(\theta)d\theta\ (l=0) \\ \frac{2(-1)^i B_{rem}}{\alpha r}\int_{\theta_i-\frac{\alpha}{2}}^{\theta_i+\frac{\alpha}{2}} \cos\left(\frac{l\pi}{\alpha}\left(\theta-\theta_i+\frac{\alpha}{2}\right)\right)v_i(\theta)d\theta\ (l\geq 1) \end{cases} \\ \begin{cases} \frac{(-1)^i B_{rem}}{\alpha r}\int_{\theta_i-\frac{\alpha}{2}}^{\theta_i+\frac{\alpha}{2}} \cos(\theta-\theta_i) v_i(\theta)d\theta\ (l=0) \\ \frac{2(-1)^i B_{rem}}{\alpha r}\int_{\theta_i-\frac{\alpha}{2}}^{\theta_i+\frac{\alpha}{2}} \cos(\theta-\theta_i)\cos\left(\frac{l\pi}{\alpha}\left(\theta-\theta_i+\frac{\alpha}{2}\right)\right)v_i(\theta)d\theta\ (l\geq 1) \end{cases} \\ \begin{cases} \frac{(-1)^i B_{rem}\left(1-\alpha_p\frac{\pi}{\alpha}\right)}{\alpha r}\int_{\theta_i-\frac{\alpha}{2}}^{\theta_i+\frac{\alpha}{2}} \sin\left(\alpha_p\frac{\pi}{\alpha}(\theta-\theta_i)\right)u_i(\theta)d\theta + \\ +\frac{(-1)^i B_{rem}}{r}\int_{\theta_i-\frac{\alpha}{2}}^{\theta_i+\frac{\alpha}{2}} \cos\left(\alpha_p\frac{\pi}{\alpha}(\theta-\theta_i)\right)v_i(\theta)d\theta\ (l=0) \\ \frac{(-1)^i B_{rem}\left(1-\alpha_p\frac{\pi}{\alpha}\right)}{r}\int_{\theta_i-\frac{\alpha}{2}}^{\theta_i+\frac{\alpha}{2}} \sin\left(\alpha_p\frac{\pi}{\alpha}(\theta-\theta_i)\right)\cos\left(\frac{l\pi}{\alpha}\left(\theta-\theta_i+\frac{\alpha}{2}\right)\right)u_i(\theta)d\theta + \\ \frac{2(-1)^i B_{rem}}{\alpha r}\int_{\theta_i-\frac{\alpha}{2}}^{\theta_i+\frac{\alpha}{2}} \cos\left(\alpha_p\frac{\pi}{\alpha}(\theta-\theta_i)\right)\cos\left(\frac{l\pi}{\alpha}\left(\theta-\theta_i+\frac{\alpha}{2}\right)\right)v_i(\theta)d\theta\ (l\geq 1) \end{cases} \end{cases} . \tag{6.41}$$

The solution of the PDE, i.e. the vector potential function, is also written to the eigenfunctions expansion by separating the variables

$$A_z^{I_i}(r,\theta) = \sum_{l=0}^{L} R_l^{I_i}(r)\cos\left(\frac{l\pi}{\alpha}\left(\theta-\theta_i+\frac{\alpha}{2}\right)\right). \tag{6.42}$$

Substituting (6.42) at (6.21) and accounting also (6.11), the following ODE emerges

$$\frac{d^2R_l^{I_i}(r)}{dr^2}+\frac{1}{r}\frac{dR_l^{I_i}(r)}{dr}-\left(\frac{l\pi}{\alpha r}\right)^2 R_l^{I_i}(r) = f_l^{I_i}(r), \tag{6.43}$$

which is non-homogeneous and can be solved easily by summing the homogeneous with a non-homogeneous solution. Which can be found by utilising the method of variation of parameters.

$$R_l^{I_i}(r) = \begin{cases} \begin{cases} A_0^{I_i}+B_0^{I_i}\ln r, \text{ if } l=0 \\ \sum_{l=1}^{L} A_l^{I_i} r^{\frac{l\pi}{\alpha}} + B_l^{I_i} r^{-\frac{l\pi}{\alpha}} - F_l^{I_i} r, \text{ if } l\geq 1, \text{ radial, parallel,} \end{cases} \\ \begin{cases} A_0^{I_i}+B_0^{I_i}\ln r \text{ if } l=0 \\ \sum_{l=1}^{L} A_l^{I_i} r^{\frac{l\pi}{\alpha}} + B_l^{I_i} r^{-\frac{l\pi}{\alpha}} - G_l^{I_i} r - F_l^{I_i}\left(1-\alpha_p\frac{\pi}{\alpha}\right) r, \text{ if } l\geq 1, \text{ Halbach} \end{cases} \end{cases}, \tag{6.44}$$

which $F_l^{I_i}$, $G_l^{I_i}$ are given for each magnetization pattern distribution and are equal with

$$F_l^{I_i} = \begin{cases} \frac{2(-1)^i B_{rem}(1-(-1)^l)}{\alpha\left(\left(\frac{l\pi}{\alpha}\right)^2-1\right)}, \text{ radial} \\ \frac{2(-1)^i B_{rem}(1-(-1)^l)}{\alpha\left(\left(\frac{l\pi}{\alpha}\right)^2-1\right)}\cos\left(\frac{\alpha}{2}\right), \text{ parallel} \\ \frac{2(-1)^i B_{rem} E_l^{I_i}}{\alpha\left(\left(\frac{l\pi}{\alpha}\right)^2-1\right)}, \text{ Halbach} \end{cases} . \tag{6.45}$$

$$G_l^{I_i} = \begin{cases} \frac{2(-1)^i B_{rem}(1-(-1)^l)}{\alpha\left(\left(\frac{l\pi}{\alpha}\right)^2-1\right)}\cos\left(\alpha_p\frac{\pi}{2}\right), \text{ Halbach} \end{cases}$$

The above equations show that when $l\pi/\alpha = 1$, the excitation functions are not defined. However, equality is never true in the specific study because the rotor configuration would have surface full-pitched magnets, and there wouldn't be any iron on the lateral sides. The tangential component of the magnetic field strength on the rotor back iron is zero i.e.

$$H_\theta^{I_i}(R_1,\theta) = 0. \tag{6.46}$$

Considering the equations which relate to the magnetic vector potential, the magnetic flux density, field intensity and (6.42), the below equation

$$\sum_{l=0}^{L} \left.\frac{dR_l^{I_i}}{dr}\right|_{r=R_1} \cdot \cos\left(\frac{l\pi}{\alpha}\left(\theta-\theta_i+\frac{\alpha}{2}\right)\right) = \begin{cases} 0, \text{ radial} \\ (-1)^i B_{rem}\sin(\theta-\theta_i)u_i(\theta), \text{ parallel} \\ (-1)^i B_{rem}\sin\left(\alpha_p\frac{\pi}{\alpha}(\theta-\theta_i)\right)u_i(\theta), \text{ Halbach} \end{cases} \tag{6.47}$$

By exploiting the orthogonality of the above boundary condition, one more initial condition is developed for the ODE (6.43), which offers one more equation for the constants of the order $l=0$ and $l\geq 1$ for each magnetisation distribution i.e.

$$\left.\frac{dR_l^{I_i}}{dr}\right|_{r=R_1} = \begin{cases} \begin{cases} 0 \text{ if } l=0 \\ 0 \text{ if } l\geq 1, \text{ radial} \end{cases} \\ \begin{cases} 0 \text{ if } l=0 \\ -F_l^{I_i} \text{ if } l\geq 1, \text{ parallel} \end{cases} \\ \begin{cases} 0 \text{ if } l=0 \\ F_l^{I_i}\left(\left(\frac{l\pi}{\alpha}\right)^2-1\right) \text{ if } l\geq 1, \text{Halbach.} \end{cases} \end{cases} \tag{6.48}$$

The final magnetic vector potential function for each magnetization distribution pattern can be determined by combining (6.42), (6.44) and (6.48) and is the following function for each magnetization case

$$\begin{aligned} A_z^{I_i}(r,\theta) = A_0^{I_i} + \sum_{l=1}^{L} A_l^{I_i}\frac{P_{l\pi/\alpha}(r,R_1)}{P_{l\pi/\alpha}(R_2,R_1)}\cos\left(\frac{l\pi}{\alpha}\left(\theta-\theta_i+\frac{\alpha}{2}\right)\right) + \\ \begin{cases} -\sum_{l=1}^{L} F_l^{I_i}\left(r+\frac{\alpha R_1}{l\pi}\left(\frac{R_1}{r}\right)^{\frac{l\pi}{\alpha}}\right), \text{ radial} \\ -\sum_{l=1}^{L} F_l^{I_i} r, \text{ parallel} \\ -\sum_{l=1}^{L} F_l^{I_i}\left(\left(1-\alpha_p\frac{\pi}{\alpha}\right)r+\frac{\alpha R_1}{l\pi}\left(\left(\frac{l\pi}{\alpha}\right)^2-\alpha_p\frac{\pi}{\alpha}\right)\left(\frac{R_1}{r}\right)^{\frac{l\pi}{\alpha}}\right) \\ -\sum_{l=1}^{L} G_l^{I_i}\left(r+\frac{\alpha R_1}{l\pi}\left(\frac{R_1}{r}\right)^{\frac{l\pi}{\alpha}}\right), \text{ Halbach} \end{cases} \\ \cdot\cos\left(\frac{l\pi}{\alpha}\left(\theta-\theta_i+\frac{\alpha}{2}\right)\right). \end{aligned} \tag{6.49}$$

6.6 Solution of Laplace's and Poisson's equations in the other subdomains

,This section gives the analytical expression for the magnetic vector potential for the other three regions; air-gap, slot-opening and slot. Laplace's equation is solved in the air gap and slot opening, and there is no source of magnetisation. Since there will be a current for the slot subdomain, a current density is created; hence Poisson's equation yields.

6.6.1 Solution of Laplace's in the air-gap - Region II

In the air-gap Laplace's equation applies

$$\nabla^2 \cdot A_z^{II} = 0 \begin{cases} R_2 \leq r \leq R_3 \\ 0 < \theta < 2\pi \end{cases}, \tag{6.50}$$

which is the Dirichlet problem in an annulus. The solution for (6.50) according to [116] is

$$\begin{aligned} A_z^{II}(r,\theta) = &\sum_{n=1}^{N} \left(A_n^{II} \frac{R_2}{n} \frac{P_n(r,R_3)}{E_n(R_2,R_3)} + B_n^{II} \frac{R_3}{n} \frac{P_n(r,R_2)}{E_n(R_3,R_2)} \right) \cos(n\theta) + \\ &\sum_{n=1}^{N} \left(C_n^{II} \frac{R_2}{n} \frac{P_n(r,R_3)}{E_n(R_2,R_3)} + D_n^{II} \frac{R_3}{n} \frac{P_n(r,R_2)}{E_n(R_3,R_2)} \right) \sin(n\theta) \end{aligned}, \tag{6.51}$$

which the scaling functions have been used here as well.

6.6.2 Solution of Laplace's on the jth slot-opening - Region III$_j$

In the slot-opening, Laplace's equation applies

$$\nabla^2 \cdot A_z^{III_j} = 0 \begin{cases} R_3 \leq r \leq R_4 \\ \theta_j - \frac{\gamma}{2} \leq \theta \leq \theta_j + \frac{\gamma}{2} \end{cases} \tag{6.52}$$

The radial component of the magnetic field intensity in the lateral sides of the region since the iron has an infinite magnetic permeability

$$H_r^{III_j}\left(r, \theta_j - \frac{\gamma}{2}\right) = 0 \qquad H_r^{III_j}\left(r, \theta_j + \frac{\gamma}{2}\right) = 0 \tag{6.53}$$

which entails the two homogeneous boundary conditions

$$\left.\frac{\partial A_z^{III_j}}{\partial \theta}\right|_{\theta=\theta_j-\frac{\gamma}{2}} = 0 \quad \left.\frac{\partial A_z^{III_j}}{\partial \theta}\right|_{\theta=\theta_j+\frac{\gamma}{2}} = 0. \tag{6.54}$$

The above boundary conditions lead to the following eigenfunctions

$$\Theta_k^{III_j}(\theta) = \cos\left(\frac{k\pi}{\gamma}\left(\theta-\theta_j+\frac{\gamma}{2}\right)\right), \ k = 1,2,\ldots,K. \tag{6.55}$$

The solution of (6.52) for the j[th] slot-opening is given in [116] with the scaling functions included and is

$$\begin{aligned} &A_z^{III_j}(r,\theta) = A_0^{III_j} + B_0^{III_j}\ln r + \\ &\sum_{k=1}^{K}\left(A_k^{III_j}\frac{E_{k\pi/\gamma}(r,R_4)}{E_{k\pi/\gamma}(R_3,R_4)} - B_k^{III_j}\frac{E_{k\pi/\gamma}(r,R_3)}{E_{k\pi/\gamma}(R_3,R_4)}\right)\cdot\cos\left(\frac{k\pi}{\gamma}\left(\theta-\theta_j+\frac{\gamma}{2}\right)\right). \end{aligned} \tag{6.56}$$

6.6.3 Solution of Poisson's on the j[th] Slot - Region IV$_j$

In the i[th] slot, Poisson's equation applies

$$\nabla^2\cdot A_z^{IV_j} = -\mu_0 J_j \begin{cases} R_4 \le r \le R_5 \\ \theta_j - \frac{\delta}{2} \le \theta \le \theta_j + \frac{\delta}{2} \end{cases}. \tag{6.57}$$

The radial and the tangential component of the magnetic field intensity in the lateral sides and the end of the slot are, respectively zero

$$\begin{cases} H_r^{IV_j}\left(r,\theta_j-\frac{\delta}{2}\right) = 0 \quad H_r^{IV_j}\left(r,\theta_j+\frac{\delta}{2}\right) = 0 \\ H_\theta^{IV_j}(R_5,\theta) = 0 \end{cases}, \tag{6.58}$$

which lead to the following homogeneous boundary conditions

$$\begin{cases} \left.\frac{\partial A_z^{IV_j}}{\partial \theta}\right|_{\theta=\theta_j-\frac{\delta}{2}} = 0 \quad \left.\frac{\partial A_z^{IV_j}}{\partial \theta}\right|_{\theta=\theta_j+\frac{\delta}{2}} = 0 \\ \left.\frac{\partial A_z^{IV_j}}{\partial r}\right|_{r=R_5} = 0 \end{cases} \tag{6.59}$$

The first line of boundary conditions (6.59) leads to the following eigenfunctions

$$\Theta_m^{IV_j}(\theta) = \cos\left(\frac{m\pi}{\delta}\left(\theta - \theta_j + \frac{\gamma}{2}\right)\right),\ m = 1,2,\ldots,M. \tag{6.60}$$

The excitation term of (6.57) is expanded to the above eigenfunctions

$$\sum_{m=0}^{M} f_m^{IV_j}(r)\cos\left(\frac{m\pi}{\delta}\left(\theta - \theta_j + \frac{\gamma}{2}\right)\right) = -\mu_0 J_j, \tag{6.61}$$

and by exploiting the orthogonality of the functions, two equations are obtained, i.e.

$$f_m^{IV_j}(r) = \begin{cases} -\mu_0 J_j, \text{ if } m = 0 \\ 0, \qquad \text{if } m \geq 1 \end{cases} \tag{6.62}$$

The solution of (6.57) is expanded using the eigenfunctions

$$A_z^{IV_j}(r,\theta) = \sum_{m=0}^{M} R_m^{IV_j}(r)\cos\left(\frac{m\pi}{\delta}\left(\theta - \theta_j + \frac{\delta}{2}\right)\right). \tag{6.63}$$

By substituting (6.62) to (6.57), the following ODE (Ordinary Differential Equation) is generated

$$\frac{d^2 R_m^{IV_j}(r)}{dr^2} + \frac{1}{r}\frac{dR_m^{IV_j}(r)}{dr} - \left(\frac{m\pi}{\delta r}\right)^2 R_m^{IV_j}(r) = f_m^{IV_j}(r), \tag{6.64}$$

which is non-homogeneous for $m = 0$ and homogeneous for $m \geq 1$. Equation (6.63) can be solved similarly using the method of variation of parameters, and the solution of the radial function is

$$R_m^{IV_j}(r) = \begin{cases} A_0^{IV_j} + \frac{1}{2}\mu_0 J_j\left(R_5^2 \ln r - \frac{r^2}{2}\right), \text{ if } m = 0 \\ \sum_{m=1}^{M} A_m^{IV_j} r^{\frac{m\pi}{\delta}} + B_m^{IV_j} r^{-\frac{m\pi}{\delta}}, \quad \text{if } m \geq 1 \end{cases}. \tag{6.65}$$

By substituting (6.63) to the boundary condition written on the second row of (6.58) yields

$$\sum_{m=0}^{M} \left.\frac{dR_m^{IV_j}}{dr}\right|_{r=R_5} \cdot \cos\left(\frac{m\pi}{\delta}\left(\theta - \theta_j + \frac{\delta}{2}\right)\right) = 0, \text{ if } m \geq 0 \tag{6.66}$$

By substituting (6.64) to (6.65) the final scaled closed form solution is

$$R_m^{IV_j}(r) = \begin{cases} A_0^{IV_j} + B_0^{IV_j}\ln r - \mu_0 J_j \frac{r^2}{4}, \qquad \text{if } m = 0 \\ \sum_{m=1}^{M} A_m^{IV_j} \frac{\left(\frac{r}{R_5}\right)^{\frac{m\pi}{\delta}} + \left(\frac{R_5}{r}\right)^{-\frac{m\pi}{\delta}}}{\left(\frac{R_4}{R_5}\right)^{\frac{m\pi}{\delta}} - \left(\frac{R_5}{R_4}\right)^{-\frac{m\pi}{\delta}}}, \text{ if } m \geq 1 \end{cases}. \tag{6.67}$$

By substituting (6.66) to (6.63) the final magnetic vector potential function for the j[th] slot is

$$\begin{aligned} A_z^{IV_j}(r,\theta) =& A_0^{IV_j} + \frac{1}{2}\mu_0 J_j \left(R_5^2 \ln r - \frac{r^2}{2} \right) + \\ & \sum_{m=1}^{M} A_m^{IV_j} \frac{\delta R_4}{m\pi} \frac{P_{m\pi/\delta}(r,R_5)}{E_{m\pi/\delta}(R_4,R_5)} \cos\left(\frac{m\pi}{\delta} \left(\theta - \theta_j + \frac{\delta}{2} \right) \right) \end{aligned}. \tag{6.68}$$

6.7 Interface conditions between each subdomain

The interface conditions are used to determine the coefficients in the closed-form solution. Between every two regions„ a layer or boundary line separates them. The perpendicular to the surface component of the magnetic flux density is continuous to the interface. The parallel to the surface component of the magnetic field intensity is continuous on the interface. So the radial component of the magnetic flux density is continuous between Regions I_i and II, II and III_j and IV_j. Furthermore, the tangential component of the magnetic field intensity is continuous between the interface of the regions noted above. Instead of the radial component of the magnetic flux density, the axial component of the magnetic vector potential function can be used to ease the calculation of the interface conditions, as according to (6.6), by integration it ends up in an interface condition between potential functions. The following three equations prove mathematically that it is equivalent,

$$\begin{aligned} & B_r^{I_i}(R_2,\theta) = B_r^{II}(R_2,\theta) \\ & \left. \frac{1}{R_2} \frac{\partial A_z^{I_i}}{\partial \theta} \right|_{r=R_2} = \left. \frac{1}{R_2} \frac{\partial A_z^{II}}{\partial \theta} \right|_{r=R_2}, \\ & A_z^{I_i}(R_2,\theta) = A_z^{II}(R_2,\theta) \end{aligned} \tag{6.69}$$

$$\begin{aligned} & B_r^{II}(R_3,\theta) = B_r^{III_j}(R_3,\theta) \\ & \left. \frac{1}{R_3} \frac{\partial A_z^{II}}{\partial \theta} \right|_{r=R_3} = \left. \frac{1}{R_3} \frac{\partial A_z^{III_j}}{\partial \theta} \right|_{r=R_3}, \\ & A_z^{II}(R_3,\theta) = A_z^{III_j}(R_3,\theta) \end{aligned} \tag{6.70}$$

$$\begin{aligned} & B_r^{III_j}(R_4,\theta) = B_r^{IV_j}(R_4,\theta) \\ & \left. \frac{1}{R_4} \frac{\partial A_z^{III_j}}{\partial \theta} \right|_{r=R_4} = \left. \frac{1}{R_4} \frac{\partial A_z^{IV_j}}{\partial \theta} \right|_{r=R_4}. \\ & A_z^{II}(R_3,\theta) = A_z^{III_j}(R_3,\theta) \end{aligned} \tag{6.71}$$

So the interface continues in terms of potential function between the regions is

$$A_z^{I_i}(R_2,\theta) = A_z^{II}(R_2,\theta) \begin{cases} \theta_i - \frac{\beta}{2} \leq \theta \leq \theta_i + \frac{\beta}{2}, \text{ Surface-mounted PM machine} \\ \theta_i - \frac{\alpha}{2} \leq \theta \leq \theta_i + \frac{\alpha}{2}, \text{ Surface-inset PM machine} \end{cases}, \quad (6.72)$$

$$A_z^{II}(R_3,\theta) = A_z^{III_j}(R_3,\theta), \text{ if } \theta_j - \frac{\gamma}{2} \leq \theta \leq \theta_j + \frac{\gamma}{2}, \quad (6.73)$$

and

$$A_z^{III_j}(R_4,\theta) = A_z^{IV_j}(R_4,\theta), \text{ if } \theta_j - \frac{\delta}{2} \leq \theta \leq \theta_j + \frac{\delta}{2}. \quad (6.74)$$

In the interface conditions concerning the magnetic field intensity and coupling the magnet region with the air gap and the slot-opening region with the air gap, there is a varying sign in the magnet region and the slot region. The latter entails that integration of the whole cycle has to take place. The interface conditions are

$$H_\theta^{II}(R_2,\theta) = \begin{cases} H_\theta^{I_i}(R_2,\theta) \text{ if } \begin{cases} \theta_i - \frac{\beta}{2} \leq \theta \leq \theta_i + \frac{\beta}{2}, \text{ Surface-mounted PM machine} \\ \theta_i - \frac{\alpha}{2} \leq \theta \leq \theta_i + \frac{\alpha}{2}, \text{ Surface-inset PM machine} \end{cases} \\ 0 \qquad \text{elsewhere} \end{cases}, \quad (6.75)$$

$$H_\theta^{II}(R_3,\theta) = \begin{cases} H_\theta^{III_j}(R_3,\theta), \text{ if } \theta_j - \frac{\gamma}{2} \leq \theta \leq \theta_j + \frac{\gamma}{2} \\ 0 \qquad \text{elsewhere} \end{cases}, \quad (6.76)$$

and

$$H_\theta^{IV_j}(R_4,\theta) = \begin{cases} H_\theta^{III_j}(R_4,\theta), \text{ if } \theta_j - \frac{\gamma}{2} \leq \theta \leq \theta_j + \frac{\gamma}{2} \\ 0 \qquad \text{elsewhere} \end{cases}. \quad (6.77)$$

In each region, the magnetic field intensity can connect with the magnetic vector potential using (6.7)

$$
\begin{aligned}
H_{\theta}^{I_i}(r,\theta) &= -\frac{1}{\mu_0\mu_r}\frac{\partial A_z^{I_i}(r,\theta)}{\partial r} - \frac{1}{\mu_r}M_{\theta}^{I_i}(r,\theta) \\
H_{\theta}^{II}(r,\theta) &= -\frac{1}{\mu_0}\frac{\partial A_z^{II}(r,\theta)}{\partial r} \\
H_{\theta}^{III_j}(r,\theta) &= -\frac{1}{\mu_0}\frac{\partial A_z^{III_j}(r,\theta)}{\partial r} \\
H_{\theta}^{IV_j}(r,\theta) &= -\frac{1}{\mu_0}\frac{\partial A_z^{IV_j}(r,\theta)}{\partial r}
\end{aligned}
\tag{6.78}
$$

6.8 System of linear equations with the to-be determined coefficients

This section shows the expansions of the interface conditions and, finally, the system of the linear equation of each machine topology. The number of equations is equal to the number of unknown coefficients.

6.8.1 Surface-mounted mounted permanent-magnet machine - Region I_i

Interface condition (6.72) offers the following two equations. The development is feasible due to the exploitation of the orthogonality of the trigonometric functions. The first equation is developed by integrating (6.72) along the boundaries of the polar angle for the surface-mounted topology

$$
\int_{\theta_i-\frac{\beta}{2}}^{\theta_i+\frac{\beta}{2}} A_z^{I_i}(R_2,\theta)d\theta = \int_{\theta_i-\frac{\beta}{2}}^{\theta_i+\frac{\beta}{2}} A_z^{II}(R_2,\theta)d\theta, \tag{6.79}
$$

which leads to the equation

$$
\begin{aligned}
A_0^{I_i} = &\sum_{n=1}^{N}\left(A_n^{II}\frac{R_2}{n\beta}\frac{P_n(R_2,R_3)}{E_n(R_2,R_3)} + B_n^{II}\frac{R_3}{n\beta}\frac{2}{E_n(R_3,R_2)}\right)R(n,i) + \\
&\sum_{n=1}^{N}\left(C_n^{II}\frac{R_2}{n\beta}\frac{P_n(R_2,R_3)}{E_n(R_2,R_3)} + D_n^{II}\frac{R_3}{n\beta}\frac{2}{E_n(R_3,R_2)}\right)S(n,i)
\end{aligned}
\tag{6.80}
$$

The integrals $R(n,i)$ and $S(n,i)$ are given on the text to come. Equation (6.72) can also offer

$$
\begin{aligned}
&\int_{\theta_i-\frac{\beta}{2}}^{\theta_i+\frac{\beta}{2}} A_z^{I_i}(R_2,\theta)\cos\left(\frac{l\pi}{\beta}\left(\theta-\theta_i+\frac{\beta}{2}\right)\right)d\theta = \\
&\int_{\theta_i-\frac{\beta}{2}}^{\theta_i+\frac{\beta}{2}} A_z^{II}(R_2,\theta)\cos\left(\frac{l\pi}{\beta}\left(\theta-\theta_i+\frac{\beta}{2}\right)\right)d\theta
\end{aligned}
\tag{6.81}
$$

which leads to the following equation for each magnetization distribution pattern

$$\begin{aligned} A_l^{I_i} = & \sum_{n=1}^{N} \left(A_n^{II} \frac{2R_2}{n\beta} \frac{P_n(R_2,R_3)}{E_n(R_2,R_3)} + B_n^{II} \frac{2R_3}{n\beta} \frac{2}{E_n(R_3,R_2)} \right) F(l,n,i) + \\ & \sum_{n=1}^{N} \left(C_n^{II} \frac{2R_2}{n\beta} \frac{P_n(R_2,R_3)}{E_n(R_2,R_3)} + D_n^{II} \frac{2R_3}{n\beta} \frac{2}{E_n(R_3,R_2)} \right) G(l,n,i) = \\ & \begin{cases} F_l^{I_i} \left(R_2 + \frac{\beta R_1}{l\pi} \left(\frac{R_1}{R_2} \right)^{\frac{l\pi}{\beta}} \right), \text{ radial} \\ F_i^{I_i} R_2 - R_1 \left(\frac{\beta}{l\pi} F_l^{I_i} + \frac{2(-1)^i B_{rem} E_l^{I_i}}{l\pi} \left(\frac{R_1}{R_2} \right)^{\frac{l\pi}{\beta}} \right), \text{ parallel} \\ F_l^{I_i} \left(\left(\left(1 - \alpha_p \frac{\pi}{\alpha} \right) R_2 + \frac{\beta R_1}{l\pi} \left(\left(\frac{l\pi}{\beta} \right)^2 - \alpha_p \frac{\pi}{\alpha} \right) + \left(\frac{R_1}{R_2} \right)^{\frac{l\pi}{\beta}} \right) \right. \\ G_l^{I_i} \left(R_2 + \frac{\beta R_1}{l\pi} \left(\frac{R_1}{R_2} \right)^{\frac{l\pi}{\beta}} \right), \text{ Halbach} \end{cases} \end{aligned} . \tag{6.82}$$

The integrals $F(l,n,i)$ and $G(l,n,i)$ are given on the text to come. Boundary condition (6.75) offers the following two equations by exploiting the orthogonality of functions that the closed form solution of Region I_i has

$$\begin{aligned} A_n^{II} &= \frac{1}{\pi} \sum_{i=1}^{P} \int_{\theta_i - \frac{\beta}{2}}^{\theta_i + \frac{\beta}{2}} \frac{1}{\mu_r} \frac{\partial A_z^{I_i}}{\partial r} \cos(n\theta) d\theta \\ C_n^{II} &= \frac{1}{\pi} \sum_{i=1}^{P} \int_{\theta_i - \frac{\beta}{2}}^{\theta_i + \frac{\beta}{2}} \frac{1}{\mu_r} \frac{\partial A_z^{I_i}}{\partial r} \sin(n\theta) d\theta \end{aligned} , \tag{6.83}$$

which leads to the following two equations. The first for each magnetization pattern of the surface-mounted topology is

$$\begin{aligned} A_n^{II} = & \sum_{i=1}^{P} \sum_{l=1}^{L} A_l^{I_i} \frac{l}{\beta R_2 \mu_r} \frac{E_{l\pi/\beta}(R_2,R_1)}{P_{l\pi/\beta}(R_2,R_1)} F(l,n,i) + \\ & \begin{cases} -\sum_{i=1}^{P} \sum_{l=1}^{L} \frac{F_l^{I_i}}{\pi\mu_r} \left(1 - \left(\frac{R_1}{R_2} \right)^{\frac{l\pi}{\beta}+1} \right) F(l,n,i), \text{ radial} \\ -\sum_{i=1}^{P} \sum_{l=1}^{L} \frac{1}{\pi\mu_r} \left(F_l^{I_i} - \left(\frac{\beta}{l\pi} F_l^{I_i} + \frac{2(-1)^i B_{rem} E_l^{I_i}}{l\pi} \right) \left(\frac{R_1}{R_2} \right)^{\frac{l\pi}{\beta}+1} \right) F(l,n,i) \\ -\sum_{i=1}^{P} \frac{(-1)^i B_{rem}}{\pi\mu_r} I(n,1,i), \text{ parallel} \\ -\sum_{i=1}^{P} \sum_{l=1}^{L} \frac{F_l^{I_i}}{\pi\mu_r} \left(1 - \alpha_p \frac{\pi}{\alpha} - \left(\left(\frac{l\pi}{\beta} \right)^2 - \alpha_p \frac{\pi}{\alpha} \right) \left(\frac{R_1}{R_2} \right)^{\frac{l\pi}{\beta}+1} \right) F(l,n,i) \\ -\sum_{i=1}^{P} \sum_{l=1}^{L} \frac{G_l^{I_i}}{\pi\mu_r} \left(1 - \left(\frac{R_1}{R_2} \right)^{\frac{l\pi}{\beta}+1} \right) F(l,n,i) - \sum_{i=1}^{P} \frac{(-1)^i B_{rem}}{\pi\mu_r} I\left(n, \alpha_p \frac{\pi}{\alpha}, i \right), \text{ Halbach} \end{cases} \end{aligned} , \tag{6.84}$$

and the second one is

$$C_n^{II} = \sum_{i=1}^{P}\sum_{l=1}^{L} A_l^{I_i} \frac{l}{\beta R_2 \mu_r} \frac{E_{l\pi/\beta}(R_2,R_1)}{P_{l\pi/\beta}(R_2,R_1)} G(l,n,i) + \begin{cases} -\sum_{i=1}^{P}\sum_{l=1}^{L} \frac{F_l^{I_i}}{\pi\mu_r}\left(1-\left(\frac{R_1}{R_2}\right)^{\frac{l\pi}{\beta}+1}\right) G(l,n,i), \text{ radial} \\ -\sum_{i=1}^{P}\sum_{l=1}^{L} \frac{1}{\pi\mu_r}\left(F_l^{I_i} - \left(\frac{\beta}{l\pi}F_l^{I_i} + \frac{2(-1)^i B_{rem} E_l^{I_i}}{l\pi}\right)\left(\frac{R_1}{R_2}\right)^{\frac{l\pi}{\beta}+1}\right) G(l,n,i) \\ -\sum_{i=1}^{P} \frac{(-1)^i B_{rem}}{\pi\mu_r} J(n,1,i), \text{ parallel} \\ -\sum_{i=1}^{P}\sum_{l=1}^{L} \frac{F_l^{I_i}}{\pi\mu_r}\left(1-\alpha_p\frac{\pi}{\alpha} - \left(\left(\frac{l\pi}{\beta}\right)^2 - \alpha_p\frac{\pi}{\alpha}\right)\left(\frac{R_1}{R_2}\right)^{\frac{l\pi}{\beta}+1}\right) G(l,n,i) \\ -\sum_{i=1}^{P}\sum_{l=1}^{L} \frac{G_l^{I_i}}{\pi\mu_r}\left(1-\left(\frac{R_1}{R_2}\right)^{\frac{l\pi}{\beta}+1}\right) G(l,n,i) - \sum_{i=1}^{P} \frac{(-1)^i B_{rem}}{\pi\mu_r} J\left(n,\alpha_p\frac{\pi}{\alpha},i\right), \text{ Halbach} \end{cases} . \tag{6.85}$$

The integrals met above are calculated as follows

$$\begin{gathered} \int_{\theta_i-\frac{\beta}{2}}^{\theta_i+\beta/2} \cos\left(\frac{l\pi}{\beta}\left(\theta-\theta_i+\frac{\beta}{2}\right)\right) v_i(\theta)\,d\theta = \\ \cos\left(\frac{l\pi}{\beta}\left(\frac{-\alpha+\beta}{2}\right)\right) - \cos\left(\frac{l\pi}{\beta}\left(\frac{\alpha+\beta}{2}\right)\right) = \\ -2\sin\left(-\frac{l\pi}{\beta}\frac{\alpha}{2}\right)\sin\left(\frac{l\pi}{\beta}\frac{\beta}{2}\right) = \\ 2\sin\left(\frac{l\pi}{2}\frac{\alpha}{\beta}\right)\sin\left(\frac{l\pi}{2}\right) \end{gathered}, \tag{6.86}$$

$$\begin{gathered} \int_{\theta_i-\frac{\beta}{2}}^{\theta_i+\beta/2} \cos(\theta-\theta_i)\cos\left(\frac{l\pi}{\beta}\left(\theta-\theta_i+\frac{\beta}{2}\right)\right) v_i(\theta)\,d\theta = \\ \cos\left(-\frac{\alpha}{2}\right)\cos\left(\frac{l\pi}{\beta}\left(\frac{-\alpha+\beta}{2}\right)\right) - \cos\left(\frac{\alpha}{2}\right)\cos\left(\frac{l\pi}{\beta}\left(\frac{\alpha+\beta}{2}\right)\right) = \\ -2\sin\left(-\frac{l\pi}{\beta}\frac{\alpha}{2}\right)\sin\left(\frac{l\pi}{\beta}\frac{\beta}{2}\right)\cos\left(\frac{\alpha}{2}\right) = \\ 2\sin\left(\frac{l\pi}{2}\frac{\alpha}{\beta}\right)\sin\left(\frac{l\pi}{2}\right)\cos\left(\frac{\alpha}{2}\right) \end{gathered}, \tag{6.87}$$

$$\begin{gathered} \int_{\theta_i-\frac{\beta}{2}}^{\theta_i+\beta/2} \cos\left(\alpha_p\frac{\pi}{\alpha}(\theta-\theta_i)\right)\cos\left(\frac{l\pi}{\beta}\left(\theta-\theta_i+\frac{\beta}{2}\right)\right) v_i(\theta)\,d\theta = \\ \cos\left(-\alpha_p\frac{\pi}{2}\right)\cos\left(\frac{l\pi}{\beta}\left(\frac{-\alpha+\beta}{2}\right)\right) - \cos\left(\alpha_p\frac{\pi}{2}\right)\cos\left(\frac{l\pi}{\beta}\left(\frac{\alpha+\beta}{2}\right)\right) = \\ -2\sin\left(-\frac{l\pi}{\beta}\frac{\alpha}{2}\right)\sin\left(\frac{l\pi}{\beta}\frac{\beta}{2}\right)\cos\left(\alpha_p\frac{\pi}{2}\right) = \\ 2\sin\left(\frac{l\pi}{2}\frac{\alpha}{\beta}\right)\sin\left(\frac{l\pi}{2}\right)\cos\left(\alpha_p\frac{\pi}{2}\right) \end{gathered}, \tag{6.88}$$

$$\begin{cases} R(n,i) = \int_{\theta_i-\frac{\beta}{2}}^{\theta_i+\frac{\beta}{2}} \cos(n\theta) d\theta = \frac{2}{n} \sin\left(\frac{n\beta}{2}\right) \cos\left(n\theta_i + \frac{n\beta}{2}\right) \\ S(n,i) = \int_{\theta_i-\frac{\beta}{2}}^{\theta_i+\frac{\beta}{2}} \sin(n\theta) d\theta = \frac{2}{n} \sin\left(\frac{n\beta}{2}\right) \sin\left(n\theta_i + \frac{n\beta}{2}\right) \end{cases}, \tag{6.89}$$

$$\begin{cases} F(l,n,i) = \int_{\theta_i-\frac{\beta}{2}}^{\theta_i+\frac{\beta}{2}} \cos(n\theta) \cos\left(\frac{l\pi}{\beta}\left(\theta-\theta_i+\frac{\beta}{2}\right)\right) d\theta = \\ \begin{cases} -\frac{n\beta^2\left((-1)^l \sin(n(\theta_i+\beta)) - \sin(n\theta_i)\right)}{(l\pi)^2-(n\beta)^2}, \text{ if } l\pi \neq n\beta \\ \frac{\beta}{2}\left(\cos(n\theta_i) + \frac{1}{l\pi}\sin(n\beta)\cos(n(\theta_i+\beta))\right), \text{ if } l\pi = n\beta \end{cases} \\ G(l,n,i) = \int_{\theta_i-\frac{\beta}{2}}^{\theta_i+\frac{\beta}{2}} \sin(n\theta) \cos\left(\frac{l\pi}{\beta}\left(\theta-\theta_i+\frac{\beta}{2}\right)\right) d\theta = \\ \begin{cases} \frac{n\beta^2\left((-1)^l \cos(n(\theta_i+\beta)) - \cos(n\theta_i)\right)}{(l\pi)^2-(n\beta)^2}, \text{ if } l\pi \neq n\beta \\ \frac{\beta}{2}\left(\sin(n\theta_i) + \frac{1}{l\pi}\sin(n\beta)\sin(n(\theta_i+\beta))\right), \text{ if } l\pi = n\beta \end{cases} \end{cases}, \tag{6.90}$$

$$E_l^{I_i} = \begin{cases} \int_{\theta_i-\frac{\beta}{2}}^{\theta_i+\frac{\beta}{2}} \sin(\theta-\theta_i) \cos\left(\frac{l\pi}{\beta}\left(\theta-\theta_i+\frac{\beta}{2}\right)\right) u_i(\theta) d\theta = \\ \frac{1}{1+\frac{l\pi}{\beta}} \sin\left(\frac{\alpha}{2}+\frac{l\pi}{2}\frac{\alpha}{\beta}\right) \sin\left(\frac{l\pi}{2}\right) - \frac{1}{1-\frac{l\pi}{\beta}} \sin\left(\frac{\alpha}{2}-\frac{l\pi}{2}\frac{\alpha}{\beta}\right) \sin\left(\frac{l\pi}{2}\right), \text{ parallel} \\ \int_{\theta_i-\frac{\beta}{2}}^{\theta_i+\frac{\beta}{2}} \sin\left(\alpha_p \frac{\pi}{\alpha}(\theta-\theta_i)\right) \cos\left(\frac{l\pi}{\beta}\left(\theta-\theta_i+\frac{\beta}{2}\right)\right) u_i(\theta) d\theta = \\ \begin{cases} \frac{1}{\alpha_p \frac{\pi}{\alpha}+\frac{l\pi}{\beta}} \sin\left(\frac{l\pi}{2}\right) \sin\left(\alpha_p \frac{\pi}{2}+\frac{l\pi}{2}\frac{\alpha}{\beta}\right) - \frac{1}{\alpha_p \frac{\pi}{\alpha}-\frac{l\pi}{\beta}} \sin\left(\frac{l\pi}{2}\right) \sin\left(\alpha_p \frac{\pi}{2}-\frac{l\pi}{2}\frac{\alpha}{\beta}\right), \text{if } \beta\alpha_p \neq l\alpha \\ \sin\left(\frac{\alpha_p \pi \beta}{2\alpha}\right)\left(\frac{\alpha}{2\pi\alpha_p}\sin(\alpha_p\pi) - \frac{\alpha}{2}\right), \text{if } \beta\alpha_p = l\alpha, \text{ Halbach} \end{cases} \end{cases}, \tag{6.91}$$

$$\begin{cases} I(n,1,i) = \int_{\theta_i-\frac{\beta}{2}}^{\theta_i+\frac{\beta}{2}} \cos(n\theta) \sin(\theta-\theta_i) u_i(\theta) d\theta = \\ \begin{cases} \left(\frac{1}{n+1}\sin\left((n+1)\frac{\alpha}{2}\right) - \frac{1}{n-1}\sin\left((n-1)\frac{\alpha}{2}\right)\right)\sin(n\theta_i), \text{if } n \neq 1 \\ \frac{\alpha}{2}\left(\frac{\sin(\alpha)}{\alpha}-1\right)\sin(n\theta_i), \text{if } n = 1 \end{cases} \\ J(n,1,i) = \int_{\theta_i-\frac{\beta}{2}}^{\theta_i+\frac{\beta}{2}} \sin(n\theta) \sin(\theta-\theta_i) u_i(\theta) d\theta \\ \begin{cases} -\left(\frac{1}{n+1}\sin\left((n+1)\frac{\alpha}{2}\right) - \frac{1}{n-1}\sin\left((n-1)\frac{\alpha}{2}\right)\right)\cos(n\theta_i), \text{if } n \neq 1 \\ -\frac{\alpha}{2}\left(\frac{\sin(\alpha)}{\alpha}-1\right)\cos(n\theta_i), \text{if } n = 1 \end{cases} \end{cases} \tag{6.92}$$

and

$$\begin{cases} I\left(n,\alpha_p\frac{\pi}{\alpha},i\right)=\int_{\theta_i-\frac{\beta}{2}}^{\theta_i+\frac{\beta}{2}}\cos\left(n\theta\right)\sin\left(\alpha_p\frac{\pi}{\alpha}\left(\theta-\theta_i\right)\right)u_i\left(\theta\right)d\theta= \\ \begin{cases}\left(\frac{1}{n+\alpha_p\frac{\pi}{\alpha_p i}}\sin\left(n\frac{\alpha}{2}+\alpha_p\frac{\pi}{2}\right)-\frac{1}{n-\alpha_p\frac{\pi}{\alpha_p i}}\sin\left(n\frac{\alpha}{2}-\alpha_p\frac{\pi}{2}\right)\right)\sin\left(n\theta_i\right),\text{if } n\neq\pi\alpha_p \\ \frac{\alpha}{2}\left(\frac{\sin(\alpha)}{\alpha}-1\right)\sin\left(n\theta_i\right),\text{if } n=\pi\alpha_p\end{cases} \\ J\left(n,\alpha_p\frac{\pi}{\alpha},i\right)=\int_{\theta_i-\frac{\beta}{2}}^{\theta_i+\frac{\beta}{2}}\sin\left(n\theta\right)\sin\left(\alpha_p\frac{\pi}{\alpha}\left(\theta-\theta_i\right)\right)u_i\left(\theta\right)d\theta \\ \begin{cases}-\left(\frac{1}{n+\alpha_p\frac{\pi}{\alpha_p}}\sin\left(n\frac{\alpha}{2}+\alpha_p\frac{\pi}{2}\right)-\frac{1}{n-\alpha_p\frac{\pi}{\alpha_p}}\sin\left(n\frac{\alpha}{2}-\alpha_p\frac{\pi}{2}\right)\right)\cos\left(n\theta_i\right),\text{if } n\alpha\neq\pi\alpha_p \\ -\frac{\alpha}{2}\left(\frac{\sin(\alpha)}{\alpha}-1\right)\cos\left(n\theta_i\right),\text{if } n\alpha=\pi\alpha_p\end{cases}\end{cases}. \tag{6.93}$$

6.8.2 Surface-inset permanent-magnet machine Region I_i

For the machine with surface-inset magnets, the equations that connect the air gap with the magnet region are developed similarly to the surface-mounted magnet machine topology. Equation (6.72) produces the following two equations

$$\begin{aligned} A_0^{I_i}=&\sum_{n=1}^{N}\left(A_n^{II}\frac{R_2}{n\alpha}\frac{P_n(R_2,R_3)}{E_n(R_2,R_3)}+B_n^{II}\frac{R_3}{n\alpha}\frac{2}{E_n(R_3,R_2)}\right)R(n,i)+ \\ &\sum_{n=1}^{N}\left(C_n^{II}\frac{R_2}{n\alpha}\frac{P_n(R_2,R_3)}{E_n(R_2,R_3)}+D_n^{II}\frac{R_3}{n\alpha}\frac{2}{E_n(R_3,R_2)}\right)S(n,i)\end{aligned}, \tag{6.94}$$

and

$$\begin{aligned} A_l^{I_i}=&\sum_{n=1}^{N}\left(A_n^{II}\frac{2R_2}{n\alpha}\frac{P_n(R_2,R_3)}{E_n(R_2,R_3)}+B_n^{II}\frac{2R_3}{n\alpha}\frac{2}{E_n(R_3,R_2)}\right)F(l,n,i)+ \\ &\sum_{n=1}^{N}\left(C_n^{II}\frac{2R_2}{n\alpha}\frac{P_n(R_2,R_3)}{E_n(R_2,R_3)}+D_n^{II}\frac{2R_3}{n\alpha}\frac{2}{E_n(R_3,R_2)}\right)G(l,n,i)= \\ &\begin{cases}F_l^{I_i}\left(R_2+\frac{\alpha R_1}{l\pi}\left(\frac{R_1}{R_2}\right)^{\frac{l\pi}{\alpha}}\right),\text{ radial} \\ F_i^{I_i}R_2,\text{ parallel} \\ F_l^{I_i}\left(\left(\left(1-\alpha_p\frac{\pi}{\alpha}\right)R_2+\frac{\alpha R_1}{l\pi}\left(\left(\frac{l\pi}{\alpha}\right)^2-\alpha_p\frac{\pi}{\alpha}\right)\left(\frac{R_1}{R_2}\right)^{\frac{l\pi}{\alpha}}\right)\right. \\ \left.+G_l^{I_i}\left(R_2+\frac{\alpha R_1}{l\pi}\left(\frac{R_1}{R_2}\right)^{\frac{l\pi}{\alpha}}\right),\text{ Halbach}\right.\end{cases}\end{aligned}. \tag{6.95}$$

Equation (6.75) produces the following two equations

$$A_n^{II} = \sum_{i=1}^{P}\sum_{l=1}^{L} A_l^{I_i} \frac{l}{\alpha R_2 \mu_r} \frac{E_{l\pi/\alpha}(R_2,R_1)}{P_{l\pi/\alpha}(R_2,R_1)} F(l,n,i) + \begin{cases} -\sum_{i=1}^{P}\sum_{l=1}^{L} \frac{F_l^{I_i}}{\pi\mu_r}\left(1-\left(\frac{R_1}{R_2}\right)^{\frac{l\pi}{\alpha}+1}\right) F(l,n,i), & \text{radial} \\ -\sum_{i=1}^{P}\sum_{l=1}^{L} \frac{F_l^{I_i}}{\pi\mu_r} F(l,n,i) - \sum_{i=1}^{P} \frac{(-1)^i B_{rem}}{\pi\mu_r} I(n,1,i), & \text{parallel} \\ -\sum_{i=1}^{P}\sum_{l=1}^{L} \frac{F_l^{I_i}}{\pi\mu_r}\left(1-\alpha_p\frac{\pi}{\alpha}-\left(\left(\frac{l\pi}{\alpha}\right)^2-\alpha_p\frac{\pi}{\alpha}\right)\left(\frac{R_1}{R_2}\right)^{\frac{l\pi}{\alpha}+1}\right) F(l,n,i) & \\ -\sum_{i=1}^{P}\sum_{l=1}^{L} \frac{G_l^{I_i}}{\pi\mu_r}\left(1-\left(\frac{R_1}{R_2}\right)^{\frac{l\pi}{\alpha}+1}\right) F(l,n,i) - \sum_{i=1}^{P} \frac{(-1)^i B_{rem}}{\pi\mu_r} I\left(n,\alpha_p\frac{\pi}{\alpha},i\right), & \text{Halbach} \end{cases} , \tag{6.96}$$

and

$$C_n^{II} = \sum_{i=1}^{P}\sum_{l=1}^{L} A_l^{I_i} \frac{l}{\alpha R_2 \mu_r} \frac{E_{l\pi/\alpha}(R_2,R_1)}{P_{l\pi/\alpha}(R_2,R_1)} G(l,n,i) \begin{cases} -\sum_{i=1}^{P}\sum_{l=1}^{L} \frac{F_l^{I_i}}{\pi\mu_r}\left(1-\left(\frac{R_1}{R_2}\right)^{\frac{l\pi}{\alpha}+1}\right) G(l,n,i), & \text{radial} \\ -\sum_{i=1}^{P}\sum_{l=1}^{L} \frac{F_l^{I_i}}{\pi\mu_r} G(l,n,i) - \sum_{i=1}^{P} \frac{(-1)^i B_{rem}}{\pi\mu_r} J(n,1,i), & \text{parallel} \\ -\sum_{i=1}^{P}\sum_{l=1}^{L} \frac{F_l^{I_i}}{\pi\mu_r}\left(1-\alpha_p\frac{\pi}{\alpha}-\left(\left(\frac{l\pi}{\alpha}\right)^2-\alpha_p\frac{\pi}{\alpha}\right)\left(\frac{R_1}{R_2}\right)^{\frac{l\pi}{\alpha}+1}\right) G(l,n,i) & \\ -\sum_{i=1}^{P}\sum_{l=1}^{L} \frac{G_l^{I_i}}{\pi\mu_r}\left(1-\left(\frac{R_1}{R_2}\right)^{\frac{l\pi}{\alpha}+1}\right) G(l,n,i) - \sum_{i=1}^{P} \frac{(-1)^i B_{rem}}{\pi\mu_r} J\left(n,\alpha_p\frac{\pi}{\alpha},i\right), & \text{Halbach} \end{cases} . \tag{6.97}$$

The integrals appearing on the equations (6.94, 6.95, 6.96, 6.97) can be calculated with similar way, that were calculated in the previous case

$$
\begin{cases}
\int_{\theta_i-\frac{\alpha}{2}}^{\theta_i+\frac{\alpha}{2}} \cos\left(\frac{l\pi}{\alpha}\left(\theta-\theta_i+\frac{\alpha}{2}\right)\right) v_i(\theta) = \\
\cos\left(\frac{l\pi}{\alpha}\left(\theta_i-\frac{\alpha}{2}+\theta_i+\frac{\alpha}{2}\right)\right) - \cos\left(\frac{l\pi}{\alpha}\left(\theta_i+\frac{\alpha}{2}+\theta_i+\frac{\alpha}{2}\right)\right) = \\
\cos(0) - \cos(l\pi) = 1-(-1)^l \\
\int_{\theta_i-\frac{\alpha}{2}}^{\theta_i+\frac{\alpha}{2}} \cos(\theta-\theta_i)\cos\left(\frac{l\pi}{\alpha}\left(\theta-\theta_i+\frac{\alpha}{2}\right)\right) v_i(\theta) = \\
\cos\left(-\frac{\alpha}{2}\right)\cos\left(\frac{l\pi}{\alpha}\left(\theta_i-\frac{\alpha}{2}+\theta_i+\frac{\alpha}{2}\right)\right) - \cos\left(-\frac{\alpha}{2}\right)\cos\left(\frac{l\pi}{\alpha}\left(\theta_i+\frac{\alpha}{2}+\theta_i+\frac{\alpha}{2}\right)\right) = \\
(\cos(0)-\cos(l\pi))\cos\left(\frac{\alpha}{2}\right) = (1-(-1)^l)\cos\left(\frac{\alpha}{2}\right) \\
\int_{\theta_i-\frac{\alpha}{2}}^{\theta_i+\frac{\alpha}{2}} \cos\left(\alpha_p\frac{\pi}{\alpha}(\theta-\theta_i)\right)\cos\left(\frac{l\pi}{\alpha}\left(\theta-\theta_i+\frac{\alpha}{2}\right)\right) v_i(\theta) = \\
\cos\left(-\alpha_p\frac{\pi}{2}\right)\cos\left(\frac{l\pi}{\alpha}\left(\theta_i-\frac{\alpha}{2}+\theta_i+\frac{\alpha}{2}\right)\right) - \cos\left(\alpha_p\frac{\pi}{2}\right)\cos\left(\frac{l\pi}{\alpha}\left(\theta_i+\frac{\alpha}{2}+\theta_i+\frac{\alpha}{2}\right)\right) = \\
(\cos(0)-\cos(l\pi))\cos\left(\alpha_p\frac{\pi}{2}\right) = (1-(-1)^l)\cos\left(\alpha_p\frac{\pi}{2}\right) \\
R(n,i) = \int_{\theta_i-\frac{\alpha}{2}}^{\theta_i-\frac{\alpha}{2}} \cos(n\theta)d\theta \\
S(n,i) = \int_{\theta_i-\frac{\alpha}{2}}^{\theta_i-\frac{\alpha}{2}} \sin(n\theta)d\theta \\
F(l,n,i) = \int_{\theta_i-\frac{\alpha}{2}}^{\theta_i-\frac{\alpha}{2}} \cos(n\theta)\cos\left(\frac{l\pi}{\alpha}\left(\theta-\theta_i+\frac{\alpha}{2}\right)\right)d\theta \\
G(l,n,i) = \int_{\theta_i-\frac{\alpha}{2}}^{\theta_i-\frac{\alpha}{2}} \sin(n\theta)\cos\left(\frac{l\pi}{\alpha}\left(\theta-\theta_i+\frac{\alpha}{2}\right)\right)d\theta \\
E_l^{I_i} = \int_{\theta_i-\frac{\alpha}{2}}^{\theta_i+\frac{\alpha}{2}} \sin\left(\alpha_p\frac{\pi}{\alpha}(\theta-\theta_i)\right)\cos\left(\frac{l\pi}{\alpha}\left(\theta-\theta_i+\frac{\alpha}{2}\right)\right)u_i(\theta)\,d\theta, \text{ Halbach} \\
I(n,1,i) = \int_{\theta_i-\frac{\alpha}{2}}^{\theta_i+\frac{\alpha}{2}} \cos(n\theta)\sin(\theta-\theta_i)u_i(\theta)\,d\theta \\
J(n,1,i) = \int_{\theta_i-\frac{\alpha}{2}}^{\theta_i+\frac{\alpha}{2}} \sin(n\theta)\sin(\theta-\theta_i)u_i(\theta)\,d\theta \\
I\left(n,\alpha_p\frac{\pi}{\alpha},i\right) = \int_{\theta_i-\frac{\alpha}{2}}^{\theta_i+\frac{\alpha}{2}} \cos(n\theta)\sin\left(\alpha_p\frac{\pi}{\alpha}(\theta-\theta_i)\right)u_i(\theta)\,d\theta \\
J\left(n,\alpha_p\frac{\pi}{\alpha},i\right) = \int_{\theta_i-\frac{\alpha}{2}}^{\theta_i+\frac{\alpha}{2}} \sin(n\theta)\sin\left(\alpha_p\frac{\pi}{\alpha}(\theta-\theta_i)\right)u_i(\theta)\,d\theta
\end{cases}
\tag{6.98}
$$

6.9 Equations for the interface between Region II with III_j and III_j with IV_j

Interface condition (6.76) produces the two following equations [116]

$$
\begin{aligned}
B_n^{II} &= \frac{1}{\pi}\sum_{j=1}^{Q}\int_{\theta_j-\frac{\gamma}{2}}^{\theta_j+\frac{\gamma}{2}} \frac{\partial A_z^{IV_j}}{\partial r}\cos(n\theta)d\theta \\
D_n^{II} &= \frac{1}{\pi}\sum_{j=1}^{Q}\int_{\theta_j-\frac{\gamma}{2}}^{\theta_j+\frac{\gamma}{2}} \frac{\partial A_z^{IV_j}}{\partial r}\sin(n\theta)d\theta
\end{aligned}
\tag{6.99}
$$

$$B_n^{II} = \sum_{j=1}^{Q}\sum_{k=1}^{\infty}\frac{k}{\gamma R_3}\left(A_k^{III_j}\frac{P_{k\pi/\gamma}(R_3,R_4)}{E_{k\pi/\gamma}(R_3,R_4)} - B_k^{III_j}\frac{2}{E_{k\pi/\gamma}(R_3,R_4)}\right)F(k,n,j) + \sum_{j=1}^{Q}\frac{B_0^{III_j}}{\pi R_3}R(n,j) \tag{6.100}$$

and

$$D_n^{II} = \sum_{j=1}^{Q}\sum_{k=1}^{\infty}\frac{k}{\gamma R_3}\left(A_k^{III_j}\frac{P_{k\pi/\gamma}(R_3,R_4)}{E_{k\pi/\gamma}(R_3,R_4)} - B_k^{III_j}\frac{2}{E_{k\pi/\gamma}(R_3,R_4)}\right)G(k,n,j) + \sum_{j=1}^{Q}\frac{B_0^{III_j}}{\pi R_3}S(n,j) \tag{6.101}$$

Interface condition (6.73) produces the two following equations [116]

$$\begin{aligned} A_0^{III_j} = &\sum_{n=1}^{\infty}\left(A_n^{II}\frac{R_2}{n\gamma}\frac{2}{E_n(R_2,R_3)} + B_n^{II}\frac{R_3}{n\gamma}\frac{P_n(R_3,R_2)}{E_n(R_3,R_2)}\right)R(n,j) + \\ &\sum_{n=1}^{\infty}\left(A_n^{II}\frac{R_2}{n\gamma}\frac{2}{E_n(R_2,R_3)} + B_n^{II}\frac{R_3}{n\gamma}\frac{P_n(R_3,R_2)}{E_n(R_3,R_2)}\right)S(n,j) \\ &- B_0^{III_j}\ln(R_3) \end{aligned} \tag{6.102}$$

and

$$\begin{aligned} A_k^{III_j} = &\sum_{n=1}^{\infty}\left(A_n^{II}\frac{R_2}{n\gamma}\frac{2}{E_n(R_2,R_3)} + B_n^{II}\frac{R_3}{n\gamma}\frac{P_n(R_3,R_2)}{E_n(R_3,R_2)}\right)F(k,n,j) + \\ &\sum_{n=1}^{\infty}\left(A_n^{II}\frac{R_2}{n\gamma}\frac{2}{E_n(R_2,R_3)} + B_n^{II}\frac{R_3}{n\gamma}\frac{P_n(R_3,R_2)}{E_n(R_3,R_2)}\right)G(k,n,j) \end{aligned} \tag{6.103}$$

Equation (6.74) produces the two following equations [116]

$$\begin{aligned} A_0^{IV_j} = &A_0^{III_j} + B_0^{III_j}\ln(R_4) \\ &+ \sum_{m=1}^{\infty}A_m^{IV_j}\frac{2R_4}{\gamma}\left(\frac{\delta}{m\pi}\right)^2\frac{P_{m\pi/\gamma}(R_4,R_5)}{E_{m\pi/\gamma}(R_4,R_5)}\sin\left(\frac{m\pi\gamma}{2\delta}\right)\cos\left(\frac{m\pi}{2}\right) \\ &- \frac{1}{2}\mu_0 J_j\left(R_5^2\ln(R_4) - \frac{R_4^2}{2}\right) \end{aligned} \tag{6.104}$$

and

$$B_k^{III_j} = \sum_{m=1}^{\infty} \left(A_m^{IV_j} \frac{2\delta R_4}{m\pi\gamma} \frac{P_{m\pi/\delta}(R_4,R_5)}{E_{m\pi/\gamma}(R_4,R_5)} \right) H(m,k). \tag{6.105}$$

Lastly, interface condition (6.77) produces the following two equations [116]

$$B_0^{III_j} = \frac{\delta}{\gamma}\frac{1}{2}\mu_0 J_j (R_5^2 - R_4^2) \tag{6.106}$$

and

$$\begin{aligned} A_m^{IV_j} =& B_0^{III_j} \frac{4}{m\pi R_4} \sin\left(\frac{m\pi\beta}{2\delta}\right) \cos\left(\frac{m\pi}{2}\right) \\ &+ \sum_{k=1}^{\infty} \left(A_k^{III_j} \frac{2}{E_{k\pi/\gamma}(R_3,R_4)} - B_k^{III_j} \frac{P_{k\pi/\gamma}(R_4,R_3)}{E_{k\pi/\gamma}(R_3,R_4)} \right) \frac{2k\pi}{\delta\gamma R_4} H(m,k) \end{aligned}, \tag{6.107}$$

which the integral $H(m,k)$ is equal to

$$\begin{cases} H(m,k) = \int_{\theta_j-\frac{\gamma}{2}}^{\theta_j+\frac{\gamma}{2}} \cos\left(\frac{k\pi}{\gamma}\left(\theta-\theta_j+\frac{\gamma}{2}\right)\right) \cdot \cos\left(\frac{m\pi}{\delta}\left(\theta-\theta_j+\frac{\delta}{2}\right)\right) d\theta = \\ \begin{cases} \frac{\frac{m\pi}{\delta}}{\left(\frac{m\pi}{\delta}\right)^2-\left(\frac{k\pi}{\gamma}\right)^2} \cdot \left((-1)^k \sin\left(\frac{m\pi}{2\delta}(\gamma+\delta)\right) + \sin\left(\frac{m\pi}{2\delta}(\gamma-\delta)\right)\right), \text{ if } m\beta \neq k\delta \\ \frac{\gamma}{2}\cos\left(\frac{k\pi}{2\gamma}(\gamma-\delta)\right), \text{ if } m\beta = k\delta \end{cases} \end{cases} . \tag{6.108}$$

The coefficients to be determined are $A_0^{I_i}, A_l^{I_i}, A_n^{II}, B_n^{II}, C_n^{II}, D_n^{II}, A_0^{III_j}, B_0^{III_j}, A_k^{III_j}, B_k^{III_j}, A_0^{IV_j}$ and $A_m^{IV_j}$. The constants $A_0^{I_i}$, $A_l^{I_i}$, A_n^{II} and C_n^{II}, which couple the constants of the air-gap with the ones of the magnet region, are calculated using the dependent equations (6.80, 6.82, 6.84, 6.85) for the machine with the surface-mounted magnets and equations (6.94, 6.95, 6.96, 6.97) for the machine with the surface-inset magnets. The constants $B_n^{II}, D_n^{II}, A_0^{III_j}, B_0^{III_j}, A_k^{III_j}$, $B_k^{III_j}, A_0^{IV_j}$ and $A_m^{IV_j}$, which couple the constants of the air-gap with the ones of the slot-opening and slot subdomain are (6.100, 6.101, 6.102, 6.103, 6.104, 6.105, 6.106, 6.107). The number of the unknown coefficients is 12, which is the same as the number of equations. By writing the above equations in a matrix form in programming software which offers calculations using array operations, the unknown coefficients can be determined. An algorithm was developed using the software MATLAB in Appendix B.

6.10 Air-gap magnetic field calculation

In this section, the analytical solutions for the air-gap magnetic field distribution are compared with the numerical ones obtained by 2-D FEA. A permanent-magnet motor with the specifications of Table 6.1 was designed using the commercial software package Simcenter MagNet of Infologic Design and Siemens. The two components of the air-gap magnetic flux density are calculated by substituting (6.51) to (6.6). An overlapping winding was considered since this is the type of winding that corresponds to the optimal pitch factor for the specific number of slots and poles. The number of triangular elements for each magneto-static solve was 40,780 with a polynomial order of 4 with a computational time of 10 seconds. In the analytical model for a number of harmonics equal to 250 for the air gap and half for the magnet, slot-opening and slot regions, the computational time is 2 seconds which is 5 times less than the FEA model.

6.10.1 No-load flux density distribution

The no-load flux density is the flux density which depends on the magnet shape, its magnetisation and the iron boundaries between the rotor and the stator.

Surface-mounted permanent-magnet machine topology

Figure 6.5 illustrates the results of the analytical model and the FEA for the no-load flux density components of each magnetisation distribution for the air-gap region. The magnets have a residual flux density, and the current density in each slot is zero. The analytical results are in excellent agreement with the ones obtained by FEA for all the magnetisation cases. In the region where the air gap faces the air-space of the magnet region, the magnetic flux density does not drop to zero suddenly compared to the surface-inset magnet topology, as it will be inspected in the text to come.

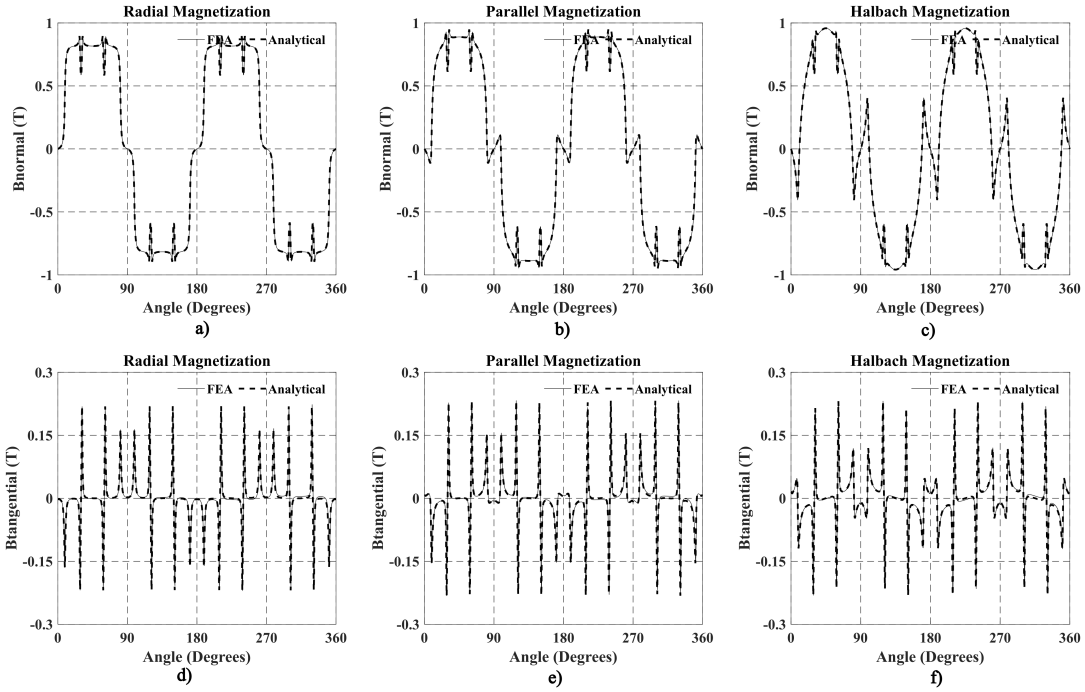

Figure 6.5: FEA and analytical results of the normal and tangential components of the no-load flux density for the air-gap region with slotted stator (Q=12) for a), d) radial, parallel b), e) and c), f) Halbach magnetisation pattern for the machine with surface-mounted magnets.

Surface-inset permanent-magnet machine topology

Figure 6.6 illustrates the results of the analytical model and the FEA for the no-load flux density components of each magnetisation distribution for the air-gap region. It is visible that the magnetic flux density components in the angles where there is the iron of infinite magnetic permeability are zero. The latter happens because the magnetic field intensity vanishes on the iron. The analytical results are in excellent agreement with the ones obtained by FEA for all the magnetisation cases. For both cases of magnets, it is evident that in the angles where there are slots, there is a dip in the radial component of the magnetic flux density.

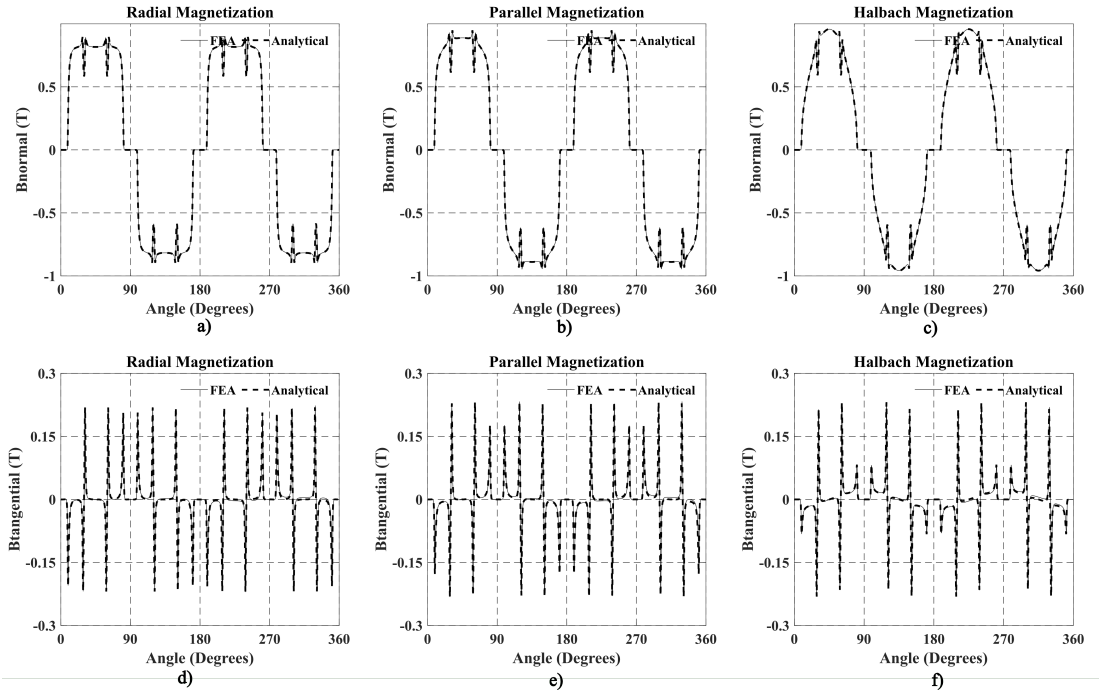

Figure 6.6: FEA and analytical results of the normal and tangential components of the no-load flux density for the air-gap region with slotted stator (Q=12) for a), d) radial, parallel b), e) and c), f) Halbach magnetisation pattern for the machine with surface-inset magnets.

6.10.2 On-load flux density distribution

The on-load flux density is the flux density which depends not only on the features of the no-load magnetic flux density but also on the currents in the slots. It is a superposition of the permanent-magnet field and the armature reaction field. Since the spatial distribution of the magnetic flux density is studied, an instant of the 3-phase currents waveform is used. Specifically, the current density in each phase is $J_a = -I/S_{slot}$, $J_b = I/(2S_{slot})$ and $J_c = I/(2S_{slot})$, which corresponds to an instant of the armature reaction field. S_{slot} is the area of one slot. Figures 6.7 and 6.8 present the on-load magnetic flux density distribution for the surface-mounted and -inset magnet machine topology, respectively.

Surface-mounted permanent-magnet machine topology

Figure 6.7 presents the results for the on-load flux density of each magnetisation pattern for the surface-mounted permanent-magnet machine. It is evident that the armature reaction field greatly influences the air-gap magnetic flux density. These results are in adequate agreement with the numerical ones for this case as well.

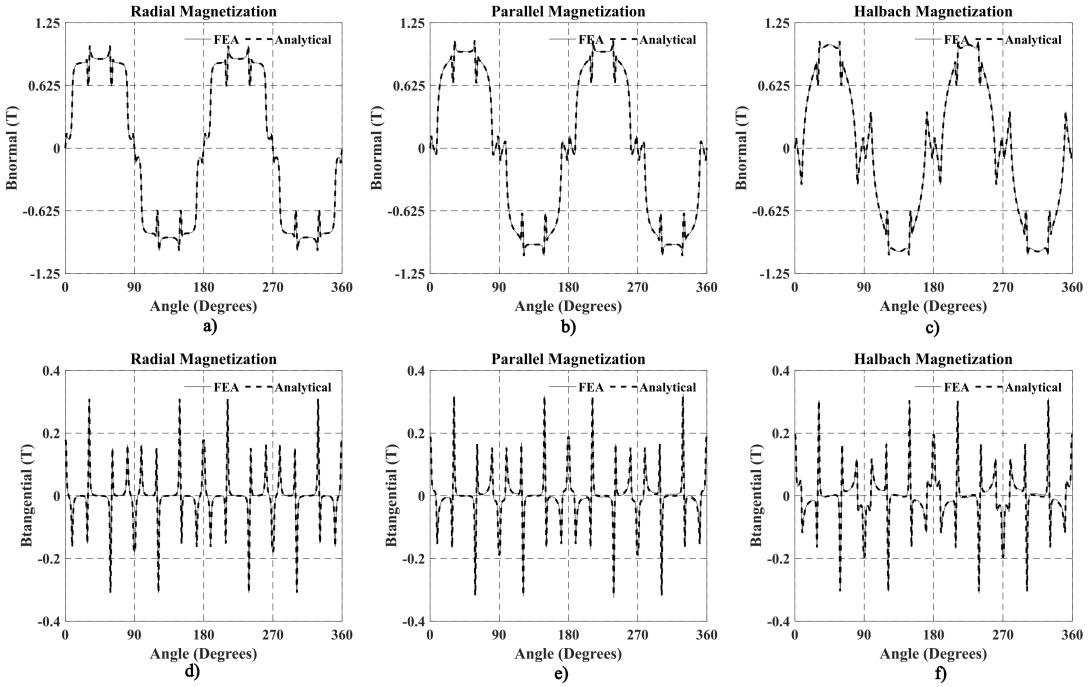

Figure 6.7: FEA and analytical results of the normal and tangential components of the on-load flux density for the air-gap region with slotted stator (Q=12) for a), d) radial, parallel b), e) and c), f) Halbach magnetisation pattern for the machine with surface-mounted magnets $(3A/mm^2)$.

Surface-inset permanent-magnet machine topology

Figure 6.8 presents the results for the on-load flux density components when the current density of each magnetisation pattern for the surface-inset permanent-magnet machine. These results are in excellent agreement with the numerical ones for this case as well. In the regions where the air-gap faces the iron material of the rotor, the air-gap magnetic flux density displays only the armature reaction field.

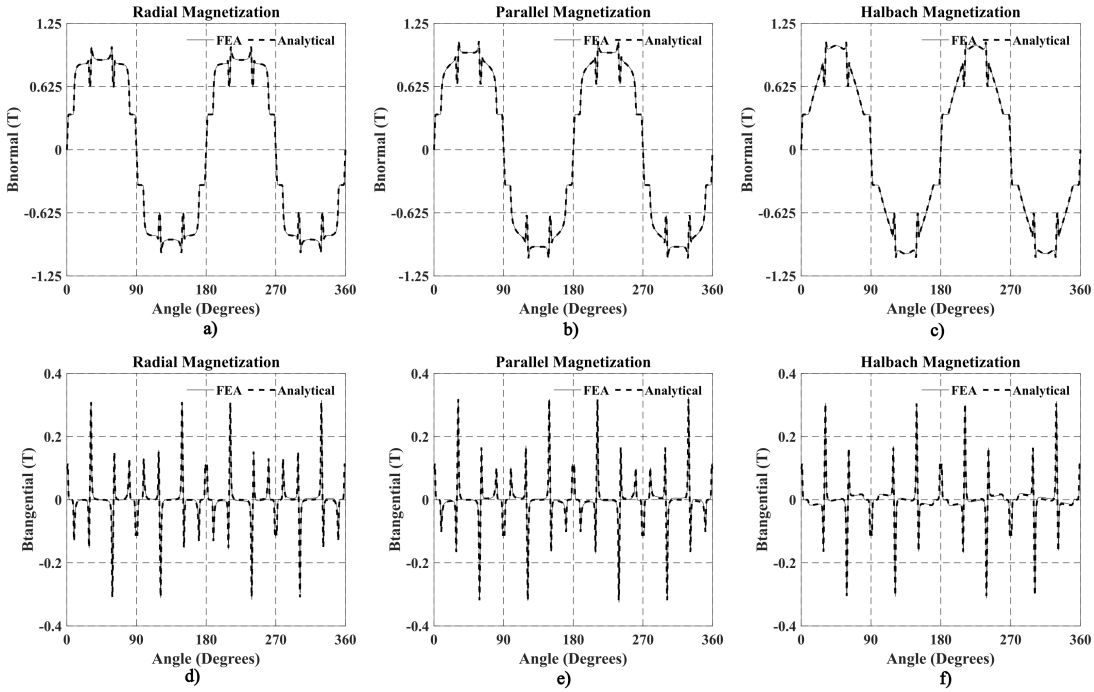

Figure 6.8: FEA and analytical results of the normal and tangential components of the on-load flux density for the air-gap region with slotted stator (Q=12) for a), d) radial, parallel b), e) and c), f) Halbach magnetisation pattern for the machine with surface-inset magnets $(3A/mm^2)$.

6.11 Torque and Back-EMF calculation

The types of torque and the Back-EMF are considered key parameters for the study of permanent-magnet machines as they are the nameplate parameters. More specifically, the mean value of output torque and the line-to-line voltage is two nameplate parameters. The magnetic flux density for every rotor angle is paramount for calculating these parameters.

6.12 Cogging-torque and Back-EMF

The magnetic flux for the j$^{\text{th}}$ slot can be averaged by calculating the surface integral of the slot region over the geometric slot area

$$\Phi^{IV_j}(\theta_{0r}) = \frac{L_{st}}{S_{slot}} \int_{R_4}^{R_5} \int_{\theta_j - \frac{\delta}{2}}^{\theta_j + \frac{\delta}{2}} A_z^{IV_j}(r,\theta) r \, dr d\theta, \tag{6.109}$$

which yields that the magnetic flux of each tooth is

$$\Phi^{IV_j}(\theta_{0r}) = L_{st}A_0^{IV_j} + \frac{\mu_0 J_j \delta L_{st}}{R_5^2 - R_4^2}\left(R_5^4\left(\ln R_5 - \frac{5}{8}\right) + R_5^2 R_4^2\left(\frac{1}{2} - \ln R_4\right) + \frac{1}{8}R_4^4\right), \quad (6.110)$$

where L_{st} and S_{slot} are the axial length and the area of a slot, respectively. The flux-linkage matrix

$$\begin{bmatrix}\Psi_a \\ \Psi_b \\ \Psi_c\end{bmatrix} = N_{ph}[C]\begin{bmatrix}\Phi_1 & \dots & \Phi_{Q-1} & \Phi_Q\end{bmatrix}^T, \quad (6.111)$$

with winding matrix equal to

$$C = \begin{bmatrix}1 & 0 & 0 & -1 & 0 & 0 & 1 & 0 & 0 & -1 & 0 & 0 \\ 0 & 0 & 1 & 0 & 0 & -1 & 0 & 0 & 1 & 0 & 0 & -1 \\ 0 & -1 & 0 & 0 & 1 & 0 & 0 & -1 & 0 & 0 & 1 & 0\end{bmatrix} \quad (6.112)$$

for overlapping winding. N_{ph} is the total number of turns that are connected in series on a phase. The back-EMF vector emerges with numerical differentiation of the phase flux-linkage signal i.e.

$$\begin{bmatrix}\mathscr{E}_a \\ \mathscr{E}_b \\ \mathscr{E}_c\end{bmatrix} = \omega_m \frac{d}{d\theta_{0r}}\begin{bmatrix}\Psi_a \\ \Psi_b \\ \Psi_c\end{bmatrix} \quad (6.113)$$

and amplitude is proportional to the mechanical speed of rotation ω_m. To calculate the Back-EMF distribution, a repetition loop is created, which allows the position of the rotor to vary as the repetitions go forward. This repetition is embedded inside another repetition which concerns the magnetic flux produced by each tooth as (6.110) supports. In every repetition, the constant $A_0^{IV_j}$ is calculated for the new rotor position, so a magnetic flux value using (6.110) is obtained every time. Since the Back-EMF is calculated, the current density is zero, so the second term of (6.110) is zero. Then in the same repetition, the flux-linkage matrix is calculated using (6.111), which in this case, the winding matrix (6.112) is used to divide the three phases. The flux linkage also depends proportionally on the total number of turns that are in series per phase. The latter depends on how many coils connect in series. In this case, there are two coils per phase connected in series. The Back-EMF is calculated in a per-turn form for comparison purposes. Also, each slot is considered a full solid conductor, so the fill factor is considered equal to one. The final Back-EMF is calculated employing (6.113), in which the flux-linkage waveform is differentiated with respect to the rotor angle.

The torque is defined as the tangential force created in the air gap between the magnets and the teeth whilst there isn't any current source in the slots. It can be calculated using Maxwell Stress theory and is equal to the following integral for a prespecified rotor position at the middle of the air-gap

Each torque value is calculated by integrating the product of the components of the air-gap magnetic flux density in the mid-radius of the air gap. The appropriate air-gap magnetic flux density components depend on the kind of torque that is to be calculated,. The torque in analytical form is

$$T_\theta(\theta_{0r}) = \frac{L_{st}R_e^2}{\mu_0}\int_0^{2\pi} B_r^{II}(R_e,\theta)B_\theta^{II}(R_e,\theta)\,d\theta. \tag{6.114}$$

By calculating the above integral analytically, the following equation was developed in [116]

$$T_\theta(\theta_{0r}) = \frac{\pi L_{st}R_e^2}{\mu_0}\sum_{n=1}^{\infty}(W_nX_n + Y_nZ_n), \tag{6.115}$$

where

$$\begin{aligned}
W_n &= -A_n^{II}\frac{R_2}{R_e}\frac{P_n(R_e,R_3)}{E_n(R_2,R_3)} - B_n^{II}\frac{R_3}{R_e}\frac{P_n(R_e,R_2)}{E_n(R_3,R_2)}\\
X_n &= -C_n^{II}\frac{R_2}{R_e}\frac{E_n(R_e,R_3)}{E_n(R_2,R_3)} - D_n^{II}\frac{R_3}{R_e}\frac{E_n(R_e,R_2)}{E_n(R_3,R_2)}\\
Y_n &= +C_n^{II}\frac{R_2}{R_e}\frac{P_n(R_e,R_3)}{E_n(R_2,R_3)} + D_n^{II}\frac{R_3}{R_e}\frac{P_n(R_e,R_2)}{E_n(R_3,R_2)}\\
Z_n &= -A_n^{II}\frac{R_2}{R_e}\frac{E_n(R_e,R_3)}{E_n(R_2,R_3)} - B_n^{II}\frac{R_3}{R_e}\frac{E_n(R_e,R_2)}{E_n(R_3,R_2)}
\end{aligned}. \tag{6.116}$$

Equation (6.115) offers the torque at a specific point in the air-gap, summing the spatial harmonics of the air gap. So by varying the rotor angle using a repetition loop, the torque waveform can be calculated.

Surface-mounted permanent-magnet machine topology

The cogging-torque is the tangential force between the rotor component and the stator teeth. To calculate the cogging torque, the rotor angle varies, and at each point, the torque is calculated using (6.115, 6.116) whilst there is no current source in the stator slots. Figure 6.9a, 6.9b and 6.9c present analytical and FEA results of the cogging torque for each magnetisation pattern for the machine with the surface-mounted magnets. It is visible that the magnetisation pattern plays a decisive role in the signal. The Halbach magnetisation pattern offers lower cogging torque. The Halbach magnetisation has the lowest cogging torque. The cogging

torque is the main noise source in surface-mounted permanent-magnet machines, the only component that adds ripple to the mutual torque. However, the electromagnetic torque can have a high torque ripple even when the cogging torque is low. The cogging torque period depends on the number of slots and poles. More specifically, the number of the repeated signals is the Least Common Multiple of number slots and poles. So, in this case, the number of poles is 4, the number of slots is 12, the LCM is 12. The analytical results come in good agreement with the numerical. The coupling of all slots and poles accounts for the analytical solution, so there are no approximations.

Figure 6.9d, 6.9e and 6.9f presents the analytical and numerical results of the Back-EMF for each magnetisation pattern for the machine with the surface-mounted magnets. It is visible that the magnetisation pattern plays an important role in the shape of the Back-EMF waveform. The slotting effect is also noticeable in the Back-EMF waveform. The analytical results come in good agreement with the numerical.

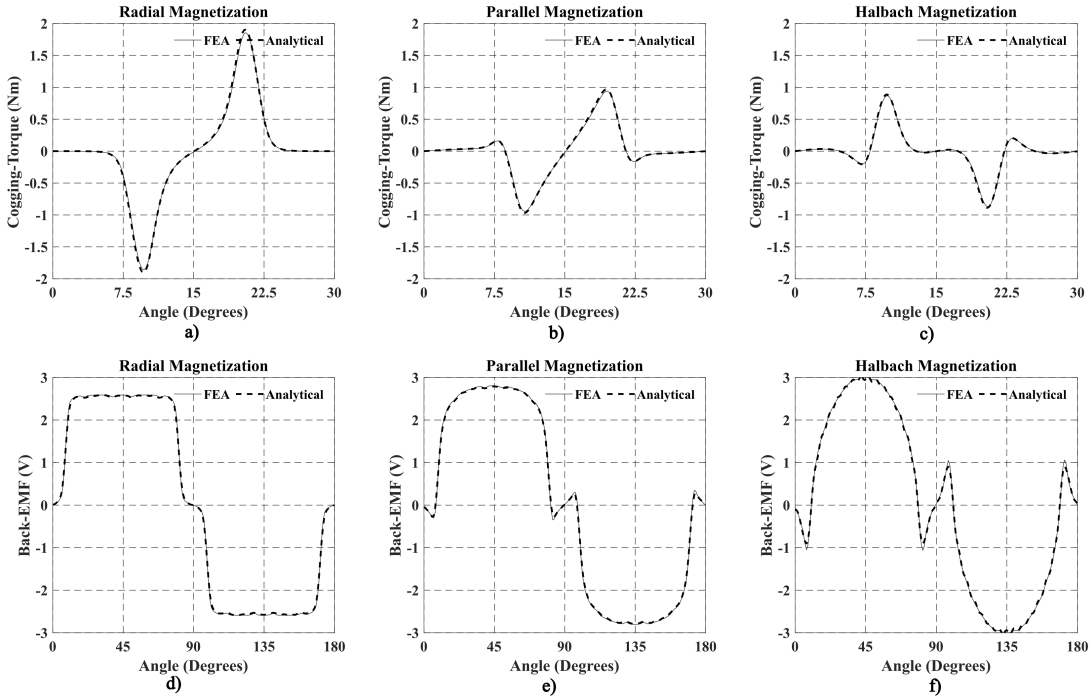

Figure 6.9: FEA and analytical results of the cogging torque and back-EMF considering that the whole slot area is a solid conductor for a), d) radial, b), e) parallel and c), f) Halbach magnetisation pattern for the machine with surface-mounted magnets.

Surface-inset permanent-magnet machine topology

Similarly, Figure 6.9a, 6.9b and 6.9c presents the analytical and numerical results of the cogging torque for each magnetisation pattern for the machine with the surface-inset magnets. Here the cogging torque for the case of the Halbach magnetisation pattern is even lower in amplitude compared to the one calculated for the surface-mounted magnet topology. Figure 6.9d, 6.9e, and 6.9f presents the analytical and numerical results for the Back-EMF waveform. In the arcs where both sides of the air-gap face infinite permeable iron, the Back-EMF takes the value zero.

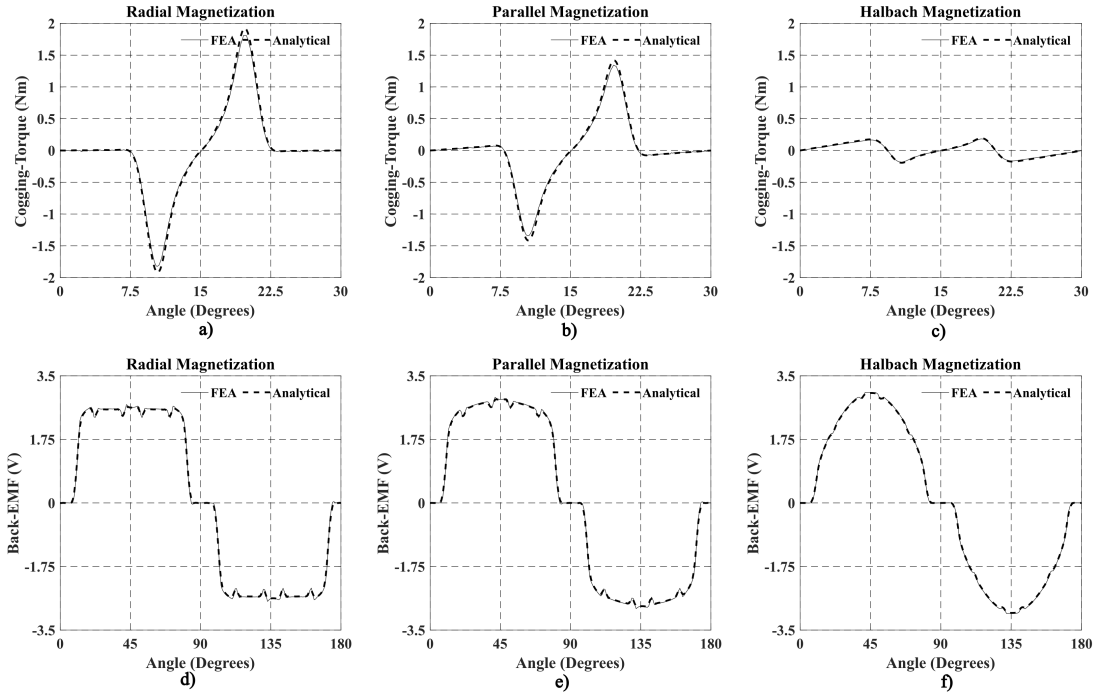

Figure 6.10: FEA and analytical results of the cogging torque and back-EMF considering that the whole slot area is a solid conductor for a), d) radial, b), e) parallel and c), f) Halbach magnetisation pattern for the machine with surface-inset magnets.

6.12.1 Static and electromagnetic torque

Static torque is the torque developed in the air gap when the stator coils carry a constant current, and each value corresponds to an instance of the 3-phase currents waveform. As the rotor rotates, the stator magnetic flux density vector stays constant, so the torque angle varies. This waveform determined the torque capacity of a permanent-magnet motor.

Surface-mounted permanent-magnet machine topology

Figure 6.11a, 6.11b and 6.11c presents the analytical and numerical results for the static torque of each magnetization pattern for surface-mounted magnet topology. The analytical with the numerical results are in good agreement.

The electromagnetic torque is the torque for specified angle delta as the stator creates a rotating magnetic field as the rotor does, and the two fields create a constant torque angle. Figure 6.11d, 6.11e and 6.11f present the analytical and numerical results for the electromagnetic torque of each magnetization pattern for surface-mounted magnet topology. For the case of the Halbach magnetisation pattern, the torque ripple is much higher than the other two patterns. The ripple has to do mostly with the higher order harmonics created by the mutual torque, as the cogging torque has a low value. The analytical results are also here in good agreement with the numerical.

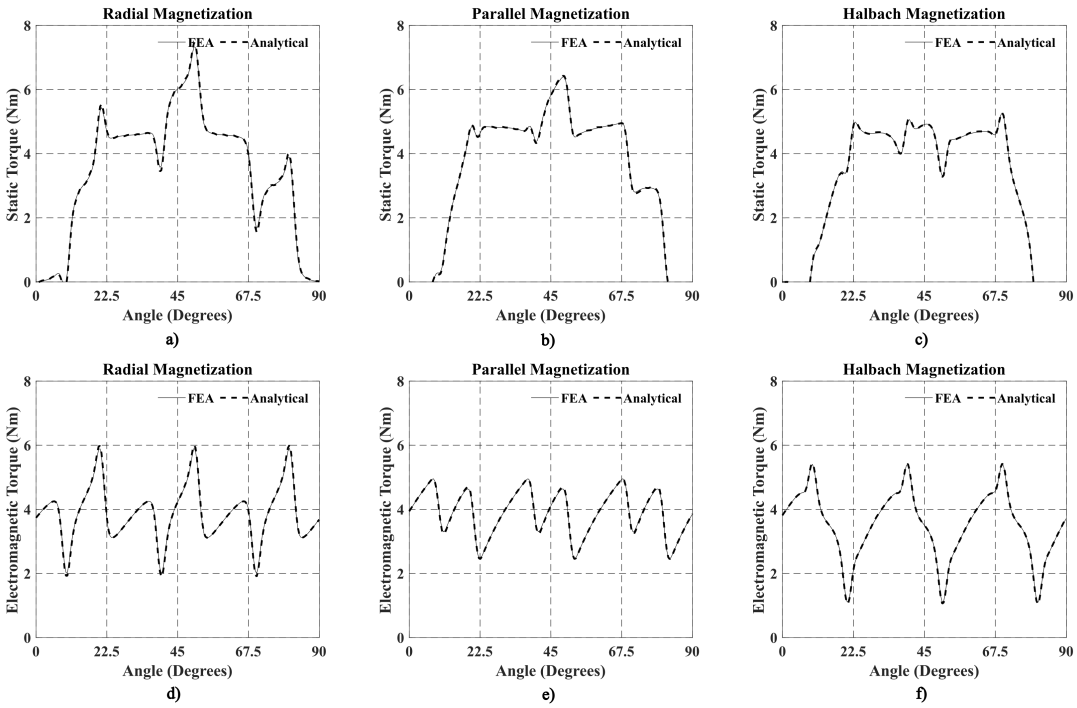

Figure 6.11: FEA and analytical results of the Static and Electromagnetic Torque for a), d) radial, b), e) parallel, and c), f) Halbach magnetisation pattern for the machine with surface-mounted magnets $(1A/mm^2)$.

Surface-inset permanent-magnet machine topology

Figure 6.12a, 6.12b, and 6.12c shows the analytical and numerical results of the static torque as a function of the angle for each magnetisation distribution for the surface-inset magnet topology. It can be seen that where the rotor iron is located, the torque falls rapidly to zero. Figure 6.12d, 6.12e and 6.12f shows the electromagnetic torque of a load for each magnetization pattern of the surface-inset magnet machine. In this case, the Halbach magnetisation pattern offers the lowest torque ripple. The analytical model results are in excellent agreement with the numerical results in both cases.

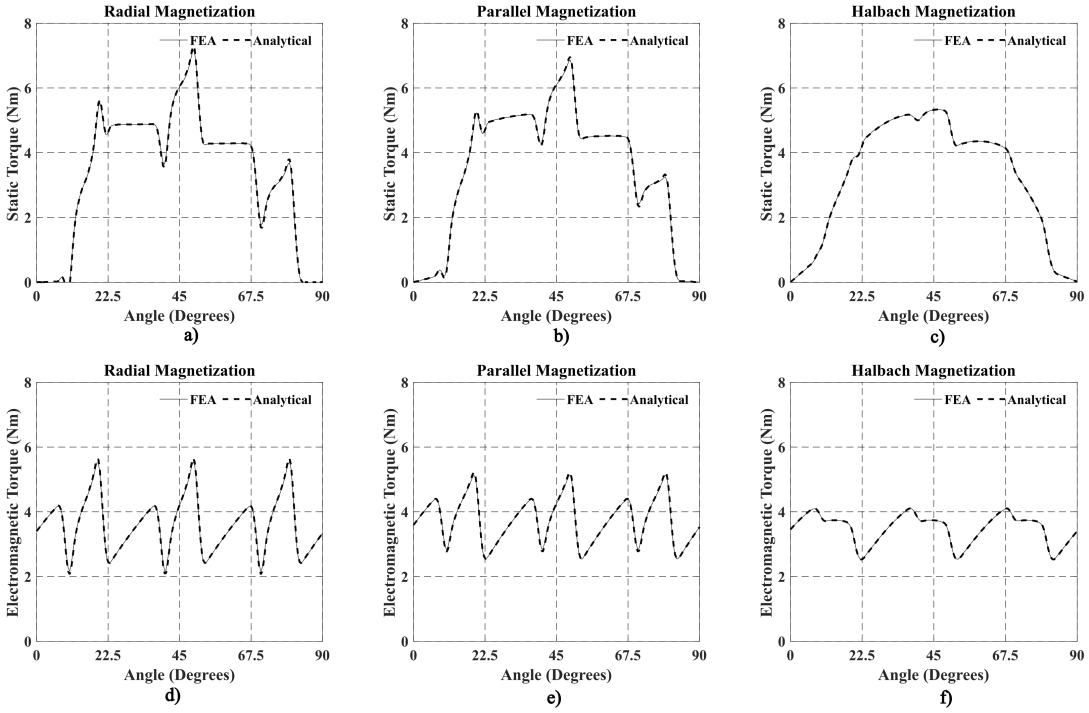

Figure 6.12: FEA and analytical results of the Static and Electromagnetic Torque for a), d) radial, b), e) parallel, and c), f) Halbach magnetisation pattern for the machine with surface-inset magnets $(1A/mm^2)$.

6.13 Conclusion

This chapter presents a novel analytical model for calculating the air-gap field distribution in permanent-magnet motors with surface-mounted and -inset magnets. The model is based on expressing its pole's magnetisation distribution using the Heaviside function's aid and inputting in the partial differential equations. The three basic magnetisation distribution patterns were considered, radial, parallel and Halbach. The PDE of magnet regions were solved in great detail using the method of eigenfunction expansions. The normal and tangential component of the no-load and on-load magnetic field distribution was computed with great accuracy. The proposed algorithm is general enough to be used for every number of slots and poles and accounts for the impact of the adjacent magnets and slots. Furthermore, the cogging-torque, back-EMF, torque-angle delta characteristic and on-load torque are calculated for each type of magnetisation pattern. Finite-Element Analysis results of a 12-slot, 4-pole motor were used to validate the proposed analytical model. This new way of modelling is sufficiently general to be used in other motor configurations and for the preliminary stages of the motor design process. Due to the additional reluctance torque component, permanent-magnet machines with surface-inset magnets produce more torque. The magnetisation pattern played a determinant role even in the motion-generated quantities, i.e. Back-EMF, electromagnetic torque.

The proposed algorithm is general enough to be used for every number of slots and poles and accounts for the impact of the adjacent magnets and slots. Lastly, for the machine with surface-inset magnets, the cogging torque is less when the magnetisation pattern is Halbach. Consequently, the electromagnetic torque ripple is also less than the surface-mounted magnet machine. This algorithm runs five times faster than the current Finite-Element Analysis software packages without sacrificing accuracy.

PART IV

Conclusions and contributions

Chapter 7

Conclusions and contributions of the hereunto dissertation

This chapter summarises the conclusions extracted by working on this dissertation. In the second stage are stated the contributions made to the field of permanent-magnet synchronous machines. Lastly, the chapter finishes with proposals for the future continuation of this work.

7.1 Conclusions

The conclusions made are the following:

- Noninvasive fault detection methods monitor features of signals extracted directly from the machine with the significant advantage that they do not require any additional sensors leading to more complex methods. These methods, in most cases, are too complex to be applied in industrial environments.
- The state-of-the-art noninvasive methods can successfully detect partial demagnetisation and dynamic eccentricity. The faults fall in the category of dynamic faults generally. The latter occurs as there is relative motion between the unbalanced magnetic flux occurred by the faults and the conductors of the stator winding. Many works suggested that a challenging problem is discrimination between these two faults because they appear to have a similar impact on the operating machine. More specifically, the harmonics generated by the two faults during the application of the MCSA method are identical. However, even at low severities, the partial demagnetisation fault creates a high amplitude in these harmonics. On the contrary, the amplitude of the harmonics generated by dynamic eccentricity has much lower variation as the severity increases, especially in coreless machines. Knowing which harmonics to monitor is critical as it is the only way to monitor the amplitude variation to extract a conclusion about which fault occurred.

- An easier way to separate the two rotor faults is the search-coil voltage signature analysis, as there is no harmonic cancellation due to the stator winding. The partial demagnetisation fault creates a higher harmonic content in the voltage amplitude spectrum of a single coil. However, this method comes with an expense that is intrusive. To address the latter issue, the method that uses a search-coil that negates the induced voltage under balanced conditions shows that it can also be utilised to detect partial demagnetisation faults and separate the two faults without applying further signal processing. This method appeared to be also valuable for detecting and distinguishing the dynamic axis and angular misalignment in axial-flux permanent-magnet machines, which, to the author's best knowledge, had never been studied before.
- Static faults like the inter-turn fault and static eccentricity showed that they could not be adequately detected using features extracted from the stator winding as they do not create relatively variant magnetic flux in the conductors. However, in cases with a ferromagnetic stator core, the fault causes saturation in a few rotor positions, so a low varying magnetic flux is created that can be exploited to create a diagnostic scheme. In cases with no stator core in the machine, these faults do not create a static unbalanced magnetic flux, so they cannot be detected with any known conventional diagnostic methods. The complexity of the signal processing technique did not seem to help with detecting this category of faults. The problem was solved using two search coils, one in the rotor to create variant magnetic flux and one in the stator to sense that flux.
- After a comprehensive literature review, it was concluded that not just detecting but separating between faults could be a challenging problem. By using state-of-the-art diagnostic methods with sensors or without, so creating a cost-effective, simple and easy-to-implement fault detection technique seems imperative. To address this issue, the method which uses two magnetically coupled search coils is introduced, making it possible to detect all faults online, using conventional coils that are easy to implement in the machine. This method is invasive as it uses additional sensors; however, the effectiveness and simplicity of the method compensate for this drawback. Furthermore, its simplicity makes the method appropriate for industrial environments.
- The experimental amplitude spectrum of permanent-magnet machines contains a high number of harmonics, so when a fault happens, it is unclear which harmonics are generated by the fault. Reports suggest that the order of the harmonics generated by a faulty condition depends on the number of pole pairs of the machine, which is true. However, this work showed that there is a strong coil number dependency. Furthermore, in an experimental environment, the harmonics generated due to a faulty condition exist in the machine; hence, knowing which harmonics to monitor is essential to monitor their amplitude early to record their variation over time.

- Commercial software packages utilising the Finite-Element Method to calculate the quantities of an electric machine demand a significant computational time, especially in the cases in which the machine demands modelling through a 3-D solver. The development of analytical models, which require a low computational time an essential way to extract features in every case study. When a permanent magnet machine is simulated using a commercial software package under a faulty condition, the whole geometry of the machine is demanded, which entails an even more significant computational time.
- Regarding the comparison between the surface-mounted and -inset permanent-magnet machines using the developed analytical model. Surface-inset magnet machines have better performance characteristics due to the reluctance torque component. The Halbach magnetisation pattern proved more beneficial for the surface-inset magnet machine as the on-load torque has the lowest torque ripple. The above magnetisation pattern is appropriate for applications where the machine's noise and vibration must be kept to a minimum. Lastly, the Halbach magnetisation pattern creates less cogging torque for both rotor topologies. The parallel magnetisation is the second best scenario as long as the pole number of the machine does not increase a lot. The radial magnetisation offers a high mean torque but creates a significant vibration and noise due to the high spatial harmonic content of the magnetic flux density and the high cogging torque.

7.2 Contributions

The main contributions made to the field of electric machines are the following:

- Detection of the partial demagnetisation fault in permanent-magnet machines using the method which uses one search-coil that negates the induced voltage under balanced conditions. Furthermore, the method was also applied in axial-flux permanent-magnet machines, showing that it works for the dynamic axis and angular misalignment faults.
- A new fault diagnostic technique utilises the magnetic flux involving two search coils to detect all the faults occurring in permanent-magnet synchronous machines. One in the rotor and one in the stator, which couple magnetically only when the machine is faulty and made it possible to detect all faults that are taking place in permanent-magnet machines. This method contributed by transforming the static faults into dynamic and created quantities proportional to the fault severity.
- An analytical voltage formula that predicts the exact harmonics increasing in amplitude when dynamic eccentricity occurs in permanent-magnet machines. The formula showed that these harmonics depend not only on the pole pair number of the machine but also on the number of coils that determines which harmonics cancel. The experimental validation showed that knowing the harmonics is imperative due to the high number of irrelevant harmonic frequencies on machines' amplitude spectrum.

- A magnetic field computation algorithm based on the subdomain technique which calculated the magnetic flux density, Back-EMF and torque distribution for permanent-magnet machines with surface-mounted and surface-inset magnets for the three common magnetisation distribution patterns; radial, parallel and Halbach. The magnetisation was modelled as a difference of Heaviside functions. The eigenfunction expansions solution method made it possible to obtain the analytical solution. This work showed how to extract an analytical solution for the calculation of magnetic field distribution by exploiting the integral properties of the Heaviside and delta functions.

7.3 Proposals for future work

The future work which can be conducted for the continuation of this work is the following:

- The phenomenon of rotor ovalization which is caused by the unbalanced magnetic pull makes its appearance in very large machines. The impact of this fault is similar to the dynamic eccentricity fault with the only difference that there are two minimum and two maximum air-gaps. The proposed air-gap flux monitoring method with the two magnetically-coupled search-coils was not tested for the discussed phenomenon. Investigating whether this method is capable of detecting the ovalization effect is worth investigating in a future work.
- Experimental investigation of the proposed air-gap flux diagnostic method with the two magnetically coupled search-coils in medium and high speed machines. The method was validated using direct-drive permanent-magnet generators which are physically large and they run on low speeds. So the centrifugal force on the rotor search-coil was low, meaning that the mounting demands for the coil were low. By utilising the method in a high speed machine the mounting demands will increase. The latter entails the possibility for the need of a more sophisticated mounting method for operating the machine without danger that the coil being unstuck from the rotor.
- The proposed subdomain analytical model can be expanded to account demagnetized magnets. The way that the model was developed was using an expansion of an analytical solution in each magnet pole. Furthermore, the model allows to segment the magnet region into various arcs with different residual flux density values without the need to consider new region inside the magnet as the classic subdomain model would demand.

Appendix A

Fault implementation on the environment of FEA software package Simcenter Magnet 2-D/3-D

In this Appendix, the way that the faults are implemented using simulation on a PM machine is presented. The machine that is used is the permanent-magnet synchronous machine with 12 coils and 8 poles of Figure 2.16. The faults presented are the partial demagnetization of a magnet, the inter-turn fault in a coil of the winding and the two type of eccentricity faults; static and dynamic.

A.1 Demagnetizing a magnet

To demagnetize a magnet, a new permanent-magnet material is created which is of the same magnet type as the other ones. Its B-H characteristic is shifted towards the origin so both the residual magnetic flux density and coercivity are reduced on the same rate. This models the demagnetization of a permanent-magnet due to the temperature increment. However, as the temperature increases the characteristic of the magnet NdFeB N42 has the tendency to become more and more nonlinear as Figure A.1 presents.

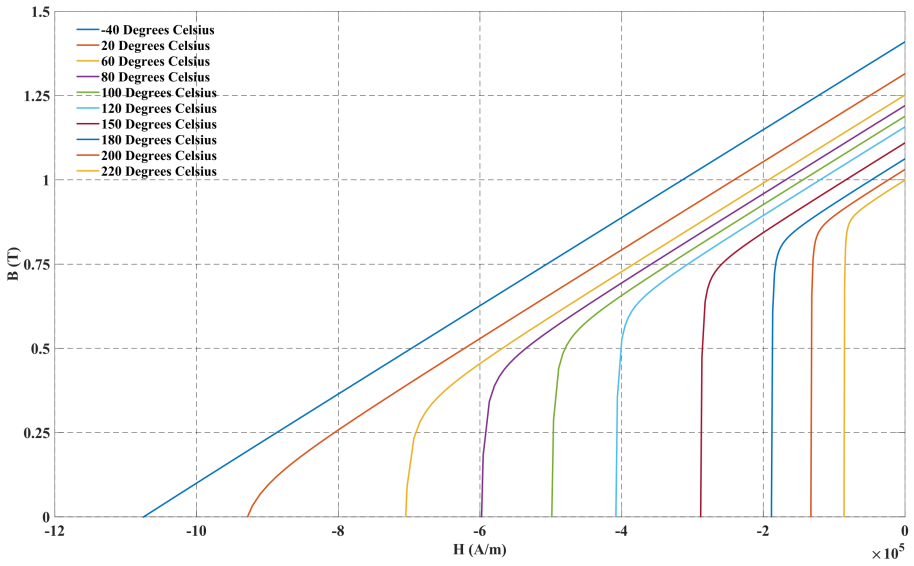

Figure A.1: NdFeB magnetic material characteristic of grade N42 for various temperatures.

A magnet with its magnetic characteristic demagnetized, can be created by clicking to the Tools tab and choosing the New User Material command, Figure A.2 illustrates the process.

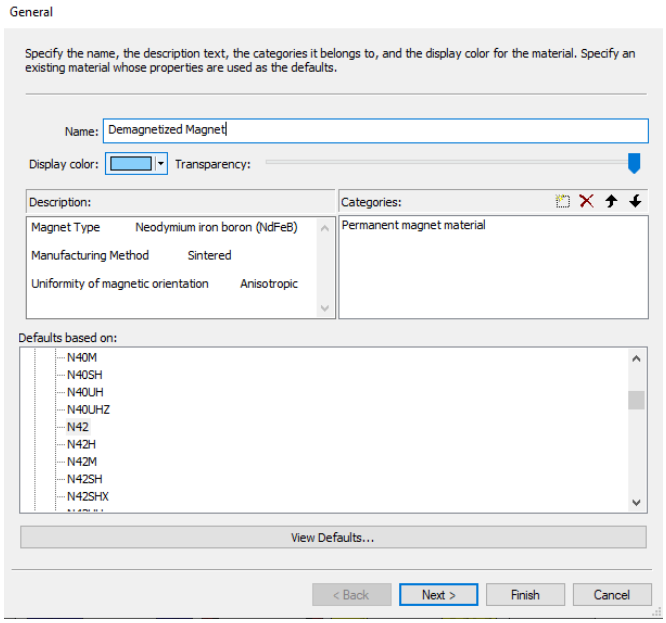

Figure A.2: Creation of a NdFeB N42 magnet.

By clicking next to the above window, the magnetic characteristic at 20^{o} is presented, in forms of data as Figure A.3 presents.

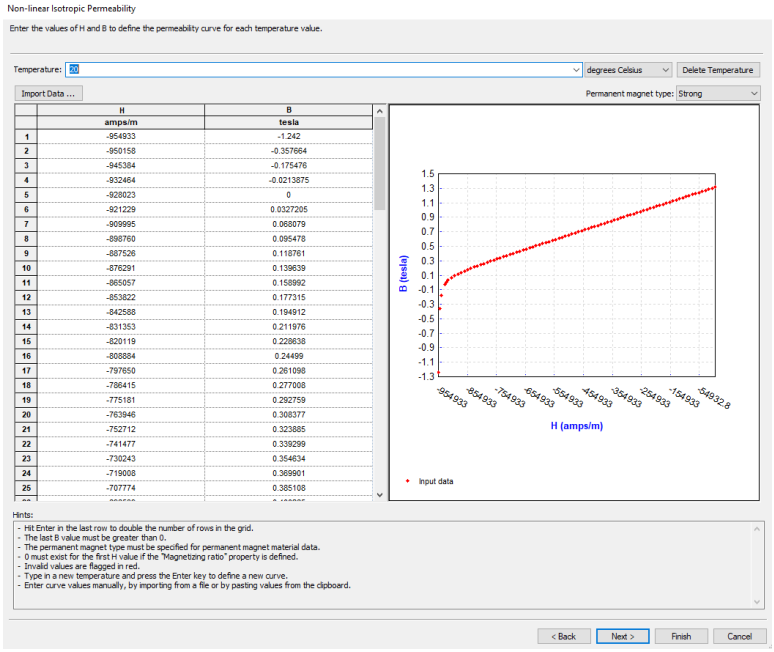

Figure A.3: Magnetic characteristic at 20^{o} for the NdFeB N42 magnet.

By entering the B-H data shown on Figure A.3 on a programming software which expresses the variables in an array format, i.e. MATLAB. The magnetic characteristic can be modified. It can either follow the lines presented in Figure A.1 or it can be one with a further reduction of the residual magnetic flux density. After the demagnetized characteristic is modified in MATLAB it can be substituted for the corresponding temperature and the material can be created by clicking on the Finish button. The solver by default works at room temperature, i.e. 20^{o} but the temperature can be changed by clicking to the Extension tab and choosing Modeling Toolbox as shown in Figure A.4. By choosing System on the Parameters tab after the window opens the default temperature can be changed. For instance, in this case the demagnetized characteristic should be defined for operation on the chosen temperature.

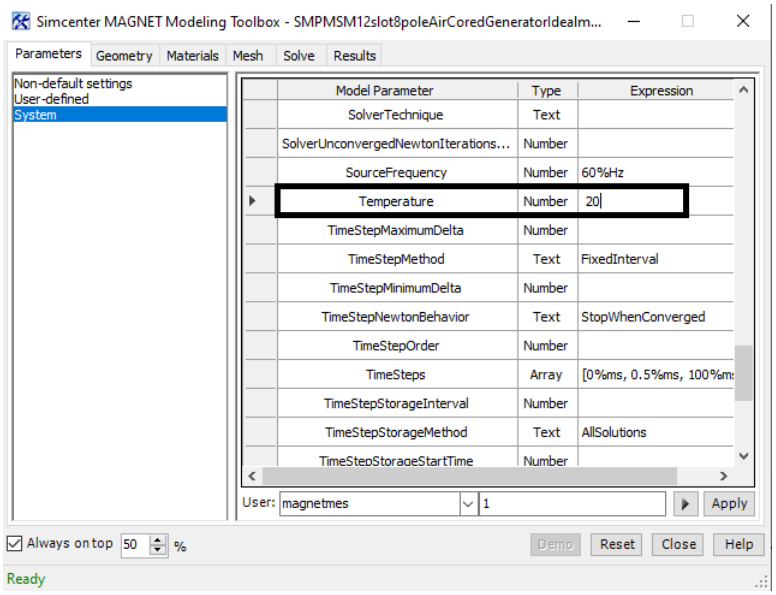

Figure A.4: Window used to change the system temperature.

After the material is created on the Material tab of the Project Bar, the material can be assigned to one of the magnets.

A.2 Shorting a turn of of a coil

To short the turn of a coil, the coil itself has to be segmented into two components. The first component will be the one that is the healthy part of the coil and contributed normally into the circuit a coil with the only difference that has a lower number of turns. The reduction in the number of turns has to correspond to the reduction of the surface of the coil. The faulty part of the coil is shorted and except the physical resistance and inductance that the shorted loop has, an additional resistance is required to model the contact resistance which is basically the resistance in the point where the insulation collapsed. Figure A.5 presents the two different coils segmented. The coil with the bigger surface corresponds to the healthy part of the coil and continues to connect with the other healthy coils and it will have a lower peak value of voltage due to the reduced number of turns. The shorted coil is also shown on the same figure. Figure A.6 shows the electric circuit of the fault condition. The phase in which the fault took place, the healthy coil is connected in series and the faulty coil is shorted with low valued resistance.

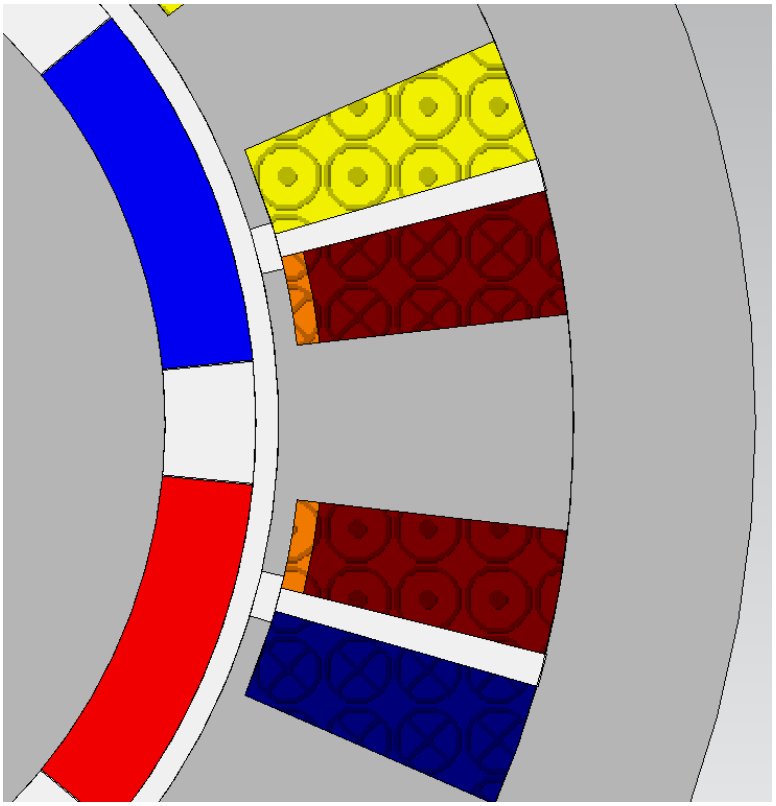

Figure A.5: Creating the geometry of the inter-turn fault.

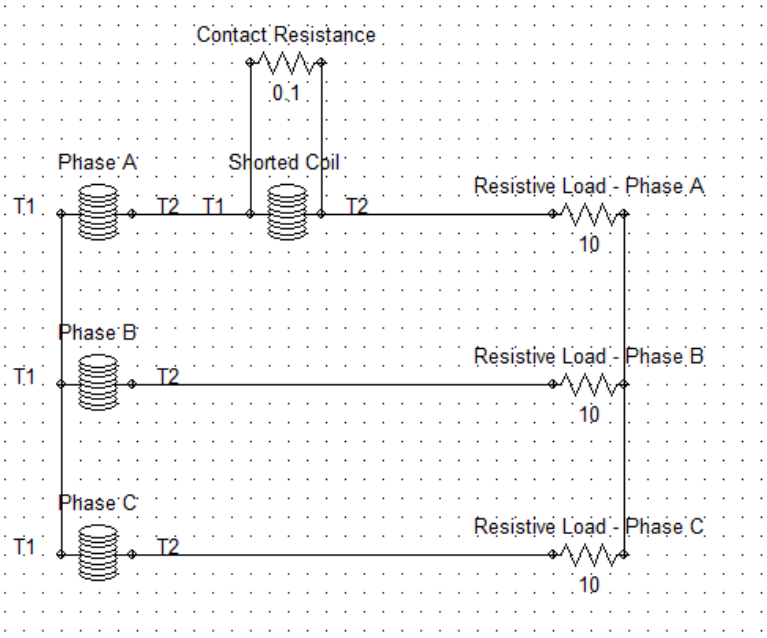

Figure A.6: Electric circuit of the machine during inter-turn fault conditions.

A.3 Making the rotor eccentric

In the rotor eccentricity fault, the rotor is displaced towards a direction, which expresses the position of the minimum air-gap. Whether it will be static or dynamic eccentricity it depends on the axis of rotation. Generally, to implement eccentricity faults, the model is divided into two motion components, #Stator and #Rotor. Each component includes the components which each region owns. The #Stator component has center of rotation the origin point (x,y,z)=(0,0,0) as Figure A.7 supports. This in both fault conditions stays as is.

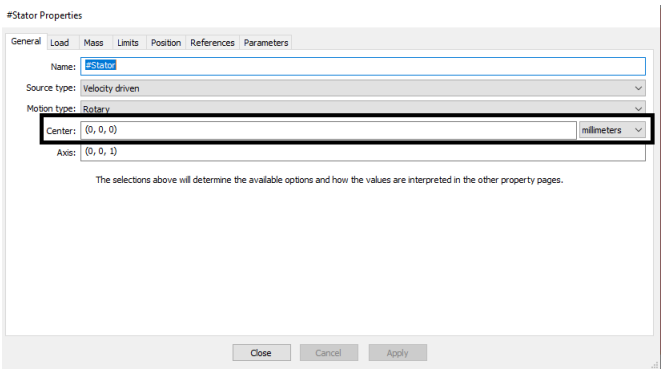

Figure A.7: Defining the center of the Stator component.

Furthermore, the rotor in both cases becomes displaced into a direction. For instance, this direction can be the at $\theta = 0$ as Figure A.8 supports. The mechanical air-gap has a length of 0.5 mm in this case, so by shifting the rotor for 0.25 mm with direction at $\theta = 0$. This leads to 50% percent of eccentricity.

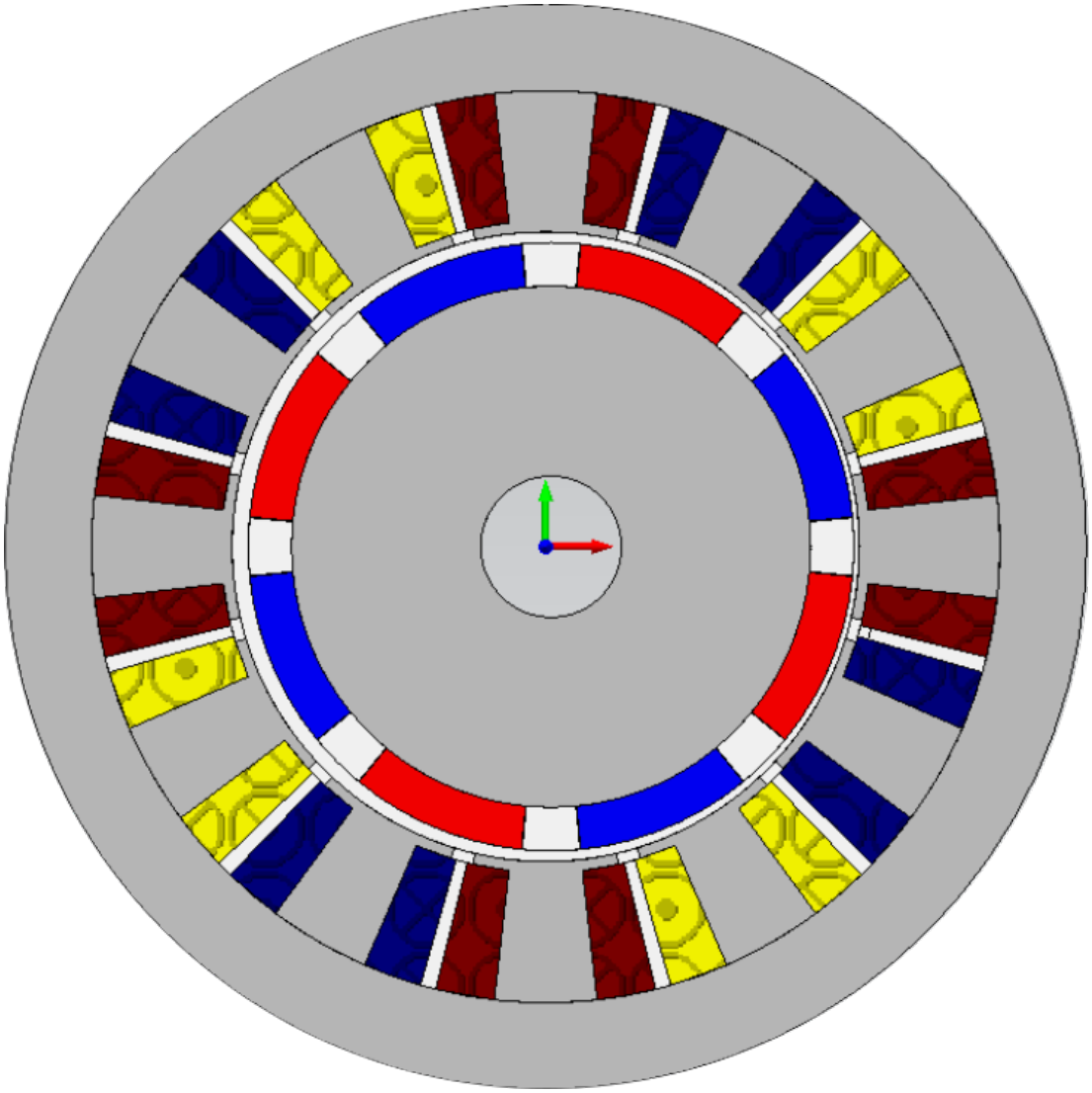

Figure A.8: Eccentric rotor with 50% eccentricity fault.

A.3.1 Static eccentricity

In the static eccentricity fault, the rotor axis rotates on a new stationary center different than the one of the stator. In this case the #Rotor component must have a center of rotation same as the coordinates of the new center, i.e. (x,y,z)=(0.25,0,0) as Figure A.9 illustrates.

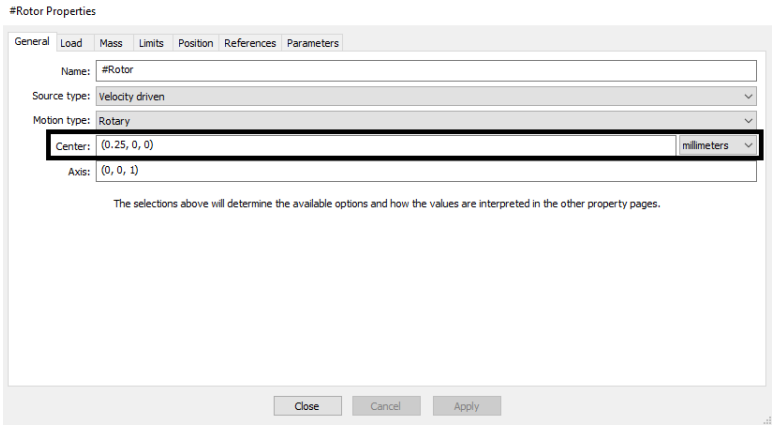

Figure A.9: Defining the coordinates of the #Rotor component to simulate static eccentricity.

A.3.2 Dynamic eccentricity

In the dynamic eccentricity fault, the axis of rotation coincides with the one of the stator, which entails the center of rotation to execute a circular motion. To implement the fault using the simulation software, the #Rotor component being displaced must have center of rotation coordinates (x,y,z)=(0,0,0), which coincides with the center of the stator. This entails that the axis of rotation will execute a circular trajectory.

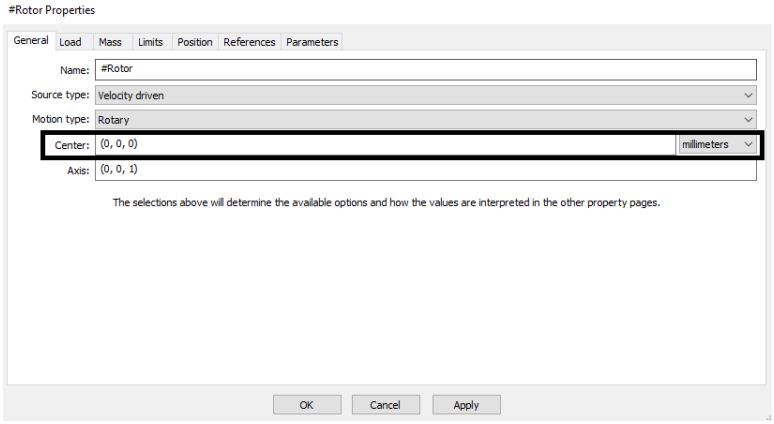

Figure A.10: Defining the coordinates of the #Rotor component to simulate dynamic eccentricity.

Appendix B

Codes on the software MATLAB for the magnetic field computation algorithms of Chapter 6

B.1 Main program

The below code is the main function that is used for the calculation of the magnetic field distribution on the air-gap for two cases. The first case happens when there is not current in the slots so the magnetic flux density is only influenced by the slotting effect of the stator bore. In the second case, the stator slots carry currents which since one moment is examined this can be any instant that the 3-phase currents have. For instance, if one current is on the positive peak value the other to will be on their half negative values.

```
% Calculation of the spatial magnetic flux density distribution for an initial angle
% This code calculates no-load and on-load magnetic flux density distribution

tic % measures the computational time of the algorithm for the code that is interpolated by tic toc

clear all;                  % Cleans Workspace in each run
clc;                        % Cleans Command Window in each run
P=4;                        % Total number of poles
Q=12;                       % Total number of slots
Brem=1.0;                   % Residual flux density in each PM
mur=1.0;                    % Relative permeability of the PM
mu0=4*pi*1e-07;             % Vacuum permeability
thetai0=-1*pi/P;            % Initial rotor PM angle (rad)
thetaj0=-0*pi/Q;            % Initital stator slot angle (rad)
N=250;                      % Number of total harmonics in the air-gap region

R1=42*1e-03;                % Radius of the rotor back iron cylinder (m)
R2=50*1e-03;                % Radius of the permanent-magnets (m)
R3=51*1e-03;                % Radius of the stator core (m)
R4=53*1e-03;                % Radius of the slot-opening (m)
R5=65*1e-03;                % Radius of the slot (m)

ap=0.8;                     % Ratio of pole-arc to pole-arc
alpha=ap*2*pi/P;            % Permanent-magnet angle (rad)
beta=alpha/ap;              % Pitch angle (rad)
gamma=3*pi/180;             % Slot opening angle (rad)
delta=15*pi/180;            % Slot angle (rad)

Sslot=(delta/2)*(R5^2-R4^2);% Area of a slot
I=0*3*185.3540;             % Current value chosen for the specified instant (A)
Jrms=I/Sslot;               % RMS value of the current density in each slot (A/m^2)
```

```
%Jrms=1*1e06;               % Alternative value for the current density value
J=zeros(Q,1);               % Initiation of the current density vector
phi0=+0*pi/4;               % Initial angle of the armature reaction magnetic field (rad)
% The iteration loop used to assign current density value in each stator slot
for j=3:3:Q

    J(j,1)=-Jrms*(-1)^(j+1)*sin(90*pi/180+120*pi/180+phi0);
    J(j-1,1)=Jrms*(-1)^(j+1)*sin(90*pi/180-120*pi/180+phi0);
    J(j-2,1)=-Jrms*(-1)^(j+1)*sin(90*pi/180+phi0);

end

% Here the coefficients of each subdomain are calculated using a function
% The input of the function are the dimensions and the operational characteristics of the machine
% The initial angle of the rotor and stator is also an input in the function
% f is substituted with 6 names, which each name corresponds to the calculation of a magnetic field ...
      distribution
% f -> SurfaceMountedRadial calculates the air-gap magnetic field for the surface-mounted topology under ...
      radial magnetization
% f -> SurfaceMountedParallel calculates the air-gap magnetic field for the surface-mounted topology ...
      under parallel magnetization
% f -> SurfaceMountedHalbach calculates the air-gap magnetic field for the surface-mounted topology under ...
      parallel magnetization
% f -> SurfaceInsetRadial calculates the air-gap magnetic field for the surface-inset topology under ...
      radial magnetization
% f -> SurfaceInsetParallel calculates the air-gap magnetic field for the surface-inset topology under ...
      parallel magnetization
% f -> SurfaceInsetHalbach calculates the air-gap magnetic field for the surface-inset topology under ...
      Halbach magnetization

[A0Ii,AlIi,AnII,BnII,CnII,DnII,A0IIIj,AkIIIj,BkIIIj,A0IVj,AmIVj] =
f(P,Q,Brem,mur,mu0,J,thetai0,thetaj0,R1,R2,R3,R4,R5,ap,alpha,beta,gamma,delta,N);

Re=(R2+R3)/2;                   % Radius on the middle of the air-gap
theta=linspace(0,360,1001);     % Polar angle coordinate vector in degrees

Bnormal=zeros(size(theta));     % Normal component of the magnetic field as a function of the angular ...
      coordinate
Btangential=zeros(size(theta));% Tangential component of the magnetic field as a function of the angular ...
      coordinate

font_size=20;                   % font size of the graph

for n=1:N

    Bnormal=Bnormal+(1./Re).*((AnII(n).*R2.*(((Re./R3).^(n)+(R3./Re).^(n))./((R2/R3)^(n)-(R3/R2)^(n)))
    +BnII(n).*R3.*((Re./R2).^(n)+(R2./Re).^(n))./((R3/R2)^(n)-(R2/R3)^(n))).*(-sind(n.*theta))...
    +(CnII(n).*R2.*(((Re./R3).^(n)+(R3./Re).^(n))./((R2/R3)^(n)-(R3/R2)^(n)))
    +DnII(n).*R3.*((Re./R2).^(n)+(R2./Re).^(n))./((R3/R2)^(n)-(R2/R3)^(n))).*cosd(n.*theta));

    Btangential=Btangential-(1./Re).*((AnII(n).*R2.*(((Re./R3).^(n)-(R3./Re).^(n))./((R2/R3)^(n)-(R3/R2)^(n)))
    +BnII(n).*R3.*((Re./R2).^(n)-(R2./Re).^(n))./((R3/R2)^(n)-(R2/R3)^(n))).*cosd(n.*theta)...
    +(CnII(n).*R2.*(((Re./R3).^(n)-(R3./Re).^(n))./((R2/R3)^(n)-(R3/R2)^(n)))
    +DnII(n).*R3.*((Re./R2).^(n)-(R2./Re).^(n))./((R3/R2)^(n)-(R2/R3)^(n))).*sind(n.*theta));

end

Bnormal=Bnormal';               % Converts the horizontal vector into vertical
Btangential=Btangential';       % Converts the horizontal vector into vertical


subplot(2,1,1)
plot(theta,Bnormal,'k','LineWidth',2); % Command used to plot the normal component of magnetic flux density
legend({'Normal Component'},'Box','off')
xlim([0 360])
grid on
set(gcf,'color','white')
set(gca,'FontSize', font_size, 'FontName','Times New Roman','FontWeight','bold')
xlabel('Angular position (Deg)', 'FontName','Times New Roman','FontSize', font_size, 'FontWeight', 'bold')
ylabel('Normal component (T)', 'FontName','Times New Roman','FontSize',font_size, 'FontWeight', 'bold')
%set(gca,'YTick',[-1:0.5:1],'YMinorGrid','off')
set(gca,'XTick',[0:360/P:360],'XMinorGrid','off')
ax = gca;
ax.GridLineStyle = '--';
ax.GridColor = 'k';  % [R, G, B]
```

```
ax.GridAlpha = 1;

subplot(2,1,2)
plot(theta,Btangential,'k','LineWidth',2); % Command used to plot the tangential component of magnetic ...
      flux density
legend({'Tangential Component'},'Box','off')
xlim([0 360])
grid on
set(gcf,'color','white')
set(gca,'FontSize', font_size, 'FontName','Times New Roman','FontWeight','bold')
xlabel('Angular position (Deg)', 'FontName','Times New Roman','FontSize', font_size, 'FontWeight', 'bold')
ylabel('Tangential component (T)', 'FontName','Times New Roman','FontSize',font_size, 'FontWeight', 'bold')
%set(gca,'YTick',[-0.4:0.1:0.4],'YMinorGrid','off')
set(gca,'XTick',[0:360/P:360],'XMinorGrid','off');
ax = gca;
ax.GridLineStyle = '--';
ax.GridColor = 'k';  % [R, G, B]
ax.GridAlpha = 1;
max_Bn=max(Bnormal)          % Peak value of the normal component of the magnetic flux density
max_Bt=max(Btangential)      % Peak value of the tangential component of the magnetic flux density

toc
```

The next code calculates the Back-EMF waveform of a phase for each permanent-magnet rotor topology and magnetization pattern. To calculate the Back-EMF waveform of a phase, the equations (6.110, 6.111, 6.112, 6.113) were employed.

```
% Per-turn Back-EMF Calculation (Brem=1.0 Jrms=0)

tic % measures the computational time of the algorithm for the code that is interpolated by tic toc

%clear all;                        % Cleans Workspace in each run
clc;                               % Cleans Command Window in each run
P=4;                               % Total number of poles
Q=12;                              % Total number of slots
Brem=1.0;                          % Residual flux density in each PM
mur=1.0;                           % Relative permeability of the PM
mu0=4*pi*1e-07;                    % Vacuum permeability
thetai0=-1*pi/P;                   % Initial rotor PM angle (rad)
thetaj0=-0*pi/Q;                   % Initial stator slot angle (rad)
N=70;                              % Number of total harmonics in the air-gap region

R1=42*1e-03;                       % Radius of the rotor back iron cylinder
R2=50*1e-03;                       % Radius of the permanent-magnets
R3=51*1e-03;                       % Radius of the stator core
R4=53*1e-03;                       % Radius of the slot-opening
R5=65*1e-03;                       % Radius of the slot

ap=0.8;                            % Ratio of pole-arc to pole-arc
alpha=ap*2*pi/P;                   % Permanent-magnet angle (rad)
beta=alpha/ap;                     % Pole pitch angle (rad)
gamma=3*pi/180;                    % Slot opening angle (rad)
delta=15*pi/180;                   % Slot angle (rad)

Sslot=(delta/2)*(R5^2-R4^2);       % Area of a slot
I=0;                               % Current value chosen for the specified instant (A)
%Jrms=I/Sslot;                     % RMS value of the current density in each slot
%Jrms=0*1e06;                      % RMS value of the current density in each slot (A/m^2)
J=zeros(Q,1);                      % Initiation of the current density vector
%phi0=-90*pi/180+45*pi/180;        % Initial angle of the armature reaction magnetic field (rad)
% The iteration loop used to assign current density value in each stator slot

font_size=20;                      % font size of the graph
T=200;                             % Total number of Back-EMF points along two pole pitches
n=1500;                            % Mechanical speed of rotation (RPM)
omega_r=n*2*pi/60;                 % Mechanical speed of rotation (rad/sec)
Lst=100*1e-03;                     % Axial length of the machine (m)

% C is the winding matrix and defines the type of the winding
% Any type of winding can be used
```

```
44
45  % C = [ 1 -1 0 0 0  0 ;
46  %       0  0 0 0 1 -1 ;
47  %       0 0 1 -1 0  0 ];  % 6 slots non-overlapping overlapping winding
48
49  % C = [ 1  -1  0   0  0   0  1  -1  0  0  0  0 ;
50  %       0   0  0   0  1  -1  0   0  0  0  1 -1 ;
51  %       0   0  1  -1  0   0  0   0  1 -1  0  0 ]; % 12 slots non-overlapping winding
52
53  C = [ 1   0  0  -1   0  0  1   0  0  -1   0   0 ;  % 12 slots concentrated overlapping
54        0   0  1   0   0 -1  0   0  1   0   0  -1 ;
55        0  -1  0   0   1  0  0  -1  0   0   1   0 ];
56
57  % C = [ 1  0  0  -1   0  0  1  0  0  1  0  0  1  0  0  -1   0  0  1  0  0  1  0  0;  % 24 slots ...
        concentrated overlapping
58  %       0  1  0   0  -1  0  0  1  0  0 -1  0  0  1  0   0  -1  0  0  1  0  0 -1  0;
59  %       0  0  1   0   0 -1  0  0  1  0  0 -1  0  0  1   0   0 -1  0  0  1  0  0 -1];
60
61  Nph=1;                              % Number of turns connected in series per phase, equal with 1 or the ...
        per-turn Back-EMF calculation
62  Tp=(2*pi)/(P/2);                   % Spatial period of Back-EMF (rad)
63
64  % The magnetic flux vector has T rows and Q columns meaning that in the rows the iteration are stored and ...
        in each column defines for which slot is stored
65  Phi=zeros(T,Q);                    % Initiation of the slot magnetic flux array
66
67  % The magnetic flux-linkage has also the same as the slot magnetic flux array
68  % The winding matrix C is multiplied with this array to convert into zero those columns-slots that do not ...
        belong on the corresponding phase
69  Psi_a=zeros(T,Q);                  % Initiation of the magnetic flux-linkage array of phase A
70  Psi_b=zeros(T,Q);                  % Initiation of the magnetic flux-linkage array of phase B
71  Psi_c=zeros(T,Q);                  % Initiation of the magnetic flux-linkage array of phase C
72
73  % The Back-EMF vector is aparted by the total number of iterations as
74  E_a=zeros(T,1);                    % Initiation of the Back-EMF vector of phase A
75  E_b=zeros(T,1);                    % Initiation of the Back-EMF vector of phase B
76  E_c=zeros(T,1);                    % Initiation of the Back-EMF vector of phase C
77
78  phi=linspace(0,Tp,T);              % Initiation of the angular coordinate of the Back-EMF vector
79  % The vector extends from 0 till 180 degrees at 200 points
80  J=zeros(Q,1);                      % Initiation of the current density vector which is zero in this case ...
        because the Back-EMF is the voltage on the stator coils when the stator slots do not have current
81
82  % t is the index of the repetition
83  % For each repetition the unknown coefficients are calculated for the specific rotor angle for each slot
84  for t=1:T
85  % In each repetition the initial angle of the rotor increases so the Back-EMF is computed for the ...
        pre-specified initial angle thetai
86      thetai0=thetai0+Tp/T;
87
88
89      %for j=3:3:Q
90
91      %    J(j,1)=Jrms*(-1)^(j+1)*sin((P/2)*thetai0+90*pi/180-120*pi/180+phi0);
92      %    J(j-1,1)=-Jrms*(-1)^(j+1)*sin((P/2)*thetai0+90*pi/180+120*pi/180+phi0);
93      %    J(j-2,1)=Jrms*(-1)^(j+1)*sin((P/2)*thetai0+90*pi/180+phi0);
94
95      %end
96
97      for j=1:Q
98
99          [A0Ii,AlIi,AnII,BnII,CnII,DnII,A0IIIj,AkIIIj,BkIIIj,A0IVj,AmIVj] = ...
                f(P,Q,Brem,mur,mu0,J,thetai0,thetaj0,R1,R2,R3,R4,R5,ap,alpha,beta,gamma,delta,N);
100
101         %if (j==1)||(j==4)||(j==7)||(j==10)
102
103
104             Phi(t,j)=Lst*A0IVj(j,1)+...
105             (delta*J(j,1)*mu0*Lst/(2*Sslot))*(R5^4*(log(R5)-5/8)+R5^2*R4^2*(1/2-log(R4))+(1/8)*R4^2);
106             Phi(t,j)=Lst*A0IVj(j,1)+(Lst/Sslot)*(mu0*J(j,1)*delta*R5^4*log(R5)/4-
107             mu0*J(j,1)*delta*R5^2*R4^2*log(R4)/4-mu0*J(j,1)*delta*R5^4/8+
108             mu0*J(j,1)*delta*R5^2*R4^2/8-mu0*J(j,1)*delta*R5^4/16+mu0*J(j,1)*delta*R4^4/16);
109
110         %end
111
```

```
    end

    Psi_a(t,:)=Nph*C(1,:).*Phi(t,:);     % Filling the magnetic-flux linkage vector of phase A
    %Psi_b(t,:)=Nph*C(2,:).*Phi(t,:);    % Filling the magnetic-flux linkage vector of phase B
    %Psi_c(t,:)=Nph*C(3,:).*Phi(t,:);    % Filling the magnetic-flux linkage vector of phase C

    % The below quantity still defines the magnetic flux-linkage of a phase at a mechanical angular speed
    E_a(t,1)=omega_r*(Psi_a(t,1)+Psi_a(t,4)+Psi_a(t,7)+Psi_a(t,10));
    %E_b(t,1)=omega_r*(Psi_b(t,3)+Psi_b(t,6)+Psi_b(t,9)+Psi_b(t,12));
    %E_c(t,1)=omega_r*(Psi_c(t,2)+Psi_c(t,5)+Psi_c(t,8)+Psi_c(t,11));

end

% By differentiating numerically the vectors E_a, E_b and E_c, the Back-EMF of each phase is obtained at ...
     the defined angular speed
E_a=gradient(E_a)./gradient(phi)';            % Back-EMF of phase A
%E_b=gradient(E_b)./gradient(phi)';           % Back-EMF of phase B
%E_c=gradient(E_c)./gradient(phi)';           % Back-EMF of phase C

theta=linspace(0,360/(P/2),length(phi)); % Angular coordinate of the Back-EMF function
%plot(theta,E_a,'k.','MarkerSize',10);
plot(theta,E_a,'b','LineWidth',2)        % Command used to plot the graph of the Back-EMF
%hold on
%plot(theta,E_b,'r','LineWidth',2)
%plot(theta,E_c,'g','LineWidth',2)
%hold off
%legend({'Back EMF'},'Box','off')
set(gcf,'color','white')
set(gca,'FontSize', font_size, 'FontName','Times New Roman','FontWeight','bold')
xlabel('Angular position (Deg)', 'FontName','Times New Roman','FontSize', font_size, 'FontWeight', 'bold')
ylabel('Voltage (V)', 'FontName','Times New Roman','FontSize',font_size, 'FontWeight', 'bold')
%set(gca,'YTick',[-0.4:0.1:0.4],'YMinorGrid','off')
set(gca,'XTick',[0:360/P:360],'XMinorGrid','off');
ax = gca;
ax.GridLineStyle = '--';
ax.GridColor = 'k';  % [R, G, B]
ax.GridAlpha = 1;
%ylim([-3 3])
xlim([0 360/(P/2)])
grid on
rms(E_a)   % RMS value of Back-EMF waveform of phase A
max(E_a)   % Peak value of Back-EMF waveform of phase A

toc
```

The below code was used to calculate the analytical results for the cogging torque. The equations that were used are (6.114, 6.115, 6.116). For the calculation of cogging torque, the current in the slots is zero and the rotor has to rotate so also a repetition loop is required here.

```
% Cogging Torque Calculation (Brem=1.0 Jrms=0)

tic % measures the computational time of the algorithm for the code that is interpolated by tic toc

%clear all;                          % Cleans Workspace in each run
clc;                                 % Cleans Command Window in each run
P=4;                                 % Total number of poles
Q=12;                                % Total number of slots
Brem=1.0;                            % Residual flux density in each PM
mur=1.0;                             % Relative permeability of the PM
mu0=4*pi*1e-07;                      % Vacuum permeability
thetai0=-1*pi/P;                     % Initial rotor PM angle (rad)
thetaj0=-0*pi/Q;                     % Initial stator slot angle (rad)
N=150;                               % Number of total harmonics in the air-gap region

R1=42*1e-03;                         % Radius of the rotor back iron cylinder
R2=50*1e-03;                         % Radius of the permanent-magnets
R3=51*1e-03;                         % Radius of the stator core
R4=53*1e-03;                         % Radius of the slot-opening
```

```
R5=65*1e-03;                        % Radius of the slot

ap=0.8;                             % Ratio of pole-arc to pole-arc
alpha=ap*2*pi/P;                    % Permanent-magnet angle
beta=alpha/ap;                      % Pole pitch angle
gamma=3*pi/180;                     % Slot opening angle
delta=15*pi/180;                    % Slot angle

Sslot=(delta/2)*(R5^2-R4^2);        % Area of a slot
I=0;                                % Slot current, equal to zero for this algorithm
Jrms=I/Sslot;                       % RMS value of the current density in each slot
J=zeros(Q,1);                       % Initiation of the slot current density vector
T=200;                              % Number of p

Tem=zeros(N,1);                     % Torque vector which stores the spatial harmonics of the air-gap
Tcog=zeros(size(T));                % Cogging torque vector which has T points

Tp_cogging=(2*pi)/lcm(Q,P);         % Cogging torque period (rad)
%Tp_cogging=(2*pi);                 % Cogging torque periods in the whole air-gap circumference (rad)
Tp_cogging_deg=360/lcm(Q,P);        % Cogging torque period (deg)
%Tp_cogging_deg=360;                % Cogging torque periods in the whole air-gap circumference (deg)
phi=linspace(0,Tp_cogging,T);       % Angular coordinate

Re=(R2+R3)/2;                       % Mid-radius of the air-gap (m)
Lst=100*1e-03;                      % Axial length of the machine (m)

for t=1:T

    thetai0=thetai0+Tp_cogging/T; % Variation of the rotor angle for each repetition

    [A0Ii,AlIi,AnII,BnII,CnII,DnII,A0IIIj,AkIIIj,BkIIIj,A0IVj,AmIVj] =
    f(P,Q,Brem,mur,mu0,J,thetai0,thetaj0,R1,R2,R3,R4,R5,ap,alpha,beta,gamma,delta,N);

    for n = 1:N

        P_e3 = (Re/R3)^n + (R3/Re)^n;
        P_e2 = (Re/R2)^n + (R2/Re)^n;
        E_e3 = (Re/R3)^n - (R3/Re)^n;
        E_e2 = (Re/R2)^n - (R2/Re)^n;

        E_23 = (R2/R3)^n - (R3/R2)^n;
        E_32 = (R3/R2)^n - (R2/R3)^n;

        Wn=-AnII(n)*(R2/Re)*P_e3/E_23 - BnII(n)*(R3/Re)*P_e2/E_32;
        Xn=-CnII(n)*(R2/Re)*E_e3/E_23 - DnII(n)*(R3/Re)*E_e2/E_32;
        Yn=+CnII(n)*(R2/Re)*P_e3/E_23 + DnII(n)*(R3/Re)*P_e2/E_32;
        Zn=-AnII(n)*(R2/Re)*E_e3/E_23 - BnII(n)*(R3/Re)*E_e2/E_32;

        Tem(n,1)=(pi*Re^2*Lst/(mu0))*(Wn*Xn+Yn*Zn);  % Filling of the vector with the spatial harmonic ...
             components for a specific rotor position

    end

    Tcog(t,1)=sum(Tem); % All the spatial harmonics are summed so the value of the cogging torque for the ...
          specific rotor position is obtained

end

theta=linspace(0,Tp_cogging_deg,length(phi)); % Angular coordinate of the cogging torque function
plot(theta,Tcog,'k','LineWidth',1.25);        % Command used to plot the graph of the cogging torque
xlim([0 Tp_cogging_deg]);
grid on
rms(Tcog)            % RMS value of the cogging torque signal
max(Tcog)            % Peak value of the cogging torque signal
toc
```

The torque - angle delta characteristic is calculated using the same formulae with the only difference that there is DC current in the slots. The current is chose in such manner to be on a tim

```
% Static total torque Brem= 1,0 T Jrms<>0 and DC

tic % measures the computational time of the algorithm for the code that is interpolated by tic toc

%clear all;                          % Cleans Workspace in each run
clc;                                 % Cleans Command Window in each run
P=4;                                 % Total number of poles
Q=12;                                % Total number of slots
Brem=1.0;                            % Residual flux density in each PM
mur=1.0;                             % Relative permeability of the PM
mu0=4*pi*1e-07;                      % Vacuum permeability
thetai0=-1*pi/P;                     % Initial rotor PM angle (rad)
thetaj0=-0*pi/Q;                     % Initial stator slot angle (rad)
N=150;                               % Number of total harmonics in the air-gap region

R1=42*1e-03;                         % Radius of the rotor back iron cylinder
R2=50*1e-03;                         % Radius of the permanent-magnets
R3=51*1e-03;                         % Radius of the stator core
R4=53*1e-03;                         % Radius of the slot-opening
R5=65*1e-03;                         % Radius of the slot

ap=0.8;                              % Ratio of pole-arc to pole-arc
alpha=ap*2*pi/P;                     % Permanent-magnet angle (rad)
beta=alpha/ap;                       % Pole pitch angle (rad)
gamma=3*pi/180;                      % Slot opening angle (rad)
delta=15*pi/180;                     % Slot angle (rad)

Re=(R2+R3)/2;                        % Mid-radius of the air-gap (m)
Lst=100*1e-03;                       % Axial length of the machine (m)

Sslot=(delta/2)*(R5^2-R4^2);         % Area of a slot
%=5.560620000000000e+02;             % Slot current
%Jrms=I/Sslot;                       % RMS value of the current density in each slot (Calculated with known ...
      current)
Jrms=1*1e06;                         % RMS value of the current density in each slot (Predefined)
I=Jrms*Sslot;                        % Slot current (calculated with known current density)
J=zeros(Q,1);                        % Initiation of the current density vector
phi0=0*pi/2;                         % Initial angle of the armature reaction field vector
T=200;                               % Number of calculated points of the signal

% Filling each slot with a current density value with DC currents
for j=3:3:Q

    J(j,1)=Jrms*(-1)^(j+1)*sin(90*pi/180+120*pi/180+phi0);
    J(j-1,1)=-Jrms*(-1)^(j+1)*sin(90*pi/180-120*pi/180+phi0);
    J(j-2,1)=Jrms*(-1)^(j+1)*sin(90*pi/180+phi0);

end

Tstatic=zeros(N,1);              % Initiation of the static toque vector which contains the spatial ...
     air-gap harmonics for a specified rotor position
T_static=zeros(size(T));         % Initiation of the static torque vector which contains the values of ...
     the static torque for each rotor position
Tp_static=2*pi/P;                % Period of the static torque (rad)
Tp_static_deg=360/P;             % Period of the static torque (rad)
phi=linspace(0,Tp_static_deg,T); % Angular coordinate of the static torque


for t=1:T

    thetai0=thetai0+Tp_static/T;

    [A0Ii,AlIi,AnII,BnII,CnII,DnII,A0IIIj,AkIIIj,BkIIIj,A0IVj,AmIVj] =
    f(P,Q,Brem,mur,mu0,J,thetai0,thetaj0,R1,R2,R3,R4,R5,ap,alpha,beta,gamma,delta,N);

    for n = 1:N

        P_e3 = (Re/R3)^n + (R3/Re)^n;
        P_e2 = (Re/R2)^n + (R2/Re)^n;
        E_e3 = (Re/R3)^n - (R3/Re)^n;
        E_e2 = (Re/R2)^n - (R2/Re)^n;

        E_23 = (R2/R3)^n - (R3/R2)^n;
        E_32 = (R3/R2)^n - (R2/R3)^n;

```

```
73          Wn=-AnII(n)*(R2/Re)*P_e3/E_23 - BnII(n)*(R3/Re)*P_e2/E_32;
74          Xn=-CnII(n)*(R2/Re)*E_e3/E_23 - DnII(n)*(R3/Re)*E_e2/E_32;
75          Yn= CnII(n)*(R2/Re)*P_e3/E_23 + DnII(n)*(R3/Re)*P_e2/E_32;
76          Zn=-AnII(n)*(R2/Re)*E_e3/E_23 - BnII(n)*(R3/Re)*E_e2/E_32;
77
78          Tstatic(n,1)=(pi*Re^2*Lst/(mu0))*(Wn*Xn+Yn*Zn);
79
80      end
81
82      T_static(t,1)=sum(Tstatic);
83
84  end
85
86
87  theta=linspace(0,Tp_static_deg,length(phi)); % Angular coordinate of the static torque function
88  plot(theta,T_static,'k','LineWidth',1.25);   % Command used to plot the graph of the static torque
89  xlim([0 Tp_static_deg]);
90  grid on
91  toc
```

The electromagnetic torque is calculated in a similar manner as the static torque with the difference that the slots currents are not constant. They follow sinusoidal variation as the rotor position changes. More specifically, the currents have 120^o difference with each other the sinewave repeat two times in a whole mechanical period for a two pole pair machine.

```
1   % Electromagnetic Torque Calculation (Brem=1.0 T Jrms=1A/mm^2)
2
3   tic % measures the computational time of the algorithm for the code that is interpolated by tic toc
4
5   %clear all;                          % Cleans Workspace in each run
6   clc;                                 % Cleans Command Window in each run
7   P=4;                              % Number of poles
8   Q=12;                             % Number of slots
9   Brem=1.0*1;                       % Residual flux density in each PM
10  mur=1.0;                          % Relative permeability of the PM
11  mu0=4*pi*1e-07;                   % Vacuum permeability
12  thetai0=-1*pi/P;                  % Initial rotor PM angle
13  thetaj0=0*pi/Q;                   % Initital stator slot angle
14  N=50;                             % Number of total harmonics in the air-gap region
15
16  R1=42*1e-03;                      % Radius of the rotor back iron cylinder
17  R2=50*1e-03;                      % Radius of the permanent-magnets
18  R3=51*1e-03;                      % Radius of the stator core
19  R4=53*1e-03;                      % Radius of the slot-opening
20  R5=65*1e-03;                      % Radius of the slot
21
22  ap=0.8;                           % Ratio of pole-arc to pole-arc
23  alpha=ap*2*pi/P;                  % Permanent-magnet angle (rad)
24  beta=alpha/ap;                    % Pole pitch angle (rad)
25  gamma=3*pi/180;                   % Slot-opening angle (rad)
26  delta=15*pi/180;                  % Slot angle (rad)
27
28  Sslot=(delta/2)*(R5^2-R4^2);      % Area of a slot
29  %Imax=5.560620000000000e+02;      % Amplitude of the sinusoidal current
30  %Jrms=Imax/Sslot;                 % Value of the current density in each slot
31  %Jrms=0*1e06;                     % By using zero current density the reluctance torque can be calculated ...
        for the case the surface-inset magnet machine for an operating point
32  J=zeros(Q,1);                     % Initiation of the current density vectof
33  phi0=45*pi/180;                   % Initial angle of the armature reaction field which is used to define the ...
        angle delta or the operating point
34  T=200;                            % Number of points that the torque is calculated
35
36  Tem=zeros(N,1);                   % Initiation of the torque vector which contains the spatial harmonics of ...
        the a specific rotor position
37  T_em=zeros(size(T));              % Initiation of the torque vector which contains the values of the on-load ...
        electromagnetic torque for each rotor position
38  Tp_em=2*pi/P;                     % Spatial signal length which the torque is calculated (rad)
39  Tp_em_deg=360/P;                  % Spatial signal length which the torque is calculated (deg)
40  phi=linspace(0,Tp_em,T);
```

```
41
42
43  Re=(R2+R3)/2;                   % Mid-radius of the air-gap (m)
44  Lst=100*1e-03;                  % Axial length of the machine (m)
45  phi=linspace(0,Tp_em_deg,T);    % Angular coordinate of the torque
46
47  for t=1:T
48
49      thetai0=thetai0+Tp_em/T;
50      % Sinusoidal variation of the slot current with rotor position
51      for j=3:3:Q
52
53          J(j,1)=Jrms*(-1)^(j+1)*sin((P/2)*thetai0+90*pi/180-120*pi/180+phi0);
54          J(j-1,1)=-Jrms*(-1)^(j+1)*sin((P/2)*thetai0+90*pi/180+120*pi/180+phi0);
55          J(j-2,1)=Jrms*(-1)^(j+1)*sin((P/2)*thetai0+90*pi/180+phi0);
56
57      end
58
59      [A0Ii,AlIi,AnII,BnII,CnII,DnII,A0IIIj,AkIIIj,BkIIIj,A0IVj,AmIVj] = ...
            SurfaceInsetRadial(P,Q,Brem,mur,mu0,J,thetai0,thetaj0,R1,R2,R3,R4,R5,ap,alpha,beta,gamma,delta,N);
60
61      for n = 1:N
62
63      P_e3 = (Re/R3)^n + (R3/Re)^n;
64      P_e2 = (Re/R2)^n + (R2/Re)^n;
65      E_e3 = (Re/R3)^n - (R3/Re)^n;
66      E_e2 = (Re/R2)^n - (R2/Re)^n;
67
68      E_23 = (R2/R3)^n - (R3/R2)^n;
69      E_32 = (R3/R2)^n - (R2/R3)^n;
70
71      Wn=-AnII(n)*(R2/Re)*P_e3/E_23 - BnII(n)*(R3/Re)*P_e2/E_32;
72      Xn=-CnII(n)*(R2/Re)*E_e3/E_23 - DnII(n)*(R3/Re)*E_e2/E_32;
73      Yn= CnII(n)*(R2/Re)*P_e3/E_23 + DnII(n)*(R3/Re)*P_e2/E_32;
74      Zn=-AnII(n)*(R2/Re)*E_e3/E_23 - BnII(n)*(R3/Re)*E_e2/E_32;
75
76      Tem(n,1)=(pi*Re^2*Lst/(mu0))*(Wn*Xn+Yn*Zn);
77
78      end
79
80      T_em(t,1)=sum(Tem);
81
82  end
83  %T_em0=T_em;
84  theta=linspace(0,Tp_em_deg,length(phi)); % Angular coordinate of the torque
85  plot(theta,T_em,'k','LineWidth',1.25);   % Command used to plot the graph of the electromagnetic torque
86  xlim([0 Tp_em_deg]);
87  ylim([0 10])
88  grid on
89  mean(T_em)     % Mean value of electromagnetic torque
90  toc
```

B.2 Function for the surface-mounted magnet topology magnetized at the

B.2.1 Radial direction

The code of the function which calculates the unknown coefficients for the case of surface-mounted magnet machine topology is presented below in full. For all the other cases only the lines of code which are replaced with the new code are going to be presented as the code remains the same in most of the lines. Only the lines which concern the excitation will change.

```
function [A0Ii,AlIi,AnII,BnII,CnII,DnII,A0IIIj,AkIIIj,BkIIIj,A0IVj,AmIVj] = ...
      SurfaceMountedRadial(P,Q,Brem,mur,mu0,J,thetai0,thetaj0,R1,R2,R3,R4,R5,ap,alpha,beta,gamma,delta,N)

L=N/2;                  % Total number of harmonics in the magnet regions - Region Ii
K=N/2;                  % Total number of harmonics in the slot-opening regions - Region IIIj
M=N/2;                  % Total number of harmonics in the slot regions - Region IVj

% Initiation of the unknown coefficients vectors of each region
% Magnet subdomain - Region Ii
A0Ii=zeros(P,1);
AlIi=zeros(P*L,1);
% Air-gap subdomain - Region II
AnII=zeros(N,1);
BnII=zeros(N,1);
CnII=zeros(N,1);
DnII=zeros(N,1);
% Slot-opening subdomain - Region IIIj
A0IIIj=zeros(Q,1);
%B0IIIj=zeros(Q,1); Since the coefficient B0IIIj could be calculated directly, it was substituted ...
      directly to the system, hence the number of unknown coefficients became 11 instead of 12 that it ...
      would be originally
AkIIIj=zeros(Q*K,1);
BkIIIj=zeros(Q*K,1);
% Slot subdomain - Region IVj
A0IVj=zeros(Q,1);
AmIVj=zeros(Q*M,1);

% Initiation of the vector which contains the solutions
X=zeros(4*N+P*L+Q+2*Q*K+Q+Q*M,1);

A61=zeros(N,P*L);
A63=zeros(N,P*L);

A15=zeros(P,N);
A25=zeros(P,N);
A35=zeros(P,N);
A45=zeros(P,N);

A16=zeros(P*L,N);
A26=zeros(P*L,N);
A36=zeros(P*L,N);
A46=zeros(P*L,N);

for i=1:P

    thetai=2*(i-1)*pi/P+thetai0;

    for n=1:N

        R_ni=(2/n)*sin(n*beta/2)*cos(n*thetai);
        S_ni=(2/n)*sin(n*beta/2)*sin(n*thetai);

        A15(i,n)=R_ni*(R2/(n*beta))*((R2/R3)^(n)+(R3/R2)^(n))/((R2/R3)^(n)-(R3/R2)^(n));
        A25(i,n)=R_ni*(R3/(n*beta))*2/((R3/R2)^(n)-(R2/R3)^(n));
        A35(i,n)=S_ni*(R2/(n*beta))*((R2/R3)^(n)+(R3/R2)^(n))/((R2/R3)^(n)-(R3/R2)^(n));
        A45(i,n)=S_ni*(R3/(n*beta))*2/((R3/R2)^(n)-(R2/R3)^(n));

        for l=1:L

            ii=(i-1)*L+l;

            if (l*pi-n*beta~=0)

                F_lni=sin(n*beta/2-l*pi/2)*cos(n*thetai-l*pi/2)/(n-l*pi/beta)+...
                sin(n*beta/2+l*pi/2)*cos(n*thetai+l*pi/2)/(n+l*pi/beta);
                G_lni=sin(n*beta/2+l*pi/2)*sin(n*thetai+l*pi/2)/(n+l*pi/beta)+...
                sin(n*beta/2-l*pi/2)*sin(n*thetai-l*pi/2)/(n-l*pi/beta);

            else

                F_lni=(beta/2)*cos(n*thetai-n*beta/2)+sin(n*beta)*cos(n*thetai+n*beta/2)/(2*n);
                G_lni=(beta/2)*sin(n*thetai-n*beta/2)+sin(n*beta)*sin(n*thetai+n*beta/2)/(2*n);

            end

```

```
            E21_lpibeta=(R2/R1)^(l*pi/beta)-(R1/R2)^(l*pi/beta);
            P21_lpibeta=(R2/R1)^(l*pi/beta)+(R1/R2)^(l*pi/beta);

            A61(n,ii)=F_lni*(l/(mur*beta*R2))*E21_lpibeta/P21_lpibeta;
            A63(n,ii)=G_lni*(l/(mur*beta*R2))*E21_lpibeta/P21_lpibeta;

            A16(ii,n)=F_lni*(2*R2/(n*beta))*((R2/R3)^(n)+(R3/R2)^(n))/((R2/R3)^(n)-(R3/R2)^(n));
            A26(ii,n)=F_lni*(2*R3/(n*beta))*2/((R3/R2)^(n)-(R2/R3)^(n));
            A36(ii,n)=G_lni*(2*R2/(n*beta))*((R2/R3)^(n)+(R3/R2)^(n))/((R2/R3)^(n)-(R3/R2)^(n));
            A46(ii,n)=G_lni*(2*R3/(n*beta))*2/((R3/R2)^(n)-(R2/R3)^(n));

        end

    end

end

A82=zeros(N,Q*K);
A92=zeros(N,Q*K);
A84=zeros(N,Q*K);
A94=zeros(N,Q*K);

A17=zeros(Q,N);
A27=zeros(Q,N);
A37=zeros(Q,N);
A47=zeros(Q,N);

A18=zeros(Q*K,N);
A28=zeros(Q*K,N);
A38=zeros(Q*K,N);
A48=zeros(Q*K,N);

for j=1:Q

    thetaj=(2*(j-1)*pi)/Q+thetaj0;

    for n=1:N

        R_nj=(2/n)*sin(n*gamma/2)*cos(n*thetaj);
        S_nj=(2/n)*sin(n*gamma/2)*sin(n*thetaj);

        A17(j,n)=R_nj*(R2/(n*gamma))*2/((R2/R3)^(n)-(R3/R2)^(n));
        A27(j,n)=R_nj*(R3/(n*gamma))*((R3/R2)^(n)+(R2/R3)^(n))/((R3/R2)^(n)-(R2/R3)^(n));
        A37(j,n)=S_nj*(R2/(n*gamma))*2/((R2/R3)^(n)-(R3/R2)^(n));
        A47(j,n)=S_nj*(R3/(n*gamma))*((R3/R2)^(n)+(R2/R3)^(n))/((R3/R2)^(n)-(R2/R3)^(n));

        for k=1:K

            jj=(j-1)*K+k;

            if (k*pi-n*gamma==0)

                F_knj=(gamma/2)*cos(n*thetaj-n*gamma/2)+sin(n*gamma)*cos(n*thetaj+n*gamma/2)/(2*n);
                G_knj=(gamma/2)*sin(n*thetaj-n*gamma/2)+sin(n*gamma)*sin(n*thetaj+n*gamma/2)/(2*n);

            else

                F_knj=(n/(n^2-(k*pi/gamma)^2))*((-1)^k*sin(n*thetaj+n*gamma/2)-sin(n*thetaj-n*gamma/2));
                G_knj=-(n/(n^2-(k*pi/gamma)^2))*((-1)^k*cos(n*thetaj+n*gamma/2)-cos(n*thetaj-n*gamma/2));

            end

            P34_kpigamma=(R3/R4)^(k*pi/gamma)+(R4/R3)^(k*pi/gamma);
            E_34_kpigamma=(R3/R4)^(k*pi/gamma)-(R4/R3)^(k*pi/gamma);

            A82(n,jj)=F_knj*(k/(gamma*R3))*P34_kpigamma/E_34_kpigamma;
            A92(n,jj)=-F_knj*(k/(gamma*R3))*2/((R3/R4)^(k*pi/gamma)-(R4/R3)^(k*pi/gamma));
            A84(n,jj)=G_knj*(k/(gamma*R3))*P34_kpigamma/E_34_kpigamma;
            A94(n,jj)=-G_knj*(k/(gamma*R3))*2/((R3/R4)^(k*pi/gamma)-(R4/R3)^(k*pi/gamma));

            A18(jj,n)=F_knj*2*(R2/(n*gamma))*2/((R2/R3)^(n)-(R3/R2)^(n));
            A28(jj,n)=F_knj*2*(R3/(n*gamma))*((R3/R2)^(n)+(R2/R3)^(n))/((R3/R2)^(n)-(R2/R3)^(n));
            A38(jj,n)=G_knj*2*(R2/(n*gamma))*2/((R2/R3)^(n)-(R3/R2)^(n));
            A48(jj,n)=G_knj*2*(R3/(n*gamma))*((R3/R2)^(n)+(R2/R3)^(n))/((R3/R2)^(n)-(R2/R3)^(n));

```

```
148
149          end
150
151      end
152
153  end
154
155  A119=zeros(Q,Q*M);
156  A1110=zeros(Q*K,Q*M);
157
158  for j=1:Q
159
160      for m=1:M
161
162          P45_mpidelta=(R4/R5)^(m*pi/delta)+(R5/R4)^(m*pi/delta);
163          E45_mpidelta=(R4/R5)^(m*pi/delta)-(R5/R4)^(m*pi/delta);
164
165          A119(j,m)=sin(0.5*m*pi*gamma/delta)*cos(0.5*m*pi)*(2*R4/gamma)*...
166          (delta/(m*pi))^2*P45_mpidelta/E45_mpidelta;
167
168          for k=1:K
169
170              jj=(j-1)*K+k;
171
172              if (m*gamma-k*delta==0)
173
174                  H_mk=(gamma/2)*cos(0.5*k*pi*(gamma-delta)/gamma);
175
176              else
177
178                  H_mk=((m*pi/delta)/((m*pi/delta)-(k*pi/gamma)*(m*pi/delta)+(k*pi/gamma)))*...
179                  ((-1)^k*sin(0.5*m*pi*(gamma+delta)/delta)+sin(0.5*m*pi*(gamma-delta)/delta));
180
181              end
182
183              A1110(jj,m)=H_mk*(2*delta*R4/(m*pi*gamma))*P45_mpidelta/E45_mpidelta;
184
185          end
186
187      end
188
189  end
190
191  A811=zeros(Q*M,Q*K);
192  A911=zeros(Q*M,Q*K);
193
194  for j=1:Q
195
196      for k=1:K
197
198          for m=1:M
199
200              jj=(j-1)*M+m;
201
202              if (m*gamma-k*delta==0)
203
204                  H_mk=(gamma/2)*cos(0.5*k*pi*(gamma-delta)/gamma);
205
206              else
207
208                  H_mk=((m*pi/delta)/((m*pi/delta)-(k*pi/gamma)*(m*pi/delta)+(k*pi/gamma)))*...
209                  ((-1)^k*sin(0.5*m*pi*(gamma+delta)/delta)+sin(0.5*m*pi*(gamma-delta)/delta));
210
211              end
212
213              P43_kpigamma=(R4/R3)^(k*pi/gamma)+(R3/R4)^(k*pi/gamma);
214              E43_kpigamma=(R3/R4)^(k*pi/gamma)-(R4/R3)^(k*pi/gamma);
215
216              A811(jj,k)=H_mk*(2*k*pi/(delta*gamma*R4))*2/((R3/R4)^(k*pi/gamma)-(R4/R3)^(k*pi/gamma));
217              A911(jj,k)=-H_mk*(2*k*pi/(delta*gamma*R4))*P43_kpigamma/E43_kpigamma;
218
219          end
220
221      end
222
```

```
end

%       AnII    ,    BnII    ,    CnII    ,    DnII     ,  A0Ii      ,    AlIi      ,  A0IIIj    ,   AkIIIj ...
          ,     BkIIIj   ,   A0IVj    ,      AmIVj
A=[-eye(N)      ,zeros(N)     , zeros(N)    ,zeros(N)     ,zeros(N,P)  ,    A61       ,zeros(N,Q)  ...
      ,zeros(N,Q*K)   , zeros(N,Q*K) ,zeros(N,Q)   ,zeros(N,Q*M)
    zeros(N)     ,-eye(N)      , zeros(N)    ,zeros(N)     ,zeros(N,P)  ,zeros(N,P*L)  ,zeros(N,Q)  ,    A82 ...
                ,      A92       ,zeros(N,Q)   ,zeros(N,Q*M)
    zeros(N)     ,zeros(N)     , -eye(N)     ,zeros(N)     ,zeros(N,P)  ,   A63        ,zeros(N,Q)  ...
          ,zeros(N,Q*K)   ,zeros(N,Q*K)   ,zeros(N,Q)   ,zeros(N,Q*M)
    zeros(N)     ,zeros(N)     , zeros(N)    ,-eye(N)      ,zeros(N,P)  ,zeros(N,P*L)  ,zeros(N,Q)  ,   A84 ...
                ,      A94       ,zeros(N,Q)   ,zeros(N,Q*M)
      A15        ,    A25       ,    A35       ,   A45        ,-eye(P)      ,zeros(P,P*L)  ,zeros(P,Q)  ...
           ,zeros(P,Q*K)   ,zeros(P,Q*K)   ,zeros(P,Q)   ,zeros(P,Q*M)
      A16        ,    A26       ,    A36       ,   A46        ,zeros(P*L,P),-eye(P*L)      ...
           ,zeros(P*L,Q),zeros(P*L,Q*K),zeros(P*L,Q*K),zeros(P*L,Q),zeros(P*L,Q*M)
      A17        ,    A27       ,    A37       ,   A47        ,zeros(Q,P)  ,zeros(Q,P*L)  ,-eye(Q)      ...
           ,zeros(Q,Q*K)   ,zeros(Q,Q*K)   ,zeros(Q)     ,zeros(Q,Q*M)
      A18        ,    A28       ,    A38       ,   A48        ,zeros(Q*K,P),zeros(Q*K,P*L),zeros(Q*K,Q),-eye(Q*K) ...
               ,zeros(Q*K)     ,zeros(Q*K,Q),zeros(Q*K,Q*M)
    zeros(Q,N)   ,zeros(Q,N)   ,zeros(Q,N)   ,zeros(Q,N)   ,zeros(Q,P)  ,zeros(Q,P*L)  ,eye(Q)       ...
          ,zeros(Q,Q*K)   ,zeros(Q,Q*K)   ,-eye(Q)      ,     A119
    zeros(Q*K,N),zeros(Q*K,N),zeros(Q*K,N),zeros(Q*K,N),zeros(Q*K,P),zeros(Q*K,P*L),zeros(Q*K,Q),zeros(Q*K) ...
            ,-eye(Q*K)     ,zeros(Q*K,Q),     A1110
    zeros(Q*M,N),zeros(Q*M,N),zeros(Q*M,N),zeros(Q*M,N),zeros(Q*M,P),zeros(Q*M,P*L),zeros(Q*M,Q),   A811 ...
               ,    A911       ,zeros(Q*M,Q),-eye(Q*M)];

B1=zeros(N,1);
B2=zeros(N,1);
B3=zeros(N,1);
B4=zeros(N,1);
B5=zeros(P,1);
B6=zeros(P*L,1);
CC=0.0;
DD=0.0;
B7=zeros(Q,1);
B8=zeros(Q*K,1);
B9=zeros(Q,1);
B10=zeros(Q*K,1);
B11=zeros(Q*M,1);

for n=1:N

    for i=1:P

        thetai=(i-1)*2*pi/P+thetai0;

        for l=1:L

            if (l*pi-n*beta~=0)

                F_lni=sin(n*beta/2-l*pi/2)*cos(n*thetai-l*pi/2)/(n-l*pi/beta)+...
                sin(n*beta/2+l*pi/2)*cos(n*thetai+l*pi/2)/(n+l*pi/beta);
                G_lni=sin(n*beta/2+l*pi/2)*sin(n*thetai+l*pi/2)/(n+l*pi/beta)+...
                sin(n*beta/2-l*pi/2)*sin(n*thetai-l*pi/2)/(n-l*pi/beta);

            else

                F_lni=(beta/2)*cos(n*thetai-n*beta/2)+sin(n*beta)*cos(n*thetai+n*beta/2)/(2*n);
                G_lni=(beta/2)*sin(n*thetai-n*beta/2)+sin(n*beta)*sin(n*thetai+n*beta/2)/(2*n);

            end

            Fl1i=4*(-1)^i*Brem*sin(l*pi/2)*sin(l*pi*alpha/(2*beta))/(beta*((l*pi/beta)^2-1));

            AA=(Fl1i/(pi*mur))*(1-(R1/R2)^(l*pi/beta+1))*F_lni;
            BB=(Fl1i/(pi*mur))*(1-(R1/R2)^(l*pi/beta+1))*G_lni;

            CC=CC+AA;
            DD=DD+BB;

        end

        B1(n,1)=CC+B1(n,1);
        B3(n,1)=DD+B3(n,1);
```

```
            CC=0.0;
            DD=0.0;

        end

    end


    for n=1:N

        for j=1:Q

            thetaj=(2*(j-1)*pi)/Q+thetaj0;

            R_nj=(2/n)*sin(n*gamma/2)*cos(n*thetaj);
            S_nj=(2/n)*sin(n*gamma/2)*sin(n*thetaj);

            B0IIIj=(delta/gamma)*(1/2)*mu0*J(j,1)*(R5^2-R4^2);

            B2(n,1)=B2(n,1)-(B0IIIj*R_nj/(pi*R3));
            B4(n,1)=B4(n,1)-(B0IIIj*S_nj/(pi*R3));

        end

    end

    for i=1:P

        for l=1:L

            ii=(i-1)*L+l;

            FlIi=4*(-1)^i*Brem*sin(l*pi/2)*sin(l*pi*alpha/(2*beta))/(beta*((l*pi/beta)^2-1));
            B6(ii,1)=-FlIi*(R2+(R1*beta/(l*pi))*(R1/R2)^(l*pi/beta));

        end

    end

    for j=1:Q

        B0IIIj=(delta/gamma)*(1/2)*mu0*J(j,1)*(R5^2-R4^2);
        B7(j,1)=log(R3)*B0IIIj;
        B9(j,1)=-(1/2)*mu0*J(j,1)*(R5^2*log(R4)-R4^2/2)+B0IIIj*log(R4);

        for m=1:M

            jj=(j-1)*M+m;

            B11(jj,1)=-(4/(m*pi*R4))*B0IIIj*sin(m*pi*gamma/(2*delta))*cos(m*pi/2);

        end

    end

    B = [B1 ; B2 ; B3 ; B4 ; B5 ; B6 ; B7 ; B8 ; B9 ; B10 ; B11 ];

    % Calculation of solution by solving the system using the created arrays A and B
    X=A\B;

    % Dividing the solution into each coefficient to be used on the main program for calculations
    AnII=X(1:N,1);
    BnII=X(N+1:2*N,1);
    CnII=X(2*N+1:3*N,1);
    DnII=X(3*N+1:4*N,1);
    A0Ii=X(4*N+1:4*N+P,1);
    AlIi=X(4*N+P+1:4*N+P+P*L,1);
    A0IIIj=X(4*N+P+P*L+1:4*N+P+P*L+Q,1);
    AkIIIj=X(4*N+P+P*L+Q+1:4*N+P+P*L+Q+Q*K,1);
    BkIIIj=X(4*N+P+P*L+Q+Q*K+1:4*N+P+P*L+Q+2*Q*K,1);
    A0IVj=X(4*N+P+P*L+Q+2*Q*K+1:4*N+P+P*L+Q+2*Q*K+Q,1);
    AmIVj=X(4*N+P+P*L+Q+2*Q*K+Q+1:4*N+P+P*L+Q+2*Q*K+Q+Q*M,1);

    end
```

The only lines need to be changed for calculating the other magnetization patterns even for the other machine topology are the lines 252-291 and 312-323. These loops are substituted by other loops which correspond to other magnetization pattern and machine topology. In the next subsection every code for each case is given.

B.2.2 Parallel direction

```
for n=1:N

    for i=1:P

        thetai=(i-1)*2*pi/P+thetai0;

        for l=1:L

            El1i=(1/(1+l*pi/beta))*sin(alpha/2+l*pi*alpha/(2*beta))*sin(l*pi/2)-...
            (1/(1-l*pi/beta))*sin(alpha/2-l*pi*alpha/(2*beta))*sin(l*pi/2);
            Fl1i=(4*(-1)^i*Brem*cos(alpha/2)*sin(l*pi*alpha/(2*beta))*sin(l*pi/2)/(beta*((l*pi/beta)^2-1)));

            if (l*pi-n*beta==0)

                F_lni=(beta/2)*cos(n*thetai-n*beta/2)+sin(n*beta)*cos(n*thetai+n*beta)/(2*n);
                G_lni=(beta/2)*sin(n*thetai-n*beta/2)+sin(n*beta)*sin(n*thetai+n*beta)/(2*n);

            else

                F_lni=+(n/(n^2-(l*pi/beta)^2))*((-1)^l*sin(n*thetai+n*beta/2)-sin(n*thetai-n*beta/2));
                G_lni=-(n/(n^2-(l*pi/beta)^2))*((-1)^l*cos(n*thetai+n*beta/2)-cos(n*thetai-n*beta/2));

            end


            AA=(1/(pi*mur))*(Fl1i-(Fl1i+(2/beta)*(-1)^i*Brem*El1i)*(R1/R2)^(l*pi/beta+1))*F_lni;
            BB=(1/(pi*mur))*(Fl1i-(Fl1i+(2/beta)*(-1)^i*Brem*El1i)*(R1/R2)^(l*pi/beta+1))*G_lni;

            CC=CC+AA;
            DD=DD+BB;

        end

        if (n-1==0)

            In1i=-(alpha/2)*sin(thetai)+(sin(alpha)*sin(thetai))/2;
            Jn1i=(alpha/2)*cos(thetai)-(sin(alpha)*cos(thetai))/2;


        else

            In1i=(1/(n+1))*sin(n*alpha/2+alpha/2)*sin(n*thetai)-...
            (1/(n-1))*sin(n*alpha/2-alpha/2)*sin(n*thetai);
            Jn1i=(1/(n-1))*sin(n*alpha/2-alpha/2)*cos(n*thetai)-...
            (1/(n+1))*sin(n*alpha/2+alpha/2)*cos(n*thetai);

        end

        B1(n,1)=CC+B1(n,1)+((-1)^i*Brem*In1i/(pi*mur));
        B3(n,1)=DD+B3(n,1)+((-1)^i*Brem*Jn1i/(pi*mur));
        CC=0.0;
        DD=0.0;

    end

end

for i=1:P

    for l=1:L

```

```
        ii=(i-1)*L+l;

        El1i=(1/(1+l*pi/beta))*sin(alpha/2+l*pi*alpha/(2*beta))*sin(l*pi/2)-...
        (1/(1-l*pi/beta))*sin(alpha/2-l*pi*alpha/(2*beta))*sin(l*pi/2);
        FlIi=(4*(-1)^i*Brem*cos(alpha/2)*sin(l*pi*alpha/(2*beta))*sin(l*pi/2)/(beta*((l*pi/beta)^2-1)));
        B6(ii,1)=-FlIi*R2-R1*((beta/(l*pi))*FlIi+(2*(-1)^i*Brem*El1i/(l*pi)))*(R1/R2)^(l*pi/beta);

    end

end
```

B.2.3 Halbach direction

```
for n=1:N

    for i=1:P

        thetai=(i-1)*2*pi/P+thetai0;

        for l=1:L

            if (beta*ap-alpha*l==0)

                E_l1i=(alpha/(2*ap*pi))*sin(ap*pi)*sin(ap*pi*beta/(2*alpha))-...
                (alpha/2)*sin(ap*pi*beta/(2*alpha));

            else

                E_l1i=sin(l*pi/2)*(sin(ap*pi/2+l*pi*alpha/(2*beta))/(ap*pi/alpha+l*pi/beta)-...
                sin(ap*pi/2-l*pi*alpha/(2*beta))/(ap*pi/alpha-l*pi/beta));

            end


            FlIi=(2*(-1)^i*Brem*E_l1i/(beta*((l*pi/beta)^2-1)));
            GlIi=(4*(-1)^i*Brem*cos(ap*pi/2)*sin(l*pi/2)*sin(l*pi*alpha/(2*beta))/(beta*((l*pi/beta)^2-1)));


            if (l*pi-n*beta==0)


                F_lni=(beta/2)*cos(n*thetai-n*beta/2)+sin(n*beta)*cos(n*thetai+n*beta/2)/(2*n);
                G_lni=(beta/2)*sin(n*thetai-n*beta/2)+sin(n*beta)*sin(n*thetai+n*beta/2)/(2*n);

            else

                F_lni=(n/(n^2-(l*pi/beta)^2))*((-1)^l*sin(n*thetai+n*beta/2)-sin(n*thetai-n*beta/2));
                G_lni=-(n/(n^2-(l*pi/beta)^2))*((-1)^l*cos(n*thetai+n*beta/2)-cos(n*thetai-n*beta/2));

            end

            AA=(FlIi/(pi*mur))*(1-ap*pi/alpha-((l*pi/beta)^2-ap*pi/alpha)*(R1/R2)^(l*pi/beta+1))*F_lni+...
            (GlIi/(pi*mur))*(1-(R1/R2)^(l*pi/beta+1))*F_lni;
            BB=(FlIi/(pi*mur))*(1-ap*pi/alpha-((l*pi/beta)^2-ap*pi/alpha)*(R1/R2)^(l*pi/beta+1))*G_lni+...
            (GlIi/(pi*mur))*(1-(R1/R2)^(l*pi/beta+1))*G_lni;

            CC=CC+AA;
            DD=DD+BB;

        end

        if (n*alpha-pi*ap==0)

            I_napi=-(alpha/2)*sin(n*thetai)+sin(n*thetai)*sin(n*alpha)/(2*n);
            J_napi=(alpha/2)*cos(n*thetai)-cos(n*thetai)*sin(n*alpha)/(2*n);

        else

            I_napi=sin(n*thetai)*(sin(n*alpha/2+ap*pi/2)/(n+ap*pi/alpha)-...
            sin(n*alpha/2-ap*pi/2)/(n-ap*pi/alpha));
```

```
            J_napi=cos(n*thetai)*(sin(n*alpha/2-ap*pi/2)/(n-ap*pi/alpha)-...
            sin(n*alpha/2+ap*pi/2)/(n+ap*pi/alpha));

        end

        B1(n,1)=CC+B1(n,1)+((-1)^i*Brem/(pi*mur))*I_napi;
        B3(n,1)=DD+B3(n,1)+((-1)^i*Brem/(pi*mur))*J_napi;
        CC=0.0;
        DD=0.0;

    end

end

for i=1:P

    for l=1:L

        ii=(i-1)*L+l;

        if (beta*ap-alpha*l==0)

            E_l1i=(alpha/(2*ap*pi))*sin(ap*pi)*sin(ap*pi*beta/(2*alpha))-...
            (alpha/2)*sin(ap*pi*beta/(2*alpha));

        else

            E_l1i=sin(l*pi/2)*(sin(ap*pi/2+l*pi*alpha/(2*beta))/(ap*pi/alpha+l*pi/beta)-...
            sin(ap*pi/2-l*pi*alpha/(2*beta))/(ap*pi/alpha-l*pi/beta));

        end


        F1Ii=(2*(-1)^i*Brem*E_l1i/(beta*((l*pi/beta)^2-1)));
        G1Ii=(4*(-1)^i*Brem*cos(ap*pi/2)*sin(l*pi/2)*sin(l*pi*alpha/(2*beta))/(beta*((l*pi/beta)^2-1)));


        B6(ii,1)=-F1Ii*((1-ap*pi/alpha)*R2+(beta*R1/(l*pi))*((l*pi/beta)^2-ap*pi/alpha)*(R1/R2)^(l*pi/beta))-...
        G1Ii*(R2+(beta*R1/(l*pi))*(R1/R2)^(l*pi/beta));

    end

end
```

B.3 Function for the surface-inset magnet topology magnetized at the

B.3.1 Radial direction

```
for n=1:N

    for i=1:P

        thetai=(i-1)*2*pi/P+thetai0;

        for l=1:L


            F1Ii=(2*(-1)^i*Brem*((-1)^l-1)/(alpha*((l*pi/alpha)^2-1)));

            if (l*pi-n*alpha==0)

                F_lni=(alpha/2)*cos(n*thetai-n*alpha/2)+sin(n*alpha)*cos(n*thetai+n*alpha)/(2*n);
                G_lni=(alpha/2)*sin(n*thetai-n*alpha/2)+sin(n*alpha)*sin(n*thetai+n*alpha)/(2*n);

```

```
            else

                F_lni=+(n/(n^2-(l*pi/alpha)^2))*((-1)^l*sin(n*thetai+n*alpha/2)-sin(n*thetai-n*alpha/2));
                G_lni=-(n/(n^2-(l*pi/alpha)^2))*((-1)^l*cos(n*thetai+n*alpha/2)-cos(n*thetai-n*alpha/2));

            end


            AA=-(FlIi/(pi*mur))*(1-(R1/R2)^(l*pi/alpha+1))*F_lni;
            BB=-(FlIi/(pi*mur))*(1-(R1/R2)^(l*pi/alpha+1))*G_lni;

            CC=CC+AA;
            DD=DD+BB;

        end

        B1(n,1)=CC+B1(n,1);
        B3(n,1)=DD+B3(n,1);
        CC=0.0;
        DD=0.0;

    end

end

for i=1:P

    for l=1:L

        ii=(i-1)*L+l;
        FlIi=(2*(-1)^i*Brem*((-1)^l-1)/(alpha*((l*pi/alpha)^2-1)));
        B6(ii,1)=FlIi*(R2+(alpha*R1/(l*pi))*(R1/R2)^(l*pi/alpha));

    end

end
```

B.3.2 Parallel direction

```
for n=1:N

    for i=1:P

        thetai=(i-1)*2*pi/P+thetai0;

        for l=1:L


            FlIi=(2*(-1)^i*Brem*cos(alpha/2)*(1-(-1)^l)/(alpha*((l*pi/alpha)^2-1)));

            if (l*pi-n*alpha==0)

                F_lni=(alpha/2)*cos(n*thetai-n*alpha/2)+sin(n*alpha)*cos(n*thetai+n*alpha)/(2*n);
                G_lni=(alpha/2)*sin(n*thetai-n*alpha/2)+sin(n*alpha)*sin(n*thetai+n*alpha)/(2*n);

            else

                F_lni=+(n/(n^2-(l*pi/alpha)^2))*((-1)^l*sin(n*thetai+n*alpha/2)-sin(n*thetai-n*alpha/2));
                G_lni=-(n/(n^2-(l*pi/alpha)^2))*((-1)^l*cos(n*thetai+n*alpha/2)-cos(n*thetai-n*alpha/2));

            end


            AA=(FlIi/(pi*mur))*F_lni;
            BB=(FlIi/(pi*mur))*G_lni;

            CC=CC+AA;
            DD=DD+BB;

        end
```

```

        if (n-1==0)

            In1i=-(alpha/2)*sin(thetai)+(sin(alpha)*sin(thetai))/2;
            Jn1i=(alpha/2)*cos(thetai)-(sin(alpha)*cos(thetai))/2;


        else

            In1i=(1/(n+1))*sin(n*alpha/2+alpha/2)*sin(n*thetai)-(1/(n-1))*sin(n*alpha/2-alpha/2)*sin(n*thetai);
            Jn1i=(1/(n-1))*sin(n*alpha/2-alpha/2)*cos(n*thetai)-(1/(n+1))*sin(n*alpha/2+alpha/2)*cos(n*thetai);

        end

        B1(n,1)=CC+B1(n,1)+((-1)^i*Brem*In1i/(pi*mur));
        B3(n,1)=DD+B3(n,1)+((-1)^i*Brem*Jn1i/(pi*mur));
        CC=0.0;
        DD=0.0;

    end

end

for i=1:P

    for l=1:L

        ii=(i-1)*L+l;
        FlIi=(2*(-1)^i*Brem*cos(alpha/2)*(1-(-1)^l)/(alpha*((l*pi/alpha)^2-1)));
        B6(ii,1)=-FlIi*R2;

    end

end
```

B.3.3 Halbach direction

```
for n=1:N

    for i=1:P

        thetai=(i-1)*2*pi/P+thetai0;

        for l=1:L

            if (l-ap==0)

                E_l1i=(alpha/(2*ap*pi))*sin(ap*pi)*sin(ap*pi/2)-(alpha/2)*sin(ap*pi/2);

            else

                E_l1i=((ap*pi/alpha)/((ap*pi/alpha)^2-(l*pi/alpha)^2))*cos(ap*pi/2)*(1-(-1)^l);

            end


            FlIi=(2*(-1)^i*Brem*E_l1i/(alpha*((l*pi/alpha)^2-1)));
            GlIi=(2*(-1)^i*Brem*cos(ap*pi/2)*(1-(-1)^l)/(alpha*((l*pi/alpha)^2-1)));


            if (l*pi-n*alpha==0)


                F_lni=(alpha/2)*cos(n*thetai-n*alpha/2)+sin(n*alpha)*cos(n*thetai+n*alpha/2)/(2*n);
                G_lni=(alpha/2)*sin(n*thetai-n*alpha/2)+sin(n*alpha)*sin(n*thetai+n*alpha/2)/(2*n);

            else

                F_lni=(n/(n^2-(l*pi/alpha)^2))*((-1)^l*sin(n*thetai+n*alpha/2)-sin(n*thetai-n*alpha/2));
                G_lni=-(n/(n^2-(l*pi/alpha)^2))*((-1)^l*cos(n*thetai+n*alpha/2)-cos(n*thetai-n*alpha/2));
```

```
34
35              end
36
37              AA=(FlIi/(pi*mur))*(1-ap*pi/alpha-((l*pi/alpha)^2-ap*pi/alpha)*(R1/R2)^(l*pi/alpha+1))*F_lni+...
38              (GlIi/(pi*mur))*(1-(R1/R2)^(l*pi/alpha+1))*F_lni;
39              BB=(FlIi/(pi*mur))*(1-ap*pi/alpha-((l*pi/alpha)^2-ap*pi/alpha)*(R1/R2)^(l*pi/alpha+1))*G_lni+...
40              (GlIi/(pi*mur))*(1-(R1/R2)^(l*pi/alpha+1))*G_lni;
41
42              CC=CC+AA;
43              DD=DD+BB;
44
45          end
46
47          if (n*alpha-pi*ap==0)
48
49              I_napi=-(alpha/2)*sin(n*thetai)+sin(n*thetai)*sin(n*alpha)/(2*n);
50              J_napi=(alpha/2)*cos(n*thetai)-cos(n*thetai)*sin(n*alpha)/(2*n);
51
52          else
53
54              I_napi=sin(n*thetai)*(sin(n*alpha/2+ap*pi/2)/(n+ap*pi/alpha)-...
55              sin(n*alpha/2-ap*pi/2)/(n-ap*pi/alpha));
56              J_napi=cos(n*thetai)*(sin(n*alpha/2-ap*pi/2)/(n-ap*pi/alpha)-...
57              sin(n*alpha/2+ap*pi/2)/(n+ap*pi/alpha));
58
59          end
60
61          B1(n,1)=CC+B1(n,1)+((-1)^i*Brem/(pi*mur))*Kn;
62          B3(n,1)=DD+B3(n,1)+((-1)^i*Brem/(pi*mur))*Ln;
63          CC=0.0;
64          DD=0.0;
65
66      end
67
68  end
69
70  for i=1:P
71
72      for l=1:L
73
74          ii=(i-1)*L+l;
75
76          if (l-ap==0)
77
78              E_l1i=(alpha/(2*ap*pi))*sin(ap*pi)*sin(ap*pi/2)-(alpha/2)*sin(ap*pi/2);
79
80          else
81
82              E_l1i=((ap*pi/alpha)/((ap*pi/alpha)^2-(l*pi/alpha)^2))*cos(ap*pi/2)*(1-(-1)^l);
83
84          end
85
86
87          FlIi=(2*(-1)^i*Brem*E_l1i/(alpha*((l*pi/alpha)^2-1)));
88          GlIi=(2*(-1)^i*Brem*cos(ap*pi/2)*(1-(-1)^l)/(alpha*((l*pi/alpha)^2-1)));
89
90
91          B6(ii,1)=-FlIi*R2*(1-ap*pi/alpha+(alpha/(l*pi))*((l*pi/alpha)^2-ap*pi/alpha)*(R1/R2)^(l*pi/alpha+1))-...
92          GlIi*R2*(1+(alpha/(l*pi))*(R1/R2)^(l*pi/alpha+1));
93
94      end
95
96  end
```

Bibliography

[1] Vigneshwaran Gurusamy, Gerard-Andre; Capolino, Bilal Akin, Humberto Henao, Raphael;l Romary, and Remus Pusca. Recent trends in magnetic sensors and flux-based condition monitoring of electromagnetic devices. *IEEE Transactions on Industry Applications*, 58(4):4668–4684, 2022.

[2] Jawad Faiz and Ehsan Mazaheri-Tehrani. Demagnetization modeling and fault diagnosing techniques in permanent magnet machines under stationary and nonstationary conditions: An overview. *IEEE Transactions on Industry Applications*, 53(3):2772–2785, 2017.

[3] Jawad Faiz and Hossein Nejadi-Koti. Eccentricity fault diagnosis indices for permanent magnet machines: state-of-the-art. *IET Electric Power Applications*, 13(9):1241–1254, 2019.

[4] Jawad Faiz, Hossein Nejadi-Koti, and Zahra Valipour. Comprehensive review on inter-turn fault indexes in permanent magnet motors. *IET Electric Power Applications*, 11(1):142–156, 2017.

[5] H.A Toliyat, S. Nandi, S. Choi, and H. Meshgin-Kelk. *Electric Machines Modeling, Condition Monitoring, and Fault Diagnosis*. Taylor and Francis, 01 2013, pages 1-5, 10, 20-22.

[6] Simon Jonathan Watson, Beth J. Xiang, Wenxian Yang, Peter J. Tavner, and Christopher J. Crabtree. Condition monitoring of the power output of wind turbine generators using wavelets. *IEEE Transactions on Energy Conversion*, 25(3):715–721, 2010.

[7] Nuno M. A. Freire and Antonio J. Marques Cardoso. Fault detection and condition monitoring of pmsgs in offshore wind turbines. *Machines*, 9(11):260, Oct 2021.

[8] P. J. Tavner, J. Xiang, and F. Spinato. Reliability analysis for wind turbines. *Wind Energy*, 10(1):1–18, 2007.

[9] P.J. Tavner. Review of condition monitoring of rotating electrical machines. *IET Electric Power Applications*, 2:215–247(32), July 2008.

[10] Pinjia Zhang, Yi Du, Thomas G. Habetler, and Bin Lu. A survey of condition monitoring and protection methods for medium-voltage induction motors. *IEEE Transactions on Industry Applications*, 47(1):34–46, 2011.

[11] Oladapo Omotade Ogidi, Paul S. Barendse, and Mohamed A. Khan. Fault diagnosis and condition monitoring of axial-flux permanent magnet wind generators. *Electric Power Systems Research*, 136:1–7, 2016.

[12] Seyyed Mehdi Mirimani, Abolfazl Vahedi, Fabrizio Marignetti, and Roberto Di Stefano. An online method for static eccentricity fault detection in axial flux machines. *IEEE Transactions on Industrial Electronics*, 62(3):1931–1942, 2015.

[13] W.T. Thomson and A. Barbour. On-line current monitoring and application of a finite element method to predict the level of static airgap eccentricity in three-phase induction motors. *IEEE Transactions on Energy Conversion*, 13(4):347–357, 1998.

[14] A. Siddique, G.S. Yadava, and B. Singh. A review of stator fault monitoring techniques of induction motors. *IEEE Transactions on Energy Conversion*, 20(1):106–114, 2005.

[15] Wei Li, Anhua Li, and Huijie Wang. Anisotropic fracture behavior of sintered rare-earth permanent magnets. *IEEE Transactions on Magnetics*, 41(8):2339–2342, 2005.

[16] Z. Q. Zhu, L. J. Wu, and Z. P. Xia. An accurate subdomain model for magnetic field computation in slotted surface-mounted permanent-magnet machines. *IEEE Transactions on Magnetics*, 46(4):1100–1115, 2010.

[17] Cha-Seung Jun, Ohbong Kwon, and Byung-Il Kwon. Sensitivity comparison of open-circuit airgap flux between surface-mounted permanent magnet and spoke-type permanent magnet machines considering manufacturing tolerances. *IEEE Access*, 7:165908–165918, 2019.

[18] Wenming Tong, Shiqi Li, Xuelong Pan, Shengnan Wu, and Renyuan Tang. Analytical model for cogging torque calculation in surface-mounted permanent magnet motors with rotor eccentricity and magnet defects. *IEEE Transactions on Energy Conversion*, 35(4):2191–2200, 2020.

[19] Jiajing Fu and Changsheng Zhu. Subdomain model for predicting magnetic field in slotted surface mounted permanent-magnet machines with rotor eccentricity. *IEEE Transactions on Magnetics*, 48(5):1906–1917, 2012.

[20] U. Kim and D.K. Lieu. Magnetic field calculation in permanent magnet motors with rotor eccentricity: without slotting effect. *IEEE Transactions on Magnetics*, 34(4):2243–2252, 1998.

[21] Cenwei Shi, Lin Peng, Zhen Zhang, and Tingna Shi. Analytical modeling and analysis of permanent-magnet motor with demagnetization fault. *Sensors*, 22(23):9440, Dec 2022.

[22] Ehsan Mazaheri-Tehrani and Jawad Faiz. Airgap and stray magnetic flux monitoring techniques for fault diagnosis of electrical machines: An overview. *IET Electric Power Applications*, 16(3):277–299, 2022.

[23] Yao Da, Xiaodong Shi, and Mahesh Krishnamurthy. A new approach to fault diagnostics for permanent magnet synchronous machines using electromagnetic signature analysis. *IEEE Transactions on Power Electronics*, 28(8):4104–4112, 2013.

[24] Matteo Leandro, Nada Elloumi, Alberto Tessarolo, and Jonas Kristiansen Nland. Analytical iron loss evaluation in the stator yoke of slotless surface-mounted pm machines. *IEEE Transactions on Industry Applications*, pages 1–1, 2022.

[25] Duane Hanselman. *Brushless Permanent Magnet Motor Design*. Magna Physics Publishing, 2nd edition, 01 2003, pages 34-38, 82-86, 86-90.

[26] Jacek Gieras, Chong Wang, and Joseph Lai. *Noise of Polyphase Electric Motors*. Taylor Francis Group, 01 2005, pages 326-332.

[27] Steven Chapman. *Electric machinery fundamentals*. McGraw Hill, 5th edition, 01 2012, pages 180, 183, 494.

[28] Conggan Ma, Chaoyi Chen, Qing Li, Haibo Gao, Qiang Kang, Jianguang Fang, Hongwei Cui, Kaibing Teng, and Xiaowen Lv. Analytical calculation of no-load magnetic field of external rotor permanent magnet brushless direct current motor used as in-wheel motor of electric vehicle. *IEEE Transactions on Magnetics*, 54(4):1–6, 2018.

[29] Jacek Gieras, Rong-Jie Wang, and Maarten J Kamper. *Axial flux permanent-magnet brushless machines*. Springer, 2nd edition, 01 2008, pages 18-19, 94-99,175-188.

[30] Pooja Khatri and Xu Wang. Comprehensive review of a linear electrical generator for ocean wave energy conversion. *IET Renewable Power Generation*, 14(6):949–958, 2020.

[31] Konstantinos N. Gyftakis and Antonio J. Marques Cardoso. Reliable detection of stator interturn faults of very low severity level in induction motors. *IEEE Transactions on Industrial Electronics*, 68(4):3475–3484, 2021.

[32] Wiehan le Roux, Ronald G. Harley, and Thomas G. Habetler. Detecting rotor faults in low power permanent magnet synchronous machines. *IEEE Transactions on Power Electronics*, 22(1):322–328, 2007.

[33] Seyyed Mehdi Mirimani, Abolfazl Vahedi, Fabrizio Marignetti, and Enzo De Santis. Static eccentricity fault detection in single-stator–single-rotor axial-flux permanent-magnet machines. *IEEE Transactions on Industry Applications*, 48(6):1838–1845, 2012.

[34] Jawad Faiz and H. Nejadi-Koti. Demagnetization fault indexes in permanent magnet synchronous motors—an overview. *IEEE Transactions on Magnetics*, 52(4):1–11, 2016.

[35] Jongman Hong, Doosoo Hyun, Sang Bin Lee, Ji-Yoon Yoo, and Kwang-Woon Lee. Automated monitoring of magnet quality for permanent-magnet synchronous motors at standstill. *IEEE Transactions on Industry Applications*, 46(4):1397–1405, 2010.

[36] J. F. Gieras. *Permanent Magnet Motor Technology: Design and Applications*. CRC Press, 3nd edition, 01 2009, pages 34-38, 82-86, 86-90.

[37] Ieee guide for diagnostic field testing of electric power apparatus - electrical machinery. *IEEE Std 62.2-2004*, pages 1–108, 2005.

[38] Seungdeog Choi, Moinul Shahidul Haque, Md Tawhid Bin Tarek, Vamsi Mulpuri, Yao Duan, Sanjoy Das, Vijay Garg, Dan M. Ionel, M. Abul Masrur, Behrooz Mirafzal, and Hamid A. Toliyat. Fault diagnosis techniques for permanent magnet ac machine and drives—a review of current state of the art. *IEEE Transactions on Transportation Electrification*, 4(2):444–463, 2018.

[39] Arun Gandhi, Timothy Corrigan, and Leila Parsa. Recent advances in modeling and online detection of stator interturn faults in electrical motors. *IEEE Transactions on Industrial Electronics*, 58(5):1564–1575, 2011.

[40] Martin Riera-Guasp, Jose A. Antonino-Daviu, and Gérard-André Capolino. Advances in electrical machine, power electronic, and drive condition monitoring and fault detection: State of the art. *IEEE Transactions on Industrial Electronics*, 62(3):1746–1759, 2015.

[41] Satish Rajagopalan, Wiehan le Roux, Thomas G. Habetler, and Ronald G. Harley. Dynamic eccentricity and demagnetized rotor magnet detection in trapezoidal flux (brushless dc) motors operating under different load conditions. *IEEE Transactions on Power Electronics*, 22(5):2061–2069, 2007.

[42] Bashir Mahdi Ebrahimi, Jawad Faiz, and Mehrsan Javan Roshtkhari. Static-, dynamic-, and mixed-eccentricity fault diagnoses in permanent-magnet synchronous motors. *IEEE Transactions on Industrial Electronics*, 56(11):4727–4739, 2009.

[43] Taner Goktas, Mohsen Zafarani, and Bilal Akin. Discernment of broken magnet and static eccentricity faults in permanent magnet synchronous motors. *IEEE Transactions on Energy Conversion*, 31(2):578–587, 2016.

[44] Bashir Mahdi Ebrahimi and Jawad Faiz. Feature extraction for short-circuit fault detection in permanent-magnet synchronous motors using stator-current monitoring. *IEEE Transactions on Power Electronics*, 25(10):2673–2682, 2010.

[45] Prabhakar Neti and Subhasis Nandi. Stator interturn fault detection of synchronous machines using field current and rotor search-coil voltage signature analysis. *IEEE Transactions on Industry Applications*, 45(3):911–920, 2009.

[46] Julio-César Urresty, Jordi-Roger Riba, and Luís Romeral. Influence of the stator windings configuration in the currents and zero-sequence voltage harmonics in permanent magnet synchronous motors with demagnetization faults. *IEEE Transactions on Magnetics*, 49(8):4885–4893, 2013.

[47] Harold Saavedra, Julio-César Urresty, Jordi-Roger Riba, and Luís Romeral. Detection of interturn faults in pmsms with different winding configurations. *Energy Conversion and Management*, 79:534–542, 2014.

[48] Eri Maruyama, Akihito Nakahara, Akeshi Takahashi, and Kenji Miyata. Circulating current in parallel connected stator windings due to rotor eccentricity in permanent magnet motors. In *2013 IEEE Energy Conversion Congress and Exposition*, pages 2850–2855, 2013.

[49] Julio-César Urresty, Jordi-Roger Riba, and Luís Romeral. A back-emf based method to detect magnet failures in pmsms. *IEEE Transactions on Magnetics*, 49(1):591–598, 2013.

[50] BM Ebrahimi and J Faiz. Diagnosis and performance analysis of three-phase permanent magnet synchronous motors with static, dynamic and mixed eccentricity. *IET electric power applications*, 4(1):53–66, 2010.

[51] Bashir Mahdi Ebrahimi and Jawad Faiz. Demagnetization fault diagnosis in surface mounted permanent magnet synchronous motors. *IEEE Transactions on Magnetics*, 49(3):1185–1192, 2013.

[52] Julio-César Urresty, Jordi-Roger Riba, Miguel Delgado, and Luís Romeral. Detection of demagnetization faults in surface-mounted permanent magnet synchronous motors by means of the zero-sequence voltage component. *IEEE Transactions on Energy Conversion*, 27(1):42–51, 2012.

[53] Jun Hang, Jianzhong Zhang, Ming Cheng, and Jin Huang. Online interturn fault diagnosis of permanent magnet synchronous machine using zero-sequence components. *IEEE Transactions on Power Electronics*, 30(12):6731–6741, 2015.

[54] Julio-César Urresty, Jordi-Roger Riba, and Luis Romeral. Diagnosis of interturn faults in pmsms operating under nonstationary conditions by applying order tracking filtering. *IEEE Transactions on Power Electronics*, 28(1):507–515, 2013.

[55] Babak Vaseghi, Noureddine Takorabet, and Farid Meibody-Tabar. Fault analysis and parameter identification of permanent-magnet motors by the finite-element method. *IEEE Transactions on Magnetics*, 45(9):3290–3295, 2009.

[56] Thierry Boileau, Nicolas Leboeuf, Babak Nahid-Mobarakeh, and Farid Meibody-Tabar. Synchronous demodulation of control voltages for stator interturn fault detection in pmsm. *IEEE Transactions on Power Electronics*, 28(12):5647–5654, 2013.

[57] Fabien Meinguet, Eric Semail, Xavier Kestelyn, Yves Mollet, and Johan Gyselinck. Change-detection algorithm for short-circuit fault detection in closed-loop ac drives. *IET Electric Power Applications*, 8(5):165–177, 2014.

[58] Julio-César Urresty, Reza Atashkhooei, Jordi-Roger Riba, Luís Romeral, and Santiago Royo. Shaft trajectory analysis in a partially demagnetized permanent-magnet synchronous motor. *IEEE Transactions on Industrial Electronics*, 60(8):3454–3461, 2013.

[59] Jongman Hong, Sanguk Park, Doosoo Hyun, Tae-june Kang, Sang Bin Lee, Christian Kral, and Anton Haumer. Detection and classification of rotor demagnetization and eccentricity faults for pm synchronous motors. *IEEE Transactions on Industry Applications*, 48(3):923–932, 2012.

[60] David G. Dorrell, Min-Fu Hsieh, and YouGuang Guo. Unbalanced magnet pull in large brushless rare-earth permanent magnet motors with rotor eccentricity. *IEEE Transactions on Magnetics*, 45(10):4586–4589, 2009.

[61] Wesley G. Zanardelli, Elias G. Strangas, and Selin Aviyente. Identification of intermittent electrical and mechanical faults in permanent-magnet ac drives based on time–frequency analysis. *IEEE Transactions on Industry Applications*, 43(4):971–980, 2007.

[62] H. Kim. On-line mechanical unbalance estimation for permanent magnet synchronous machine drives. *IET Electric Power Applications*, 3:178–186(8), May 2009.

[63] Jianzhong Zhang, Jun Hang, and Ming Cheng. Diagnosis of mechanical unbalance fault in permanent magnet synchronous machine drives. *Electric Power Components and Systems*, 44(12):1408–1417, 2016.

[64] Kyeong-Hwa Kim. Simple online fault detecting scheme for short-circuited turn in a pmsm through current harmonic monitoring. *IEEE Transactions on Industrial Electronics*, 58(6):2565–2568, 2011.

[65] Satish Rajagopalan, Jos M. Aller, Jos A. Restrepo, Thomas G. Habetler, and Ronald G. Harley. Detection of rotor faults in brushless dc motors operating under nonstationary conditions. *IEEE Transactions on Industry Applications*, 42(6):1464–1477, 2006.

[66] Joan Pons-Llinares, Jose A. Antonino-Daviu, Martín Riera-Guasp, Sang Bin Lee, Tae-june Kang, and Chanseung Yang. Advanced induction motor rotor fault diagnosis via continuous and discrete time–frequency tools. *IEEE Transactions on Industrial Electronics*, 62(3):1791–1802, 2015.

[67] Elias G. Strangas, Selin Aviyente, and Syed Sajjad H. Zaidi. Time–frequency analysis for efficient fault diagnosis and failure prognosis for interior permanent-magnet ac motors. *IEEE Transactions on Industrial Electronics*, 55(12):4191–4199, 2008.

[68] Jordi-Roger Riba Ruiz, Javier A. Rosero, Antonio Garcia Espinosa, and Luis Romeral. Detection of demagnetization faults in permanent-magnet synchronous motors under nonstationary conditions. *IEEE Transactions on Magnetics*, 45(7):2961–2969, 2009.

[69] Takeo Ishikawa, Yutaro Seki, and Nobuyuki Kurita. Analysis for fault detection of vector-controlled permanent magnet synchronous motor with permanent magnet defect. *IEEE Transactions on Magnetics*, 49(5):2331–2334, 2013.

[70] Vicente Climente-Alarcon, Jose A. Antonino-Daviu, Martin Riera-Guasp, and Miroslav Vlcek. Induction motor diagnosis by advanced notch fir filters and the wigner–ville distribution. *IEEE Transactions on Industrial Electronics*, 61(8):4217–4227, 2014.

[71] Satish Rajagopalan, Jos M. Aller, Jos A. Restrepo, Thomas G. Habetler, and Ronald G. Harley. Analytic-wavelet-ridge-based detection of dynamic eccentricity in brushless direct current (bldc) motors functioning under dynamic operating conditions. *IEEE Transactions on Industrial Electronics*, 54(3):1410–1419, 2007.

[72] Antonio Garcia Espinosa, Javier A. Rosero, Jordi Cusidó, Luis Romeral, and Juan Antonio Ortega. Fault detection by means of hilbert–huang transform of the stator current in a pmsm with demagnetization. *IEEE Transactions on Energy Conversion*, 25(2):312–318, 2010.

[73] Jordi-Roger Riba Ruiz, Antonio Garcia Espinosa, Luís Romeral, and Jordi Cusidó. Demagnetization diagnosis in permanent magnet synchronous motors under non-stationary speed conditions. *Electric Power Systems Research*, 80(10):1277–1285, 2010.

[74] Miguel Delgado Prieto, Antonio Garcia Espinosa, Jordi-Roger Riba Ruiz, Julio César Urresty, and Juan Antonio Ortega. Feature extraction of demagnetization faults in permanent-magnet synchronous motors based on box-counting fractal dimension. *IEEE Transactions on Industrial Electronics*, 58(5):1594–1605, 2011.

[75] Anees Mohammed, Juan I. Melecio, and Siniša Djurović. Electrical machine permanent magnets health monitoring and diagnosis using an air-gap magnetic sensor. *IEEE Sensors Journal*, 20(10):5251–5259, 2020.

[76] Yonghyun Park, Chanseung Yang, Sang Bin Lee, Dong-Myung Lee, Daniel Fernandez, David Reigosa, and Fernando Briz. Online detection and classification of rotor and load defects in pmsms based on hall sensor measurements. *IEEE Transactions on Industry Applications*, 55(4):3803–3812, 2019.

[77] David Reigosa, Daniel Fernández, María Martínez, Yonghyun Park, Sang Bin Lee, and Fernando Briz. Permanent magnet synchronous machine non-uniform demagnetization detection using zero-sequence magnetic field density. *IEEE Transactions on Industry Applications*, 55(4):3823–3833, 2019.

[78] David Reigosa, Daniel Fernández, Yonghyun Park, Alberto B. Diez, Sang Bin Lee, and Fernando Briz. Detection of demagnetization in permanent magnet synchronous machines using hall-effect sensors. In *2017 IEEE Energy Conversion Congress and Exposition (ECCE)*, pages 4686–4693, 2017.

[79] Kyungjin Kang, Jeongyong Song, Chiho Kang, Sangjin Sung, and Gunhee Jang. Real-time detection of the dynamic eccentricity in permanent-magnet synchronous motors by monitoring speed and back emf induced in an additional winding. *IEEE Transactions on Industrial Electronics*, 64(9):7191–7200, 2017.

[80] Giorgos A. Skarmoutsos, Konstantinos N. Gyftakis, and Markus Mueller. Detecting partial demagnetization in afpm generators by monitoring speed and emf induced in a supplemental winding. *IEEE Transactions on Industrial Informatics*, 18(5):3295–3305, 2022.

[81] Muhammad Saad Rafaq, Hyeon-Jun Lee, Yonghyun Park, Sang Bin Lee, Marcos Orviz Zapico, Daniel Fernandez, David Reigosa, and Fernando Briz. Airgap search coil based identification of pm synchronous motor defects. *IEEE Transactions on Industrial Electronics*, 69(7):6551–6560, 2022.

[82] Yao Da, Xiaodong Shi, and Mahesh Krishnamurthy. A novel universal sensor concept for survivable pmsm drives. *IEEE Transactions on Power Electronics*, 28(12):5630–5638, 2013.

[83] Ozan Keysan and H. Bulent Ertan. Real-time speed and position estimation using rotor slot harmonics. *IEEE Transactions on Industrial Informatics*, 9(2):899–908, 2013.

[84] Xinda Song, Jiancheng Fang, and Bangcheng Han. High-precision rotor position detection for high-speed surface pmsm drive based on linear hall-effect sensors. *IEEE Transactions on Power Electronics*, 31(7):4720–4731, 2016.

[85] Gang Liu, Baodong Chen, and Xinda Song. High-precision speed and position estimation based on hall vector frequency tracking for pmsm with bipolar hall-effect sensors. *IEEE Sensors Journal*, 19(6):2347–2355, 2019.

[86] Zheng Liu, Wenping Cao, Po-Hsu Huang, Gui-Yun Tian, and James L. Kirtley. Non-invasive winding fault detection for induction machines based on stray flux magnetic sensors. In *2016 IEEE Power and Energy Society General Meeting (PESGM)*, pages 1–6, 2016.

[87] Anees Mohammed and Siniša Djurović. Electric machine bearing health monitoring and ball fault detection by simultaneous thermo-mechanical fibre optic sensing. *IEEE Transactions on Energy Conversion*, 36(1):71–80, 2021.

[88] Aleksi Riitala. *Estimating the speed of a permanent magnet synchronous machine using magnetic leakage flux, MSc thesis*. Lappeenranta University of Technology, LUT School of Energy Systems,pages 25-28, 01 2018.

[89] Teymoor Ghanbari and Amin Farjah. Application of rogowski search coil for stator fault diagnosis in electrical machines. *IEEE Sensors Journal*, 14(2):311–312, 2014.

[90] Mauricio Cuevas, Raphaël Romary, Jean-Philippe Lecointe, Fabrice Morganti, and Thierry Jacq. Noninvasive detection of winding short-circuit faults in salient pole synchronous machine with squirrel-cage damper. *IEEE Transactions on Industry Applications*, 54(6):5988–5997, 2018.

[91] Lucia Frosini, Ciprian Harlişca, and Loránd Szabó. Induction machine bearing fault detection by means of statistical processing of the stray flux measurement. *IEEE Transactions on Industrial Electronics*, 62(3):1846–1854, 2015.

[92] G. A. Skarmoutsos, K. N. Gyftakis, and M. Mueller. Mcsa versus flux monitoring for demagnetization diagnosis in axial-flux pm generators. In *2021 IEEE 13th International Symposium on Diagnostics for Electrical Machines, Power Electronics and Drives (SDEMPED)*, volume 1, pages 119–125, 2021.

[93] Pengfei Tian, Carlos A. Platero, Konstantinos N. Gyftakis, and Jose Manuel Guerrero. Stray flux sensor core impact on the condition monitoring of electrical machines. *Sensors*, 20(3), 2020.

[94] Galina Mirzaeva, Khalid Imtiaz Saad, and Mohsen Ghaffarpour Jahromi. Comprehensive diagnostics of induction motor faults based on measurement of space and time dependencies of air gap flux. *IEEE Transactions on Industry Applications*, 53(3):2657–2666, 2017.

[95] Galina Mirzaeva and Khalid Imtiaz Saad. Advanced diagnosis of stator turn-to-turn faults and static eccentricity in induction motors based on internal flux measurement. *IEEE Transactions on Industry Applications*, 54(4):3961–3970, 2018.

[96] Galina Mirzaeva and Khalid Imtiaz Saad. Advanced diagnosis of rotor faults and eccentricity in induction motors based on internal flux measurement. *IEEE Transactions on Industry Applications*, 54(3):2981–2991, 2018.

[97] Kyung-Tae Kim, Seung-Tae Lee, and Jin Hur. Diagnosis technique using a detection coil in bldc motors with interturn faults. *IEEE Transactions on Magnetics*, 50(2):885–888, 2014.

[98] Chong Zeng, Song Huang, Yongming Yang, and Dun Wu. Inter-turn fault diagnosis of permanent magnet synchronous machine based on tooth magnetic flux analysis. *IET Electric Power Applications*, 12(6):837–844, 2018.

[99] Xuyang Liu, Wenchao Miao, Qi Xu, Libing Cao, Chunhua Liu, and Philip W. T. Pong. Inter-turn short-circuit fault detection approach for permanent magnet synchronous machines through stray magnetic field sensing. *IEEE Sensors Journal*, 19(18):7884–7895, 2019.

[100] Taner Goktas, Mohsen Zafarani, Kun Wang Lee, Bilal Akin, and Terry Sculley. Comprehensive analysis of magnet defect fault monitoring through leakage flux. *IEEE Transactions on Magnetics*, 53(4):1–10, 2017.

[101] Juan I. Melecio. Fea model study of spectral signature patterns of pm demagnetisation faults in synchronous pm machines. *The Journal of Engineering*, 2019:4127–4132(5), June 2019.

[102] Maarten J. Kamper, Rong-Jie Wang, and Francois G. Rossouw. Analysis and performance of axial flux permanent-magnet machine with air-cored nonoverlapping concentrated stator windings. *IEEE Transactions on Industry Applications*, 44(5):1495–1504, 2008.

[103] Seyyed Mehdi Mirimani, Abolfazl Vahedi, and Fabrizio Marignetti. Effect of inclined static eccentricity fault in single stator-single rotor axial flux permanent magnet machines. *IEEE Transactions on Magnetics*, 48(1):143–149, 2012.

[104] Mark Thiele and Greg Heins. Computationally efficient method for identifying manufacturing induced rotor and stator misalignment in permanent magnet brushless machines. *IEEE Transactions on Industry Applications*, 52(4):3033–3040, 2016.

[105] Baocheng Guo, Yunkai Huang, Fei Peng, Jianning Dong, and Yongjian Li. Analytical modeling of misalignment in axial flux permanent magnet machine. *IEEE Transactions on Industrial Electronics*, 67(6):4433–4443, 2020.

[106] A. C. Barmpatza, J. C. Kappatou, and G. A. Skarmoutsos. Investigation of static angular and axis misalignment in an afpm generator. In *2019 IEEE Workshop on Electrical Machines Design, Control and Diagnosis (WEMDCD)*, volume 1, pages 163–168, 2019.

[107] Reemon Z. Haddad and Elias G. Strangas. On the accuracy of fault detection and separation in permanent magnet synchronous machines using mcsa/mvsa and lda. *IEEE Transactions on Energy Conversion*, 31(3):924–934, 2016.

[108] Oladapo O. Ogidi, Paul S. Barendse, and Mohamed A. Khan. Detection of static eccentricities in axial-flux permanent-magnet machines with concentrated windings using vibration analysis. *IEEE Transactions on Industry Applications*, 51(6):4425–4434, 2015.

[109] Ehsan Ajily, Mohammad Ardebili, and Karim Abbaszadeh. Magnet defect and rotor eccentricity modeling in axial-flux permanent-magnet machines via 3-d field reconstruction method. *IEEE Transactions on Energy Conversion*, 31(2):486–495, 2016.

[110] Zahra Shabahang, Mostafa Shahnazari, and Alireza Sedighi. Analysis of dynamic eccentricity in a coreless axial flux permanent magnet machine. In *2015 30th International Power System Conference (PSC)*, pages 358–362, 2015.

[111] O. O. Ogidi, P. S. Barendse, and M. A. Khan. Influence of rotor topologies and cogging torque minimization techniques in the detection of static eccentricities in axial-flux permanent-magnet machine. *IEEE Transactions on Industry Applications*, 53(1):161–170, 2017.

[112] Gojko M. Joksimović, Jakša Riger, Thomas M. Wolbank, Nedjeljko Perić, and Mario Vašak. Stator-current spectrum signature of healthy cage rotor induction machines. *IEEE Transactions on Industrial Electronics*, 60(9):4025–4033, 2013.

[113] Konstantinos N. Gyftakis, Syidy Ab Rasid, Giorgos A. Skarmoutsos, and Markus Mueller. The demagnetization harmonics generation mechanism in permanent magnet machines with concentrated windings. *IEEE Transactions on Energy Conversion*, 36(4):2934–2944, 2021.

[114] Thierry Lubin, Smail Mezani, and Abderrezak Rezzoug. Two-dimensional analytical calculation of magnetic field and electromagnetic torque for surface-inset permanent-magnet motors. *IEEE Transactions on Magnetics*, 48(6):2080–2091, 2012.

[115] Z.Q. Zhu, D. Howe, and Z.P. Xia. Prediction of open-circuit airgap field distribution in brushless machines having an inset permanent magnet rotor topology. *IEEE Transactions on Magnetics*, 30(1):98–107, 1994.

[116] Thierry Lubin, Smail Mezani, and Abderrezak Rezzoug. 2-d exact analytical model for surface-mounted permanent-magnet motors with semi-closed slots. *IEEE Transactions on Magnetics*, 47(2):479–492, 2011.

[117] Peixin Liang, Feng Chai, Lei Chen, and Yunpeng Wang. Analytical prediction of no-load stator iron losses in spoke-type permanent-magnet synchronous machines. *IEEE Transactions on Energy Conversion*, 33(1):252–259, 2018.

[118] Alberto Tessarolo. Analytical determination of slot leakage field and inductances of electric machines with double-layer windings and semiclosed slots. *IEEE Transactions on Energy Conversion*, 30(4):1528–1536, 2015.

[119] Alberto Tessarolo. Leakage field analytical computation in semiclosed slots of unsaturated electric machines. *IEEE Transactions on Energy Conversion*, 30(2):431–440, 2015.

[120] Zhen Zhang, Changliang Xia, Huimin Wang, and Tingna Shi. Analytical field calculation and analysis of surface inset permanent magnet machines with high saliency ratio. *IEEE Transactions on Magnetics*, 52(12):1–12, 2016.

[121] Akbar Rahideh and Theodosios Korakianitis. Analytical magnetic field distribution of slotless brushless machines with inset permanent magnets. *IEEE Transactions on Magnetics*, 47(6):1763–1774, 2011.

[122] Akbar Rahideh and Theodosios Korakianitis. Analytical armature reaction field distribution of slotless brushless machines with inset permanent magnets. *IEEE Transactions on Magnetics*, 48(7):2178–2191, 2012.

[123] Akbar Rahideh, Mohammad Mardaneh, and Theodosios Korakianitis. Analytical 2-d calculations of torque, inductance, and back-emf for brushless slotless machines with surface inset magnets. *IEEE Transactions on Magnetics*, 49(8):4873–4884, 2013.

[124] A. Bellara, H. Tiegna, Y. Amara, and G. Barakat. On load analytical modelling of the magnetic field for axial flux surface-inset permanent magnet machines with semi-closed slots. In *2012 XXth International Conference on Electrical Machines*, pages 2852–2858, 2012.

[125] H. S. Zhang, M. L. Yang, Y. Zhang, J. Y. Tuo, S. Luo, and J. Xu. Analytical calculation of surface-inset pm in-wheel motors and reduction of torque ripple. *IEEE Transactions on Magnetics*, 57(1):1–11, 2021.

[126] Linni Jian, K. T. Chau, Yu Gong, Chuang Yu, and Wenlong Li. Analytical calculation of magnetic field in surface-inset permanent magnet motors. *IEEE Transactions on Magnetics*, 45(10):4688–4691, 2009.

[127] K. Boughrara, D. Zarko, R. Ibtiouen, O. Touhami, and A. Rezzoug. Magnetic field analysis of inset and surface-mounted permanent-magnet synchronous motors using schwarz–christoffel transformation. *IEEE Transactions on Magnetics*, 45(8):3166–3178, 2009.

[128] Nady Boules. Prediction of no-load flux density distribution in permanent magnet machines. *IEEE Transactions on Industry Applications*, IA-21(3):633–643, 1985.

[129] Z.Q. Zhu, D. Howe, E. Bolte, and B. Ackermann. Instantaneous magnetic field distribution in brushless permanent magnet dc motors. i. open-circuit field. *IEEE Transactions on Magnetics*, 29(1):124–135, 1993.

[130] Z.Q. Zhu, D. Howe, and C.C. Chan. Improved analytical model for predicting the magnetic field distribution in brushless permanent-magnet machines. *IEEE Transactions on Magnetics*, 38(1):229–238, 2002.

[131] Xinghua Wang, Qingfu Li, Shuhong Wang, and Qunfeng Li. Analytical calculation of air-gap magnetic field distribution and instantaneous characteristics of brushless dc motors. *IEEE Transactions on Energy Conversion*, 18(3):424–432, 2003.

[132] K.F. Rasmussen, J.H. Davies, T.J.E. Miller, M.I. McGelp, and M. Olaru. Analytical and numerical computation of air-gap magnetic fields in brushless motors with surface permanent magnets. *IEEE Transactions on Industry Applications*, 36(6):1547–1554, 2000.

[133] FrÉdÉric Dubas and Christophe Espanet. Analytical solution of the magnetic field in permanent-magnet motors taking into account slotting effect: No-load vector potential and flux density calculation. *IEEE Transactions on Magnetics*, 45(5):2097–2109, 2009.

[134] B. L. J. Gysen, K. J. Meessen, J. J. H. Paulides, and E. A. Lomonova. General formulation of the electromagnetic field distribution in machines and devices using fourier analysis. *IEEE Transactions on Magnetics*, 46(1):39–52, 2010.

[135] D. Zarko, D. Ban, and T.A. Lipo. Analytical calculation of magnetic field distribution in the slotted air gap of a surface permanent-magnet motor using complex relative air-gap permeance. *IEEE Transactions on Magnetics*, 42(7):1828–1837, 2006.

[136] Nicolas Bracikowski, Michel Hecquet, Pascal Brochet, and Sergey V. Shirinskii. Multiphysics modeling of a permanent magnet synchronous machine by using lumped models. *IEEE Transactions on Industrial Electronics*, 59(6):2426–2437, 2012.

[137] G. Xiong and S.A. Nasar. Analysis of fields and forces in a permanent magnet linear synchronous machine based on the concept of magnetic charge. *IEEE Transactions on Magnetics*, 25(3):2713–2719, 1989.

[138] Peixin Liang, Feng Chai, Yi Li, and Yulong Pei. Analytical prediction of magnetic field distribution in spoke-type permanent-magnet synchronous machines accounting for bridge saturation and magnet shape. *IEEE Transactions on Industrial Electronics*, 64(5):3479–3488, 2017.

[139] Melita Hajdinjak and Damijan Miljavec. Analytical calculation of the magnetic field distribution in slotless brushless machines with u-shaped interior permanent magnets. *IEEE Transactions on Industrial Electronics*, 67(8):6721–6731, 2020.

[140] Zhentao S. Du and Thomas A. Lipo. High torque density and low torque ripple shaped-magnet machines using sinusoidal plus third harmonic shaped magnets. *IEEE Transactions on Industry Applications*, 55(3):2601–2610, 2019.

[141] Thierry Lubin, Smail Mezani, and Abderrezak Rezzoug. Exact analytical method for magnetic field computation in the air gap of cylindrical electrical machines considering slotting effects. *IEEE Transactions on Magnetics*, 46(4):1092–1099, 2010.

[142] Stanley Jerome Farlow. Partial differential equations for scientists and engineers. *Dover Publications, Inc*, pages 64–71, 1993.

[143] Paul W. Berg and James. L. McGregor. Elementary partial differential equations. *Holden Day*, pages 46–95, 1989.